

Alma Mater Studiorum – Università di Bologna

DOTTORATO DI RICERCA IN

INGEGNERIA CIVILE, CHIMICA, AMBIENTALE E DEI MATERIALI

Ciclo XXX

**Settore Concorsuale: SC 03/B2**

**Settore Scientifico Disciplinare: CHIM/07**

Handling of molten Poly(ethylene terephthalate) cylinders  
for preforms compression molding machines

**Presentata da: Dott. Ing. Marco Carati**

**Coordinatore Dottorato**

**Prof. Luca Vittuari**

**Supervisori**

**Prof. Maurizio Fiorini  
Prof. Ing. Francesco Ubertini  
Dott. Ing. Daniele Marastoni**

**Esame finale anno 2018**



## Abstract

This thesis describes the research done on the handling of molten Poly(ethylene terephthalate) (PET) cylinders - from now on "gobs" - for preform compression molding, which is a cutting-edge technology in the beverage field. SACMI, a world leading company in manufacturing advanced packaging plants, holds a strong background in compression molding technologies. A new way of handling gobs was investigated, i.e. the pneumatic transport through a swirl flow generated by a particular pipe design. It was developed both with Computational Fluid Dynamic simulations and extensive field tests on a prototypal compression molding machine. The very promising results led SACMI to patent the swirl flow pipe design. A new testing machine was designed and assembled to further develop the tests. The ultimate validation will be on a new compression molding machine prototype. Simultaneously, improved CFD simulations were started to increase pipe efficiency. Moreover, simulations could reduce costs and testing time of new pipe design for different preforms. By comparing the simulation video with a real field test one, a part of the process simulation was validated. Gob adhesiveness to pipe inner walls increased after many gobs passed through the pipe. The cause could be the deposition of a very thin layer of PET oligomers on the pipe wall. Cyclic oligomers, which are dissolved in PET melt, vaporize and then condense on the pipe walls which are colder than the gob. FTIR analyses supported this conclusion. Finally, the effect of metal temperature on gob adhesiveness for short time contact, typical of the preform compression molding technology, was studied and an innovative kind of experiment was designed. A tests campaign was hence performed and led to the description of a new phenomenon for which a theoretical explanation was proposed. These results give a valuable contribution on this topic to the scientific community.

# Table of Contents

<b>Abstract</b>	III
<b>Table of Contents</b>	IV
<b>List of Tables</b>	VIII
<b>List of Figures</b>	X
<b>List of Abbreviations</b>	XIX
<b>Acknowledgements</b>	XXI
<b>Chapter 1 PET PREFORM MOLDING</b>	<b>1</b>
1.1 PET BOTTLES PRODUCTION	1
1.2 SACMI BEVERAGE LINE	4
1.3 BENCHMARK: PET PREFORM INJECTION MOLDING	5
1.3.1 Double stage	8
1.3.2 Single stage	9
1.4 NEW TECHNOLOGY: PET PREFORM COMPRESSION MOLDING	9
1.5 ADVANTAGES OF COMPRESSION MOLDING VS INJECTION MOLDING	11
1.5.1 Energy savings	11
1.5.2 PET material saving	14
1.5.2.1 Absence of gate	14
1.5.2.2 Preform wall thickness	16
1.5.2.3 Flat base preform	16
1.5.2.4 Weight lightening examples	17
1.5.3 Gate defects	18
1.5.3.1 Preforms	18
1.5.3.2 Bottles	19
1.5.4 Moisture content	20
1.5.5 Weight homogeneity	23
1.5.6 PET IV	24
	IV

1.5.7	Quality controls	25
1.5.8	Acetaldehyde	27
1.6	CONCLUSION AND FUTURE INDUSTRIAL DEVELOPMENTS	30
1.7	REFERENCES	31
<b>Chapter 2</b>	<b>PET - METAL ADHESIVENESS</b>	<b>33</b>
2.1	INTRODUCTION	33
2.2	MECHANISMS OF ADHESION	34
	2.2.1 Mechanical interlocking theory	34
	2.2.2 Electrostatic theory	35
	2.2.3 Chemical bonding theory	35
2.3	WORK OF ADHESION	35
2.4	SURFACE FREE ENERGY	36
2.5	INTERFACE CHARACTERIZATION ANALYTICAL TECHNIQUES	37
	2.5.1 XPS	37
2.6	ADHESION TEST	38
2.7	METAL THERMAL DEPOSITION ON PET	39
	2.7.1 Al/PET adhesion	39
	2.7.2 Effect of PET temperature during deposition and of subsequent water absorption	42
2.8	PET COATING ON METAL: Cr/PET adhesion	43
2.9	MOLD ADHESIVENESS REDUCTION	45
2.10	MOULD TEMPERATURE EFFECT ON THERMOPLASTIC BONDING TO METALS	46
2.11	REFERENCES	49
<b>Chapter 3</b>	<b>MOLTEN PET CYLINDERS HANDLING: PNEUMATIC TRANSPORT</b>	<b>51</b>
3.1	INTRODUCTION	51
3.2	PET GOB HANDLING LITERATURE AND PATENTS	54
3.3	PRELIMINARY GOB PNEUMATIC TRANSPORT CFD SIMULATIONS	56
3.4	PRELIMINARY TESTS	59
	3.4.1 Testing machine PAM002A	59
	3.4.2 Swirl pipe manufacturing	64

3.4.3	Gob accelerated ( $\alpha = 60^\circ$ )	65
3.4.4	Gob floating ( $\alpha = 15^\circ$ )	67
3.4.4.1	<i>Geometry</i>	68
3.4.4.2	<i>Surface roughness and coatings</i>	75
3.4.4.3	<i>Temperature</i>	75
3.4.4.4	<i>Preform quality</i>	80
3.5	CONSIDERATIONS ON ADHESIVENESS	82
3.6	IMPROVED CFD SIMULATIONS	86
3.6.1	Simulation without gob	86
3.6.2	Simulation with gob	88
3.7	NEW TESTING MACHINE	91
3.8	FUTURE DEVELOPMENTS	95
3.9	REFERENCES	96
<b>Chapter 4</b>	<b>THE EFFECT OF METAL TEMPERATURE ON MOLTEN PET - METAL ADHESIVENESS FOR SHORT TIME CONTACT</b>	<b>97</b>
4.1	INTRODUCTION	97
4.2	TEST DESIGN	97
4.2.1	Test goals	97
4.2.2	Testing machine	99
4.2.3	Test equipment	101
4.2.3.1	<i>Infrared Camera</i>	101
4.2.3.2	<i>High speed video recording camera</i>	102
4.2.3.3	<i>PET hygrometer</i>	104
4.2.3.4	<i>Thermometer with thermocouples</i>	106
4.2.3.5	<i>Air hygrometer</i>	106
4.2.4	Plate heating transient time	107
4.2.5	Polymer properties and dehumidification parameters	111
4.2.6	Test methodology	111
4.3	METAL SURFACES CHARACTERIZATION	113
4.3.1	Roughness	113
4.3.2	Contact angle tests	116
4.3.2.1	<i>Instrument</i>	116

4.3.2.2	<i>Plates samples</i>	116
4.3.2.3	<i>Liquid tested</i>	116
4.3.2.4	<i>Test conditions</i>	117
4.3.2.5	<i>Results</i>	118
4.3.2.5.1	AISI316 rough surface (PAM0029A059-1A)	120
4.3.2.5.2	AISI316 polished surface (PAM0029A059-1B)	122
4.3.2.5.3	EN AW-6082-T6 rough surface (PAM0029A061-1A)	124
4.3.2.5.4	EN AW-6082-T6 polished surface (PAM0029A061-1B)	126
4.4	MODEL FOR THE ANALYSYS OF ADHESIVENESS VARIATION WITH TEMPERATURE	128
4.5	TESTING MACHINE SETTING	128
4.5.1	Plate position	130
4.5.2	Gobs size	132
4.5.3	Plate thermoregulation characterization	138
4.6	TEST RESULTS	140
4.6.1	Effect of plate temperature	140
4.6.2	Influence of monitored parameters variation on adhesiveness	147
4.6.2.1	<i>Gob weight</i>	152
4.6.2.2	<i>Water content</i>	155
4.6.2.3	<i>Conclusion</i>	160
4.6.3	Adhesiveness below sticking temperature	161
4.7	SHORT CONTACT TIME ADHESIVENESS MODEL	165
4.8	REFERENCES	166
<b>Chapter 5</b>	<b>CONCLUSIONS</b>	<b>167</b>

## List of Tables

Table 1.1	Results of DSC analysis on the gate and body of an injection molded preform.	15
Table 1.2	Preform wall thickness limit comparison between injection and compression technology.	16
Table 1.3	Preform/bottle weight reduction thanks to compression technology.	18
Table 1.4	Gate defects on injection molded preforms.	18 - 19
Table 1.5	Weight variability of compression molded preforms.	23
Table 1.6	Usual preforms weight tolerances.	23
Table 2.1	Modification of the adhesion values of Al/PET wafers with the annealing conditions of the polymer.	42
Table 3.1	Chemical composition of cleaning spray for internal pipe surface.	68
Table 4.1	Comparison of chemical composition between EN AW-6082-T6 and AISI 316.	98
Table 4.2	Comparison of physical properties between EN AW-6082-T6 and AISI 316.	98
Table 4.3	Template for data collected during tests.	112
Table 4.4	Surface tension and molecular weight values of liquids used in the tests.	117
Table 4.5	Temperature and relative humidity conditions of contact angle tests.	117
Table 4.6	Contact angle and surface free energy resulting from tests.	119
Table 4.7	Measurements of gob dimensions, weight and crystallinity.	137
Table 4.8	Minimum and maximum temperature measured on plate compared to the required one.	141
Table 4.9	Highest temperature at which all gobs bounce considering instrument measuring errors.	142
Table 4.10	Highest temperature at which all gobs bounce: difference between aluminum and stainless steel.	142
Table 4.11	Lowest temperature at which all gobs stick considering instrument measuring errors.	143
Table 4.12	Lowest temperature at which all gobs stick: difference between aluminum and stainless steel.	143
Table 4.13	Test report of gob 72.	144
Table 4.14	Test report of gob 380.	145

Table 4.15	Maximum and minimum values of the monitored parameters during tests on different plate materials.	147
Table 4.16	Parameters variation of tests at plate temperature equal to 80 °C.	147
Table 4.17	Parameters variation of tests at plate temperature equal to 85 °C.	148
Table 4.18	Parameters variation of tests at plate temperature equal to 90 °C.	148
Table 4.19	Parameters variation of tests at plate temperature equal to 95 °C.	148
Table 4.20	Parameters variation of tests at plate temperature equal to 100 °C.	149
Table 4.21	Parameters variation of tests at plate temperature equal to 105 °C.	149
Table 4.22	Parameters variation of tests at plate temperature equal to 110 °C.	150
Table 4.23	Parameters variation of tests at plate temperature equal to 115 °C.	150
Table 4.24	Parameters variation of tests at plate temperature equal to 120 °C.	150
Table 4.25	Parameters variation of tests at plate temperature equal to 125 °C.	151
Table 4.26	Parameters variation of tests at plate temperature equal to 130 °C.	151
Table 4.27	Parameters variation of tests at plate temperature equal to 135 °C.	151
Table 4.28	Average gob weight and its standard deviation for three different sample compositions.	152
Table 4.29	Part of a daily test report including the heaviest gob (351).	153
Table 4.30	Part of a daily test report including the sticking gobs just before the heaviest one (351).	154
Table 4.31	Collage of tests reports at plate temperature equal to 120 °C.	159
Table 4.32	Analysis of gob contact time on AISI 316 plate.	163
Table 4.33	Analysis of gob contact time on EN AW-6082-T6 plate.	164

## List of Figures

Figure 1.1	PET molecule.	1
Figure 1.2	PET pellets.	1
Figure 1.3	PET injection preform.	2
Figure 1.4	Illustration of the stretch blow molding process.	2
Figure 1.5	Life cycle of a plastic bottle: recycling options.	3
Figure 1.6	Entire beverage Hero line by SACMI.	4
Figure 1.7	SACMI Beverage solutions.	4
Figure 1.8	SACMI "hero LINE".	5
Figure 1.9	SACMI Packaging lab competences.	5
Figure 1.10	Estimated injection molding machine market sharing.	6
Figure 1.11	Overall diagram of an injection molding unit.	6
Figure 1.12	Illustration of reciprocating screw operation.	7
Figure 1.13	Illustration of screw operation with shooting pot.	7
Figure 1.14	72 cavities injection mold.	7
Figure 1.15	Exploded diagram of hot chamber distribution ducts on a 72 cavities mold.	8
Figure 1.16	Thermal history of a bottle: from preform to bottle using a single-stage process or a two-stage one.	9
Figure 1.17	Preform compression molding machine scheme.	10
Figure 1.18	Injection molding technology versus compression one: comparison between required cavities number to get the same productivity.	10
Figure 1.19	HeroPET4.0 layout.	11
Figure 1.20	Temperature profile over time: injection double stage (red line) compared to compression single one (green line) (a). The red area qualitatively represents the energy difference (b).	12
Figure 1.21	Temperature profiles across preform thickness.	12
Figure 1.22	Compression molded preform wall temperature before blower.	13
Figure 1.23	Compression molded preform underneck temperature before blower.	13

Figure 1.24	Compression molded preform versus injection molded one: the compression preform is without the gate (red circle).	14
Figure 1.25	DSC curves on the gate and body of an injection molded preform.	15
Figure 1.26	SACMI flat HERO base preform.	16
Figure 1.27	Preform weight lightening for 1.5 liter bottle thanks to compression molding.	17
Figure 1.28	Preform weight lightening for 0.5 liter bottle thanks to compression molding.	17
Figure 1.29	Bottle breakages starting from gate defects.	20
Figure 1.30	Moisture content inside preform wall with time from preform molding to blowing.	21
Figure 1.31	Preform moisture content affects $T_g$ .	21
Figure 1.32	PET preform crystallization halftime as function of preform relative humidity at different temperature.	22
Figure 1.33	Moisture rings on a preform and on a bottle.	22
Figure 1.34	Weight variability of compression molded preforms.	23
Figure 1.35	Weight variability of injection molded preforms.	23
Figure 1.36	Thermal stability test chamber	24
Figure 1.37	Burst test machine.	24
Figure 1.38	Percentage of dimensional variation (measuring diameters shown on the bottle on the left) and fill level drop for different IV values.	25
Figure 1.39	Burst pressure function of IV values.	25
Figure 1.40	Preforms output comparison between compression and injection molding machine.	26
Figure 1.41	Preform dome quality control with SACMI vision system.	26
Figure 1.42	Acetaldehyde (AA) molecule.	27
Figure 1.43	Generation of acetaldehyde as a function of extruder residence time and temperature for initial water content in the PET melt of 3 and 3000 ppm.	27
Figure 1.44	AA generation as function of residence time.	28
Figure 1.45	AA generation as function of process temperature.	28
Figure 1.46	AA generation as function of PET back pressure.	29
Figure 1.47	AA generation (ppm): comparison between injection and compression molding.	29

Figure 1.48	Energy and intralogistic costs comparison: Double stages benchmark and heroPET4.0 (compression single stage).	30
Figure 1.49	Costs comparison. Double stages benchmark and heroPET4.0 (compression single stage).	30
Figure 2.1	Pigmented powder deposition on components close to the cutting zone during production of colored preforms.	33
Figure 2.2	Adhesion Mechanisms: (a) mechanical interlocking; (b) electrostatic attraction; (c) direct chemical bond formation.	34
Figure 2.3	Range and bond strength of typical interatomic and intermolecular interactions.	35
Figure 2.4	Wetting effect of two liquids with the same surface tension, but different polar and disperse component, on the same solid.	36
Figure 2.5	PET film low resolution survey XPS spectrum.	37
Figure 2.6	PET film high resolution XPS spectrum with components allocation to peaks.	38
Figure 2.7	Schematization of the more frequent metal/PET peel tests.	38
Figure 2.8	TEM analysis of metal penetration (30 - 40 Å) in plain PET film (a) and in co-polyester coated PET film (b) (same scale).	39
Figure 2.9	Morphology and structure of a low adhesion (80 g/in) aluminum thin film.	40
Figure 2.10	Schematic indication of Kono's Zr/PET interaction model.	41
Figure 2.11	Schematic indication of Kono's Al/PET interaction model with deposition in vacuum (b) and after O <sub>2</sub> treatment (c).	42
Figure 2.12	Model of the interaction in the skin of the polymer between s and p valence orbital metals.	43
Figure 2.13	A steel plate coated with electrolytic chromium (ECCS) and PET coatings (Corus).	44
Figure 2.14	Bonding of PET oxygen atoms to chromium substrate.	44
Figure 2.15	Bonding of delocalized benzene ring orbital electrons to chromium substrate.	45
Figure 2.16	Ra definition according to ISO 4287:1997. Z is the deviation from the average surface line.	45
Figure 2.17	Shalnov's adhesion strength measurement schema.	46
Figure 2.18	SEM image of polycarbonate surface with no aluminum preheating (4800X).	47
Figure 2.19	SEM image of polycarbonate surface with high aluminum preheating (4800X).	47
Figure 3.1	Preform compression molding machine: gob cutting and gob loading on handling tool.	51

Figure 3.2	Preform compression molding machine: pictures of gob loading on handling tool.	52
Figure 3.3	Handling tool coupled with molding carousel in a preform compression molding machine.	53
Figure 3.4	Transferring and molding carrousels layout in a preform compression molding machine.	53
Figure 3.5	Pictures of gob transfer from handling tool to mold cavity.	54
Figure 3.6	Handling tool with rolling elements.	55
Figure 3.7	Probability of gob (molten resin) passage time with vibrations (white columns, maximum 0.12 seconds) and without vibrations (black columns, maximum 0.64 seconds).	55
Figure 3.8	Handling tool with radial holes and lower pressure on cavity.	56
Figure 3.9	Swirl flow stationary CFD simulation (CFX): inlet pipe mesh modelling.	57
Figure 3.10	Swirl flow stationary CFD simulation (CFX): geometry and boundary conditions.	57
Figure 3.11	Swirl flow stationary CFD simulation (CFX): flow streamlines and alpha ( $\alpha$ ) angle.	58
Figure 3.12	Swirl flow stationary CFD simulation (CFX): circumferential velocity and velocity vectors projection with $\alpha$ equals to 15 °.	58
Figure 3.13	Swirl flow stationary CFD simulation (CFX): circumferential velocity and velocity vectors projection with $\alpha$ equals to 60 °.	59
Figure 3.14	PAM002A: PET dryer on mezzanine.	60
Figure 3.15	PAM002A: pipe from PET dryer to extruder inlet.	60
Figure 3.16	PAM002B: preform compression molding machine plant.	61
Figure 3.17	PAM002A: transferring (7), molding (2) and preform extraction carrousels (8) seen by row 1 in figure 3.4.	63
Figure 3.18	PAM002A: handling tool for gob pneumatic transport.	64
Figure 3.19	Swirl pipe tomography scan elaborated with the software GOM Inspect ©.	65
Figure 3.20	Gob loading with $\alpha = 60^\circ$ swirl pipe.	66
Figure 3.21	Test on handling tool gob trajectory repetitiveness.	66
Figure 3.22	Average angle between gob cutting and start gob exiting from handling tool and its standard deviation for $\alpha = 60^\circ$ .	67
Figure 3.23	Different axial position of the gob depending on swirl flow rate.	67

Figure 3.24	Tested pipes and their supports	68
Figure 3.25	First geometry for $\alpha = 15^\circ$ swirl pipe.	69
Figure 3.26	Example of swirl pipe flows cyclogram.	69
Figure 3.27	Second geometry for $\alpha = 15^\circ$ swirl pipe.	70
Figure 3.28	Image of a kind of Coandă effect.	70
Figure 3.29	Third geometry for $\alpha = 15^\circ$ swirl pipe.	71
Figure 3.30	Third geometry for $\alpha = 15^\circ$ swirl pipe: detail view of Coandă effect slit.	72
Figure 3.31	Fourth geometry for $\alpha = 15^\circ$ swirl pipe: Coandă effect double-slit and evacuation holes.	72
Figure 3.32	Pipe similar to the one of fig. 3.31 assembled on PAM002A testing machine.	73
Figure 3.33	Fifth geometry for $\alpha = 15^\circ$ swirl pipe: plurality of flat rings with grooves for air feeding.	74
Figure 3.34	Fifth geometry for $\alpha = 15^\circ$ swirl pipe: detail view of flat ring with grooves.	74
Figure 3.35	PET gob handling tool performances function of its internal average surface roughness. Performances are expressed in a quantitative way that assesses the sticking behavior of the gob on metal surface after many gobs passages (the higher the number, the better the antisticking behavior of the metal surface).	75
Figure 3.36	Temperature plot of a FEM simulation to optimize heated pipe thermal insulation.	76
Figure 3.37	Heated swirl pipe: radial deformation due to high temperature.	77
Figure 3.38	Inner part of an electric rotating joint.	77
Figure 3.39	Picture of heated swirl pipe with heating thermo-resistance and thermocouple.	78
Figure 3.40	Picture of heated swirl pipe with heating thermo-resistance and thermocouple.	78
Figure 3.41	High temperature endurance tests results.	79
Figure 3.42	Gob with defect after passage through swirl pipe.	80
Figure 3.43	Gob passed through swirl pipe and taken out from the cavity mold.	81
Figure 3.44	Polarized light on a preform whose gob passed through swirl pipe.	81
Figure 3.45	FTIR spectra of white layer deposited on gob cutting knife (red) and of PET (green).	83
Figure 3.46	PET polycondensation reaction starting from EG/TPA and EG/DMT.	84

Figure 3.47	BHET molecule.	85
Figure 3.48	Ethylene Terephthalate Cyclic Dimer.	85
Figure 3.49	Polydispersity index for different PET processes and reactor sizes.	85
Figure 3.50	Swirl flow stationary CFD simulation (CFX): relative static pressure for $\alpha = 15^\circ$ .	86
Figure 3.51	(a), (b), (c), (d) Swirl flow transient CFD simulation (AcuSolve™): relative static pressure $\alpha = 15^\circ$ .	87 - 88
Figure 3.52	Swirl flow transient CFD simulation with gob (FLOW-3D): starting conditions.	89
Figure 3.53	Swirl flow transient CFD simulation with gob (FLOW-3D): mesh setting.	89
Figure 3.54	Swirl flow transient CFD simulation with gob (FLOW-3D): gob floating position after 0.05 seconds (real time) the simulation started.	90
Figure 3.55	Swirl flow transient CFD simulation with gob (FLOW-3D) compared to real process.	90
Figure 3.56	Typical layout of gob handling zone of a preform compression molding machine.	91
Figure 3.57	Possible gob handling zone layout on a preform compression molding machine.	92
Figure 3.58	PAMLAB and extruder 3D model.	92
Figure 3.59	PAMLAB mezzanine and extruder.	93
Figure 3.60	PAMLAB layout (only the part under the mezzanine).	94
Figure 3.61	Designers control PAMLAB final assembling.	95
Figure 4.1	High temperature endurance tests results.	97
Figure 4.2	Testing machine (MONOPAM).	99
Figure 4.3	Testing machine: details of cutting zone.	100
Figure 4.4	Metal plate: back view.	100
Figure 4.5	Infrared camera.	101
Figure 4.6	Plate image taken with infrared camera. Point Sp1 temperature is equal to $56.4^\circ\text{C}$ .	101
Figure 4.7	Same image of fig.4.6 taken in the same instant with on board optical camera.	102
Figure 4.8	Laptop and control unit of the high speed camera used for tests.	102
Figure 4.9	Head of the high speed camera with lamps placed before tests started.	103

Figure 4.10	Pet pellets hygrometer.	104
Figure 4.11	PET hygrometer detail: reagent ( $\text{CaH}_2$ ) placed in a mesh based above the sample container.	105
Figure 4.12	PET dryer hopper: by opening a shutter PET pellets are taken out from the lower part of the hopper for humidity content measurements.	105
Figure 4.13	Contact and immersion thermocouples with thermometer.	106
Figure 4.14	Air hygrometer.	107
Figure 4.15	Air hygrometer position during tests.	107
Figure 4.16	Indicative transient thermal simulation on steel plate.	108
Figure 4.17	Indicative steady state thermal simulation on steel plate.	108
Figure 4.18	Composed image (infrared and visible spectra) of plate assembled on the machine.	109
Figure 4.19	Plate infrared picture at 12:40:01. Point Sp1 temperature is equal to 59 °C.	109
Figure 4.20	Plate infrared picture at 12:40:21. Point Sp1 temperature is equal to 59.7 °C.	110
Figure 4.21	Plate infrared picture at 12:41:47. Point Sp1 temperature is equal to 58.8 °C.	110
Figure 4.22	Plate infrared picture at 12:45:09. Point Sp1 temperature is equal to 56.1 °C.	111
Figure 4.23	Melt temperature measurement.	113
Figure 4.24	2D roughness measurement of EN AW-6082 T6 plate.	114
Figure 4.25	2D roughness measurement of AISI 316 plate.	114
Figure 4.26	HOMMEL-ETAMIC nanoscan 855.	115
Figure 4.27	3D roughness measurement of EN AW-6082-T6 plate.	115
Figure 4.28	3D roughness measurement of AISI 316 plate.	115
Figure 4.29	Plate drawing for contact angle sessile drop test.	116
Figure 4.30	Contact angle tests: syringe automatic filling.	118
Figure 4.31	Operator manually deposits liquid drop on plate surface.	119
Figure 4.32	Contact angle measurement: water drop on AISI 316 rough surface.	120
Figure 4.33	Contact angle measurement: diiodomethane drop on AISI 316 rough surface.	120
Figure 4.34	Contact angle results of water and diiodomethane on AISI 316 rough surface.	121
Figure 4.35	Surface free tension wetting envelope of AISI 316 rough surface.	121

Figure 4.36	Contact angle measurement: water drop on AISI 316 polished surface.	122
Figure 4.37	Contact angle measurement: diiodomethane drop on AISI 316 polished surface.	122
Figure 4.38	Contact angle results of water and diiodomethane on AISI 316 polished surface.	123
Figure 4.39	Surface free tension wetting envelope of AISI 316 polished surface.	123
Figure 4.40	Contact angle measurement: water drop on EN AW-6082-T6 rough surface.	124
Figure 4.41	Contact angle measurement: diiodomethane drop on EN AW-6082-T6 rough surface.	124
Figure 4.42	Contact angle results of water and diiodomethane on EN AW-6082-T6 rough surface.	125
Figure 4.43	Surface free tension wetting envelope of EN AW-6082-T6 rough surface.	125
Figure 4.44	Contact angle measurement: water drop on EN AW-6082-T6 polished surface.	126
Figure 4.45	Contact angle measurement: diiodomethane drop on EN AW-6082-T6 polished surface.	126
Figure 4.46	Contact angle results of water and diiodomethane on EN AW-6082-T6 polished surface.	127
Figure 4.47	Surface free tension wetting envelope of EN AW-6082-T6 polished surface.	127
Figure 4.48	Testing machine: protective sheets and dehumidified air pipes.	129
Figure 4.49	Testing machine: protective sheets.	129
Figure 4.50	Gob bouncing sequence on metal plate in position A.	130
Figure 4.51	Scrap gob cutting sequence with metal plate assembled in position B.	131
Figure 4.52	Valid gob bouncing on metal plate in position B.	132
Figure 4.53	Impact on plate of three different gobs.	132
Figure 4.54	Sequence of gob impact on plate.	133
Figure 4.55	Trajectories of three different gobs photographed in three different instants of the impact.	133
Figure 4.56	Gob before contact with plate (speed measurement with Tracker© tool).	134
Figure 4.57	Gob trajectory towards the water basin.	135
Figure 4.58	Sequence of images from gob cutting to gob entering the water (see water splashes in image 3).	135
Figure 4.59	PVT curves for a PET sample.	136

Figure 4.60	Gobs that hit water.	136
Figure 4.61	Gob measured dimensions.	137
Figure 4.62	Gob length measurement with Tracker© tool.	138
Figure 4.63	Temperature characterization of gob contact point on metal plate.	139
Figure 4.64	Results of temperature characterization of gob contact point on metal plate.	139
Figure 4.65	Tests results: quantity of gobs stuck and bounced on AISI 316 and EN AW-6082-T6.	140
Figure 4.66	Test results: gobs behavior on AISI 316 and EN AW-6082-T6 at different temperatures.	141
Figure 4.67	Test 72: gob after bouncing on AISI 316 plate at 120 °C.	145
Figure 4.68	Test 380: gob after bouncing on AISI 316 plate at 130 °C.	146
Figure 4.69	Test 378: gob sticking on AISI 316 plate at 130 °C.	146
Figure 4.70	Gob weight distribution.	152
Figure 4.71	Comparison between gob 351 (top image) and gob 352 (bottom image).	153
Figure 4.72	Comparison between gob 351 (on the left) and gob 350 (on the right).	154
Figure 4.73	Comparison between gob 354 (on the left) and gob 352 (on the right).	155
Figure 4.74	Comparison between gob 354 (on the left) and gob 351 (on the right).	155
Figure 4.75	Range of gobs sticking and bouncing air dew point at different plate temperature and material.	156
Figure 4.76	Gob 71 contact video sequence: each picture follows the previous one of 0.001 s.	157
Figure 4.77	Gob 71: after the contact with the plate, the gob makes a half rotation on it before sticking to the plate surface. The image was taken few milliseconds after figure 4.76.	158
Figure 4.78	Test 123: gob sticking on AISI 316 plate at 120 °C (air dew point 12.8 °C).	158
Figure 4.79	Test 83: gob sticking on AISI 316 plate at 120 °C (air dew point 11.2 °C).	159
Figure 4.80	Test 257 gob sticking on EN-AW-6082-T6 plate at 120 °C (air dew point 12.8 °C).	160
Figure 4.81	Gob after bouncing on plate (gob points trajectories traced with Tracker© tool.)	161
Figure 4.82	Average gob speed before contact with plate (bright color) and after the contact (soft color).	162

## List of Abbreviations

AA	Acetaldehyde
AFM	Atomic Force Microscopy
ATR	Attenuated Total Reflection
BHET	Bis-Hydroxyethyl Terephthalate
CFD	Computational fluid dynamics
CSD	Carbonated Soft Drink
DLC	Diamond Like Carbon
DMT	Dimethyl Terephthalate
DOF	Degrees Of Freedom
DSC	Differential Scanning Calorimetry
ECCS	Electrolytic Chromium Coated Steel
EG	Ethylene Glycol
FDA	Food and Drug Administration
FEM	Finite Element Method
FSI	Fluid–structure interaction
FTIR	Fourier Transform Infrared Spectroscopy
HACCP	Hazard Analysis and Critical Control Points
HERO	High Efficiency Resource Optimizer
heroPET4.0	SACMI rotative single stage machine (PAM coupled with SBF)
IV	Intrinsic Viscosity
L/D	Length/Diameter
L/T	Preform Length / Wall Thickness
MONOPAM	PAM with a single molding cavity
OWRK	Owens-Wendt-Rabel-Kaelble method
PAM	Preform Advanced Molding Machine

PAM002A	PAM first industrial prototype
PAM002B	PAM second industrial prototype
PAM003	PAM third industrial prototype
PAMLAB	PAM molten pet cylinder cutting and handling tools testing machine
PBT	Poly(butylene terephthalate)
PE	Poly(ethylene)
PET	Poly(ethylene terephthalate)
PID	Proportional - Integral - Derivative
PLA	Poly(lactic acid)
PP	Poly(propylene)
PPM	Parts Per Million
PS	Poly(styrene)
PTFE	Poly(tetrafluoroethylene)
RAMAN	Raman Spectroscopy
RH	Relative Humidity
SACMI	Società Anonima Cooperativa Meccanici Imola
SBF	Stretch Blow Forming Machine
SEM	Scanning Electron Microscopy
SFE	Surface Free Energy
SFT	Surface Free Tension
SIMS	Secondary ion mass spectrometry
TEM	Transmission Electron Spectroscopy
TFS	Tin Free Steel
TPA	Terephthalic Acid
XPS	X-Ray Photoelectron Spectroscopy

## Acknowledgements

I would firstly like to express a special thanks to my supervisors:

- Prof. M. Fiorini, for his scientific support during these years;
- Prof. F. Ubertini for encouraging me to apply for a Ph.D. and for following my first year of research;
- M.Sc.Eng. D. Marastoni for giving me a challenging topic to develop.

Secondly, I would like to thank SACMI, a world-leading company with deep roots in Italy, which is approaching its hundredth anniversary and whose noble aim is to create wealth for both employees and people living in Imola and surroundings. I would also like to express my gratitude to all my colleagues who, in many ways, with their skills, helped me developing the research topic.

Thirdly, I would like to thank Elsevier, John Wiley and Sons, KRÜSS, Japanese Society of Tribologists, Dr. Kono Mari, Mecmesin, PET Planet, Plastics Europe, PROTESA, SACMI, Springer Nature for the permission to reprint some images.

Moreover, I would like to thank my family and friends who saw me very rarely during these last years of work, study and research, but who have always been there in case of need.

Finally, I would like to thank my wife Debora who has always supported me with love and sacrifice. To her I dedicate this thesis.



PAM002A with me and the technicians Mr Ridolfi M. and Mr Zama M.



# Chapter 1

## PET PREFORM MOLDING

### 1.1 PET BOTTLES PRODUCTION

Poly(ethylene terephthalate) (PET) (fig. 1.1), the world's most common and best-known polyester [1], was discovered and patented in 1941 [1]. In 1973 its use for the production of shatterproof beverage bottles was patented [1].

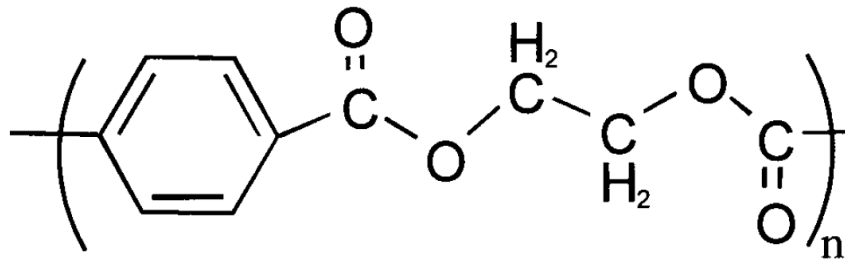


Figure 1.1 PET molecule.

It was a revolutionary discovery for the packaging world and, according to PlasticsEurope Market Research Group, in 2016, PET converter demand reached staggering 3.6 million tons a year only in EU-28 plus Norway and Switzerland [2]. This demand is rising with respect to the previous years [2, 3].



Figure 1.2 PET pellets.

Bottles production process starts from PET pellets (fig. 1.2) which are dehumidified, extruded and injected into closed molds with a preform shape. A preform (fig. 1.3) is an axial-symmetric semi-finished product: at one edge, there is the neck finish, that is, the external part of the preform opening,

the thread to seal the container with its cap and the support ring, while the opposite part with respect to the neck finish is closed by a typically hemispheric surface.



Figure 1.3 PET injection preform.

Preform is then transformed in a bottle through a process called stretch blow molding (fig. 1.4). Preforms are heated up few degrees above glass transition temperature with lamps that usually emit frequencies between 1100 and 1200 nm, because PET absorbs quite well at 1073 nm. After the heating, the preform enters a mold with bottle shape and it is stretch blown. The transformation acts in two directions, the axial (via stretching) and the radial (via blowing). PET crystallization stretch induced at a temperature slightly higher than PET glass transition temperature ( $T_g$ ) gives to the bottle particular mechanical properties. The following procedures are filling (which usually includes bottles capping), labelling and finally what it is called "secondary" packaging.

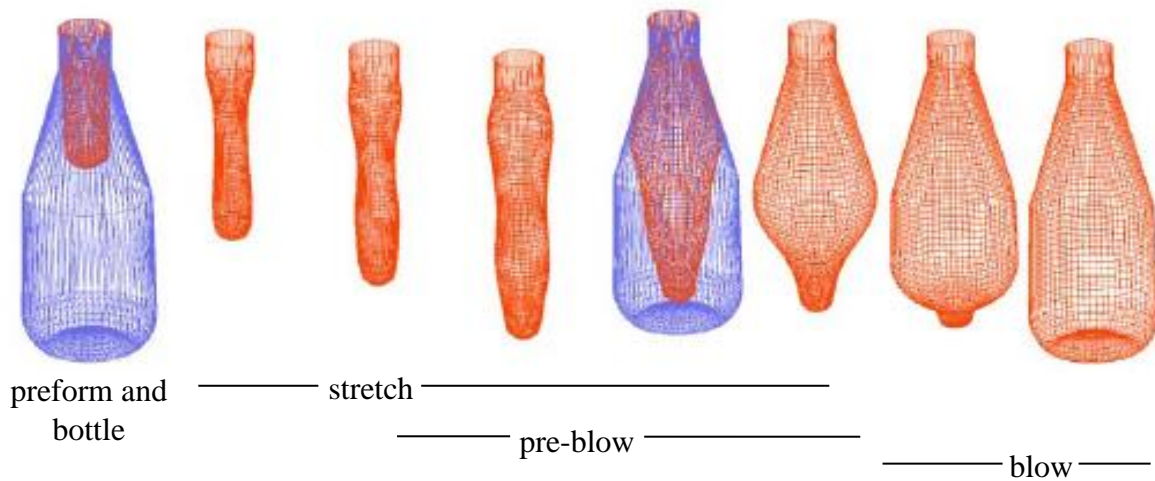


Figure 1.4 Illustration of the stretch blow molding process [1].

Finally, fig. 1.5 shows a scheme that reports the life cycle of a PET bottle [3].

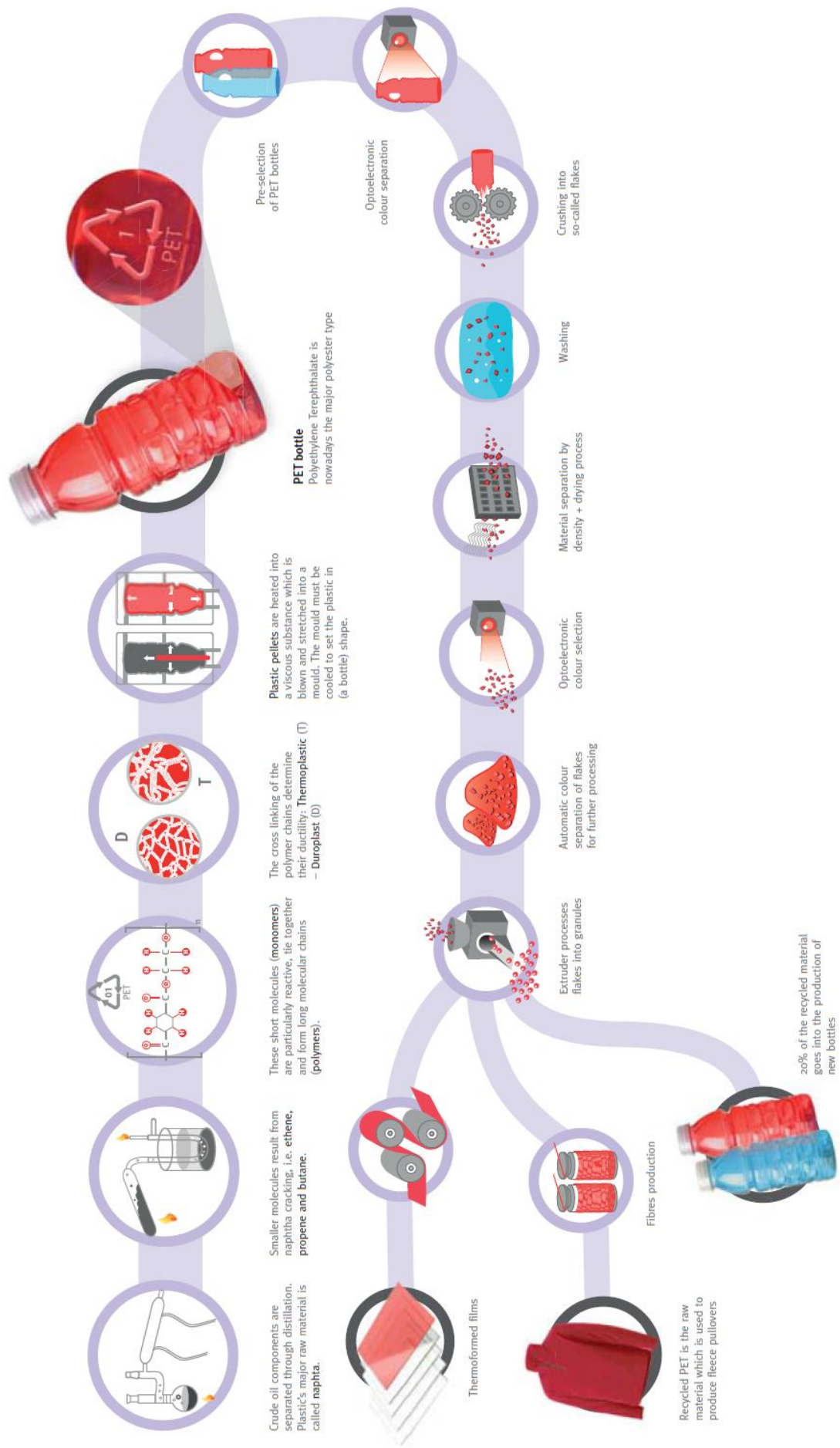


Figure 1.5 Life cycle of a plastic bottle: recycling options [3].

## 1.2 SACMI BEVERAGE LINE

This dissertation describes the results of the research done thanks to SACMI, a world leading company in manufacturing advanced packaging plants based in Imola (Italy), which is the only player on market that supplies the entire beverage line, from preforms molding machine to bottles palletizing: a turnkey plant.

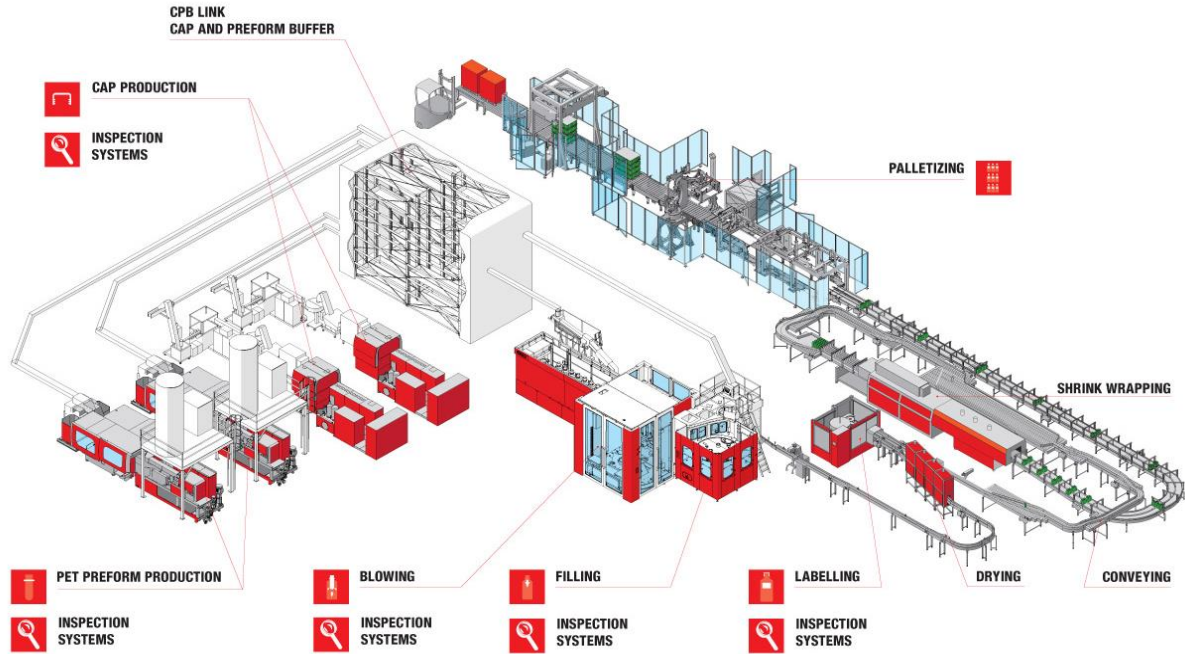


Figure 1.6 Entire beverage Hero line by SACMI [4].

Moreover, SACMI is the only player in the market that, to reduce operating costs, suggests to its customer 2 solutions (fig. 1.7):

- SACMI "hero LINE" (fig. 1.8), with a buffer (CPB) which controls contamination between preform injection and stretch blow molding machine.
- SACMI heroPET4.0, a rotative single stage compression molding machine whose advantage will be analyzed in detail in the following paragraphs.

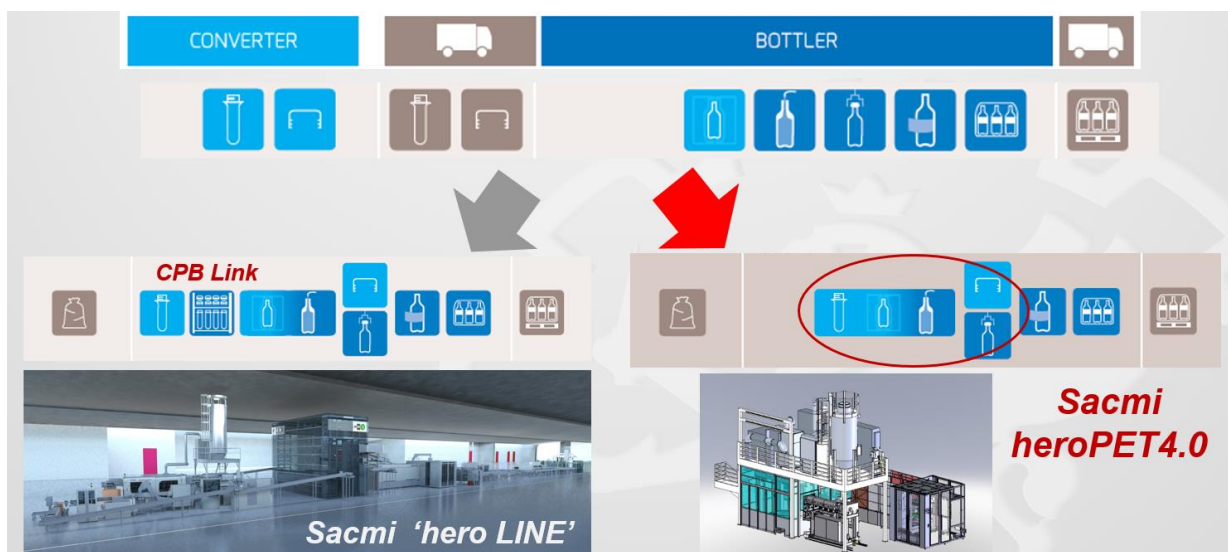


Figure 1.7 SACMI Beverage solutions [4].

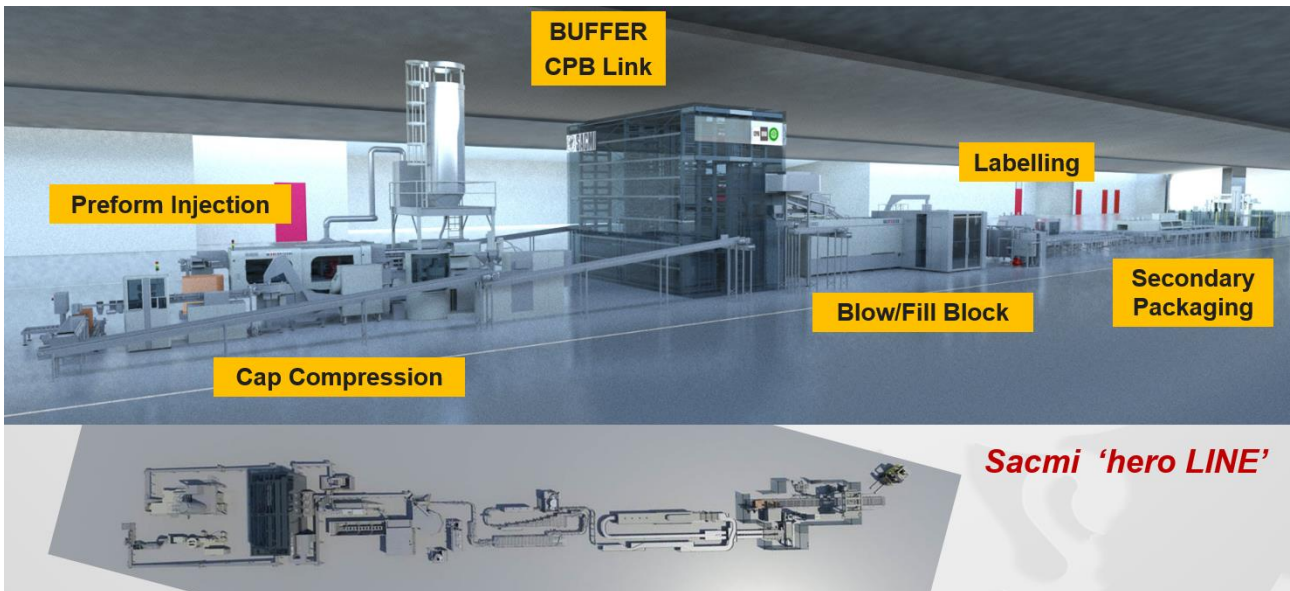


Figure 1.8 SACMI "hero LINE" [4].

Moreover SACMI offers to its customer extensive competence incorporated in the same structure (fig. 1.9).

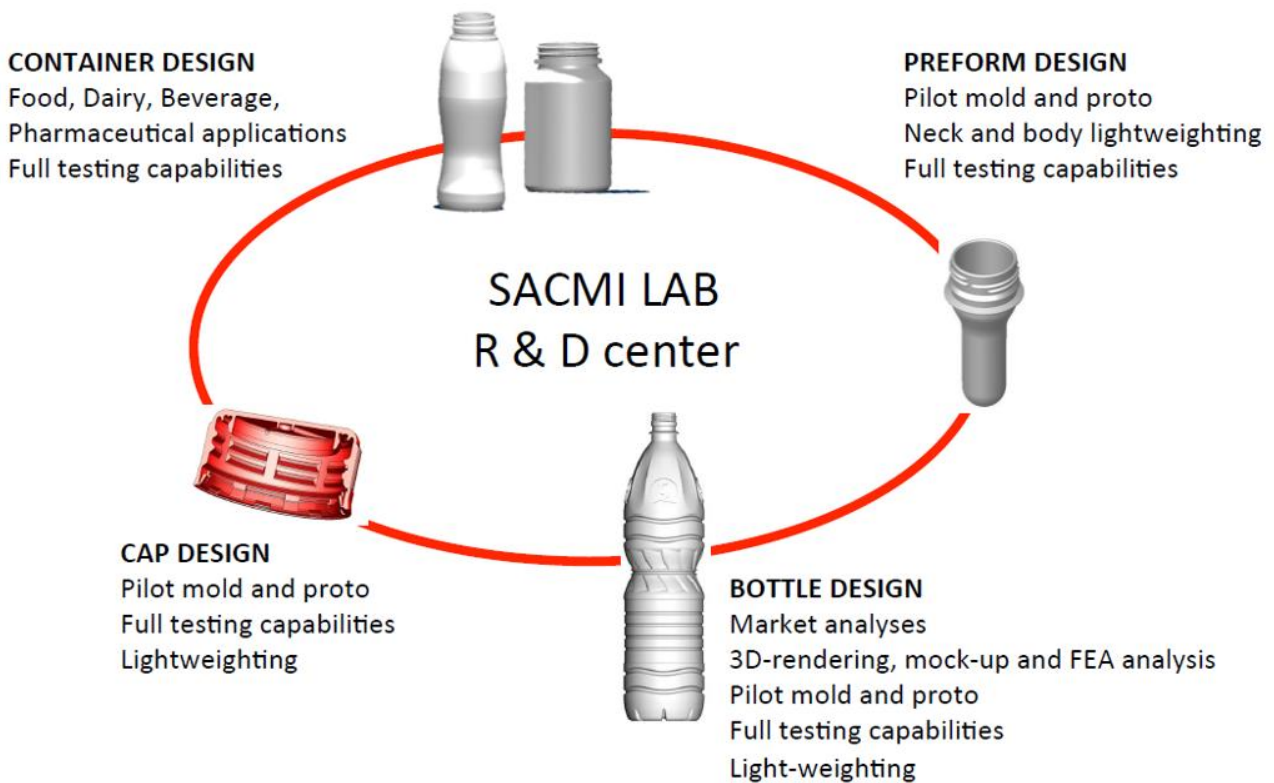


Figure 1.9 SACMI Packaging lab competences [4].

### 1.3 BENCHMARK: PET PREFORM INJECTION MOLDING

In 2016 the global injection molding machine market reached over 450 sold plants (fig. 1.10). The source is a SACMI internal analysis.

## Injection molding machine market

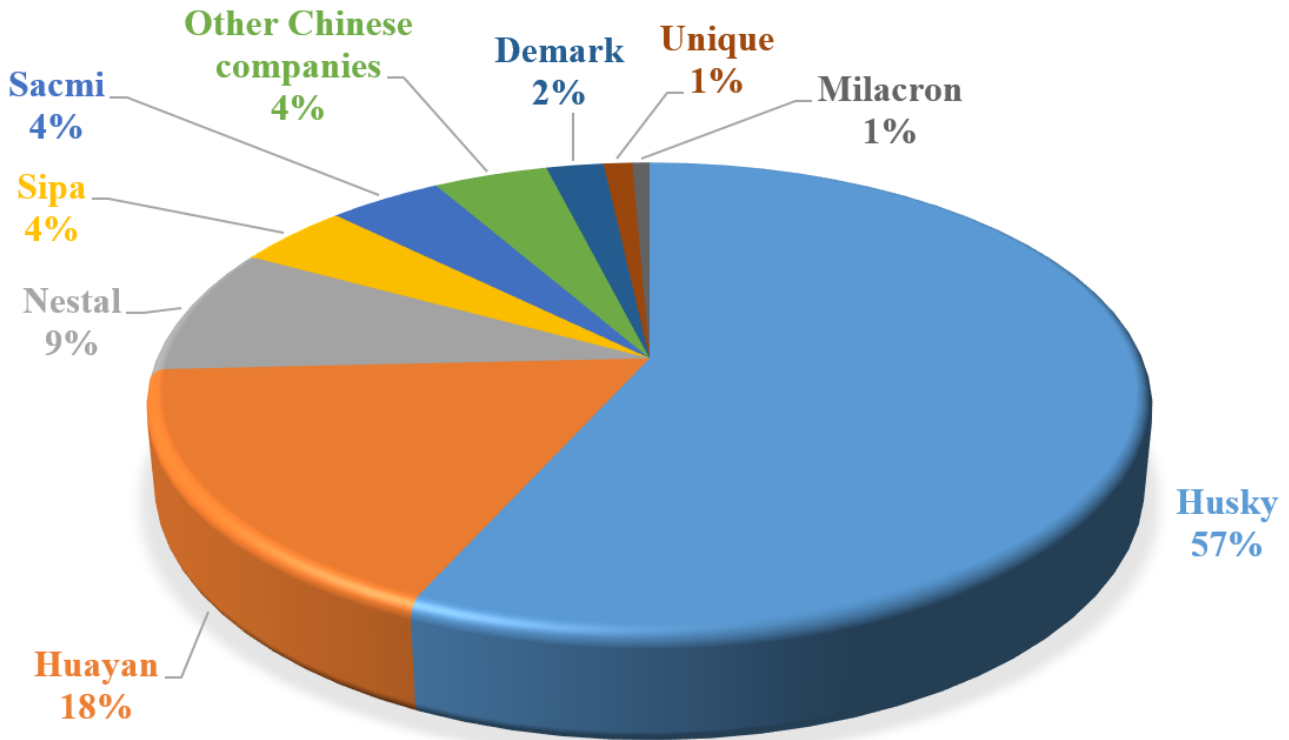


Figure 1.10 Estimated injection molding machine market sharing.

PET injection molding machine is composed by a PET dryer, an injection unit mounted on a base which also houses a press and a cooling robot (fig. 1.11).

After PET pellets dehumidification, injection molding machine involves an extruder which plasticizes and injects hot material into the closed mold (fig. 1.12). This second stage can, however, be performed with the aid of a reciprocating screw or a shooting pot (fig. 1.13).

In the shooting pot, the only function of the extruder is to plasticize the material continuously; a separate piston has the only function of injecting the plasticized material into the mold. This separation of function allows improvement of plasticization quality and reduces cycle times on plants with high flow rates because one unit plasticizes as the other injects, consequently reducing the size of the plant too.

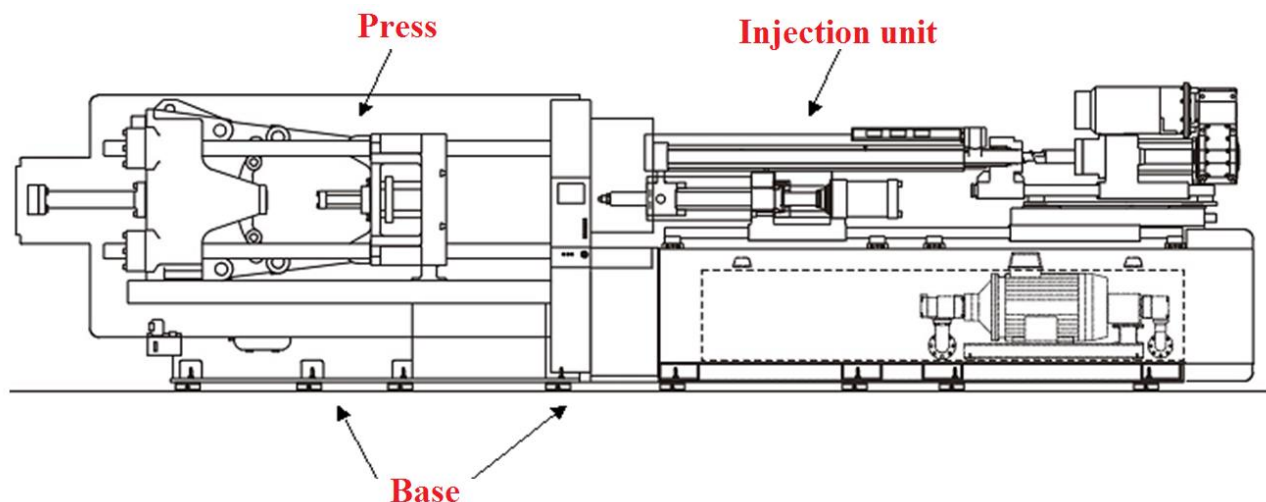


Figure 1.11 Overall diagram of an injection molding unit [1].

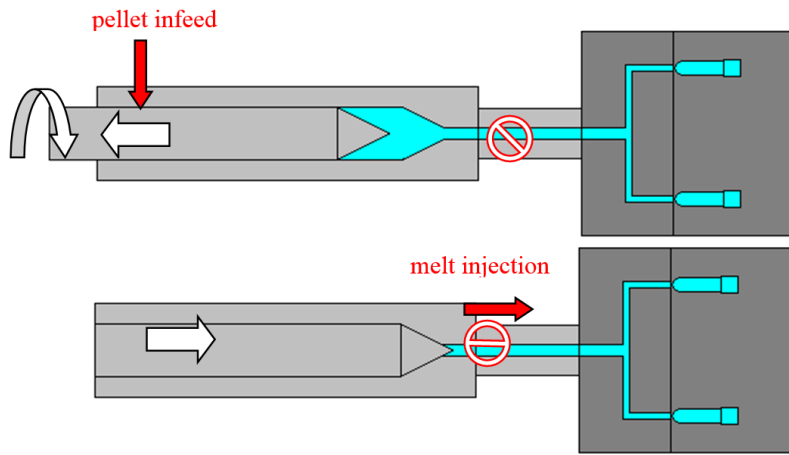


Figure 1.12 Illustration of reciprocating screw operation [1].

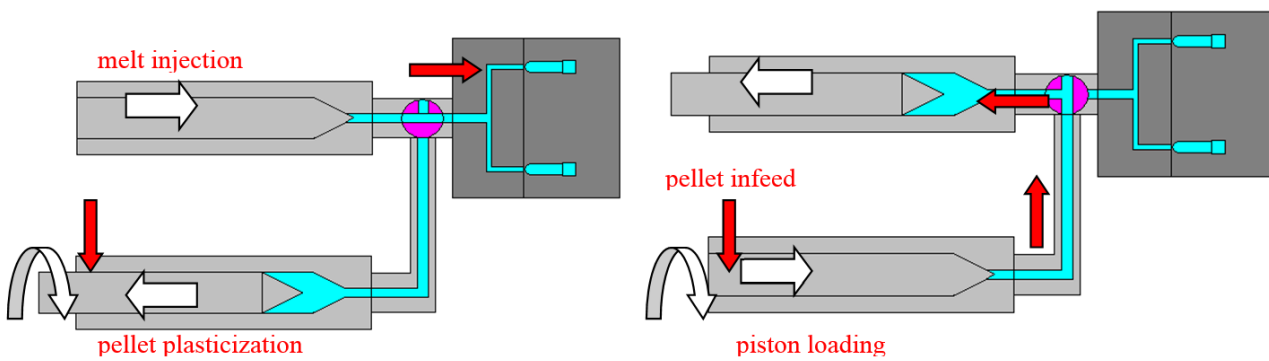


Figure 1.13 Illustration of screw operation with shooting pot [1].

The preform production mold consists of a mobile part with a certain number of cores and lips (components forming the neck finish) and a fixed part with an equal number of cavities (fig. 1.14).



Figure 1.14 72 - cavities injection mold [1].

The molten PET is distributed into cavities via a network of ducts (called hot chamber) to each injection unit (fig. 1.15). There it cools and solidifies to make the preform. Subsequently the mold opens and the preform is ejected from the mold.

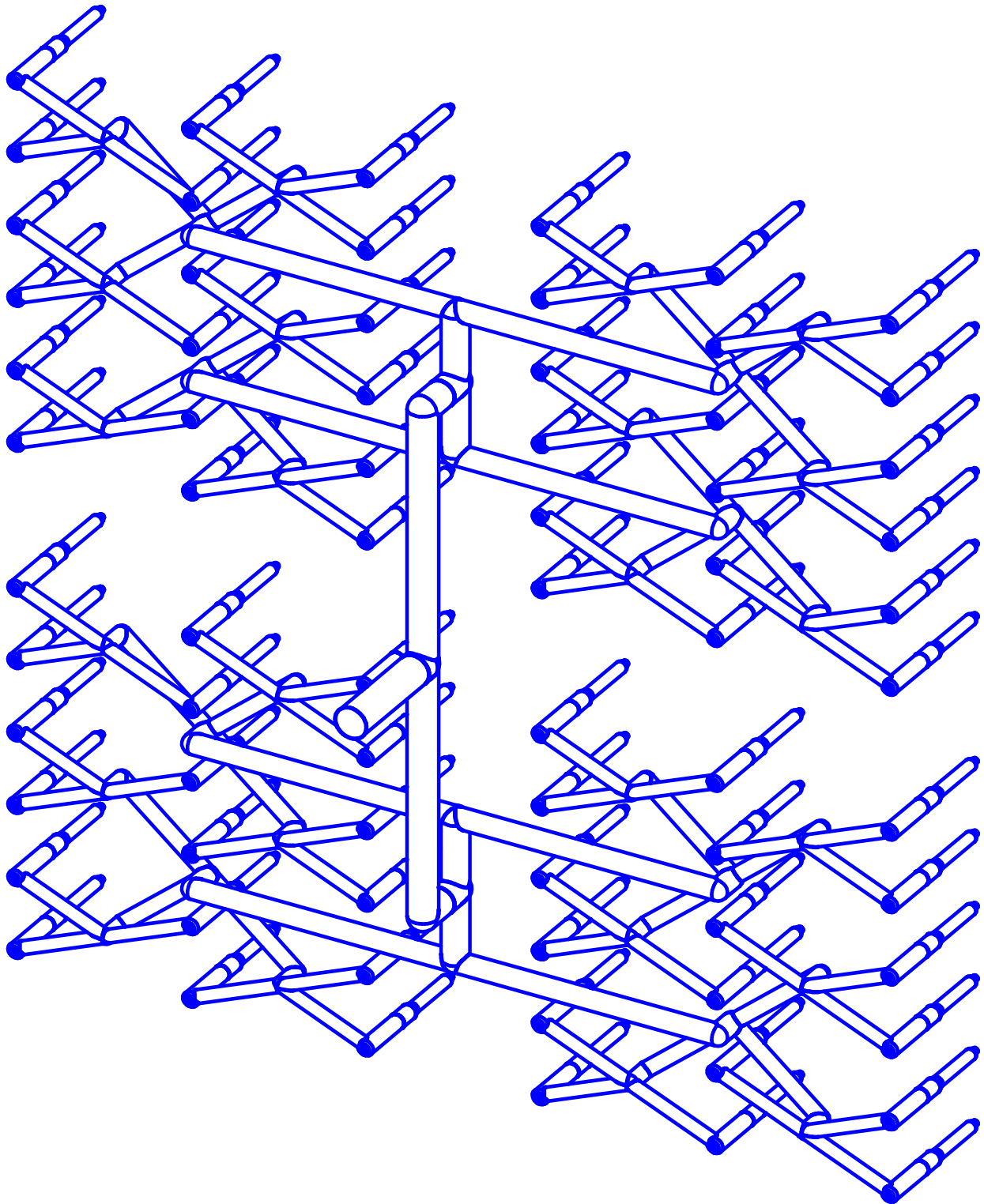


Figure 1.15 Exploded diagram of hot chamber distribution ducts on a 72-cavity mold [1].

### 1.3.1 Double stage

Finally, the preform is transferred in a post cooling unit with the purpose to lower the temperature of the preform from about 100 °C to below  $T_g$  (ideally < 60°C) so as to prevent deformation and/or

elastic returns and/or aesthetic defects. The preforms are then dropped in a box, called "octabin", to be stored during the travel from the production place (converter factory) to the blowing machine that is usually in another factory, the bottler one.

### 1.3.2 Single stage

Preforms are blown after few seconds from molding with a huge energy saving (fig. 1.16). In the past years a player in the market designed a linear single stage with blowing after preform injection molding. The productivity was lower than 22000 bph (bottles per hour) and it was not possible to put a filling or labelling machine, which are rotative, after blowing since bottles are not oriented.

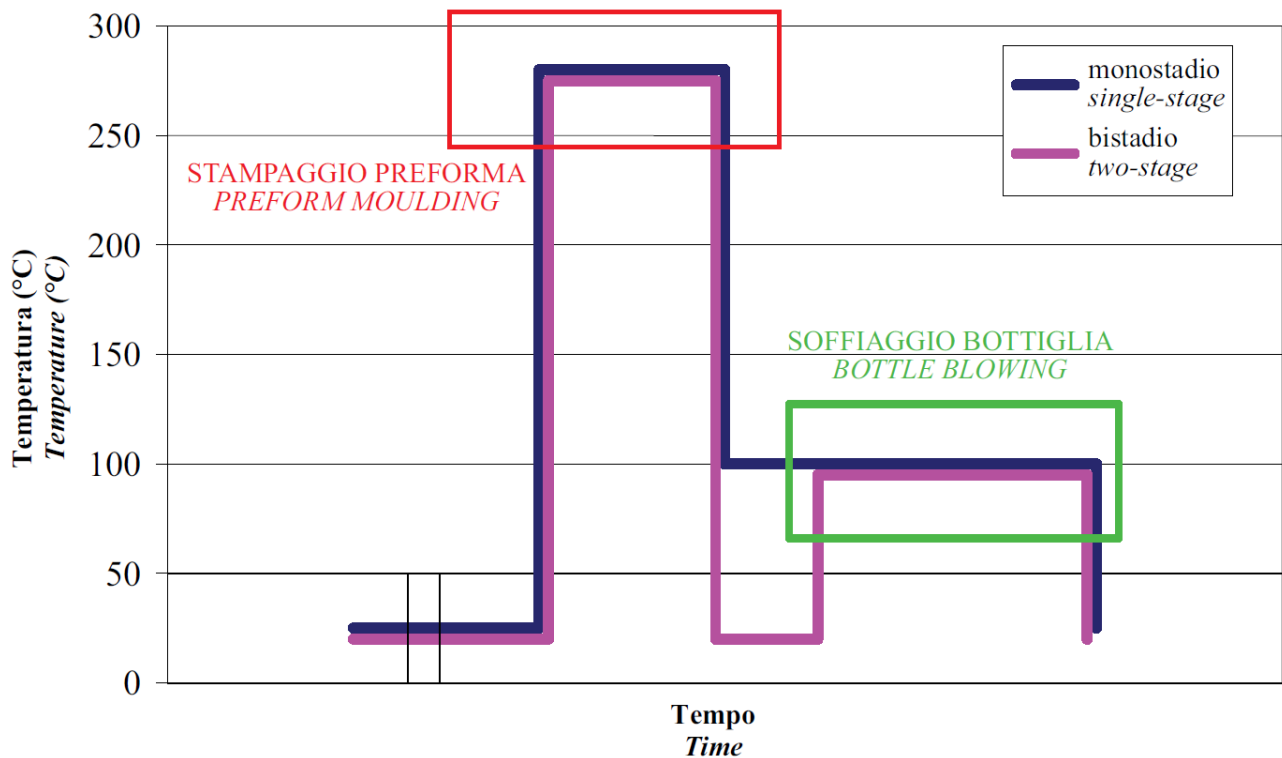


Figure 1.16 Thermal history of a bottle: from preform to bottle using a single-stage process or a two-stage one [1].

## 1.4 NEW TECHNOLOGY: PET PREFORM COMPRESSION MOULDING

As previously explained, SACMI supplies the machines for the entire beverage line. Furthermore, SACMI is developing and industrially testing (more than 50 million preforms at date of writing with a prototypal machine, named PAM003) an alternative process to produce preforms: compression molding (fig. 1.17), project PAM (Preform Advanced Molding Machine). After melting in an extruder, hot PET exits from a vertical axis nozzle whose dimensions are variable with preform geometry and mass. After the nozzle, a rotating blade cuts a cylinder of molten PET (from now on "gob"). The gob, whose weight and shape varies according to the kind of preform, is then handled and put inside an open mold cavity. From now on by handling we mean the phase starting just after gob cutting and finishing after gob insertion into the mold. Differently from injection molding, mold is open when the plastic enters and, only after gob entering the cavity, the three parts of the mold (core, cavity and lips) start closing at controlled speed and force. The closing of the mold gives the gob a preform shape. The preform is then extracted and finally post cooled.

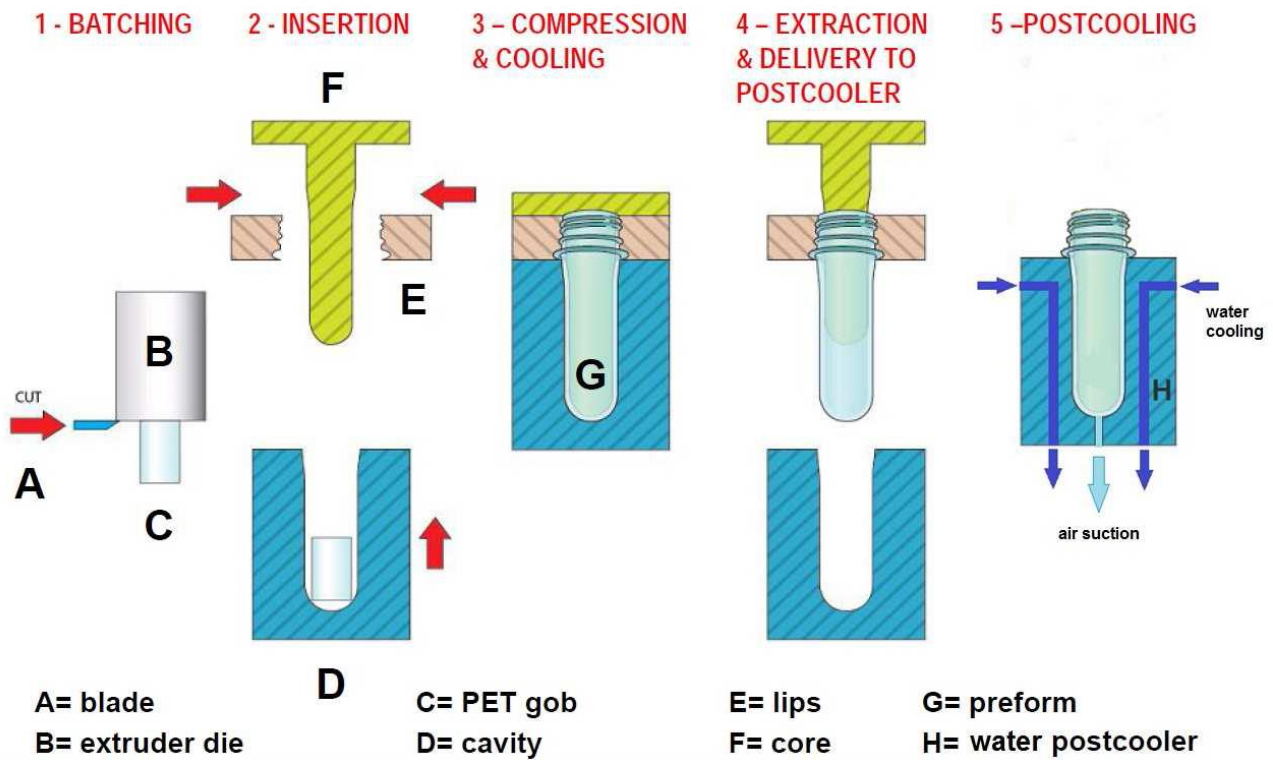


Figure 1.17 Preform compression molding machine scheme.

PAM machine with 48 molds is generally comparable to a 72 cavities mold on an injection molding machine (fig. 1.18) due to time reduction in filling cavities and lower (about 20 °C) melting temperature. That means that a preform of 9 g, which with injection molding machine benchmark has a cycle time of 5.8 seconds, with compression molding can be molded in almost 3.3 seconds.

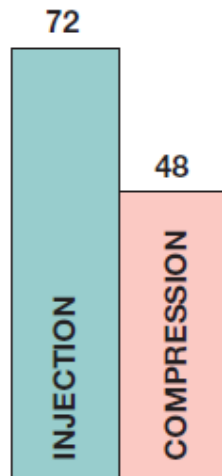


Figure 1.18 Injection molding technology versus compression one: comparison between required cavities number to get the same productivity.

The great flexibility and economical advantage of PAM machine is that, with the same machine, it is possible to convert preforms in bottles both in single stage and in double stage when at PAM, a Stretch Blow Forming Machine (SBF) is coupled.

SACMI "heroPET4.0" (fig. 1.19) is a rotative single stage: preform compression molding machine + stretch blow molding machine + filling machine. The productivity goes from 24000 to 36000 bph.

With SACMI heroPET4.0 a filling machine and even a labelling machine could be added to the process with logistic and cleaning costs savings. Moreover, the single stage layout (only preform molding and blowing) is definitely more compact compared to old low productivity linear single stage: the length of the line is only 16 meters compared to 50. Note that HeroPET4.0 is very flexible since it can work also in single stage to produce and store preforms when there is no need of filling bottles.

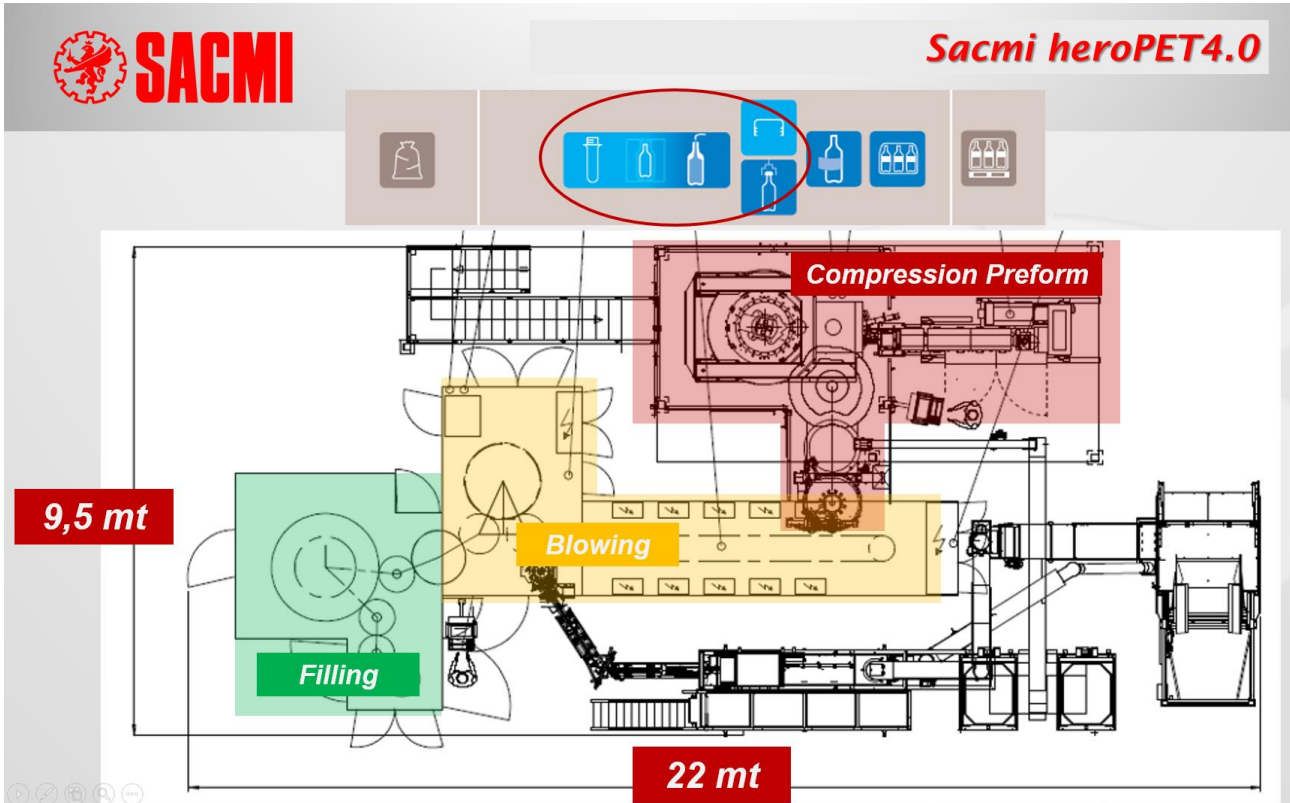


Figure 1.19 HeroPET4.0 layout [4].

## 1.5 ADVANTAGES OF COMPRESSION MOLDING VS INJECTION MOLDING

Compression molding (PAM) and single stage compression and blowing (PAM + SBF) have several advantages compared to injection molding technology. In the following paragraphs, they are explained in detail.

### 1.5.1 Energy savings

The first energy saving of preform compression molding is the lower melting temperature (about 270 °C) compared to injection (about 290 °C), due to the absence of narrow pipes or cavities.

Moreover, compression rotative single stage allows to save energy compared to double stage which is the benchmark on market for productivity higher than 22000 bph. As previously explained, preforms are no more cooled down and later heated up above glass transition temperature, but they remain at a temperature of around 80 - 100 °C to be then stretched blow molded in a blowing machine. With single stage, preforms hence are just heated locally to shape the thermal profile, then stretch-blown in a blowing machine. Fig.1.20a shows the temperature profile over time of injection molding and double stage blowing (red line) compared to compression molding and single stage blowing (green line). In fig. 1.20b the area in red gives a qualitative idea of the energy saving.

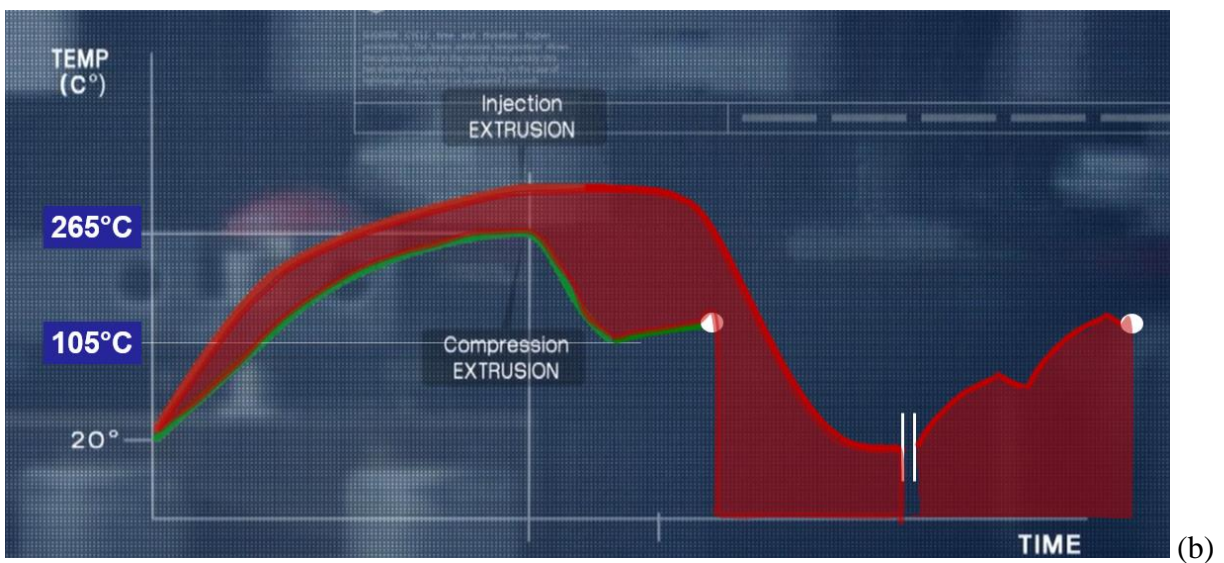
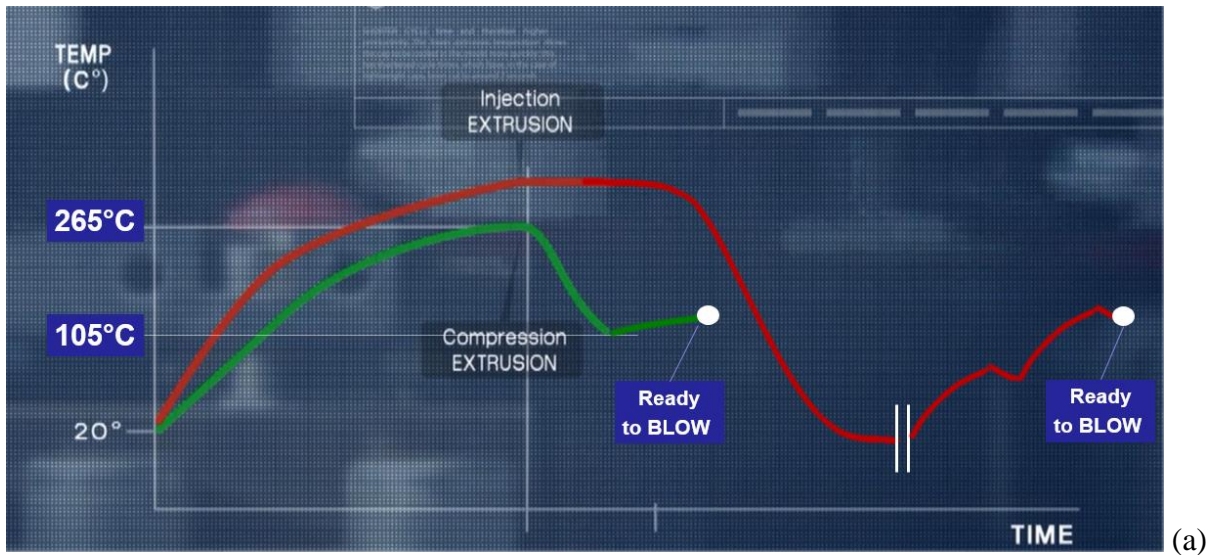


Figure 1.20 Temperature profile over time: injection double stage (red line) compared to compression single one (green line) (a). The red area qualitatively represents the energy difference (b) [4].

Finally, also single stage preform temperature profile is closer to the ideal one compared to double stage, taking into account that the inner wall stretches more.

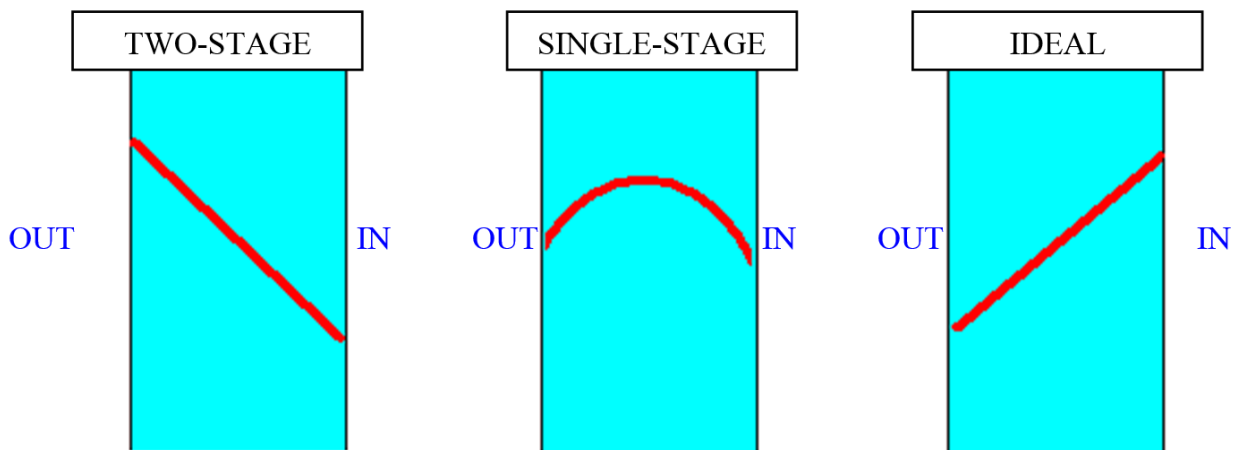


Figure 1.21 Temperature profiles across preform thickness [1].

Below some images show the advantage of compression single stage solution on preform heating in detail.

Only the external part needs to be heated up by lamps because the inner part of the preform is still hot (fig. 1.21). In double stage, due to PET low thermal conduction, the oven needs a huge air ventilation to cool down preform external surface and give time to the heat to reach the bulk without burning the side wall.

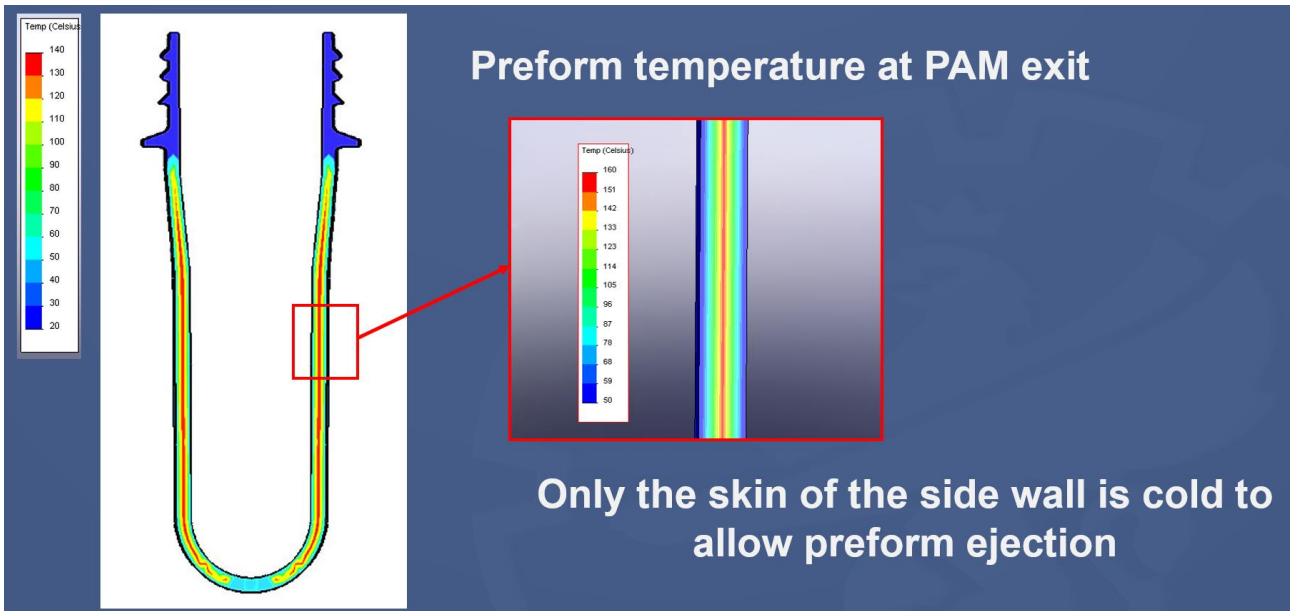


Figure 1.22 Compression molded preform wall temperature before blower [5].

Preform underneck material is the most difficult to heat up without ruining the support ring. In compression single stage underneck is already hot (fig. 1.22).

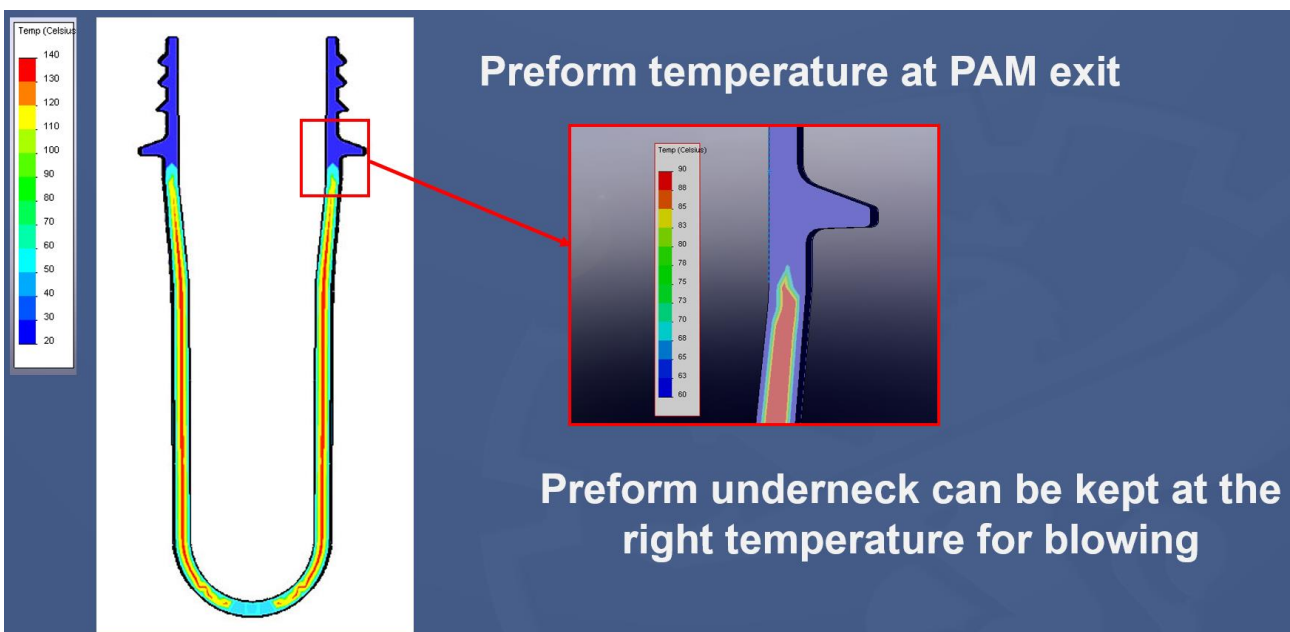


Figure 1.23 Compression molded preform underneck temperature before blower [5].

## 1.5.2 PET material saving

PET saving of compression technology compared to injection one is due to three main reasons. In addition to them, the amount of scrap material at machine start-up is reduced.

### 1.5.2.1 Absence of gate

The first cause of compression preform material saving is the absence of the injection point (called "gate", fig. 1.24) and of all defects on preform and bottle related to it (see next paragraph below). The gate is the point from which PET enters mold cavities. It is a transition zone between the plastic on the mold and the other PET which is kept melt in the hot chamber. Moreover, the gate zone is not cooled as quick as the other parts of the preform for mold technical and manufacturing reasons, so the PET starts crystallizing.

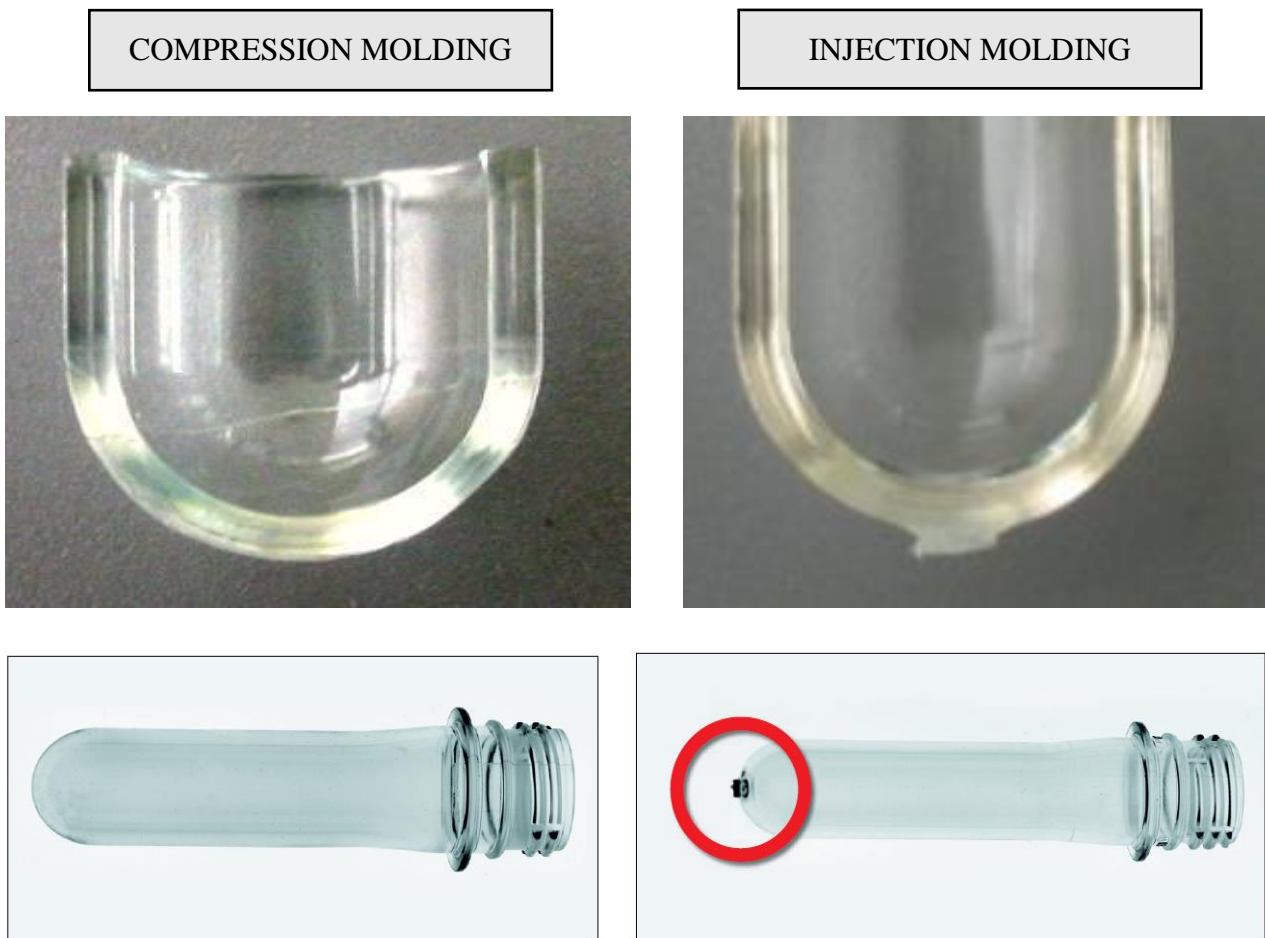


Figure 1.24 Compression molded preform versus injection molded one: the compression preform is without the gate (red circle).

The material reduction is not just due the gate itself but also a reduction in gate thickness. As a matter of fact, the zone around the gate presents PET with higher crystallinity due to the slower cooling rate. During blowing this crystallized PET cannot be used to give strength to the bottle. Therefore, compression requires a lower base thickness to give the same mechanical resistance to the bottle.

The difference in crystallinity between the body zone and the gate zone of a PET injection preform can be easily found through a local DSC (Differential Scanning Calorimetry) analysis (fig. 1.25 and tab. 1.1). The analysis was performed with a calorimeter PerkinElmer DSC8500, with a block temperature of - 90 °C and a heating rate of 20 °C/min.

## DSC curves of an injection molded preform

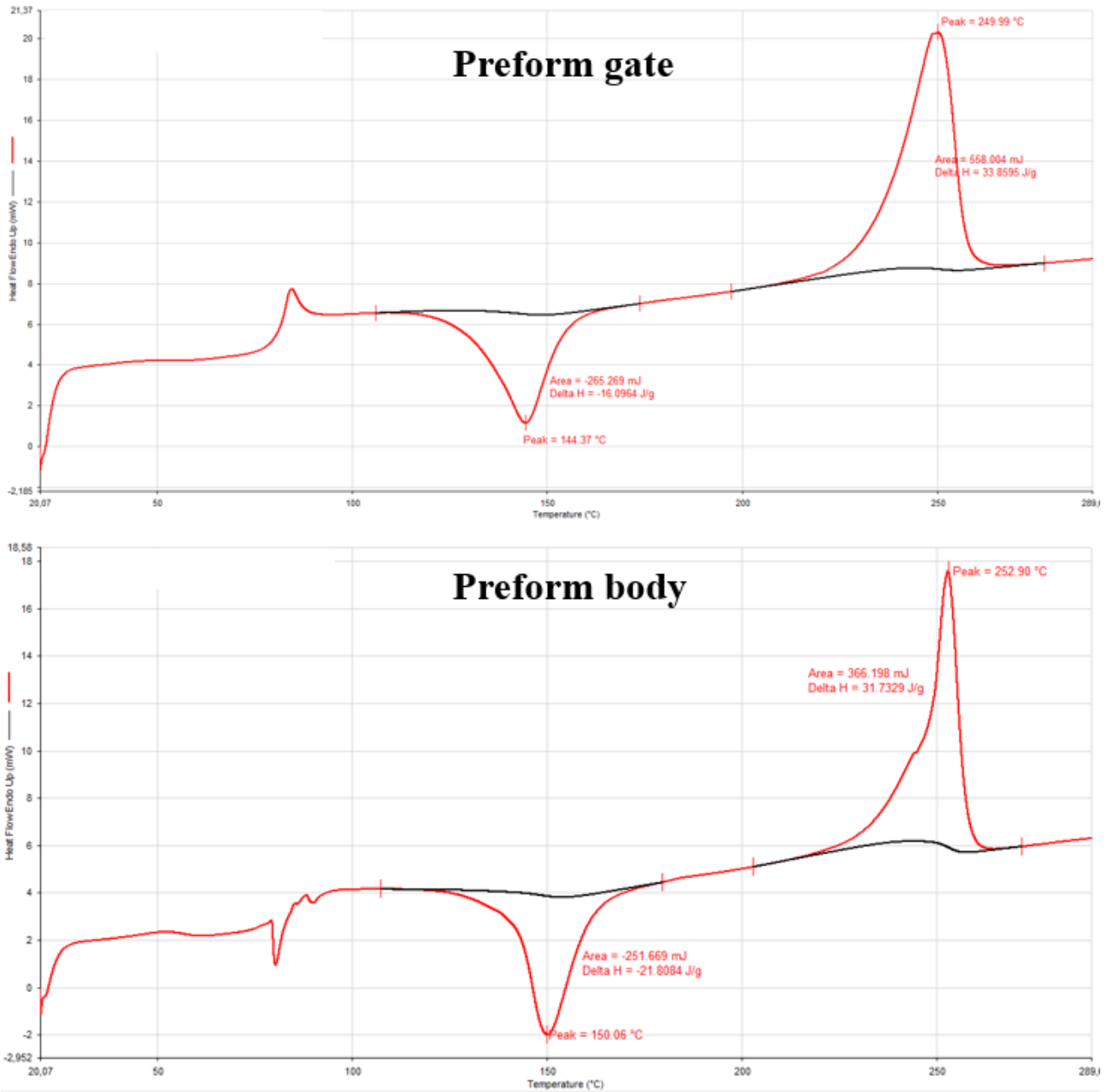


Figure 1.25 DSC curves on the gate and body of an injection molded preform.

### Thermal parameters

	$\Delta H_m$ (J/g)	$\Delta H_c$ (J/g)	$\Delta H_{eff}$ (J/g)	Crystallinity (%)	Crystallinity typical values (%)
<b>Gate</b>	33.8595	16.0964	17.7631	<b>12.7</b>	<b>11 - 15</b>
<b>Body</b>	31.7329	21.8084	9.9245	<b>7.1</b>	<b>7 - 10</b>

Table 1.1 Results of DSC analysis on the gate and body of an injection molded preform.

Crystallinity calculation was done according to the following formula:

$$crystallinity(\%) = \frac{\Delta H_m - \Delta H_c}{\Delta H_c} \cdot 100 \quad (1.1)$$

$\Delta H_c^\circ$  = fusion enthalpy of a theoretical 100 % crystalline PET (140 J/g estimated by Wunderlich [1]);

$\Delta H_m$  = fusion enthalpy of sample;

$\Delta H_c$  = crystallisation enthalpy of sample.

Higher crystallinity means higher fragility in gate zone. During bottle stretch blow molding or tests usually breakages start from gate (see details in gate defects paragraph).

### 1.5.2.2 Preform wall thickness

Compression mold preform can have a higher L/T ratio (preform length / wall thickness) and a lower minimum wall thickness compared to injection one (table 1.2).

As previously explained, in injection molding the thickness of preform wall is equal to the thickness of cavity that has to be filled. PET fluidity and viscosity coupled with mold temperature, today do not allow preform thickness lower than 1.9 mm in the industrial practice and a ratio preform length/wall thickness higher than 50, otherwise the filling of the mold is no more guaranteed due to PET solidification. Compression is different, since the proper PET quantity necessary for molding the preform is already in each mold before it starts closing/molding. PET distribution in mold volume is guaranteed by mold closing force. Moreover, compression filling time are lower preventing PET solidification.

	Injection	Compression
<b>Ratio L/T (preform length / wall thickness)</b>	50	60
<b>Minimum wall thickness (mm)</b>	1.9	1.4

Table 1.2 Preform wall thickness limit comparison between injection and compression technology.

### 1.5.2.3 Flat base preform



Figure 1.26 SACMI flat HERO base preform.

Flat base preform (fig. 1.26) - SACMI HERO base - is obtainable only with compression molding technology. Preform technologists have been trying to optimize the shape of the preform base to

minimize its weight for several years. They passed from standard hemispheric base, to conic one (eco-base) and finally Cappello design<sup>®</sup> was patented. Flat base gives the highest weight reduction as possible, guaranteeing the same bottle resistance. This shape is not obtainable with injection process where the preform base must guarantee PET flow inside the mold.

#### 1.5.2.4 Weight lightening examples

### Preform weight lightening for 1.5 liter bottle

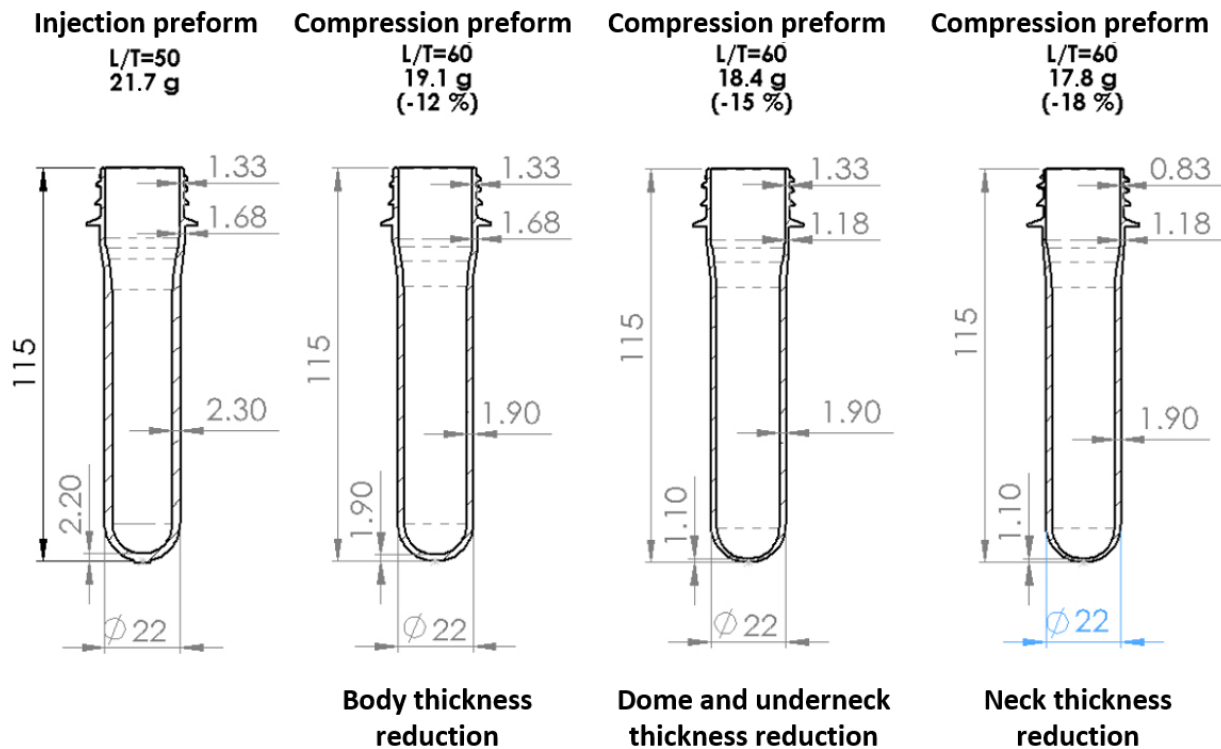


Figure 1.27 Preform weight lightening for 1.5 liter bottle thanks to compression molding.

### Preform weight lightening for 0.5 liter bottle

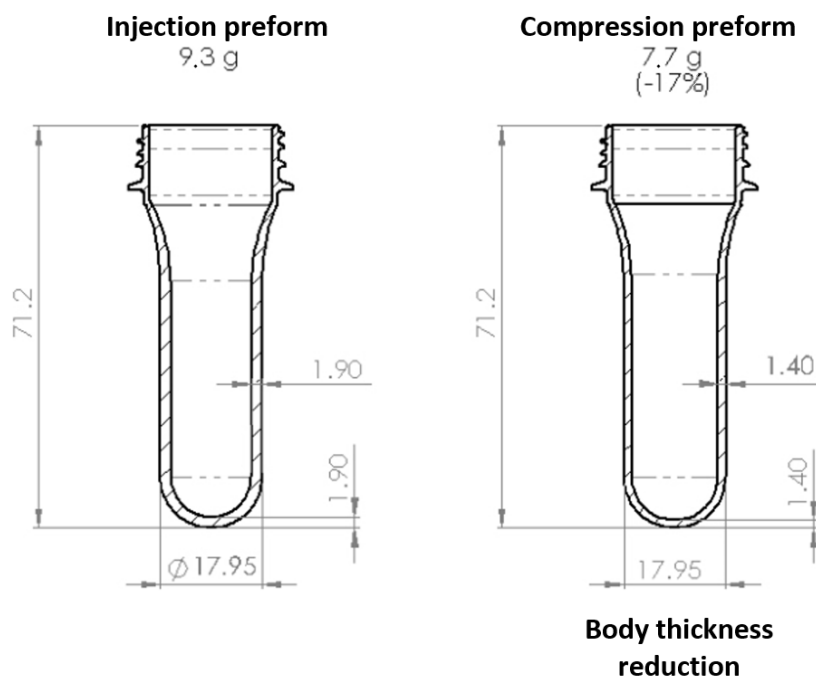


Figure 1.28 Preform weight lightening for 0.5 liter bottle thanks to compression molding.

The just mentioned three differences that characterize compression molding allow an important weight reduction. In fact, it is possible to eliminate the material which is unnecessary to stretch blow mold the bottle, but which is necessary to produce its correspondent preform by injection molding technology. The following preform drawings give an example of the potential material saving in a preform for a 1.5 liter bottle (fig. 1.27) and for a 0.5 liter one (fig. 1.28). Preform/bottle material saving can significantly vary depending on the preform particular application. The cases below report an average, without taking into account the benefit of the flat base, and they are summarized in table 1.3.

Note: weight reduction is function of the particular preform geometry: the value can vary of about  $\pm 5\%$  with respect to the one shown in the table below. Moreover, SACMI HERO base can even increase this weight reduction.

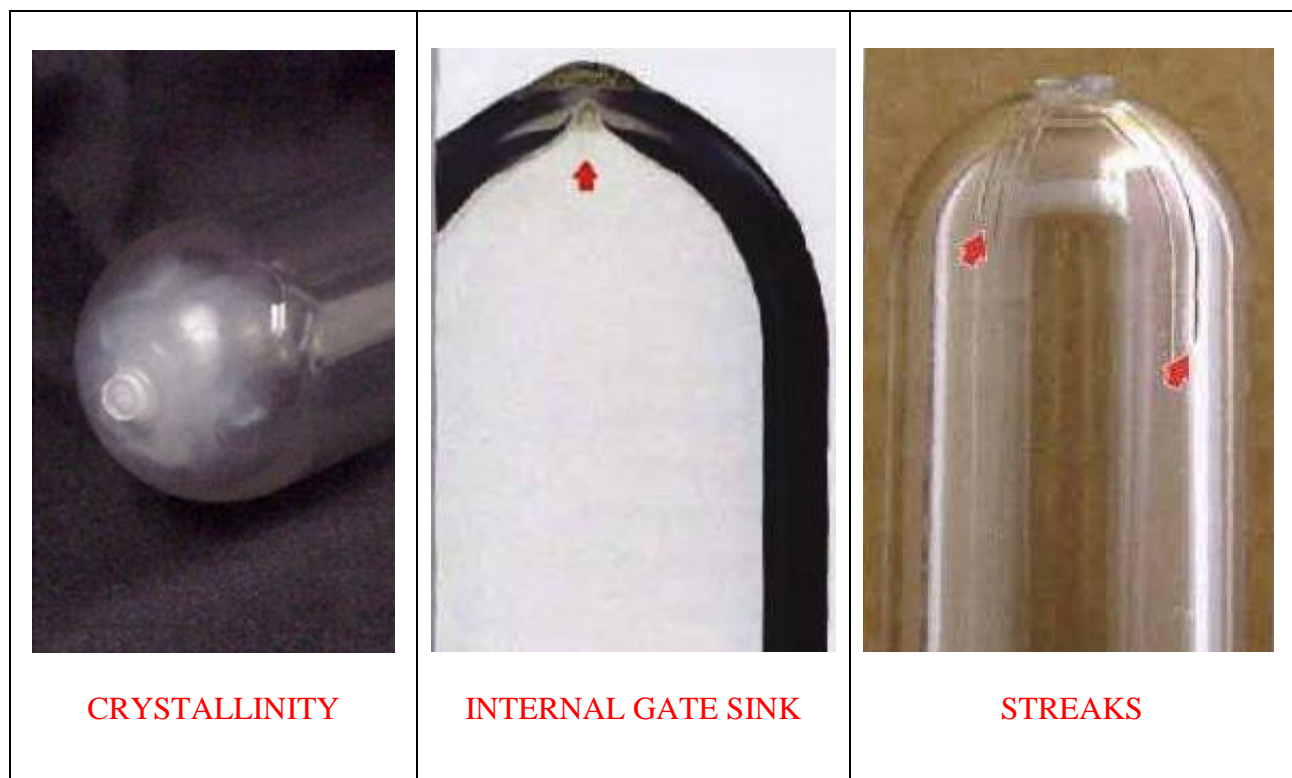
Bottle volume	Weight reduction
1.5 L	-18%
0.5 L	-17%

Table 1.3 Preform/bottle weight reduction thanks to compression technology.

### 1.5.3 Gate defects

#### 1.5.3.1 Preforms

The major part of preform defects are due to the injection point (gate). Table 1.4 shows a list of all the defects related to the gate.



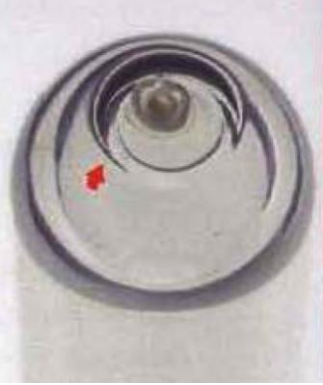
 <p style="text-align: center;"><b>GATE VOIDS / PIN HOLES</b></p>	 <p style="text-align: center;"><b>STRINGING</b></p>	 <p style="text-align: center;"><b>GATE PEELING</b></p>
 <p style="text-align: center;"><b>DROOL MARKS</b></p>	 <p style="text-align: center;"><b>GATE DEPRESSIONS</b></p>	 <p style="text-align: center;"><b>AIR HOOKS</b></p>
 <p style="text-align: center;"><b>SINKS</b></p>	 <p style="text-align: center;"><b>LONG GATE NUB</b></p>	

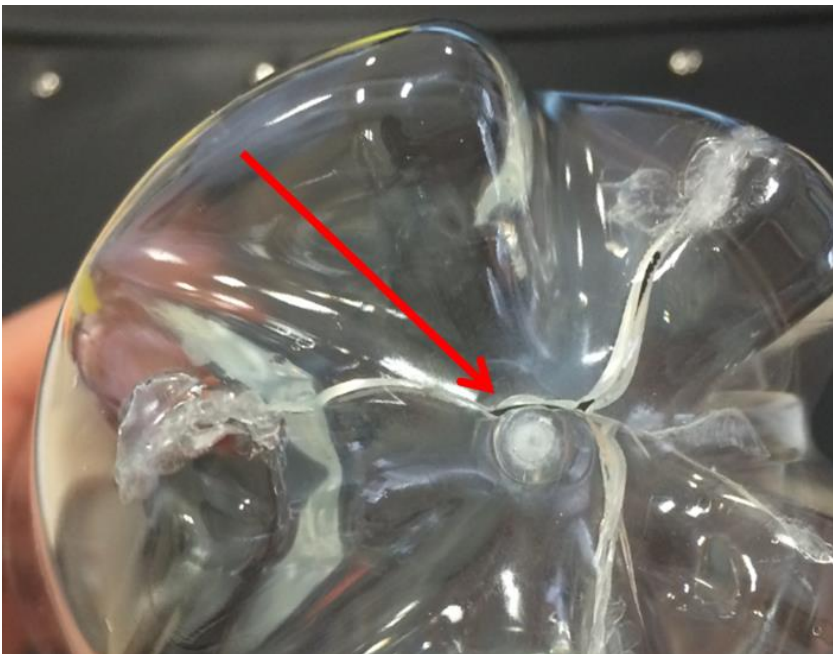
Table 1.4 Gate defects on injection molded preforms [6].

### 1.5.3.2 Bottles

As previously told, higher crystallinity means higher fragility in gate zone. During bottle stretch blow molding or tests breakages usually start from gate. Fig. 1.29 illustrates some of these bottle breakages with their relative consequences.



THIS BREAK STOP  
THE PRODUCTION!



BOTTLE BREAK  
DURING BURST  
TEST STARTING  
FROM  
CRYSTALLIZED  
GATE ZONE

Figure 1.29 Bottle breakages starting from gate defects.

#### 1.5.4 Moisture content

Preform moisture content increases with the increase in time from preform molding to bottle blowing. Moisture migrates inside the preform wall as shown in fig. 1.30.

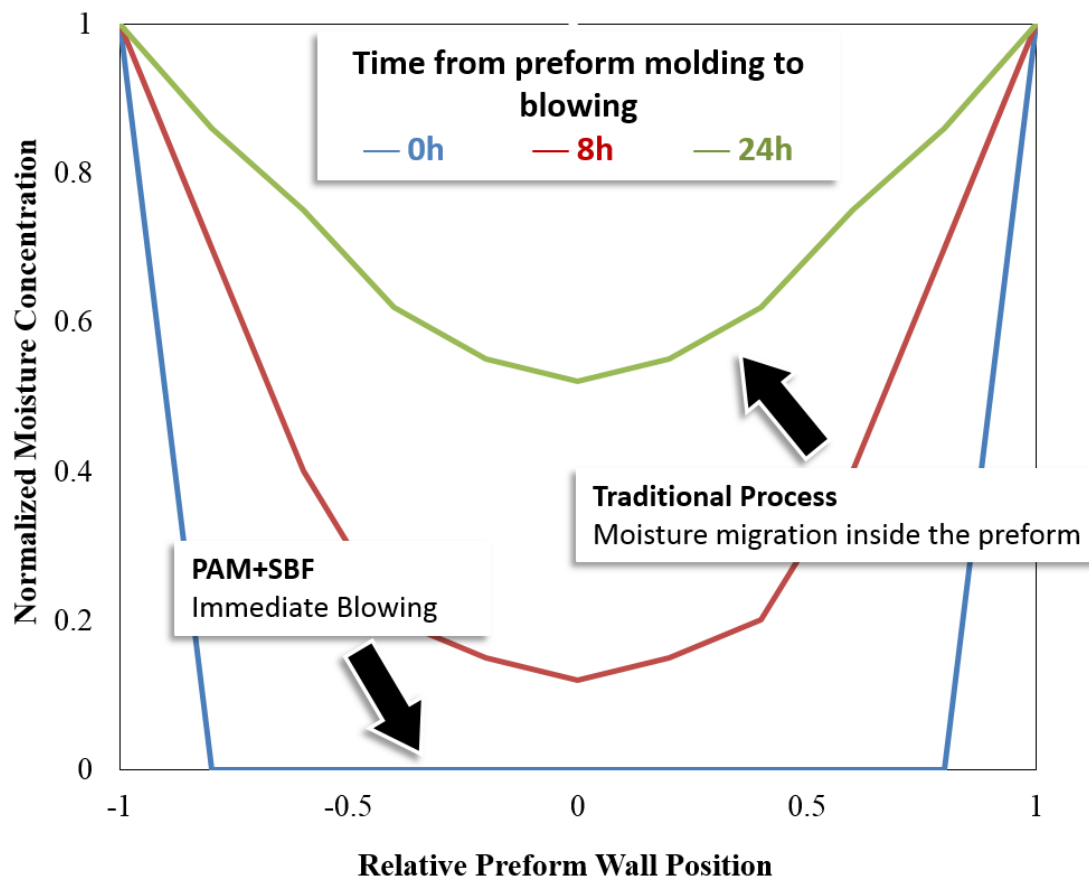


Figure 1.30 Moisture content inside preform wall with time from preform molding to blowing [5].

Moisture content affects  $T_g$  (PET glass transition temperature), in particular an increasing in moisture content means a decreasing of  $T_g$  as shown in fig. 1.31. Higher  $T_g$  means more PET Bi-orientation so higher bottle performances. This is particularly favorable for Hot Fill application.

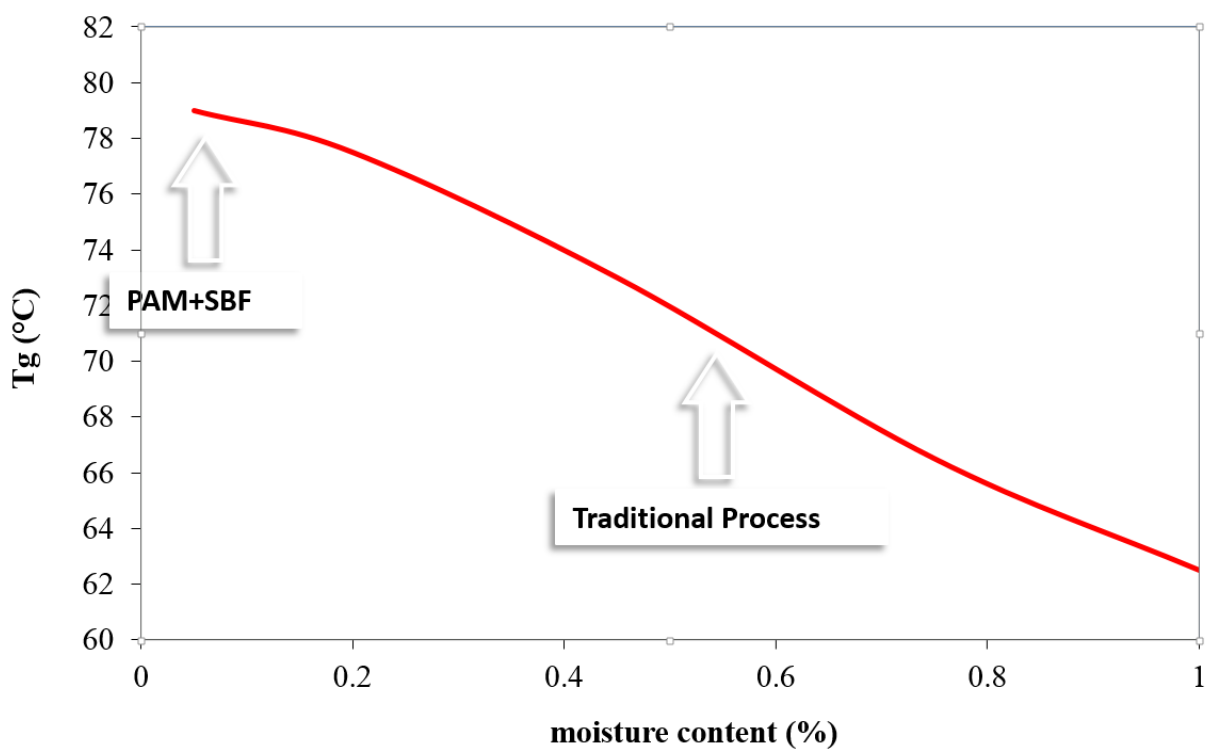


Figure 1.31 Preform moisture content affects  $T_g$  [5].

Furthermore, less moisture leads to slower thermal crystallization (fig. 1.32) which reflects in easiness of stretch blow molding. In fact, thermal crystallization is dangerous for PET bottle mechanical properties.

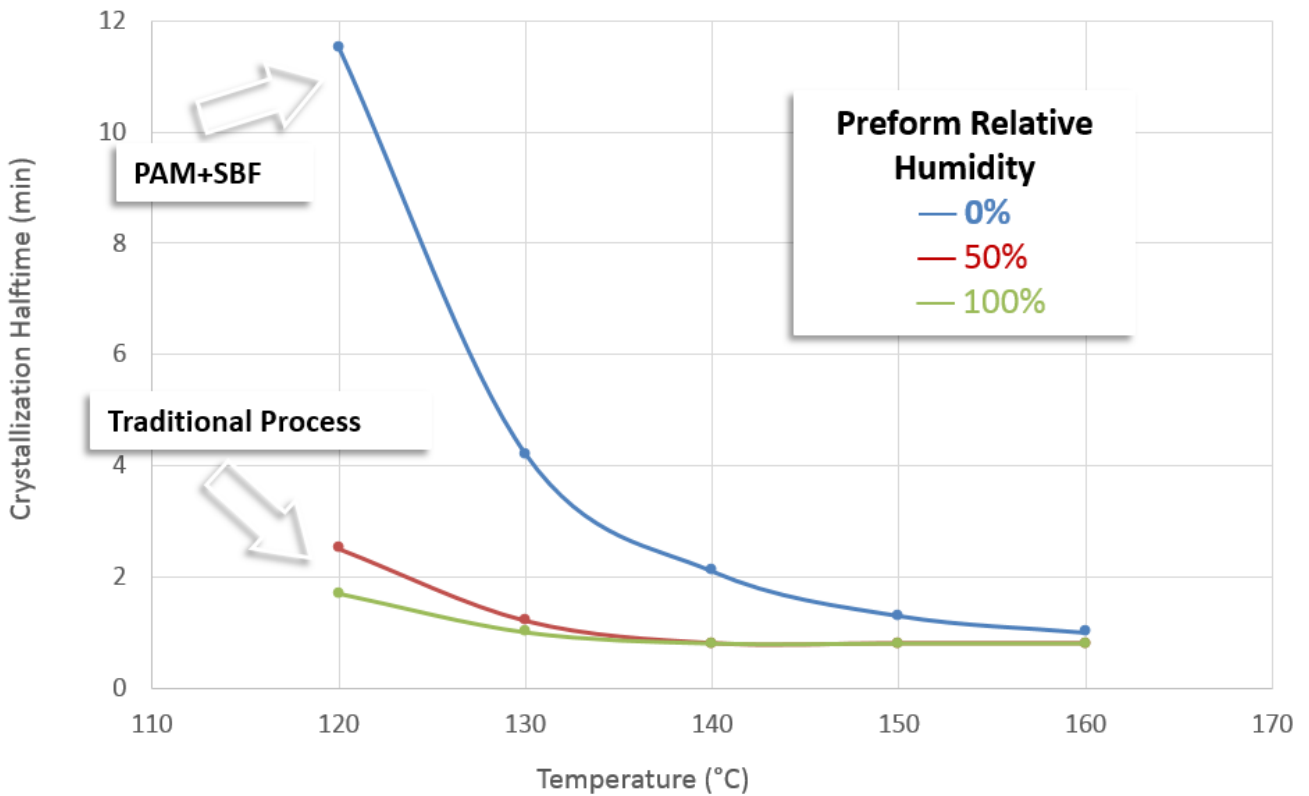


Figure 1.32 PET preform crystallization halftime as function of preform relative humidity at different temperature [5].

Moisture creates in the preforms and bottles the so called "moisture rings" (fig. 1.33) which lower bottle mechanical properties. Literature also attests that moisture reduces PET properties [7, 8]. The single stage technology is exempt from all these defects.

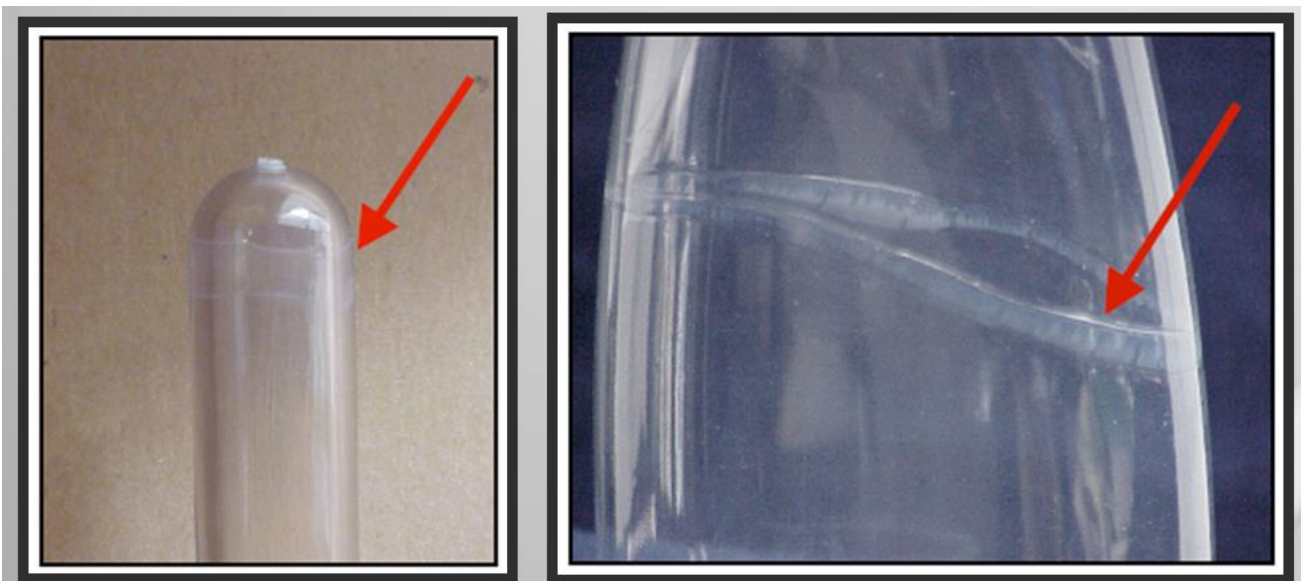


Figure 1.33 Moisture rings on a preform and on a bottle.

### 1.5.5 Weight homogeneity

Another advantage of compression molding is the higher preforms weight homogeneity compared to the injection one. Fig. 1.34 and table 1.5 show the weight variability of compression mold preforms (22.955 g). The variation is within  $\pm 0.2\%$ .

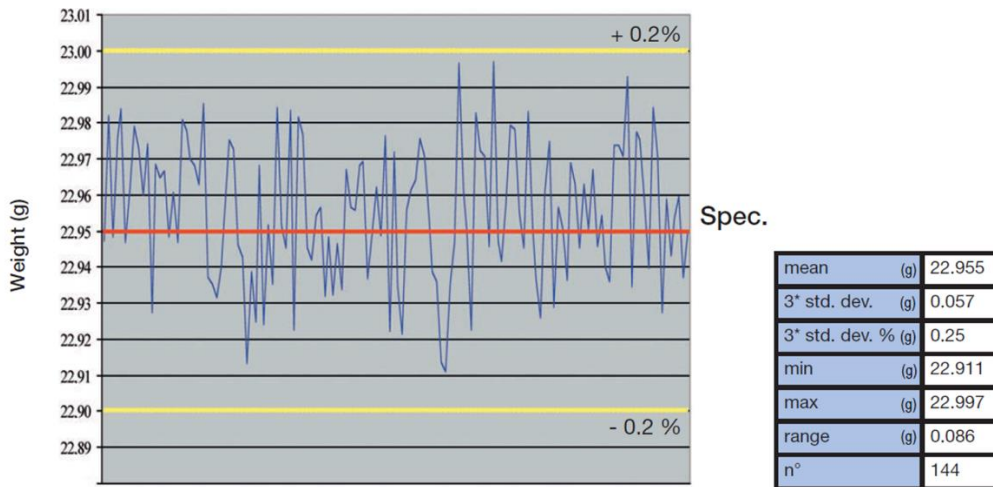


Figure 1.34 and table 1.5 Weight variability of compression molded preforms.

Fig. 1.35 illustrates the weight variability of injection mold preforms. In particular the four lines correspond to four complete molding cycles with a 72 cavities mold for 60.2 g preform. Weight variation is within + 0.3 and - 0.35. Compression reduces weight variation of 40 %. Values of usual preform weight tolerances required by preforms producers are illustrated in table 1.6. It is likely that in the future the limits will become stricter with an evident advantage for compression molding.

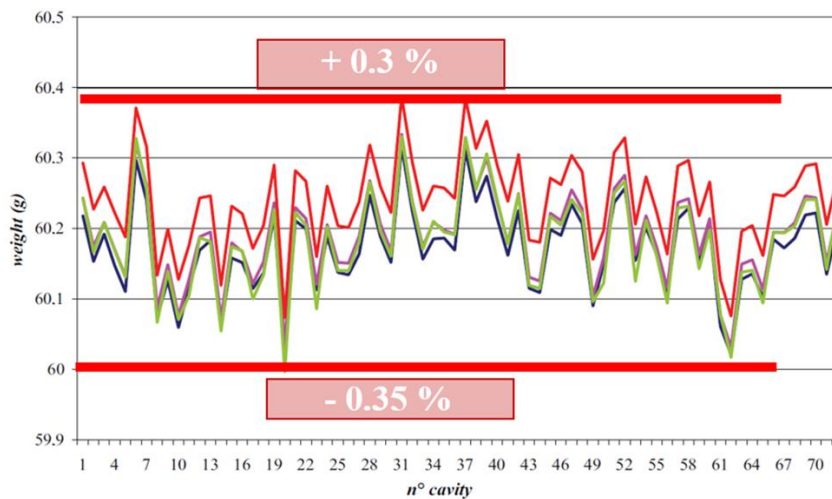


Figure 1.35 Weight variability of injection molded preforms.

Nominal weight	Tolerance
Less than 20 g	$\pm 0.2$ g
$\geq 20$ g < 35 g	$\pm 0.3$ g
$\geq 35$ g < 50 g	$\pm 0.4$ g
$\geq 50$ g	$\pm 1\%$

Table 1.6 Usual preforms weight tolerances.

## 1.5.6 PET IV

Intrinsic viscosity (IV), usually expressed in dl/g, is a parameter related to polymer molecular weight and hence is rheological properties. Literature underlines the importance of IV for strain hardening properties of oriented PET [9, 10]: the higher IV shows lower strain hardening point so higher orientation.

Thermal stabilities are important because as temperature increases, pressure increases causing the bottle to expand and creep. Excessive creep will cause the beverage fill level to drop, which will negatively affect packaging appearance and can lead to bottle missed sale. Excessive expansion will affect how the bottle fits into a carrier shell, sits on a shelf, or fits into a vending machine. For example, relevant deformation can lead to bottle instability and falling due to eversion of bottom petaloid or, if deformation occurs in the main diameters, to label breakage.

Injection mold do not allow IV values higher than 0.8 dl/g due to the increase of melt viscosity and hence troubles in mold filling. The compression mold does not have narrow channels, so it can handle IV values of 1.15 dl/g and probably even more. This means bottle with higher mechanical and thermal properties keeping the same preform weight.

In the Beverage field, there are two main tests to assess bottle properties:

1. Thermal stability test.

It is a creep test to assess dimensional stability with temperature changes. Empty bottle dimensions are measured. For CSD (carbonated soft drink) the bottle is filled with carbonated water (4.2 volumes of CO<sub>2</sub>) and kept in a chamber (fig. 1.36) at controlled temperature (38 °C) and relative humidity (95 %) for 24 hours. Bottle dimensions are measured immediately before bottles have cooled. Variations in diameters, height and filling level are measured.

2. Burst test.

Especially relevant for carbonated drink, the purpose of this test is to assess bottle performance at high pressure and determine bottle failure point when pressurized under specific conditions in a dedicated machine (fig. 1.37). For CSD it consists in rapid pressurization to 9.18 bar (135 psi), hold for 13 seconds, ramp at 0.68 bar/s (10 psi/s) to failure or 20.41 bar (300 psi).



Figure 1.36 Thermal stability test chamber [11].



Figure 1.37 Burst test machine [11].

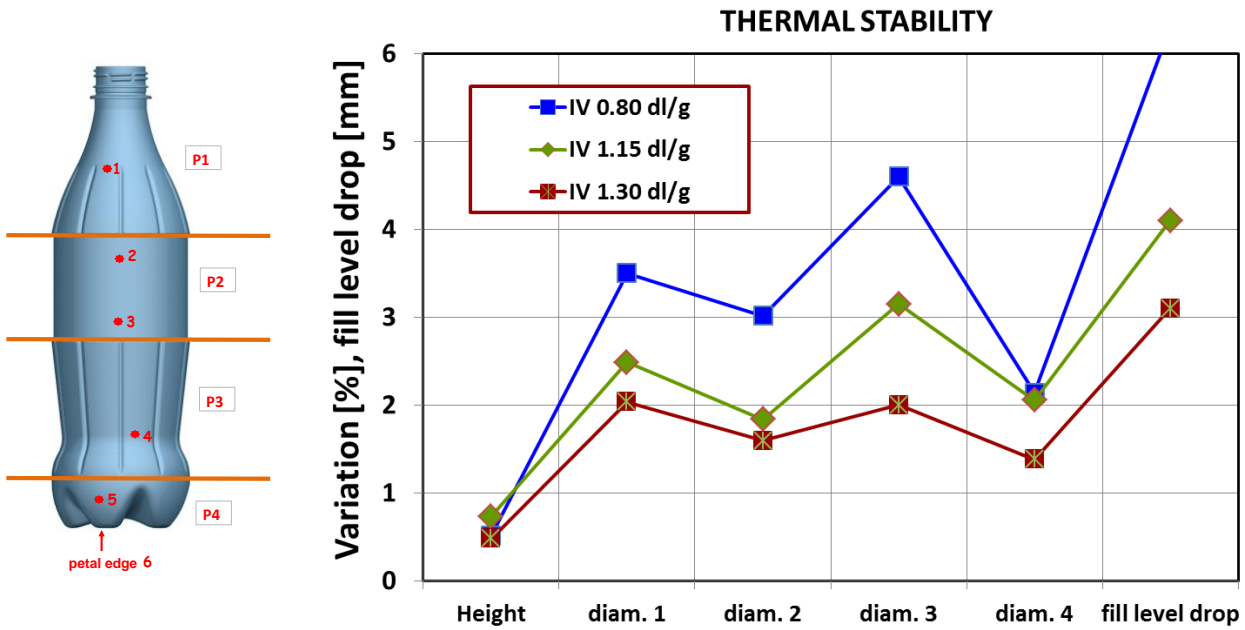


Figure 1.38 Percentage of dimensional variation (measuring diameters shown on the bottle on the left) and fill level drop for different IV values [11].

As shown in fig. 1.38, the dimensional stability of all measured bottle diameters and heights soars with higher IV values. According to data in fig. 1.38, increasing IV value reduces fill level drop.

A higher IV rises also burst pressure and make dimensional variations fall, soaring dimensional stability as shown in fig. 1.39.

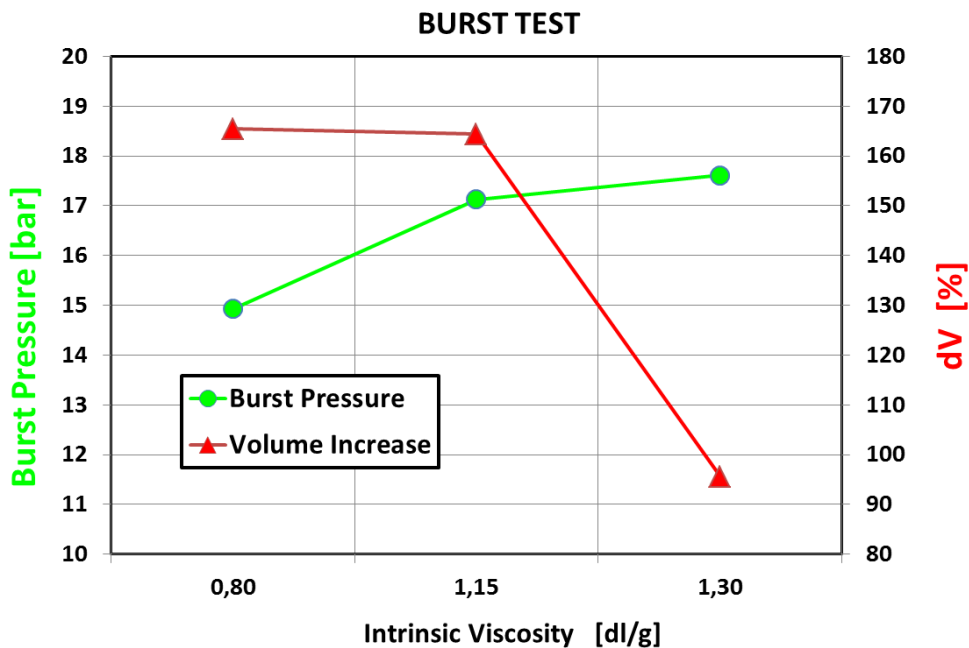


Figure 1.39 Burst pressure function of IV values [11].

To sum up, a rise in PET IV will improve thermal and mechanical properties of bottles and containers.

### 1.5.7 Quality controls

Preforms extracted from post cooling robot of an injection molding machine are dropped on a belt. The control on each preform, which is becoming a must for top level beverage companies, is very

expensive because it requires another machine that puts each preform in order on a line with the same distance the one from the other. On the other hand, compression preforms exit from the machine already ordered, so it is enough to add some cameras connected to a preform vision system. The difference between the two molding technologies is shown in fig. 1.40. SACMI has a business unit specialized in Optical Quality Controls and several patents on them applied to beverage and packaging business.

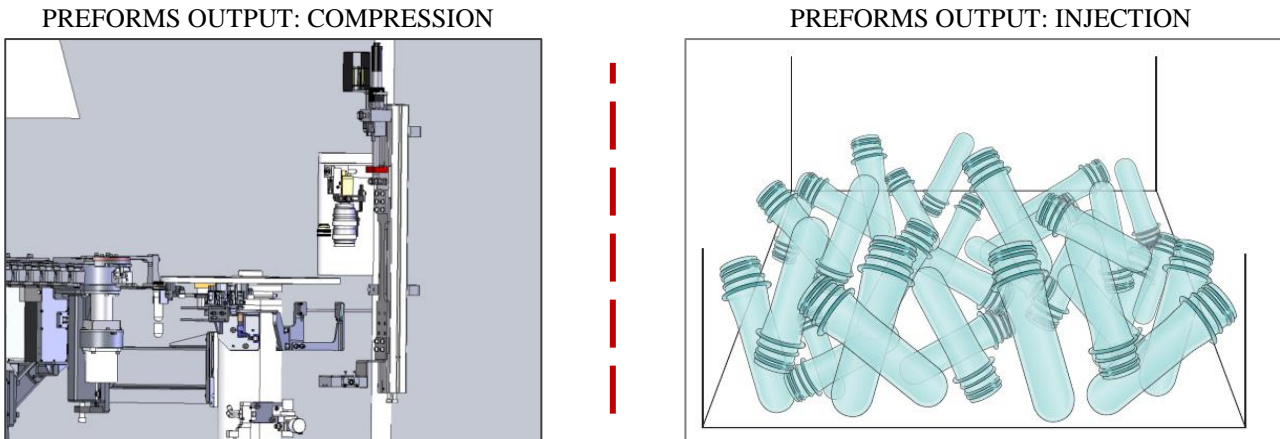


Figure 1.40 Preforms output comparison between compression and injection molding machine.

The cost of a vision system to check each preform produced falls of almost 75 % with compression molding technology. Each preform is checked with several cameras to control shape, geometry, color and defects of each zone: locking ring, neck finish, body and dome (fig. 1.41).

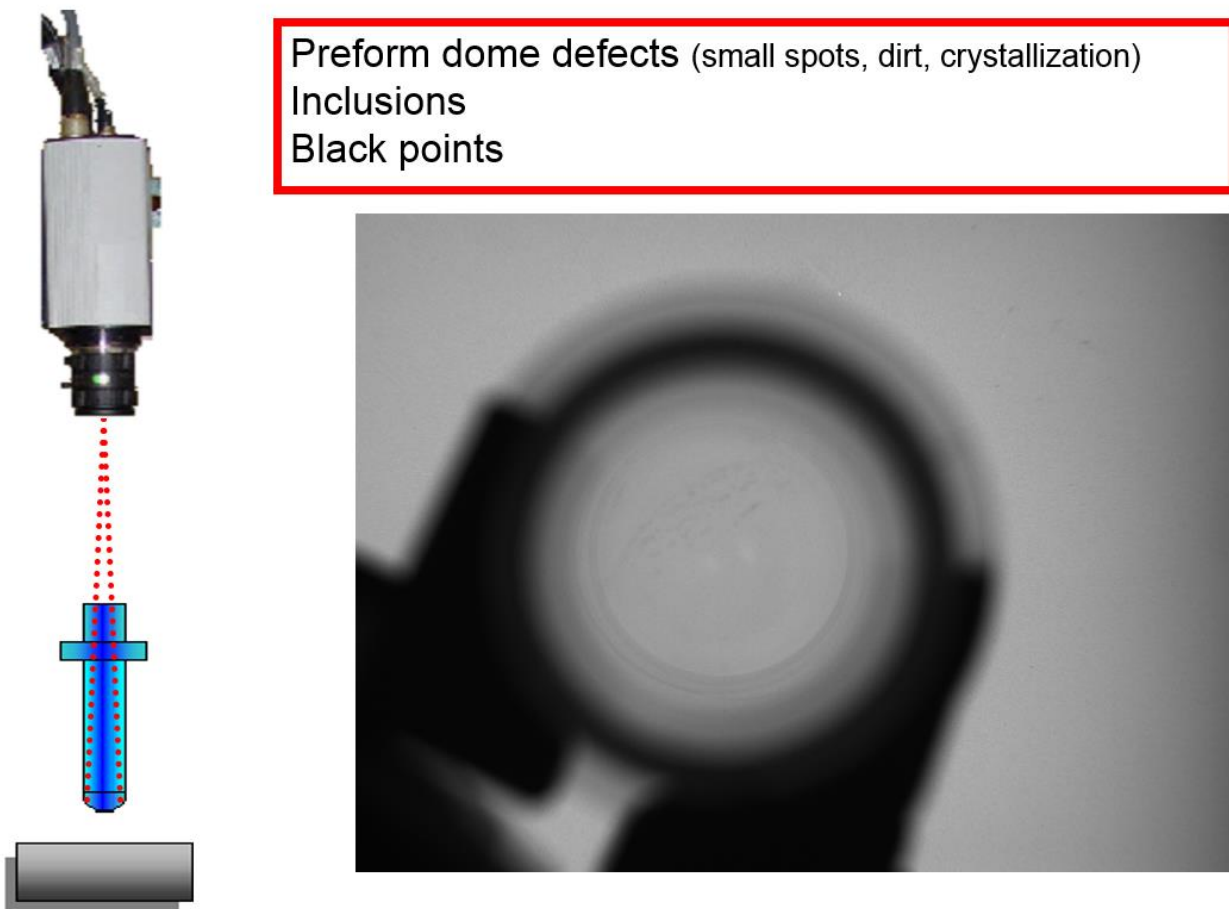


Figure 1.41 Preform dome quality control with SACMI vision system.

## 1.5.8 Acetaldehyde

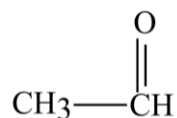


Figure 1.42 Acetaldehyde (AA) molecule.

Acetaldehyde (AA), whose chemical formula is illustrated in fig. 1.42, is a by-product of PET degradation with a high volatility ( $T_e = 20.8^\circ\text{C}$ ). It tends to modify drink tastes, especially in mineral waters. This makes AA highly undesirable in a container. Specific additives to reduce AA formation during molding have been developed and they may be added in PET compounds according to formulation recipes. AA generates at high temperature, increasing linearly with residence time (fig. 1.43 and 1.44) with a surge for temperature above  $290^\circ\text{C}$  (fig. 1.45). AA rises also for excessive mechanical strain (fig. 1.46), for example hot runners too narrow for the flow rate that makes pressure soar [1, 12].

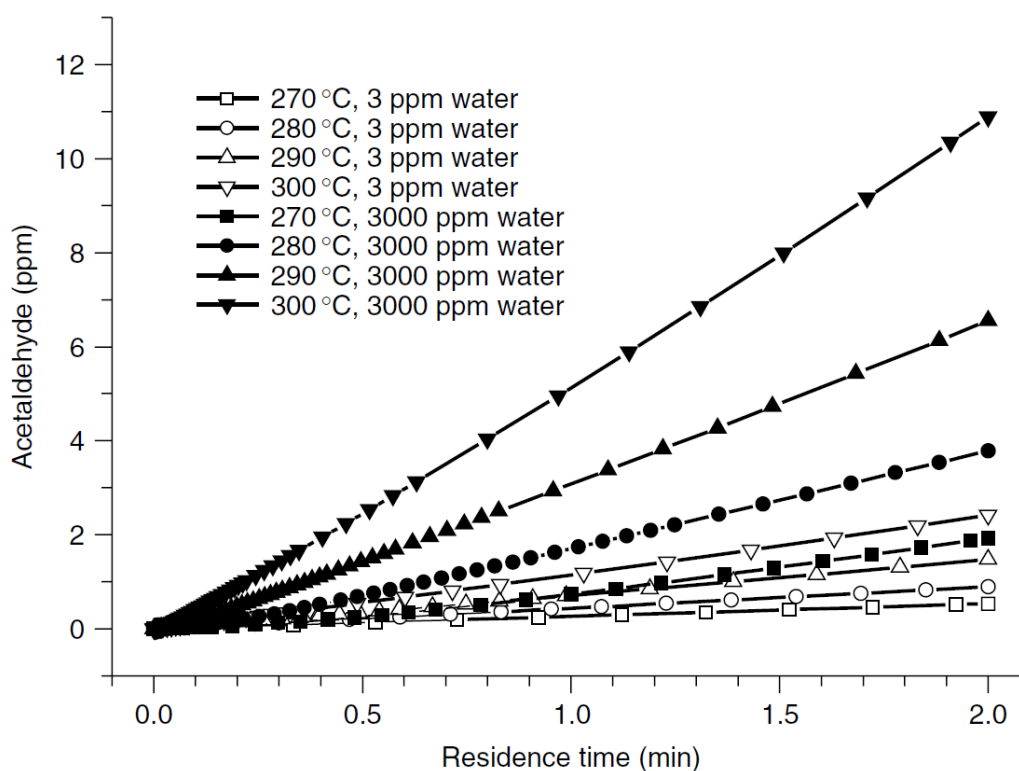


Figure 1.43 Generation of acetaldehyde as a function of extruder residence time and temperature for initial water content in the PET melt of 3 and 3000 ppm<sup>1</sup> [12].

<sup>1</sup> Reprinted from Th. Rieckmann and S. Völker, *Poly(Ethylene Terephthalate) Polymerization – Mechanism Catalysis, Kinetics, Mass Transfer and Reactor Design* ch.2 pp. 29-115 in *Modern Polyesters: Chemistry and Technology of Polyesters and Copolyesters*, J. Scheirs, T.E. Long, Ed., John Wiley & Sons, Ltd, Copyright (2003), with permission from John Wiley & Sons Ltd, The Atrium, Southern Gate, Chichester, West Sussex PO19 8SQ, England. All Rights Reserved. No part of this publication may be reproduced, stored in a retrieval system or transmitted in any form or by any means, electronic, mechanical, photocopying, recording, scanning or otherwise, except under the terms of the Copyright, Designs and Patents Act 1988 or under the terms of a licence issued by the Copyright Licensing Agency Ltd, 90 Tottenham Court Road, London W1T 4LP, UK, without the permission in writing of the Publisher. Requests to the Publisher should be addressed to the Permissions Department, John Wiley & Sons Ltd, The Atrium, Southern Gate, Chichester, West Sussex PO19 8SQ, England, or emailed to permreq@wiley.co.uk, or faxed to (+44) 1243 770620. This publication is designed to provide accurate and authoritative information in regard to the subject matter covered. It is sold on the understanding that the Publisher is not engaged in rendering professional services. If professional advice or other expert assistance is required, the services of a competent professional should be sought.

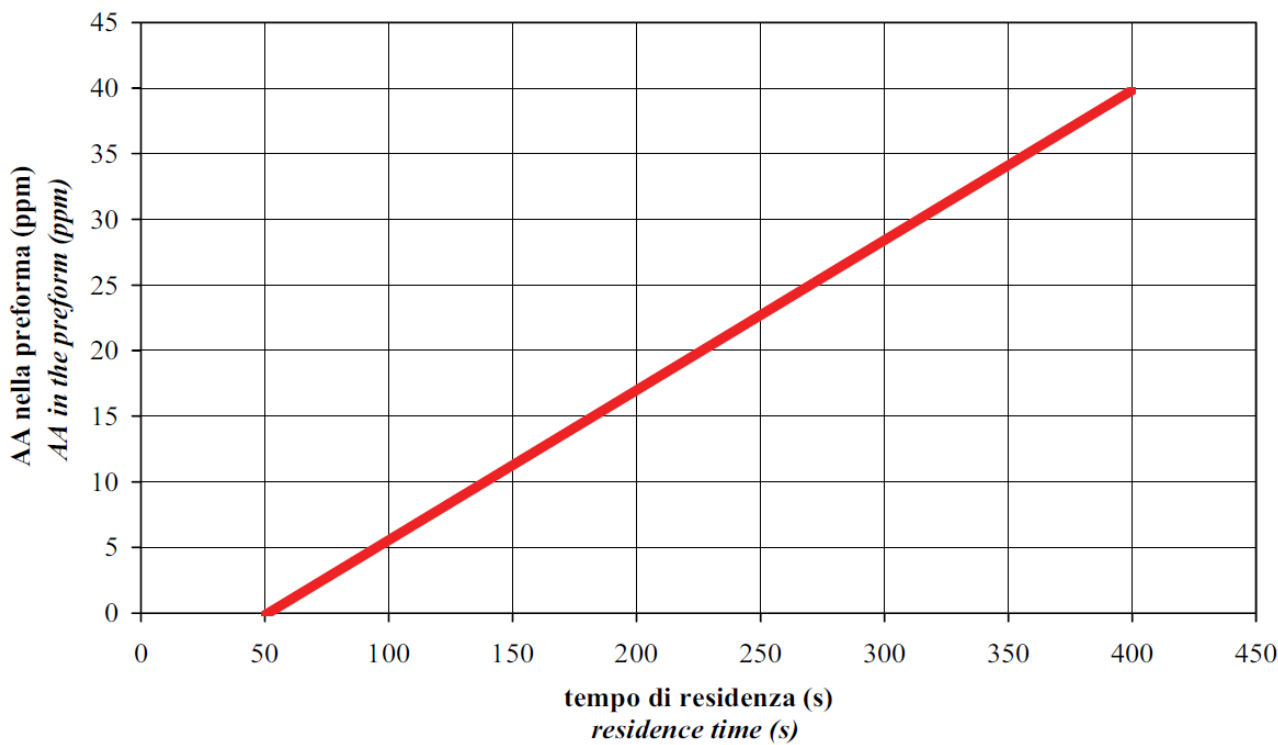


Figure 1.44 AA generation as function of residence time [1].

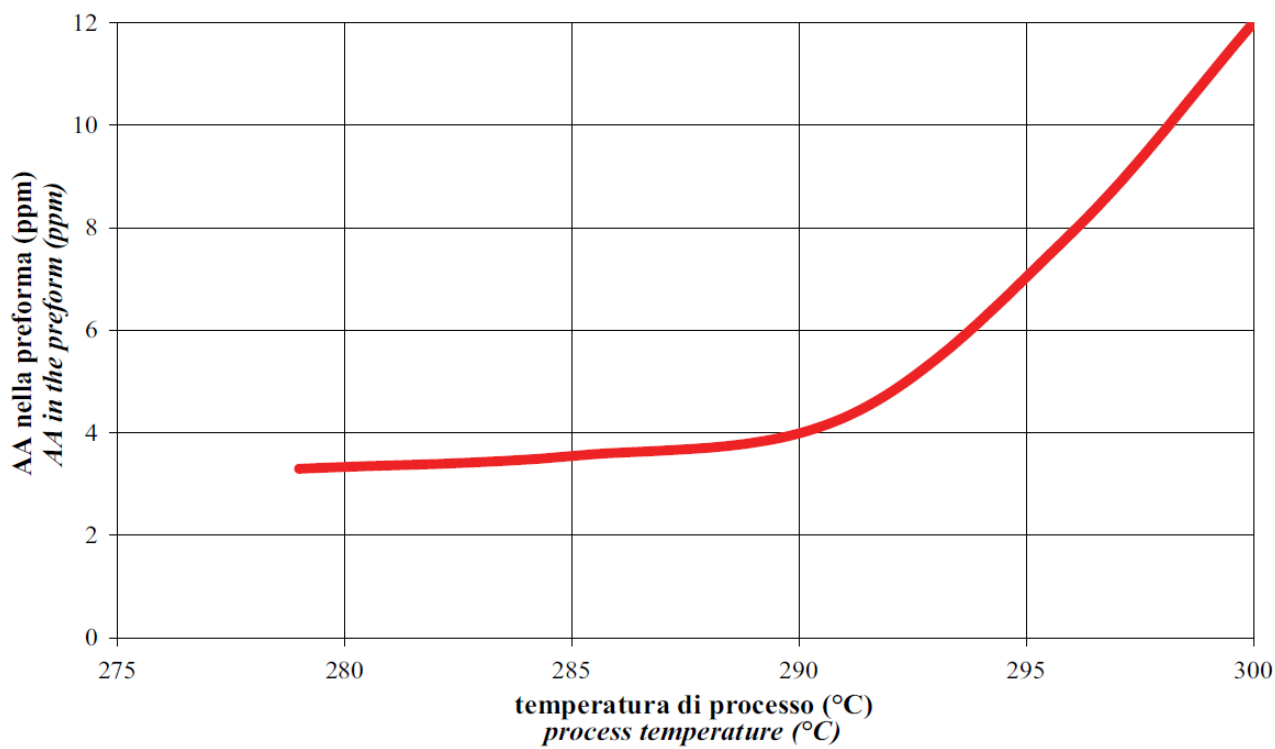


Figure 1.45 AA generation as function of process temperature [1].

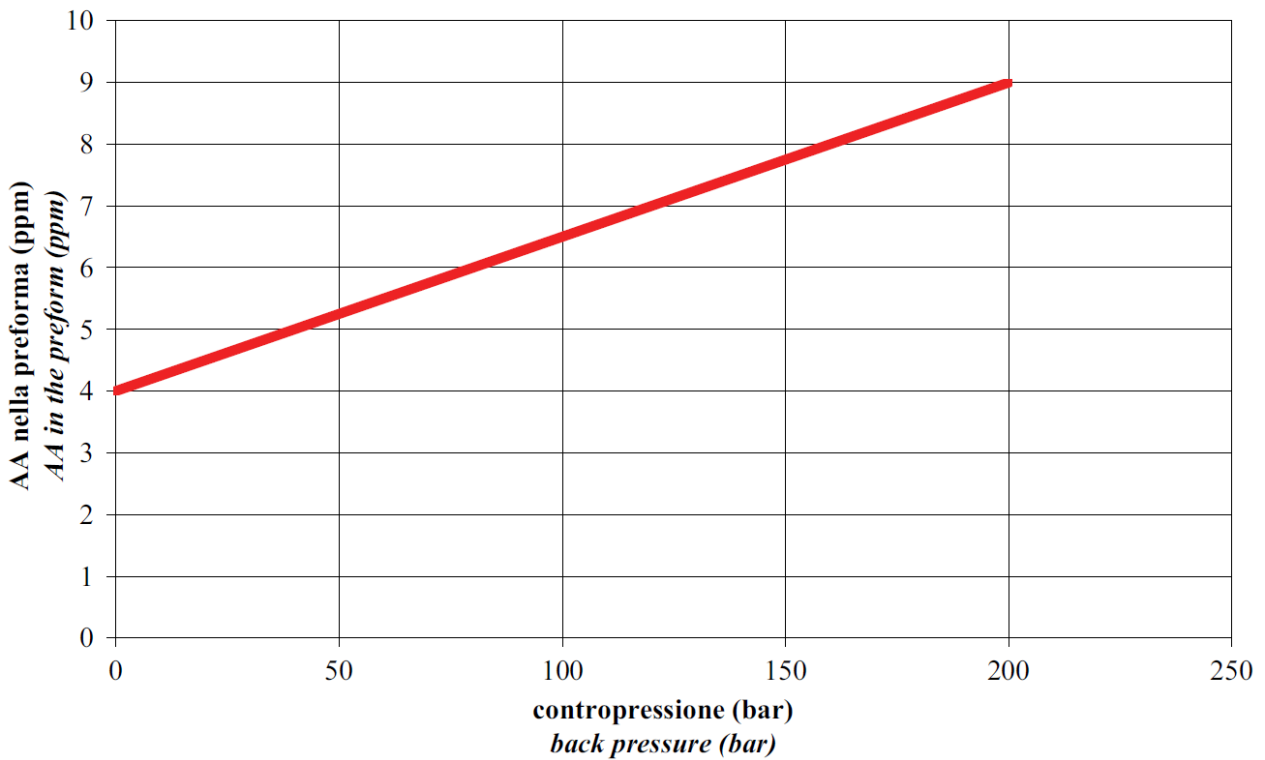


Figure 1.46 AA generation as function of PET back pressure [1].

Melt PET temperature is around 290 °C for injection molding, while for compression one the melt is around 270 °C. Moreover, compression technology does not have narrow channels. In addition, compression has a lower residence time and pressure for melt PET. All these considerations result in a significantly lower AA generation in compression molding. The graph in fig.1.47, which reports results of SACMI internal tests, gives an idea of the difference in AA generation [ppm] between injection and compression molding as function of PET IV.

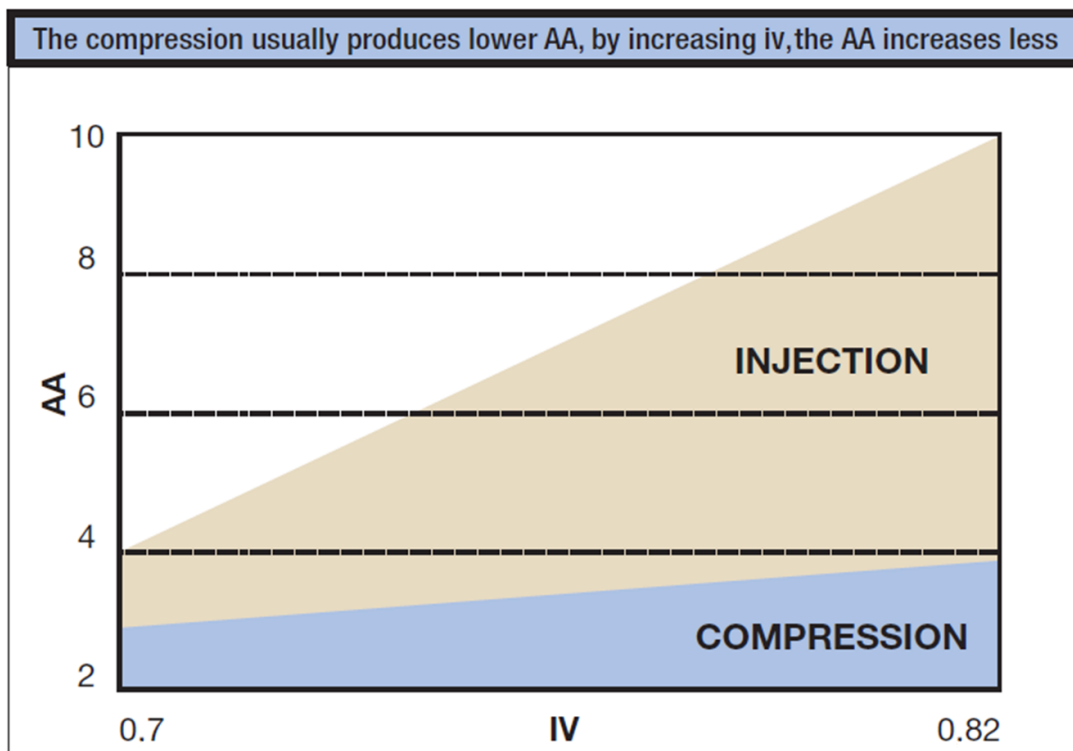


Figure 1.47 AA generation (ppm): comparison between injection and compression molding.

## 1.6 CONCLUSION AND FUTURE INDUSTRIAL DEVELOPMENTS

All the aspects analyzed in detail in the previous paragraphs lead to the conclusion that with a single stage compression molding there is an important saving in energy, intralogistic cost (fig. 1.48) and in the resin one (fig. 1.49).

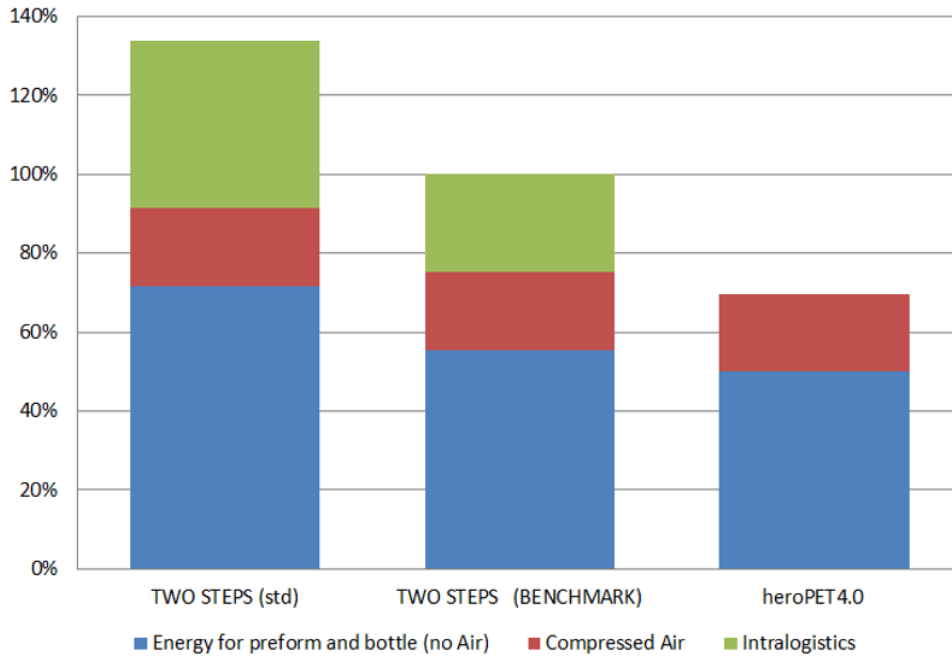


Figure 1.48 Energy and intralogistic costs comparison: Double stages benchmark and heroPET4.0 (compression single stage) [4].

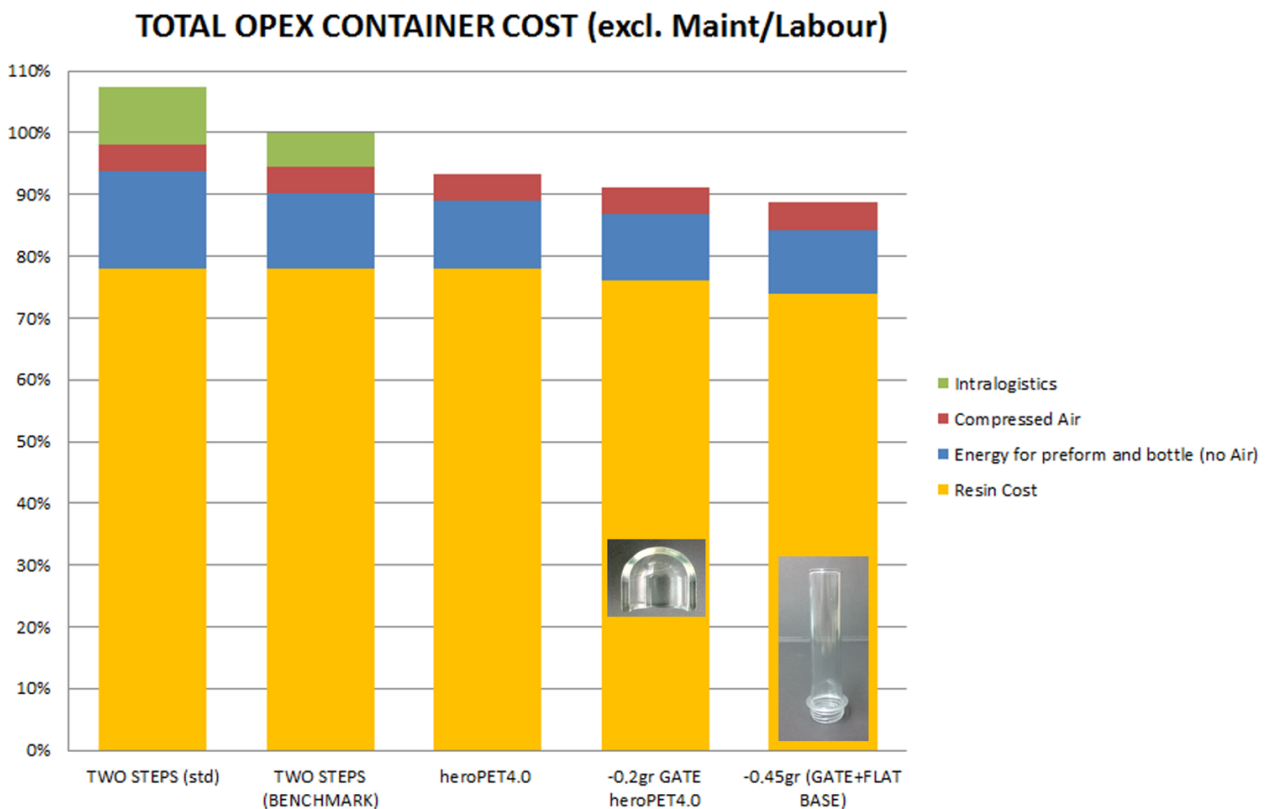


Figure 1.49 Costs comparison. Double stages benchmark and heroPET4.0 (compression single stage) [4].

Compression molding could massively enlarge the actual use of PET containers limited by injection molding technological parameters. PET could substitute glass and other plastics in Food field, Dairy, Pharms, Alcohols.

Moreover, with compression it will be easier to substitute PET with recyclable plastics or biodegradable one. SACMI has already achieved important results with poly(lactic acid) (PLA) for still water bottling.

Going back to fig. 1.49 the effects of the absence of gate and of the flat base on the resin cost were considered separately. The operating expenditure container cost analysis does not include maintenance and labor. They still have to be deeply examined.

As it will be explained in the next chapters, the actual limit of compression molding is the cutting and above all the handling of the gob due to PET adhesiveness. Actual devices are too complicated to be implemented in all markets, particularly in countries where technicians have low technical competences. The aim of this dissertation is to give some answers to these limitations so that compression molding could finally be an industrial innovative technology for preform molding.

## 1.7 REFERENCES

- [1] M. Camerani, *PET AND ITS PREFORMS Handbook*, SACMI, 2008, ISBN 88-7586-132-3.
- [2] <http://www.plasticseurope.org/en/resources/publications/plastics-facts-2017> , viewed on 03/11/2018
- [3] <http://www.plasticseurope.org/Document/plastics-the-facts-2014.aspx>., viewed on 12/10/2017.
- [4] D. Marastoni, *SACMI heroPET4.0*, PETnology, 2016, 3.
- [5] M. Savorani, *SACMI Preform Compression Molding & Stretch Blow Molding: a flexible and energy saving way from pellet to bottle*, PET World Congress, Munich, 2009.
- [6] R. Unterlander and O. Brandau, *The Rapid Guide to Perfect Preform*, PETplanet Print, 2008, Vol. 6.
- [7] S. A. Jabarin and E. A. Lofgren, *Effect of water absorption on physical properties and degree of molecular orientation of poly (ethylene terephthalate)*, Polym. Eng. Sci., 1986, Vol. 26 (9), pp. 620-625.
- [8] G. Venkateswaran and S.A. Jabarin, *Effects of Moisture and Physical Aging on the Free Blow Characteristics of PET*, Society of Plastics Engineers Annual Technical Conference, Indianapolis, 1996.
- [9] S. A. Jaborin, *Polym. Eng. Sci.*, 1984, 24 (5), p. 376.
- [10] C. Bonnebat, G. Rouillet, A. J. de Vries, *Biaxially oriented poly(ethylene terephthalate) bottles: effects of resin molecular weight on parison stretching behavior*, Polym. Eng. Sci., 1981, 21 (4), pp. 189-195.
- [11] F. Parrinello, *Aerosol and container produced with high molecular weight PET: the effect of Intrinsic Viscosity*, Annual Blow Molding Conference, Atlanta, Georgia, 2013.
- [12] Th. Rieckmann and S. Völker, *Poly(Ethylene Terephthalate) Polymerization – Mechanism Catalysis, Kinetics, Mass Transfer and Reactor Design* ch.2 pp. 29-115 in *Modern Polyesters:*

*Chemistry and Technology of Polyesters and Copolyesters*, J. Scheirs, T.E. Long, Ed., John Wiley & Sons, Ltd, 2003.

## Chapter 2

### PET - METAL ADHESIVENESS

#### 2.1 INTRODUCTION

As explained in the end of chapter 1, the main issue regarding PET preform compression molding is cutting and above all handling of the molten PET gob. Molten PET has a high adhesiveness with other materials. Moreover, adhesiveness increases if the surface has already been in contact with PET. This change in adhesiveness results in a lack of control of the process. The transferring time from the handling tool to the mold cavity can change significantly. Furthermore, the gob sometimes sticks to the handling tool wall resulting in a stop of the machine, which, if it happens frequently, is industrially unacceptable.

According to the industrial experience, PET adhesiveness is much higher than other industrial polymers such as PE and PP. Several PET gob handling solutions have been tested and many of them patented. Chapter 3 will analyze them in further details. Nowadays, with present devices, mechanical components are complicated and require a frequent manual cleaning by a specialized technician. Moreover, the process scrap is still high (around 4 % of the overall production) and it seems to be due to defects generated in the cutting and handling of the gob.

Gob handling is almost a necessity: it is not convenient to have the nozzle directly on the mold. One reason is the powder generated after several thousands of cuts with the technology in use today (see fig. 2.1). Powder can enter the mold generating defects in the preform/bottle.

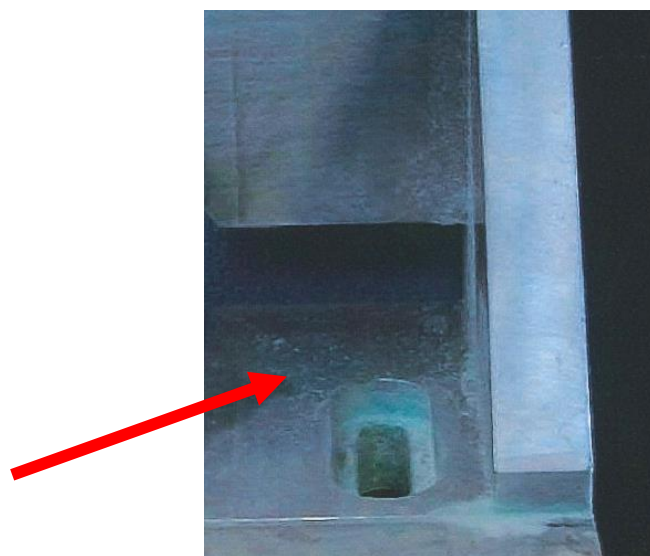


Figure 2.1 Pigmented powder deposition on components close to the cutting zone during production of colored preforms.

Moreover, the start-up of the machine, as in injection molding, generates PET scrap from the nozzle that today is cut and, with gravity, falls vertically to a bin on the ground. At present, to solve these inconveniences and others, a handling tool reaches the nozzle at proper time to take the gob. In an industrial machine, the time of handling lasts few tenth of seconds. The industrial practice shows a reduction of negative adhesiveness effects by reducing handling time. This concept will be discussed in more details in chapter 3.

This chapter is dedicated to the analysis of PET/metal adhesiveness in existing literature. Metals of interests are aluminum and stainless steel. A superficial layer of aluminum oxide and chromium oxide gives them respectively a strong corrosion resistance, which is required by FDA (Food and Drug Administration) rules. The research was hence focused on aluminum/PET and chromium/PET adhesiveness. Only few papers deal with tests to measure adhesion strength of the steel - plastic interface. Their aim is to assess ways to reduce plastic stickiness on steel dies during the forming process. Some interesting results come from thermoplastic bonding to metals via injection molding [1]. Many works are about metal-polymer interfaces formed by thermally depositing metals in vacuum onto polymer surfaces. This is due to the great relevance of metallized plastic films in the packaging industry. The researchers' goal is mainly to increase adhesion. Even if many conditions are different, above all vacuum deposition, which means Al and Cr are not oxidized, it still seems valuable to analyze the topic to understand some concepts.

Before starting the analysis of every single case of metal polymer interfaces, some paragraphs are dedicated to mechanisms of adhesion, work of adhesion, surface free energy, analytical techniques and adhesion test for polymer-metal interface characterization.

## 2.2 MECHANISMS OF ADHESION

The scientific community is still debating on adhesion mechanisms between polymers and metals. Several mechanisms have been proposed [2, 3, 4] and, according to Kono [5], we can synthetize them into three main categories (fig. 2.2), even if some authors, for example Culbertson [2], tend to ignore the second one:

- mechanical interlocking theory,
- electrostatic theory,
- adsorption theory also called chemical theory.

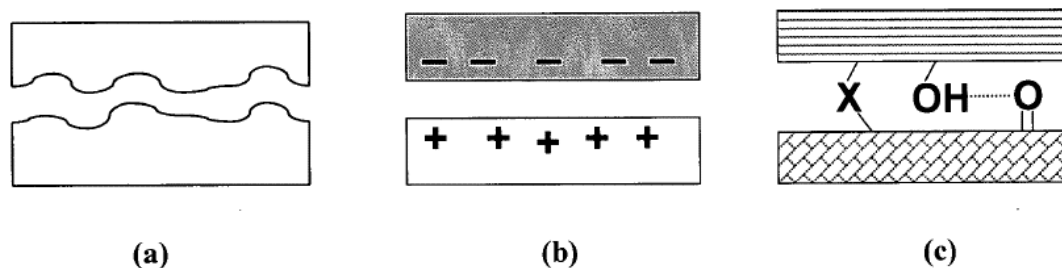


Figure 2.2 Adhesion Mechanisms: (a) mechanical interlocking; (b) electrostatic attraction; (c) direct chemical bond formation [5].

Several adhesion phenomena can be described by one of these theories or a combination of them [5, 2]. Substrate morphology, contamination on the surface, chemical interactions, the energy available during interface formation and the nucleation behavior of the deposited material influence the type of interfacial region [2].

### 2.2.1 Mechanical interlocking theory

Mechanical/physical interlocking (also called mechanical keying) is generally defined as the adhesion effect created when an adherent species penetrates into irregularities (e.g. rough surface) or porous structures at a substrate surface. This does not mean that a smooth surface necessarily results in bad

adhesion: the undersigned's experience and literature attest that good adhesion is possible even with smooth surfaces and glass [7].

### 2.2.2 Electrostatic theory

Derjaguin [8] suggested that the adhesion between two solid materials could result from an electrical double layer formed by electron transfer from one material to the other. A loss of adhesion during sample exposure to an electrical discharge [9] supports the electrostatic theory [5].

### 2.2.3 Chemical bonding theory

The chemical bonding (or adsorption) theory [3, 10] relates polymer-metal adhesion to the creation at the interface of covalent and ionic bonds (called primary bonds) and/or weaker interactions (called secondary bonds) such as hydrogen bonds and van der Waals forces (non-polar dispersion forces, dipole-dipole interactions and dipole-induced dipole interactions). Figure 2.3 indicates bond strengths and ranges of these interactions [11].

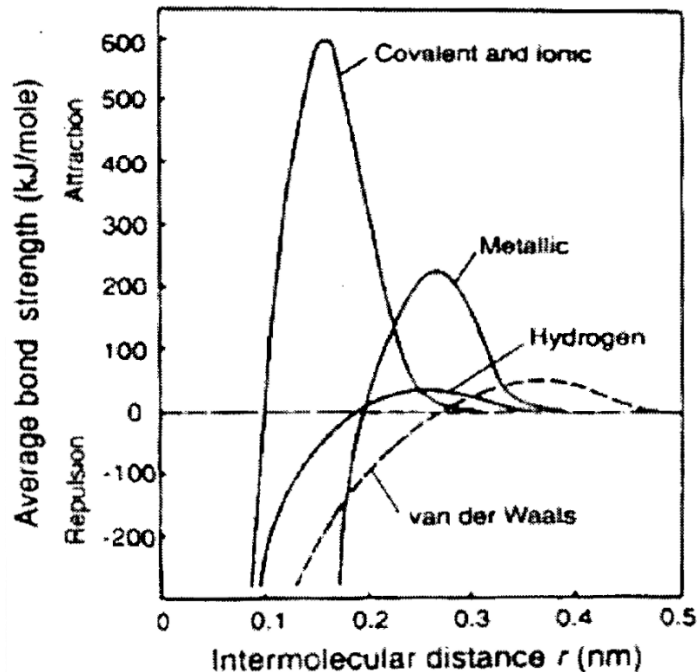


Figure 2.3 Range and bond strength of typical interatomic and intermolecular interactions<sup>1</sup> [11].

## 2.3 WORK OF ADHESION

The work of adhesion is the work that must be done to separate two adjacent phases (1 and 2) of a liquid-liquid or liquid-solid phase boundary from one another. Conversely, it is the energy which is released in the process of wetting. The units of work of adhesion are  $J/m^2$ . The work of adhesion is a measure of the strength of the contact between two phases. Its knowledge is therefore important for

---

<sup>1</sup> Reprinted, with permission from John Wiley & Sons Ltd, from D Feldmann, *Fundamentals of Adhesion*, L. H. Lee, Ed., Copyright 1991 Springer Science+Business Media New York. Originally published by Plenum Press, New York in 1991. All rights reserved. No part of this book may be reproduced, stored in a retrieval system, or transmitted in any form or by any means, electronic, mechanical, photocopying, microfilming, recording, or otherwise, without written permission from the Publisher.

processes such as coating, painting, cleaning, printing, hydrophobic or hydrophilic coating, bonding, dispersion, etc. [12].

## 2.4 SURFACE FREE ENERGY

The surface free energy (SFE) is the work which has to be expended in order to increase the size of the surface of a phase. As energy per unit area, the surface free energy has the unit  $\text{mJ}/\text{m}^2$ , wherein the equivalent unit  $\text{mN}/\text{m}$  is frequently used. The symbol used in formulas is  $\sigma$ . The term surface free energy is normally used for solid surfaces. When a liquid phase is concerned, reference is usually made to surface tension (SFT). As it is difficult to differentiate the work required to increase the size of the surface from the deformation work by measurement, the surface free energy is normally measured indirectly with the help of sessile drop contact angles with several liquids [12]. The standard method is the Owens, Wendt, Rabel and Kaelble (OWRK): the surface free energy is divided into a polar part and a disperse part. At least two liquids with known disperse and polar parts of the surface tension are required to determine the surface free energy of the solid, wherein at least one of the liquids must have a polar part higher than 0 [12, 13, 14, 15]. In the experiments described in chapter 4 the liquids are bi-distilled water and diiodomethane. The former has a low dispersion component of surface tension and a high polar component; whereas for the latter it is the contrary. Fig. 2.4 reports the wetting effect of two liquids with the same surface tension, but a different polar and disperse component, on the same solid.



Figure 2.4 Wetting effect of two liquids with the same surface tension, but different polar and disperse component, on the same solid<sup>2</sup> [12].

<sup>2</sup> Images: KRÜSS GmbH / <https://www.kruss-scientific>.

The wetting is perfect when disperse and polar components of liquid surface tension are the same of the surface free energy of the solid. To avoid confusion, it is maybe useful to also give an interfacial tension definition: it is the work required to increase the size of the interface between two adjacent phases which do not mix completely with one another. Its unit is mN/m. In the narrower sense the term relates to liquid/liquid and liquid/solid phase boundaries. Surface tension refers to liquid/gaseous interface, while surface free energy refers to solid/gaseous one [12].

## 2.5 INTERFACE CHARACTERIZATION ANALYTICAL TECHNIQUES

Literature lists many techniques used to characterize metal-polymer interface: SEM (surface morphology), TEM (cross section), FTIR, RAMAN (change from crystalline to amorphous structure of PET [16]), ATR, AFM (surface morphology), SIMS (elemental composition), XPS. This last one (XPS) deserves a brief description since it is the most widely applied in literature [6, 5, 17, 2, 18, etc.] to analyze the chemical changes of the surface composition.

### 2.5.1 XPS

XPS (X-ray photoelectron spectroscopy) experiment consists in the irradiation of a sample surface with soft X-ray radiation and measuring the kinetic energies of the photoelectrons emitted by the surface atoms. The environment from which a photoelectron originates is related to its kinetic energy, while the concentration of the relevant atoms in the sample affects the number of electrons emitted. XPS can therefore give qualitative and quantitative information. It is advantageous to plot the spectra as a function of binding energy because the latter is linked directly to the surface chemical structure. Furthermore, it is independent from the source of photons [5].

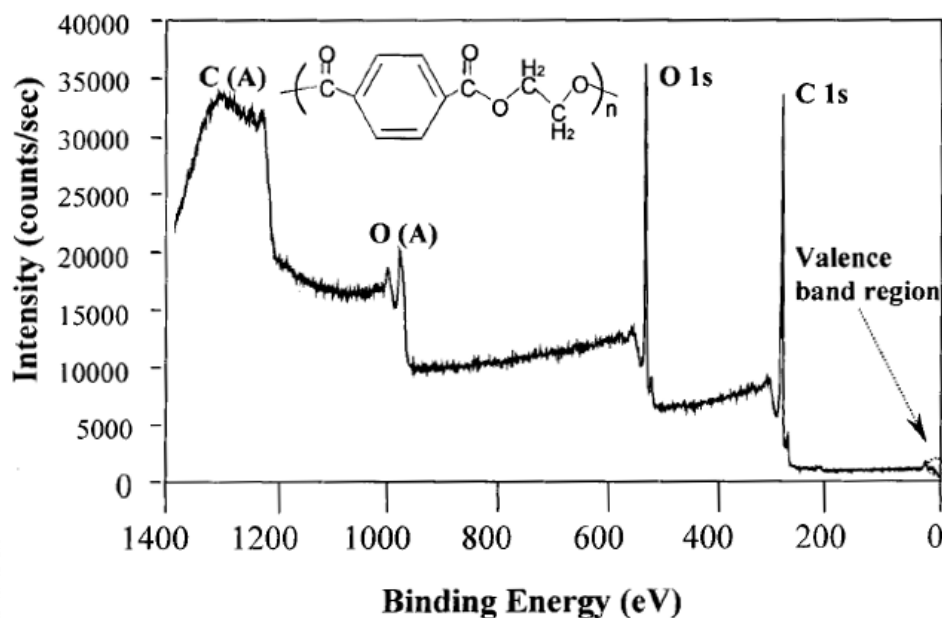


Figure 2.5 PET film low resolution survey XPS spectrum [5].

A series of peaks on a step-like background are shown on the low-resolution spectrum (also called survey scan) from PET film (see fig. 2.5). According to Kono, the peaks can be grouped into three types: (i) peaks due to photoemission from the core levels (O 1s and C 1s), (ii) structure from the valence band (binding energy in range 0 to 30 eV) and (iii) peaks due to Auger electron emission shown as C(A) and O(A) [5]. The high-resolution spectra (also called narrow scans) give more information about a sample. An example is the measured spectrum for the C 1s region from PET in

fig. 2.6. As Kono states, three major peaks correspond to phenyl carbons, methylene carbons (O-CH<sub>2</sub>CH<sub>2</sub>-O) and the ester carbon (O=C-O), and these are listed in order of increasing binding energy. This order simply correlates with the number of neighboring electron-withdrawing O atoms. A minor broad peak is noted at around 291.6 eV which corresponds to  $\pi \rightarrow \pi^*$  shake-up structure, and it is associated with a configuration interaction effect which depends on promotion of valence electrons from an occupied  $\pi$  level to an unoccupied higher  $\pi^*$  level. This feature is generally evident in XPS spectra for systems with aromatic ring structures, and its presence can be used as a proof of aromaticity in a sample [5].

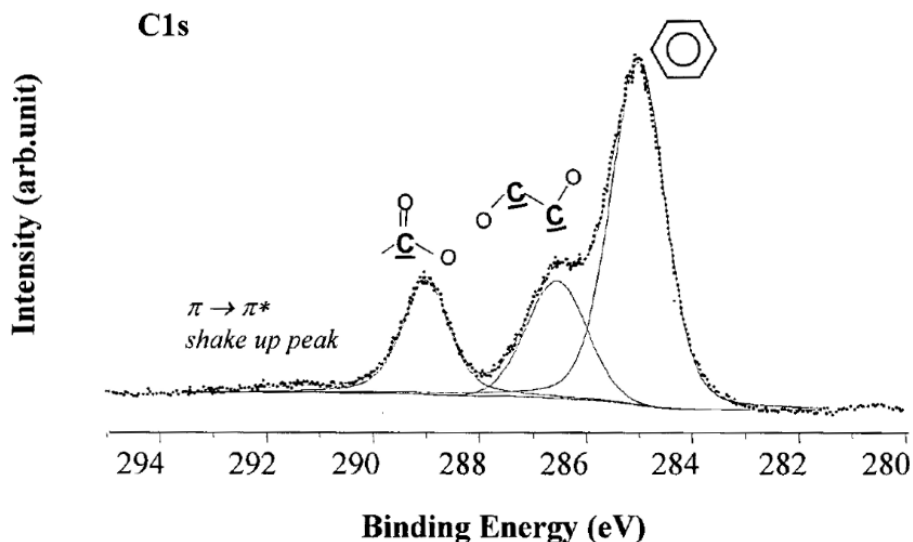


Figure 2.6 PET film high resolution XPS spectrum with components allocation to peaks [5].

## 2.6 ADHESION TEST

Several tests can be done to assess the strength of a bonding between two different materials. Regarding metal thermal deposition on PET, the more used are tape test [2] and peel test [6, 19, 17]. Both of them are described by ASTM, ISO and DIN norms. Figure 2.7 illustrates the most frequent metal/PET peel tests. The output is usually given in g/in (less frequently N/cm [6]) and the peel rate is usually between 5 and 50 cm/min [6, 19, 17]. Attention must be paid to supports preparation.

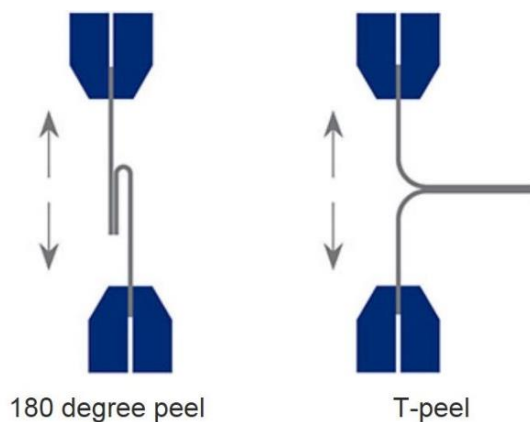


Figure 2.7 Schematization of the more frequent metal/PET peel tests<sup>3</sup> [20].

<sup>3</sup> Reprinted by permission from Mecmesin: <http://www.mecmesin.com/peel-test-adhesion-testing>

## 2.7 METAL THERMAL DEPOSITION ON PET

### 2.7.1 Al/PET adhesion

Existing literature describes extensively about polymer-metal interfaces formed by thermally depositing metals in vacuum onto polymer surfaces [6, 5, 19, 17, and 2]. In the past years, they were used for audio and video recording tapes. Nowadays the main applications are in the packaging industry and electronic devices. In general, the use of metallized films, and more specifically, the use of PET films, to achieve the barrier needed for shelf-life, has been increasing for a number of years. The cause of researchers' interest is the technological relevance, and yet there are many issues that are not well understood. In the last 40 years, several techniques have been commonly used, before and during metal deposition to improve the adhesion: corona discharge treatment [21, 22], chemical treatments (bromosulfonic acid, fluorine gas [23]), oxygen treatment [24], ion-plating treatment [25], ion beam deposition [26], electron beam deposition, magnetron sputtering and arc deposition [27]. In the last 15 years the use of laser techniques has also been deeply studied [6, 28].

In the case of metallized PET (MPET) films, it is usually recognized that the most important aspects of adhesion arise from mechanical and chemical bonding at the interface. Many researchers studied Al-PET interfaces with different techniques, but interpretations differ in some points. It is valuable to consider Culbertson [2] analysis on Al/PET bonding, which is the result of chemical and mechanical adhesion. Carbonyl, vinyl and carboxyl groups (these last two are end groups formed due to degradation during metal evaporation) on PET film surfaces contribute to the surface energy of the PET film. In the case of aluminum, a metal that forms a very stable oxide, reactions occur with the surface groups (mainly carboxyl endgroups) to form chelates (chemical adhesion). Other metals that produce oxides would likely react in a similar manner. PE and PP films present poor metal adhesion because they have a low surface energy affecting the metal wet out at the interface and no oxygen containing groups for chemical interaction. As regards to mechanical interlocking, PET film has crystalline and amorphous areas. The adhesion of the metal depends partly on the amount and size of the spherulites (crystalline areas) in the PET film. The energy from the evaporated metal is used to melt the surface giving anchors for mechanical adhesion. The amorphous areas allow the metal to "drill" farther into the film surface than the crystalline areas. According to TEM observation, the metal penetration is about 30 - 40 Å (fig. 2.8a). For PET film the metal adhesion is typically between 200 - 400 g/in. Culbertson then suggested some methods such as chemically coating the PET film with a co-polyester. The adhesion rises to 500 - 600 g/in due to an increase in mechanical adhesion thanks to lower melting temperature and lower crystallinity. TEM analyses confirmed a deeper penetration of aluminum in co-polyester coating to 50 - 60 Å (fig. 8b). No significant increase in chelated species was observed [2].

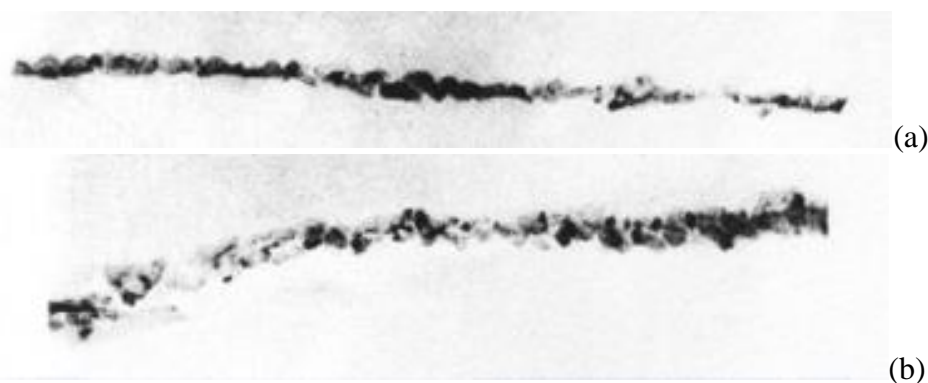


Figure 2.8 TEM analysis of metal penetration (30 - 40 Å) in plain PET film (a) and in co-polyester coated PET film (b) (same scale) [2].

In general, Culbertson suggests that to increase metal adhesion, a coated PET film (a typical coating is a very thin layer of a co-polyester) should be adopted. In this way both mechanical adhesion and chemical adhesion should improve, the latter by choosing monomers that promote increased chemical bonding.

It is important to remark that, according to Silvain and Ehrhardt's experience on Al thermally evaporated onto PET [17], low PET crystallinity results in diminished layer adhesion (80 g/in). They justify it with the fact that the deposition of Al on low crystallinity PET gives spherical precipitates (fig. 2.9) not connected with the rest of the metal layer. On the contrary, when the same metal is deposited under the same condition on a polymer with high crystallinity, a sharper interface results [17].

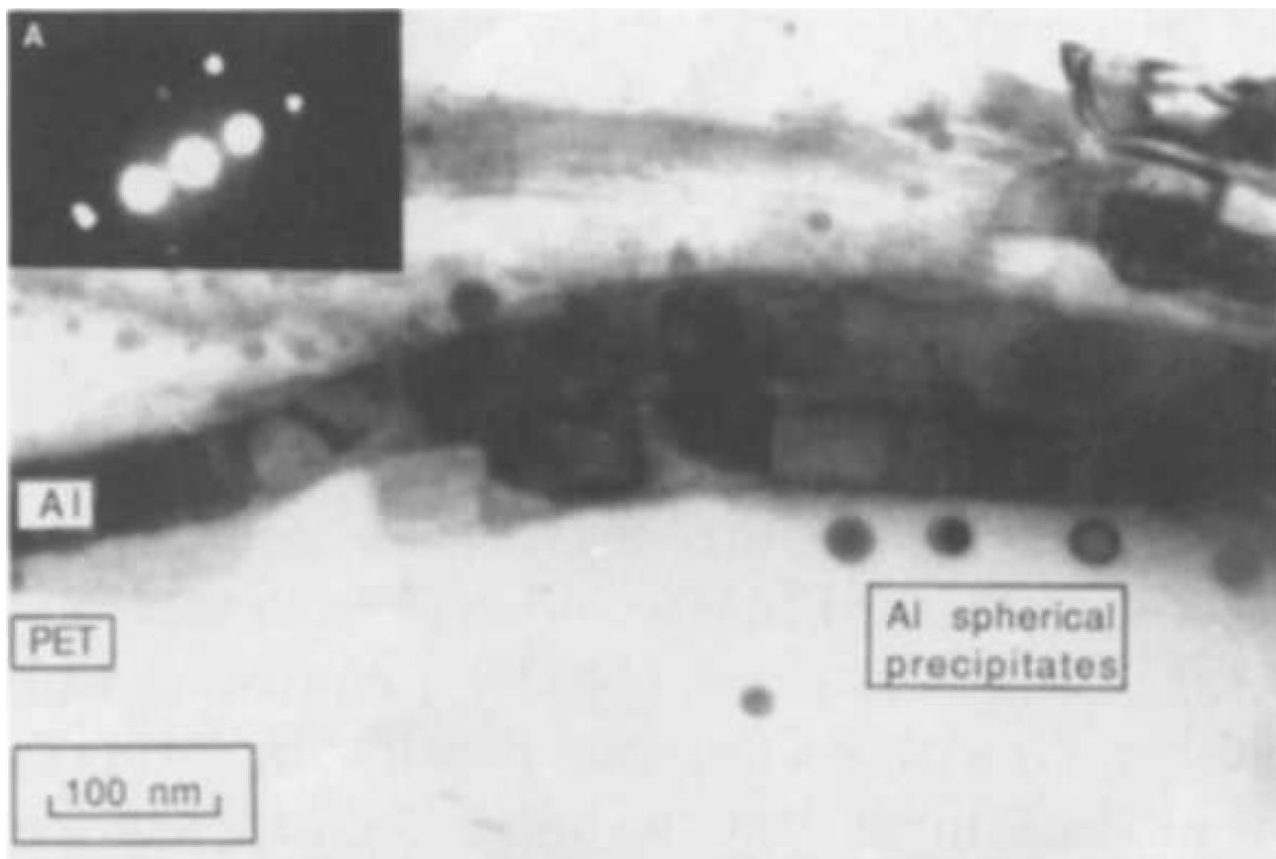


Figure 2.9 Morphology and structure of a low adhesion (80 g/in) aluminum thin film <sup>4</sup> [17].

Silvain, Veyrat and Ehrhardt [19, 17] support the theory of other researchers [29, 30] according to whom the adsorption of metallic atoms involves the breaking of the C=O double bond and the formation of a complex -C-O-M. Kono, in his PhD thesis [5] published in 2000, tries to give a deeper understanding of the matter of the chemical/adsorption adhesion between metal and polymer. His interpretation of chemical bonding Al/PET seems more reliable than Culbertson's one. This could sound strange, since Culbertson writes in 2006. It is important to underline that Culbertson's references [3, 31, 32, 33] are all older than Kono's work (apart from [31] which was presented in 2002 but is about barrier properties) and Kono had read at least one of them [3]. To help the discussion it is valuable to briefly report Kono's experiments. He undertook a new XPS study for the Al/PET system, and he used the Al metallization of polystyrene (PS) as benchmark since its molecular structure has benzene-type rings but not the ester groups (with O functionalities) present in PET. His work was presented on a comparative basis in order to highlight trends that may help to establish

<sup>4</sup> Reprinted from *Thin Solid Films*, **236**, J. F. Silvain and J. J. Ehrhardt, *An overview on metal/PET adhesion*, p. 233, Copyright (1993), with permission from Elsevier.

principles for interfacial metal-polymer bonding. He deeply analyzed quantitative changes in C 1s and O 1s by taking difference spectra [34]. In his work, he assumed that organic polymer surface metallization could change photoemission spectra in two main ways. Firstly, an attenuation from the added overlayer will occur; secondly, details of the spectra will change because of some metal-polymer interaction. The goal, Kono continued, when taking a difference spectrum, is to obtain a common reference component that is especially associated with the substrate (i.e. PET in this case) and is principally just subject to the attenuation effect. For example, Kono's XPS investigation on Zr deposition on PET revealed neither the presence of direct Zr-C bonding, nor the breaking of major bonds in the structure of the PET. Each Zr atom is then in an environment of O atoms from the PET chains, and this local situation approaches a coordination complex with  $Zr^{\delta+}-O^{\delta-}$  bonding involving both types of O atoms of the ester group (carbonyl ones and single bonded ones) fig. 2.10 [5].

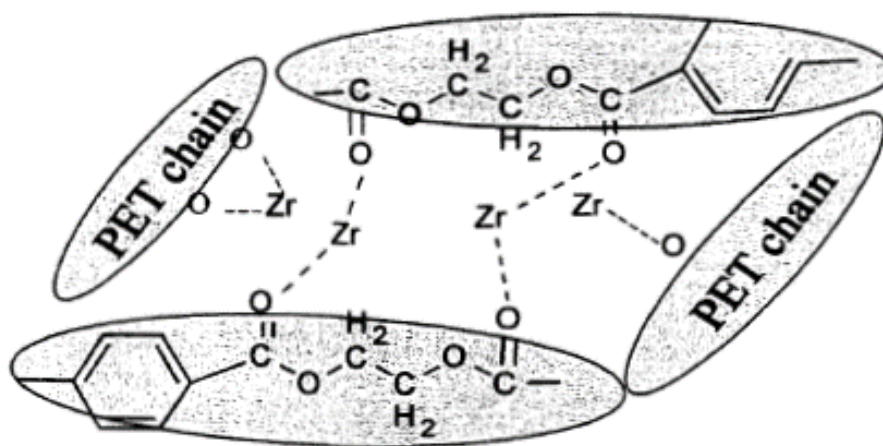


Figure 2.10 Schematic indication of Kono's Zr/PET interaction model [5].

Zr/PET interfacial region appeared not to be relevantly modified by air exposure [5].

Comparing C 1s spectra, before and after the addition of Al on PS showed essentially neither change in structure, which could be associated with either C-O or C-Al bond formation, nor any changes detected for the  $\pi \rightarrow \pi^*$  shake-up peak. Therefore, while it is clear that Al is partially oxidized during the deposition process, any direct chemical interaction between Al and the PS surface seemed negligible [5].

Moving to Al/PET, the spectral changes on depositing metal in Kono's work [5] were clearly much greater for the Al/PET system compared to Zr/PET. Kono provided evidences for the formation of direct bonds of both Al-C and Al-O types and there is a similarity with the conclusions reached in previous XPS studies [35, 36, 37, 38]. He gave the following interpretation: Al interacts with the carbonyl group by breaking the  $\pi$  bond and forming direct bonds to both C and O atoms. Changes in the C 1s spectrum, including new structure, a shift to higher binding energy and enhancement in the shake-up peak (the latter ascribable to a more localized  $\pi$ -electron system [39]) suggested the chemical bond formation between Al and the aromatic ring. The resulting model is shown in fig. 2.11 (b), while fig. 2.11(c) represents a schematic view of the oxidized Al-PET interface, after exposure to  $O_2$  [5].

It is worthy to briefly mention Kono's study on Mg/PET interfaces. According to him, Mg atoms are present on PET surface as both O-Mg-C and metallic-like clusters. The interface formed by PET and thermally-deposited Mg is relatively stable in air, but not in water. Indeed, it was shown that a water rinsing could remove the Mg component completely from the film and leave a modified PET surface behind [5].

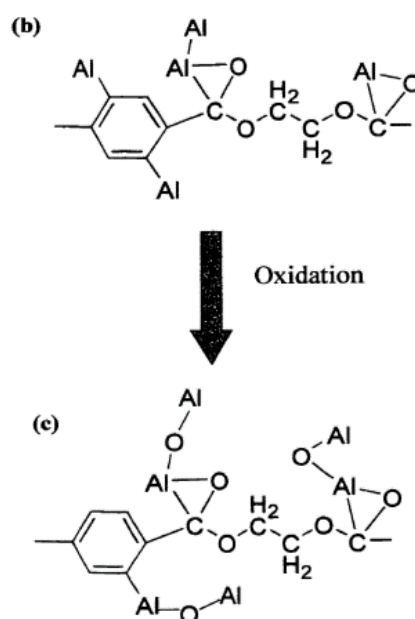


Figure 2.11 Schematic indication of Kono's Al/PET interaction model with deposition in vacuum (b) and after O<sub>2</sub> treatment (c) [5].

### 2.7.2 Effect of PET temperature during deposition and of subsequent water absorption

An annealing-induced rearrangement of the polymer chains occurring above the glass transition temperature of PET ( $T_g \approx 80$  °C) has been observed by IR measurements [24] and, in particular, a reorientation of the aromatic rings which present the tendency of becoming parallel to the surface of the sample. Conversely, an increasing number of carboxylic groups which are in the plane of the benzene ring will be present in the surface of the sample. As discussed in the previous paragraphs, carboxylic groups are sites for the creation of metal bonds [19].

In the early nineties, Silvain, Veyrat and Ehrhardt [19, 17] studied the effect of the temperature on the adhesion of thin metal films evaporated on polyethylene terephthalate (see table 2.1). Two adhesive values were measured by 180 ° peel tests in a dry and a wet atmosphere. The wet test was realized after soaping the metal/PET wafer for 1 min in water. Note that 1300 g/in is the measurement upper limit due to the mechanical properties of the bulk polymer.

Condition	Temperature (°C)	Dry adhesion (g in <sup>-1</sup> )	Wet adhesion (g in <sup>-1</sup> )
(a) Room temperature PET	Room temperature	50–200	0
(b) <i>In situ</i> heated PET, room temperature evaporation	90	400	20
(b) <i>In situ</i> heated PET, room temperature evaporation	130	1000	20
(c) <i>In situ</i> heated PET, hot evaporation	90	400	250
(c) <i>In situ</i> heated PET, hot evaporation	130	1300	1000

Table 2.1 Modification of the adhesion values of Al/PET wafers with the annealing conditions of the polymer<sup>5</sup> [19].

<sup>5</sup> Reprinted from Thin Solid Films, **221**, J. F. Silvain, A. Veyrat and J. J. Ehrhardt, *Effect of the temperature on the adhesion and the morphology of thin metal films evaporated on polyethylene terephthalate*, p. 115, Copyright (1992), with permission from Elsevier.

The increase in dry adhesion with the high temperature annealing phase prior to metal deposition, which has been done at room temperature in tests b, could mean that dry adhesion is mainly influenced by the arrangement of the polymer chains (explained few lines above) and maybe the cleaning of the PET during the annealing (water desorption) [19].

In contrast, the behavior of wet adhesion, which rockets dramatically for temperature above  $T_g$  during deposition, may be explained by the atomic diffusion of the metal into the polymer. This process increases with rising PET temperature and may lead to a growth, by cross-linking (fig. 2.12), in the cohesion of the skin of the PET. A binding model for s and p valence orbital metals are illustrated in figure 2.13 [19].

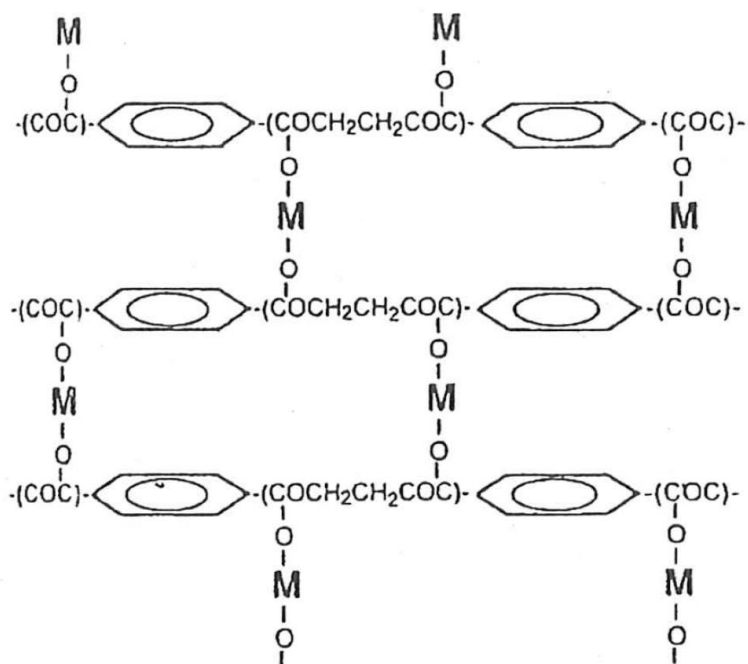


Figure 2.12 Model of the interaction in the skin of the polymer between s and p valence orbital metals<sup>6</sup> [19].

## 2.8 PET COATING ON METAL: Cr/PET ADHESION

Pet coatings are used to protect metals for food and beverage containers (aluminum, ECCS) from corrosion [40]. Chromium coated steel is a sheet or strip of steel electrolytically coated with a layer of chrome thinner than a micron. Originally called TFS (Tin Free Steel), it is now known by the acronym ECCS (Electrolytic Chromium Coated Steel). ECCS is never used without an organic protection for food products [41]. Corus Packaging Plus, the company from which Zumelzu [16, 18] took fig. 2.13, has developed "Protact", which is an ECCS substrate with multiple layers of hot PET extruded directly onto the surface of the metal [42]. Other companies have developed similar solutions [42, 43]. Generally, the lamination process utilizes a combination of heat and pressure, followed by rapid but controlled cold-water quenching, which defines the degree of crystallinity throughout the film, its adhesive bonding characteristics and its formability [43]. The PET layer has usually a thickness of 0.2 mm [18].

<sup>6</sup> Reprinted from *Thin Solid Films*, **221**, J. F. Silvain, A. Veyrat and J. J. Ehrhardt, *Effect of the temperature on the adhesion and the morphology of thin metal films evaporated on polyethylene terephthalate*, p. 119, Copyright (1992), with permission from Elsevier.

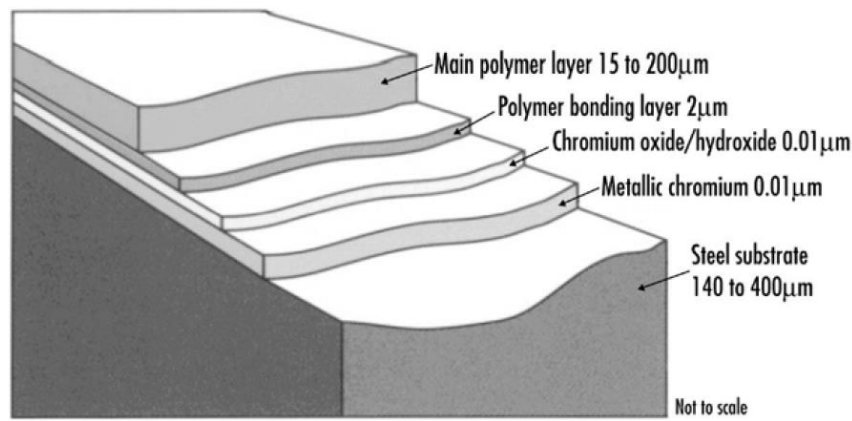


Figure 2.13 A steel plate coated with electrolytic chromium (ECCS) and PET coatings (Corus) <sup>7</sup> [16].

Characterization studies carried out by Zumelzu et al. [16, 18] proved that the adhesion of the metal polymer composite is the result of the influence of the amorphous structure of the PET at the interface level, the crystallographic orientations of the metal substrates, and the topographic features of the surface. The PET adhered to the surface by occupying the void areas and adopting the topographical form of the ECCS plate. It is well known that the chromium deposit on the ECCS plate consists of  $Cr^0$  and  $Cr^0 + Cr^{n+}$  ( $n = 2, 3$ ). To achieve the metal-polymer bonding, the chromium uses the oxygen of the PET to form links similar to those of oxide (see figure 2.14).

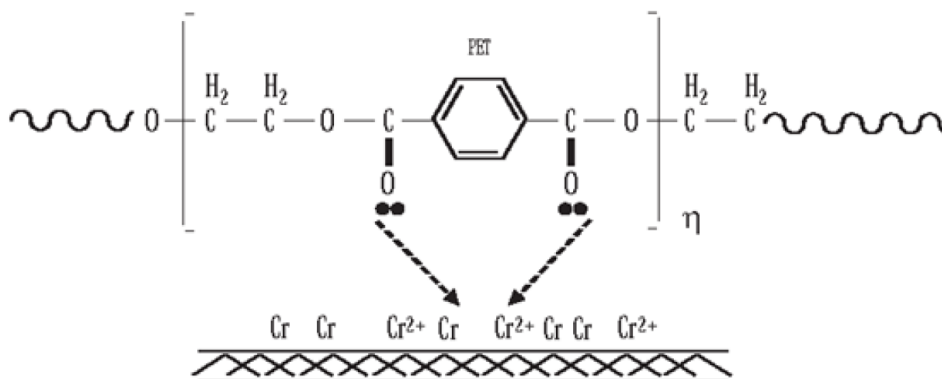


Figure 2.14 Bonding of PET oxygen atoms to chromium substrate <sup>8</sup> [16].

A bonding model that, according to Zumelzu, would explain the adhesion of the metal-polymer laminate is that of the acid-base interaction mechanism. In this model on the PET-coated ECCS plate, the carbonyl oxygen (electron pair donor = base) shares its electrons with chromium (electron pair acceptor = acid). A similar argument can be used with the electrons of the benzene ring and chromium. In the chromium benzene ring chemical bonding, there are four chromium electrons ( $Cr^{2+}$ ). The benzene ring of the PET contributes up to six electrons in pairs according to the structure of the delocalized orbitals (see Figure 2.15). As the oxygen molecules come closer, the  $Cr^{2+}$  acts like an acid and the benzene ring and oxygen atoms like a base, and the electrons exchange their positions giving rise to covalent bonds. This explains the strong adherence between the PET coating and the chromium deposit on the ECCS plate [16].

<sup>7</sup> Reprinted by permission from RightsLink Permissions Springer Customer Service Center GmbH: Springer, Surface Coatings International Part B: Coatings Transactions Vol. **89**, B1, *Structural analysis of polymer-metal laminates by electron microscopy and infrared spectroscopy*, E. Zumelzu, F. Rull, P. Schmidt et al., 2006, p. 58.

<sup>8</sup> Ibid., pag.61.

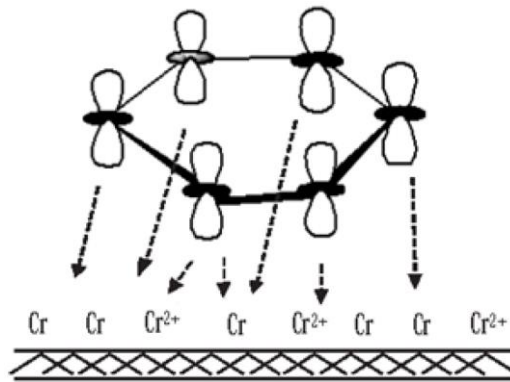


Figure 2.15 Bonding of delocalized benzene ring orbital electrons to chromium substrate<sup>9</sup> [16].

## 2.9 MOLD ADHESIVENESS REDUCTION

Few works in literature are about the reduction of PET stickiness to metals, and they are related to plastic molding.

In 2002, Zhang et al. published a paper [44] about the effect of coatings on reduction of plastic sticking on transfer molding. They used epoxy resin, not PET.

Polymer blocks are molded on mold steel surface at a pressure of about 100 bars. After molding, the epoxy block was cured at 175 °C together with the steel block for two hours and then pulled apart. The force required to separate the plastic part and the mold steel is used as an indicator of the stickiness. With respect to uncoated mold steel (not specified which mold steel), WS<sub>2</sub> and DLC coating gave the better results, reducing stickiness of 80 %. This was in accordance with contact angle tests using distilled water. The anti-stickiness best results were reached with Ra 0.5 μm [44]. Ra is defined as (arithmetical mean of deviation of the assessed profile, see fig. 2.16)

$$Ra = \frac{1}{l} \int_0^l |Z(x)| dx$$

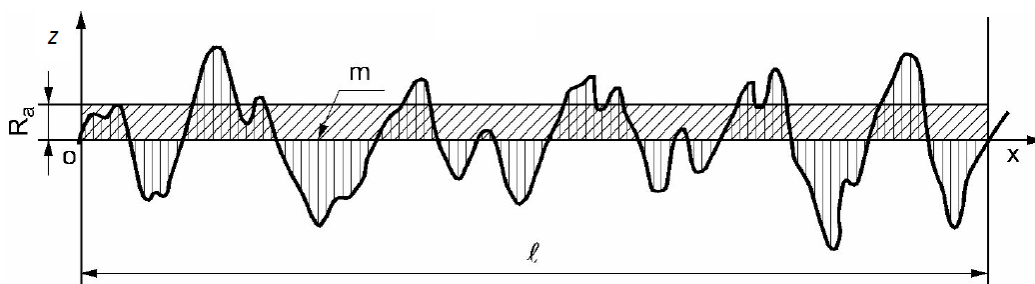


Figure 2.16 Ra definition according to ISO 4287:1997. Z is the deviation from the average surface line.

Results of similar, albeit more detailed, tests were published by Shalnov, Uemura and Ito [45] in 2012. In their work, the effectiveness of surface treatments, including mechanical polishing, plasma

<sup>9</sup> Reprinted by permission from RightsLink Permissions Springer Customer Service Center GmbH: Springer, Surface Coatings International Part B: Coatings Transactions Vol. **89**, B1, *Structural analysis of polymer-metal laminates by electron microscopy and infrared spectroscopy*, E. Zumelzu, F. Rull, P. Schmidt et al., 2006, p. 61.

nitriding, hard DLC coating and  $\text{TiB}_2$  ion implantation, were investigated with the aim to reduce the plastic sticking on the steels SKD61, HPM38 and PX5 surface. The surface finishing was characterized with surface roughness, roughness factor, hardness, friction coefficients and wettability. Adhesion strength of the steel - plastic interface for the plastic materials: polypropylene (PP), polystyrene (PS), polyethylene terephthalate (PET), poly-butylene terephthalate (PBT) were measured with a method developed ad hoc, with the concept of real surface area. It was shown that, for the different plastics, the appropriate die material and die finishing must be chosen to provide the lowest plastic sticking [45].

Shalnov (see fig. 2.17) molted the PET directly on the metal surface inside a stainless-steel bushing (1) and kept it for 40 minutes. Then he cooled it down for about 300 minutes. Finally, the PET was pulled away from the metal and the pulling force was measured.

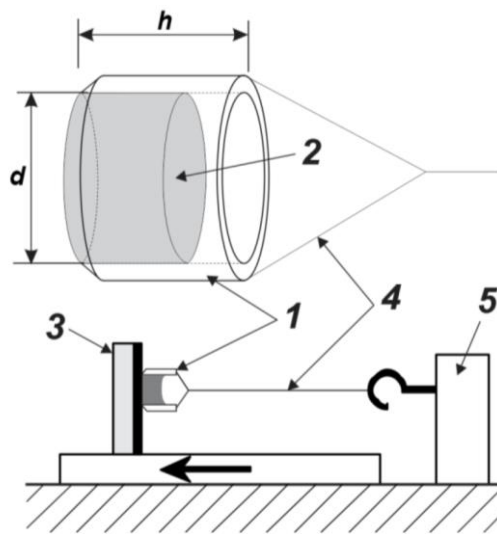


Figure 2.17 Shalnov's adhesion strength measurement schema<sup>10</sup> [45].

It is important to underline that both Zhang and Shalnov consider plastic mold contact time much longer than what happens in PET preforms industrial molding (few seconds) and even more in compression gob transferring (from 0.002 to 0.5 s).

## 2.10 MOULD TEMPERATURE EFFECT ON THERMOPLASTIC BONDING TO METALS

Thermoplastic adhesive bonding via injection molding is a method to create net shape metal-polymer macro composites with interfaces of appreciable tensile strength. Ramani's test [1] demonstrated that the force of the bonding rises with an increase in the grade of penetration of the polymer, especially at micro-roughness scale ( $< 1 \mu\text{m}$ ). He injected polycarbonate on grit blasted low carbon (1018) steel rods at different bar temperatures. Then he pulled the joint on a testing machine. The samples injected at high temperature showed higher bond strength. Ramani related it to polymer viscosity, which is primarily a function of temperature and shear rate. If the apparent viscosity is relatively insensitive to shear rate (like for polycarbonate [46]), or if the shear rate is constant, polymer viscosity is related to polymer temperature by:

<sup>10</sup> Reprinted by permission from Japanese Society of Tribologists as the copyright holder: Konstantin V. Shalnov, Kensuke Uemura, Yoshiro Ito, *Consideration on Surface Modification of Steel Dies to Reducing the Plastic Sticking in the Forming Process*, Tribology Online, 2012, 7 (3), pp.190-200

$$\eta = Ae^{\frac{E}{RT}} \quad (2.1)$$

$\eta$  = shear viscosity;  
E = viscous energy of activation of the polymer;  
R = gas constant;  
T = absolute temperature;  
A = pre-exponential coefficient [46].

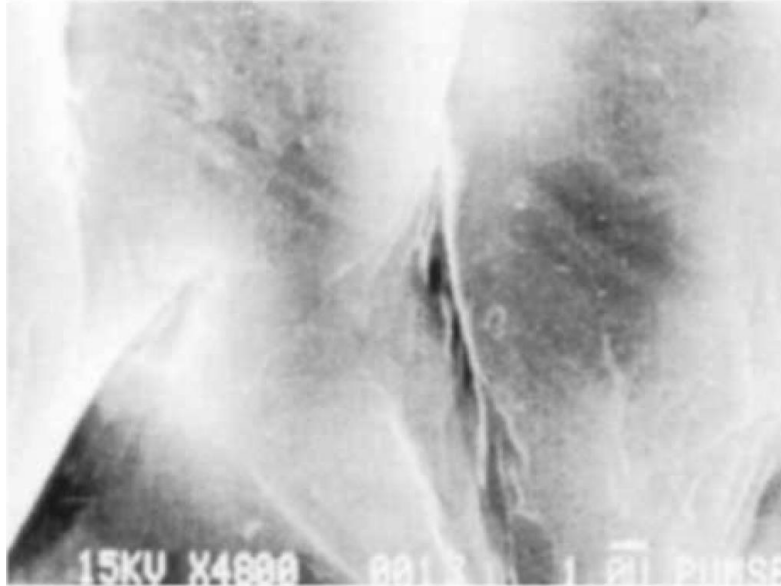


Figure 2.18 SEM image of polycarbonate surface with no aluminum preheating (4800X) <sup>11</sup>[1].

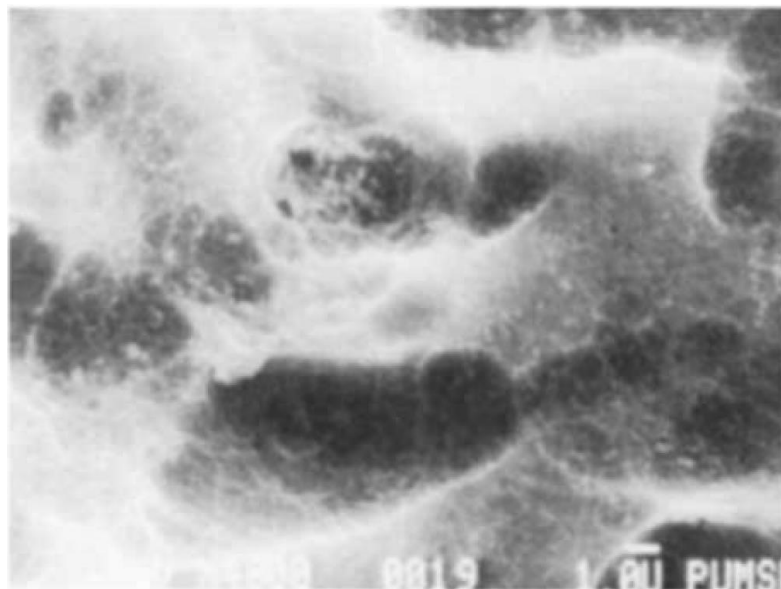


Figure 2.19 SEM image of polycarbonate surface with high aluminum preheating (4800X) <sup>12</sup>[1].

---

<sup>11</sup> Reprinted from K. Ramani and B. Moriarty, *Thermoplastic Bonding to Metals Via Injection Molding for Macro-Composite Manufacture*, Polymer Engineering & Science, Vol. **38** (5), pp.870-877, Copyright (1998) Society of Plastics Engineers, with permission from John Wiley & Sons Ltd.

<sup>12</sup> Ibidem

The significantly lower polymer viscosity at the higher metal surface temperature allows the polycarbonate to penetrate the adherent surface micro-roughness to a greater degree. He repeated the test (without pulling the samples) with aluminum alloy (6061-T6) bars grit blasted similarly to the steel. The aluminum was removed by soaking the pieces in a NaOH solution. After ultrasonic cleaning and gold/palladium sputter coating he analyzed polycarbonate interface surface on a SEM. Samples injected on high temperature bar showed a higher interfacial roughness (fig. 2.18 and fig. 2.19) [1]. In conclusion, Ramani's analysis [1] confirmed that mechanical interlocking can be an important cause of metal polymer adhesion.

## 2.11 REFERENCES

- [1] K. Ramani and B. Moriarty, *Thermoplastic Bonding to Metals Via Injection Molding for Macro-Composite Manufacture*, Polym. Eng. Sci., 1998, Vol. **38** (5), pp. 870-877.
- [2] Culbertson E., *Metal Adhesion to PET Film*, paper presented at the PLACE Conference, St Louis, MO, 2007.
- [3] K. L. Mittal, Ed. *Physicochemical Aspect of Polymer Surfaces*, Plenum Press, New York, 1983, vol. I and II.
- [4] F. Garbassi, M. Morra and E. Occhiello, Eds. *Polymer Surfaces-From Physics to Technology*, John Wiley & Sons, Chichester, 1994.
- [5] Kono M., *Studies of metal-polymer interfaces*, Ph.D. Thesis, The University of British Columbia, 2000.
- [6] S. Petit, P. Laurens, M. G. Barthes-Labrousse, J. Amouroux and F. Aréfi-Khonsari, *Al/PET adhesion: Role of an excimer laser pretreatment of PET prior to aluminum thermal evaporation*, J. Adhesion Sci. Technol., 2003, Vol. **17** (3), pp. 353-368.
- [7] J.N. Israelachvili and D. Tabor, *Proc. Roy. Soc*, 1972, **A 321**, p. 435.
- [8] B.V.Derjaguin, *Research*, 1955, **8**, 70.
- [9] C. Weaver, *J. Vac. Sci. Technol.*, 1975, **A 12**, 18.
- [10] A.J. Kinlock, *Adhesion and Adhesives*, Chapman & Hall, London, 1990.
- [11] L. H. Lee, Ed. *Fundamentals of Adhesion*, Plenum Press, New York, 1991.
- [12] <https://www.kruss-scientific.com/services/education-theory/glossary/>, viewed on 12/10/2017.
- [13] D. H. Kaelble, *Dispersion-Polar Surface Tension Properties of Organic Solids*, J. Adhesion, 1970, **2**, pp. 66-81.
- [14] D. Owens; R. Wendt, *Estimation of the Surface Free Energy of Polymers*, J. Appl. Polym. Sci, 1969, **13**, pp. 1741-1747.
- [15] W. Rabel, *Einige Aspekte der Benetzungstheorie und ihre Anwendung auf die Untersuchung und Veränderung der Oberflächeneigenschaften von Polymeren*, Farbe und Lack, 1971, **77**, (10), pp. 997-1005.
- [16] E. Zumelzu, F. Rull, P. Schmidt and A. A. Boettcher, *Structural analysis of polymer-metal laminates by electron microscopy and infrared spectroscopy*, Surf. Coat. Int. Part B: Coatings Transactions, 2006, Vol. **89**, B1, pp. 57-62.

- [17] J. F. Silvain and J. J. Ehrhardt, *An overview on metal/PET adhesion*, Thin Solid Films, 1993, **236**, pp.230-235.
- [18] E. Zumelzu, C. Angulo, C. Cabezas and R. Ugarte, *Characterisation of nanometric chromium coatings in metal-polymer composites*, Surf. Eng., 2013, vol. **29** (8).
- [19] J. F. Silvain, A. Veyrat and J. J. Ehrhardt, *Effect of the temperature on the adhesion and the morphology of thin metal films evaporated on polyethylene terephthalate*, Thin Solid Films, 1992, **221**, pp. 114-119.
- [20] <http://www.mecmesin.com/peel-test-adhesion-testing>, viewed on 12/10/2017.
- [21] B. Leclercq, M. Sotton, A. Bazkin and L. Minnasian-Saraga, *Polymer*, 1978, **18**, p. 328.
- [22] J. Amouroux, M. Goldman and M. F. Revoil, *J. Polym. Sci.*, 1982, **19**, p. 1373
- [23] L. Placed, *Coating*, 1978, **10**, p. 328.
- [24] G. A. J. Orchard, P. Spiby and I. M. Ward, *J. Polym. Sci. B Polym. Phys.*, 1990, **28**, pp. 603-621.
- [25] K. Suzuki, A.B. Christie and R.P. Howson, *Vacuum*, 1984, **34**, p. 181.
- [26] P. J. Martin, *Vacuum*, 1986, **36**, p. 585.
- [27] R.F. Bunshah, *Deposition Technologies for Films and Coating*, Noyes, New York, 1982.
- [28] Y. Kawahito, Y. Niwa and S. Katayama, *Laser direct joining between stainless steel and polyethylene terephthalate plastic and reliability evaluation of joints*, Welding International, 2014, **28** (2), pp. 107-113
- [29] L. Atanasoska, S.G. Anderson, H. M. Meyer III, Z. Lin and J. H. Weaver, *J. Vac. Sci. Technol.*, 1987, **A5**, p. 3325.
- [30] N. J. Chou, D.W. Dong, J. Kim and A.C. Liu, *J. Electrochem. Soc.*, 1984, **131** (10), p. 2335.
- [31] W. Decker and B. Henry, Proceedings of 45<sup>th</sup> Annual Technical Conference, Society of Vacuum Coaters, 2002, pp. 494-502.
- [32] T.H. Duc and Y. Jugnet, Int. Conf. on Adhesion and Surface Analysis, Loughborough University of Technology, UK, April 1990.
- [33] J. D. Rancourt, J.B. Hollenhead, and L. T. Taylor, *Chemistry of Interface Between Aluminum and Polyester Films*, J. Adhesion 1993, **40**, pp. 267-285.
- [34] D. Briggs and M.P. Seah, Eds. *Practical Surface Analysis by Auger and X-ray Photoelectron Spectroscopy*, Wiley, New York, 1990.
- [35] M. Bou, J.M. Martin, Th. Le Mogne and L. Vovelle, *Appl. Surf. Sci.*, 1991, **47**, p. 149.
- [36] Calderone, R. Lazzaroni, J. L. Brèdas, Q.T. Le and J. J. Pireaux, *J. Chem. Phys.*, 1995, **102**, p. 4299.
- [37] S. Akhter, X.L. Zhou and J. M. White, *Appl. Surf. Sci.*, 1989, **37**, p. 201.
- [38] P. Stoyanov, S. Akhter and J. M. White, *Surf. Interface Anal.*, 1990, **15**, p. 509.
- [39] J.J. Pireaux, *Synthetic Metals*, 1994, **67**, p. 39.
- [40] F. M. De Wit, et al., *The influence of pre-treatments of aluminium alloys on bonding of PET coatings*, Surf. Interface Anal., 2010, **42** (4), pp. 316-320.

- [41] <http://packaging.arcelormittal.com/>, viewed on 12/10/2017.
- [42] Bratt Les Ed., *Fish Canning Handbook*, 2010, ISBN 9781405180993.
- [43] T.A. Turner, *Canmaking for Can Fillers*, CRC Press, 2001
- [44] S. Zhang et al., *Exploring the Antisticking Properties of Solid Lubricant Thin Films in Transfer Molding*, I.J.M.P.B, 2002, **16** (6 & 7), pp. 1080-1085.
- [45] K.V. Shalnov, K. Uemura and Y. Ito, *Consideration on Surface Modification of Steel Dies to Reducing the Plastic Sticking in the Forming Process*, Tribology Online, 2012, **7** (3), pp.190-200.
- [46] R. C. Progelhof and J. L. Throne, *Polymer Engineering principles: Properties, Processes. Tests for Design*, Hanser Publishers, 1993.

## Chapter 3

# MOLTEN PET CYLINDERS HANDLING: PNEUMATIC TRANSPORT

### 3.1 INTRODUCTION

The reason for the necessity of a gob handling tool was explained at the beginning of chapter 2: it is not technically and technologically convenient to have the nozzle directly on the mold. One of the possible solutions is shown in fig. 3.1. Moreover, from a field observation, polymer melt (named E in fig. 3.1) exiting from the nozzle (component 121 in fig. 3.1) can change its behavior: sometimes it is not completely straight or the gob assumes different trajectories after cutting. The gob loading on the handling tool is hence the first difficulty to face when designing a new handling tool. In figure 3.2, pictures of correct and incorrect gob loading are shown. It is interesting to note the PET melt exiting from the nozzle in the top part of the pictures (particularly in B).

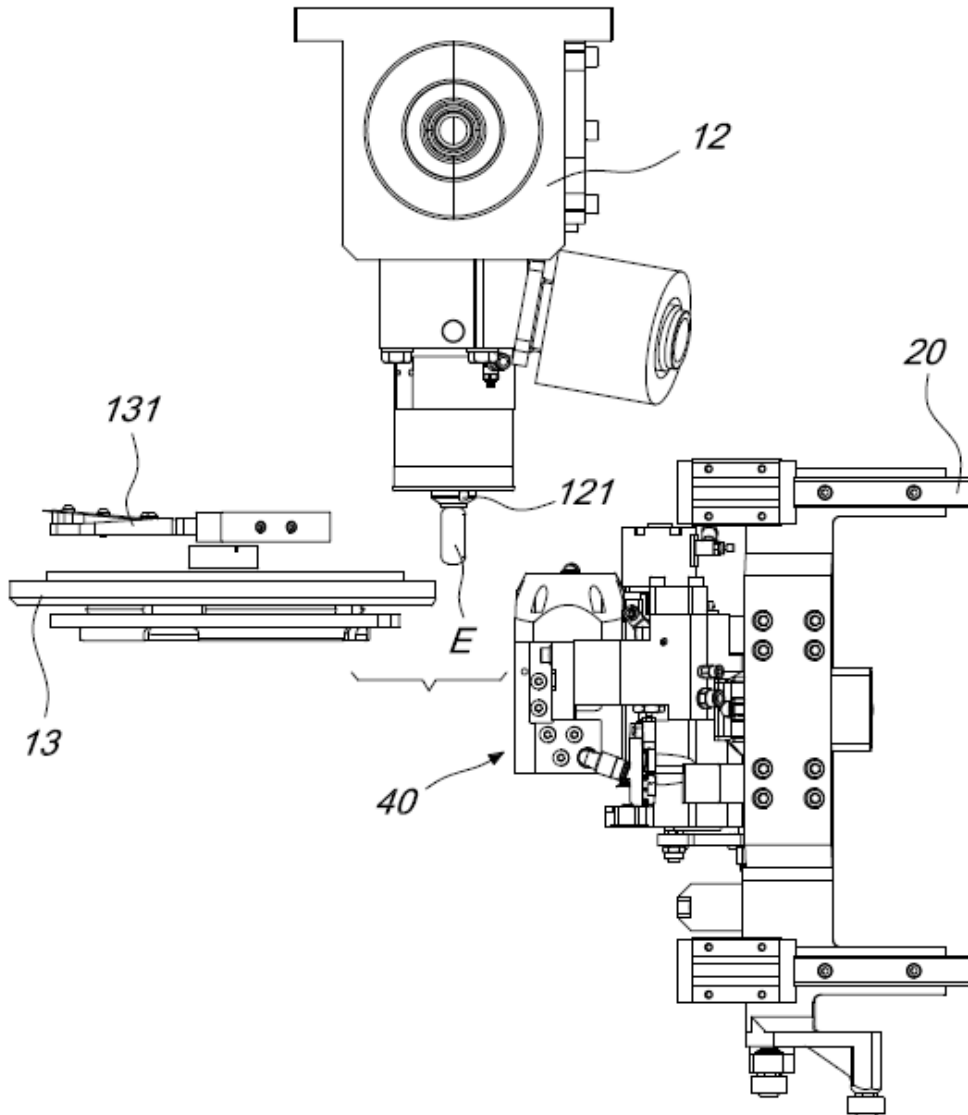


Figure 3.1 Preform compression molding machine: gob cutting and gob loading on handling tool.

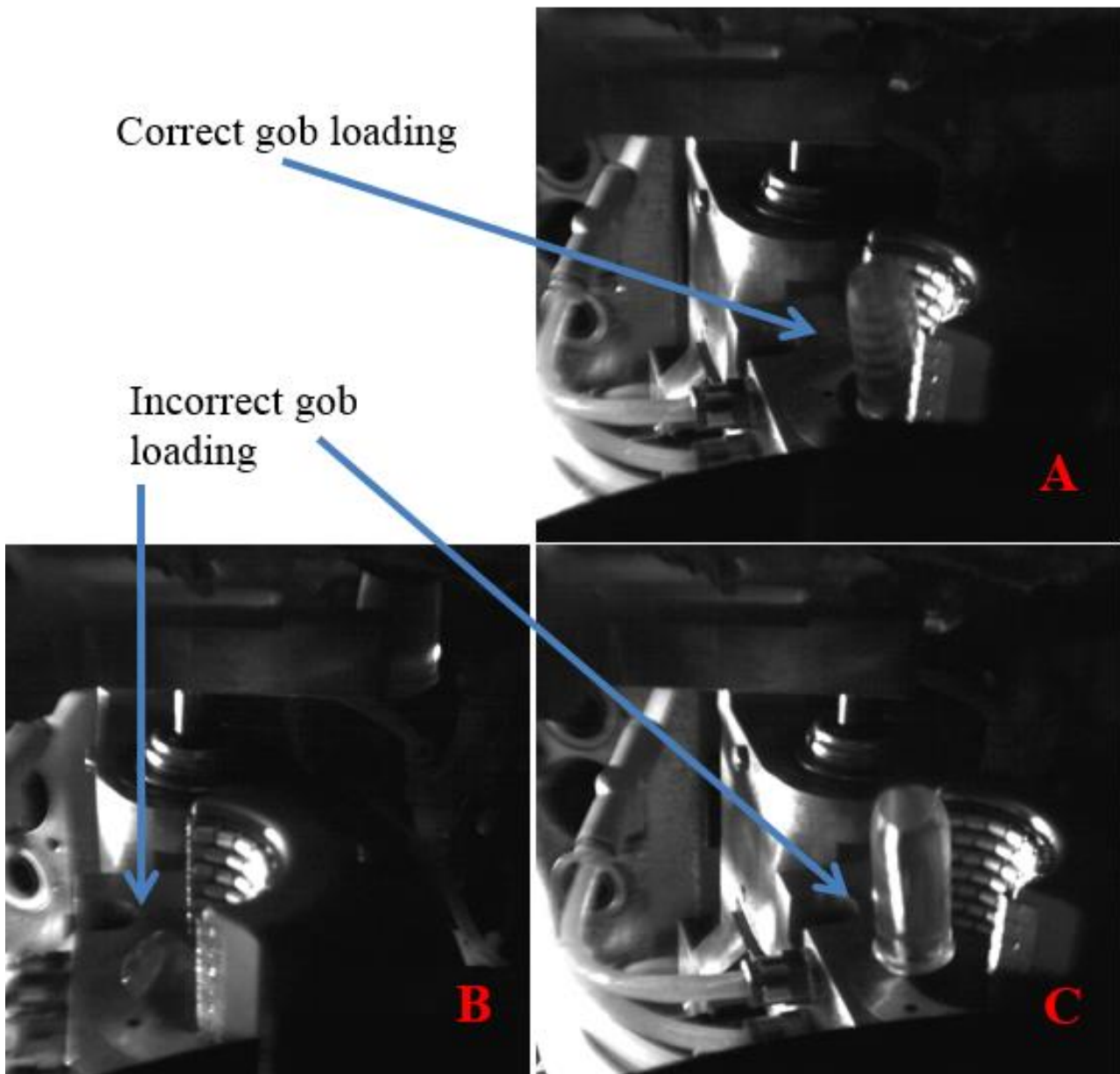


Figure 3.2 Preform compression molding machine: pictures of gob loading on handling tool.

In chapter 2, it was also anticipated that molten PET has a high adhesiveness with other materials. Moreover, adhesiveness increases if the surface has already been in contact with PET and this change in adhesiveness results in a lack of control of the process: the transferring time from the handling tool (40 in fig. 3.3) to the mold cavity (32 in fig. 3.3) can increase significantly. Usually, this gob transferring takes place in an angle of the molding carrousel (2, in fig. 3.4), where the molding carrousel itself is coupled with an insertion carrousel (7, in fig. 3.4). This angle, divided by the angular speed of the molding carrousel, results in the available transferring time. If gob-transferring time exceeds the time available, the gob is not inserted correctly in the mold cavity (B in fig. 3.5) resulting in a preform defect or worse in a stop of the machine. For a given molding carrousel diameter, an increase in the available transferring time generally means a reduction of the available molding time. This results in a lower machine productivity that can make compression molding economically less convenient. A drawback of known transferring carousels consists in the fact that it is very difficult to keep the internal walls of the transferring units clean for a sufficiently high number of cycles [1].

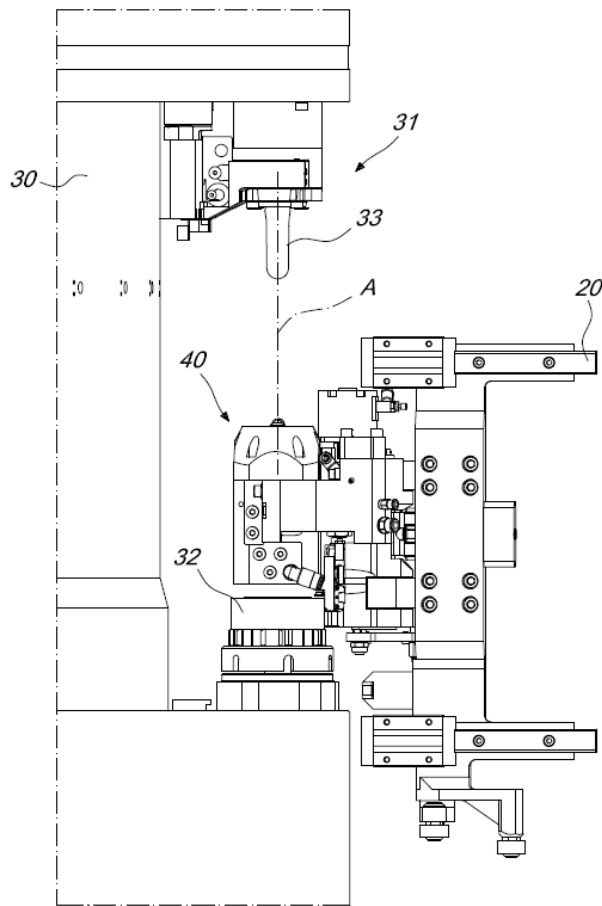


Figure 3.3 Handling tool coupled with molding carousel in a preform compression molding machine.

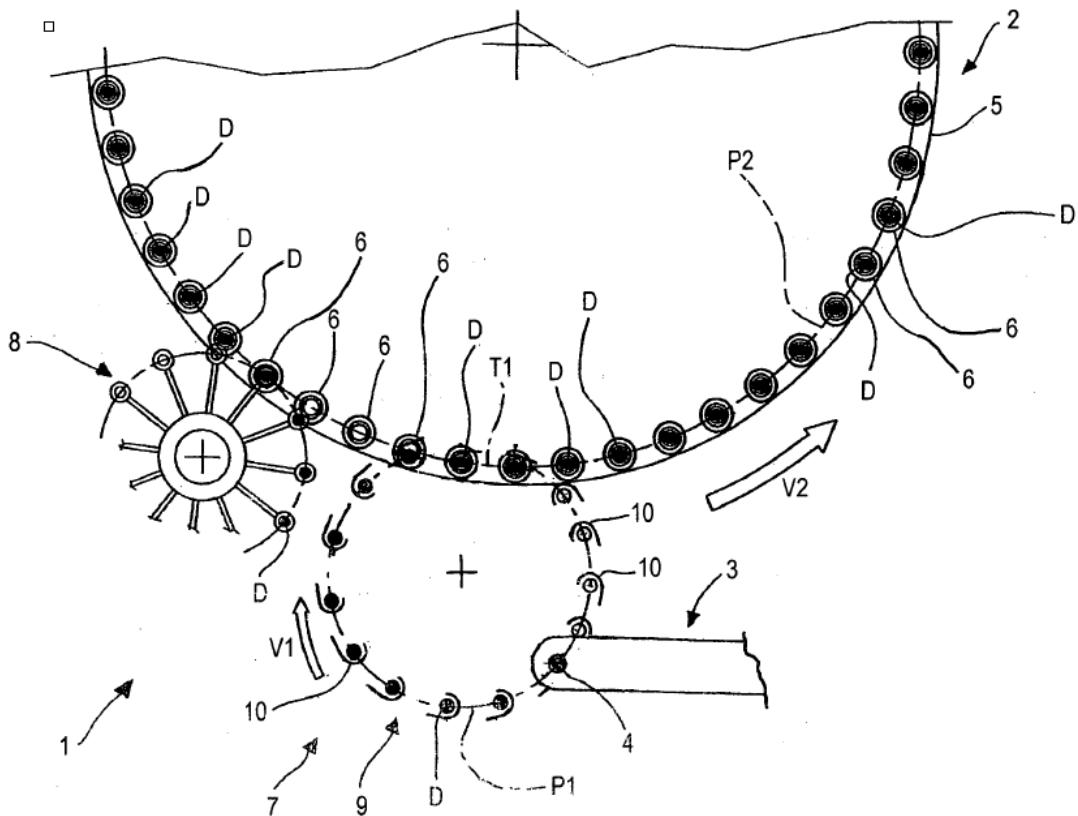


Figure 3.4 Transferring and molding carousels layout in a preform compression molding machine [1].

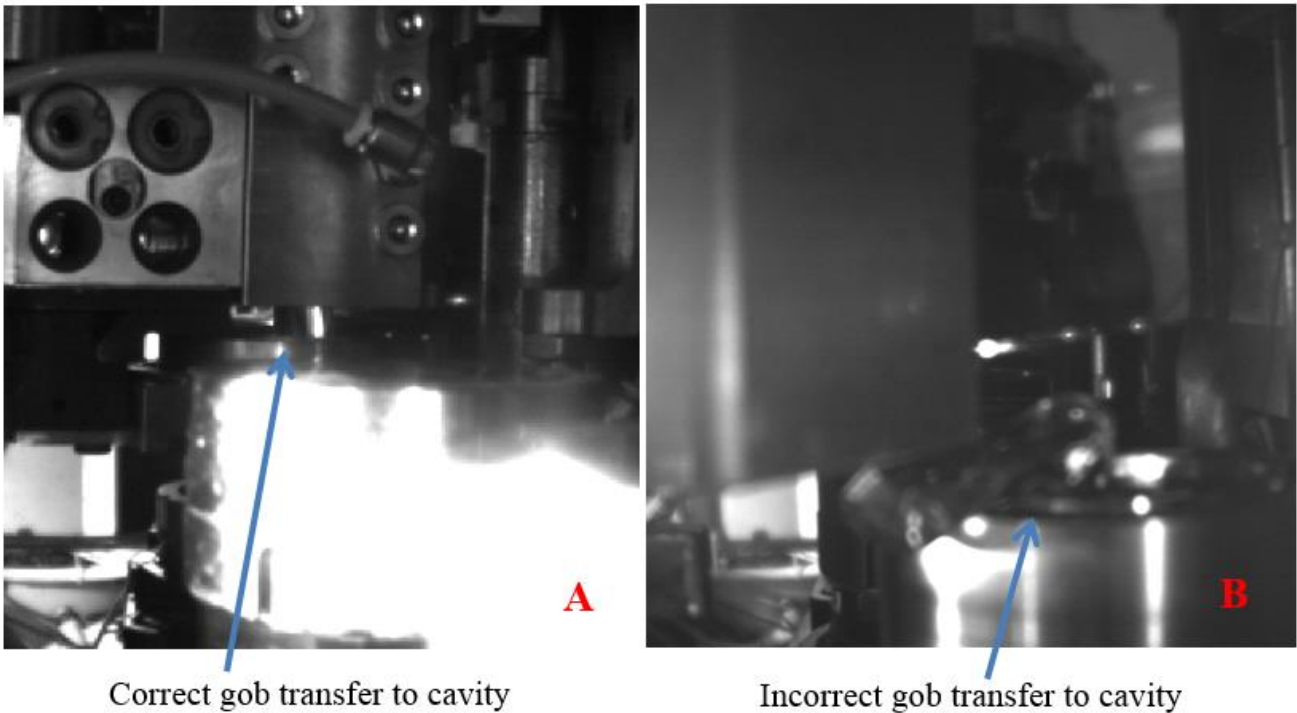


Figure 3.5 Pictures of gob transfer from handling tool to mold cavity.

SACMI had the idea of trying a PET gob pneumatic transport system, which was then developed during this PhD work. The idea was to avoid or at least reduce the contact between the gob and the handling device surface. Moreover, the possibility to slow or accelerate gob speed changing air pressure/flow rate seemed interesting. Finally, the air flow can create a force field that helps handling the aforementioned instabilities on gob loading more easily.

After an analysis of existing literature and patents on PET gob handling devices (see next paragraph), the idea seemed new and hence not in contrast with existing patents. After the encouraging results of the first tests, a PET gob pneumatic transport through a swirl pipe is now "patent pending". The following paragraph deals with design and production of a testing machine dedicated to swirl flow handling tool optimization. Finally, the last paragraph is about future developments.

### 3.2 PET GOB HANDLING LITERATURE AND PATENTS

There is almost no academic papers on PET gob handling, while there are several dozens of patents. They mainly belong to three companies: SACMI, TOYO SEIKAN (Japanese company) and GRAHAM (American one). For brevity reasons, only three types of existing patents are reported in this dissertation. One of SACMI solutions is worth mentioning [1] (fig. 3.6): it has a "U" or "C" or "J" shape upper element, from now on called "recess", for receiving the gob. The recess is provided with rolling elements for guiding the dose inside the transferring arrangement which has rolling elements too. These allow no sliding friction between the PET gob and the handling tool, substituting it with rolling friction.

Some patents (e.g. [2], [3]) report the advantages of using vibrations (generated in several ways) for gob transferring into the mold cavity. The main advantage is the reduction of the transferring time range (fig. 3.7).

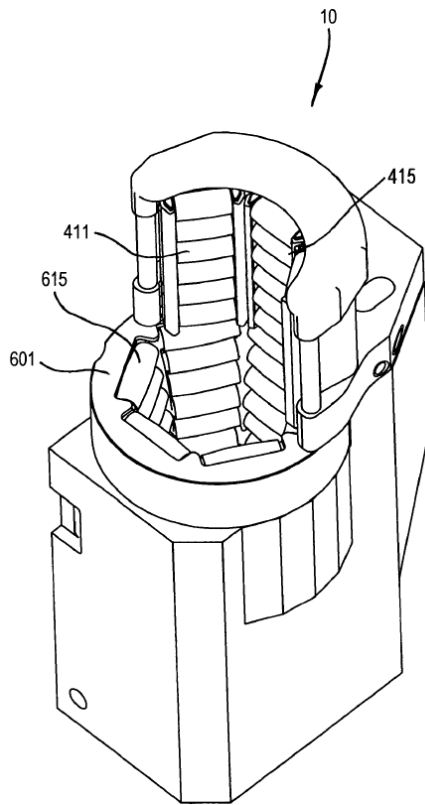


Figure 3.6 Handling tool with rolling elements [1].

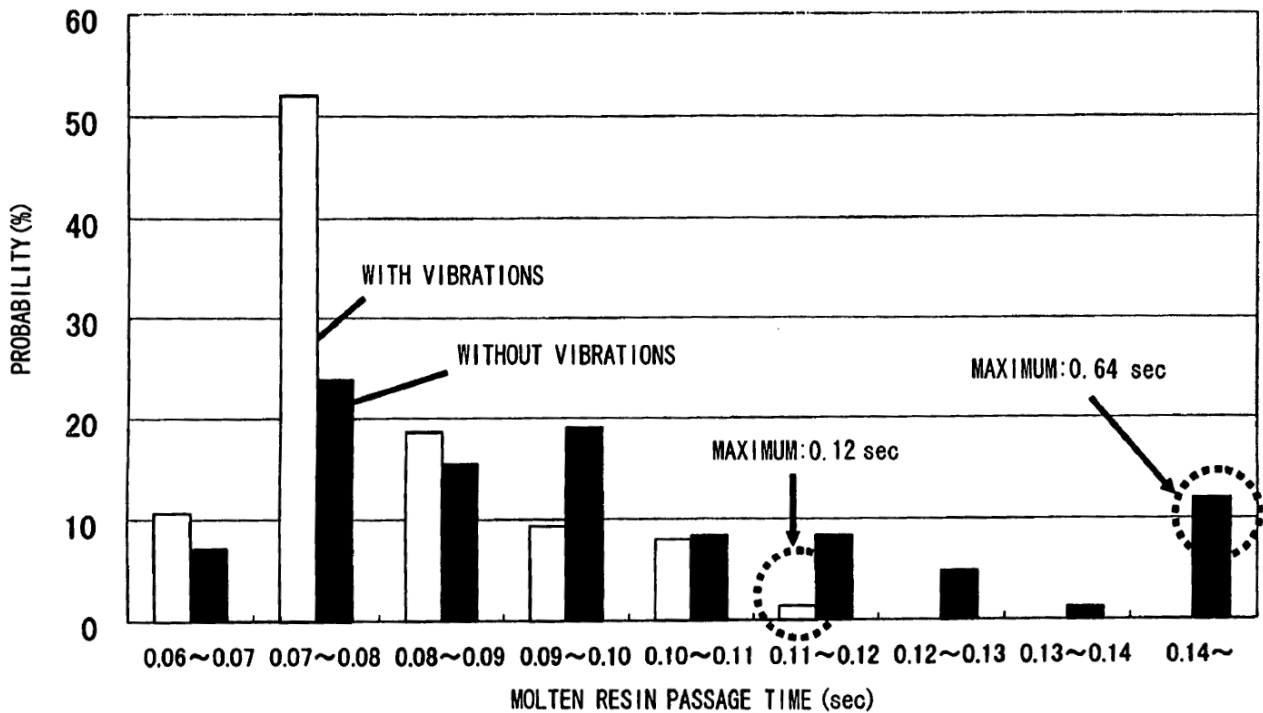


Figure 3.7 Probability of gob (molten resin) passage time with vibrations (white columns, maximum 0.12 seconds) and without vibrations (black columns, maximum 0.64 seconds) [2].

When this PhD project started, there was a patent pending solution (WO2007/094518) by Toyo which was published on 17.05.2017, EP 2404732 B1 [4]. This patent teaches to have the transfer duct (component 12 in fig. 3.8) at a greater pressure than that of the compression mold (component 3 in fig. 3.8), for example by closing the duct in an upper region and introducing compressed air through radial holes made in the side walls of the duct.

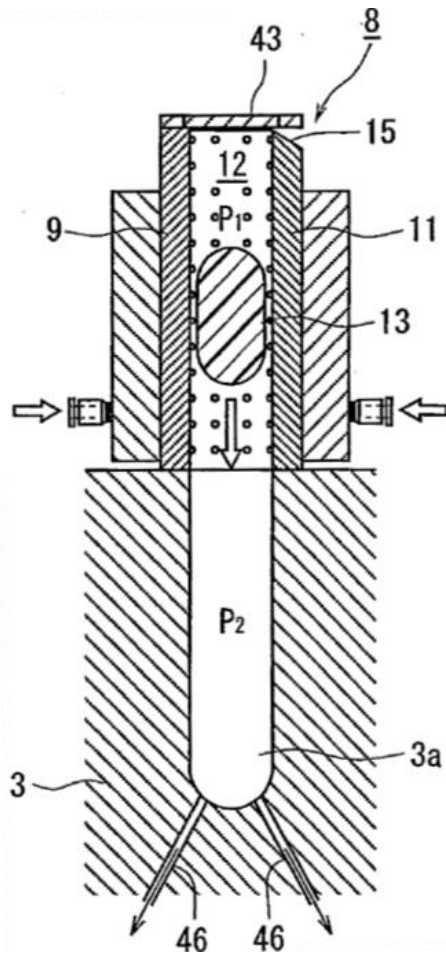


Figure 3.8 Handling tool with radial holes and lower pressure on cavity [4].

This solution is not without drawbacks, which include the fact that the gaseous stream applied to the dose in the transfer duct is directed exclusively radially with respect to the dose, leading to a non-optimal use of the duct, as it will be shown in the next paragraphs.

### 3.3 PRELIMINARY GOB PNEUMATIC TRANSPORT CFD SIMULATIONS

In the introduction of this chapter, the motivations of pneumatic transport were listed: avoid or at least reduce the contact between the gob and the handling device surface and the possibility to slow or accelerate gob speed working with air pressure/flow rate. Moreover, the air flow can create a force field that helps handling the aforementioned instabilities on gob loading more easily. It is important to remember that molten PET (about 270 °C) can be easily deformed and can easily be modelled even by air. Swirl flow, or cyclone, seemed interesting for its characteristics: no direct air injection on the gob (low risk of gob local modelling) and a theoretical gob stabilization effect due to rotation (like it happens to a bullet in a gunmetal).

The first Computational fluid dynamics (CFD) simulations were done without the gob, because modelling the gob without introducing some simplifying assumptions is very complex and time demanding, as it will be shown in the sixth paragraph of this chapter. Moreover, it is important to do some experiments to validate the simulation. The software used for this preliminary simulation is CFX which belongs to ANSYS® suite. Mesh modelling (see detail on fig 3.9) was done according to fluid dynamic good practice (see detail on fig 3.9) with a total number of elements equal to 5.7 million.

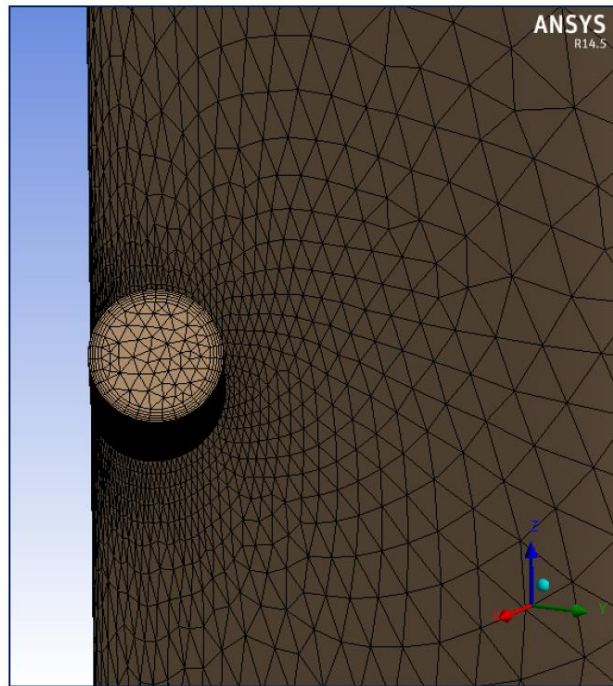


Figure 3.9 Swirl flow stationary CFD simulation (CFX): inlet pipe mesh modelling.

The physical assumptions and boundary conditions were stationary run, turbulence and compressibility. The simulated fluid was air as ideal gas, with an inlet flow rate equal to the sonic speed for each single little duct. Opening condition pressure was set equal to 1 bar. The geometry is shown in figure 3.10.

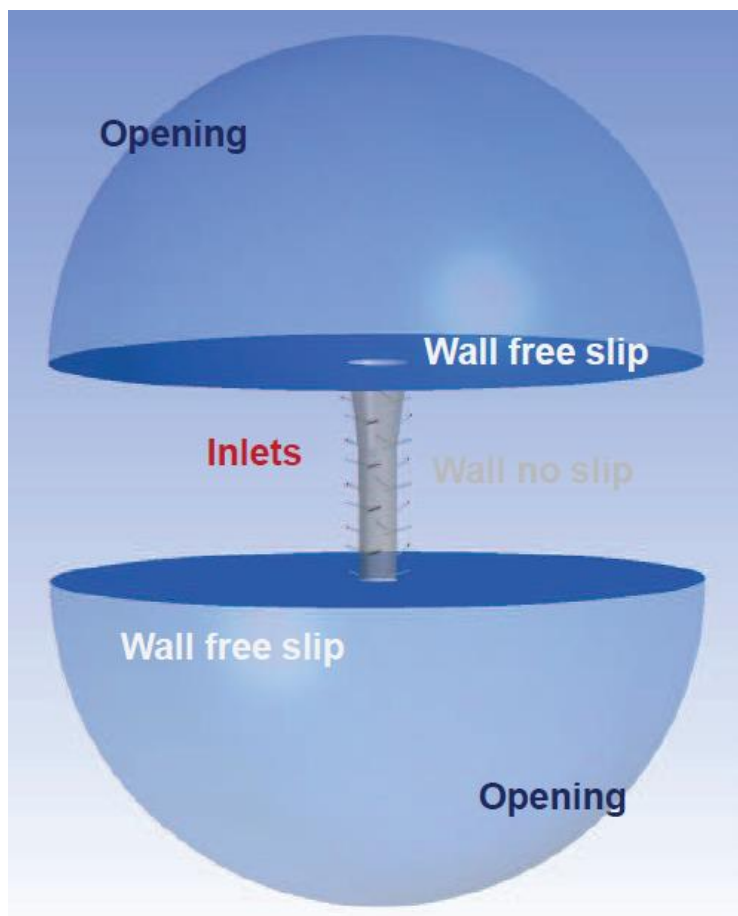


Figure 3.10 Swirl flow stationary CFD simulation (CFX): geometry and boundary conditions.

An important parameter that characterizes the flow is the angle alpha ( $\alpha$ ) shown in the fig. 3.11.

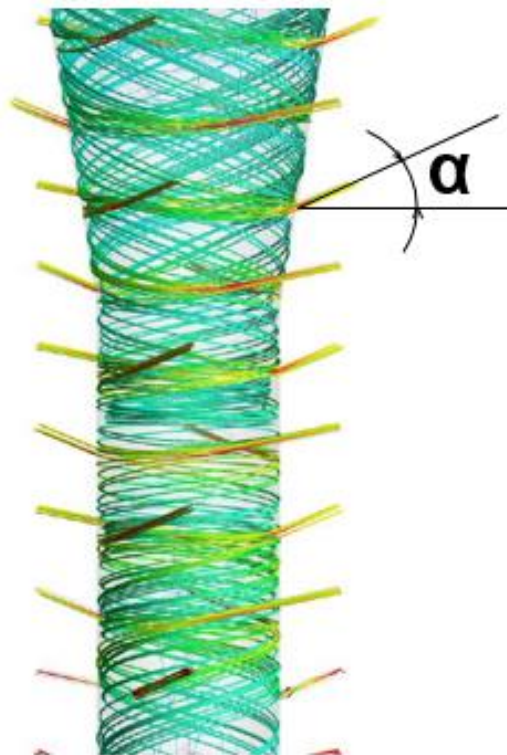


Figure 3.11 Swirl flow stationary CFD simulation (CFX): flow streamlines and alpha ( $\alpha$ ) angle.

The preliminary simulations were done with two attempted angle values,  $\alpha$  equals to  $15^\circ$  and  $\alpha$  equals to  $60^\circ$ . In fig. 3.12 and 3.13 circumferential velocity and the velocity vectors projection are shown respectively with  $\alpha$  equals to  $15^\circ$  and to  $60^\circ$ .

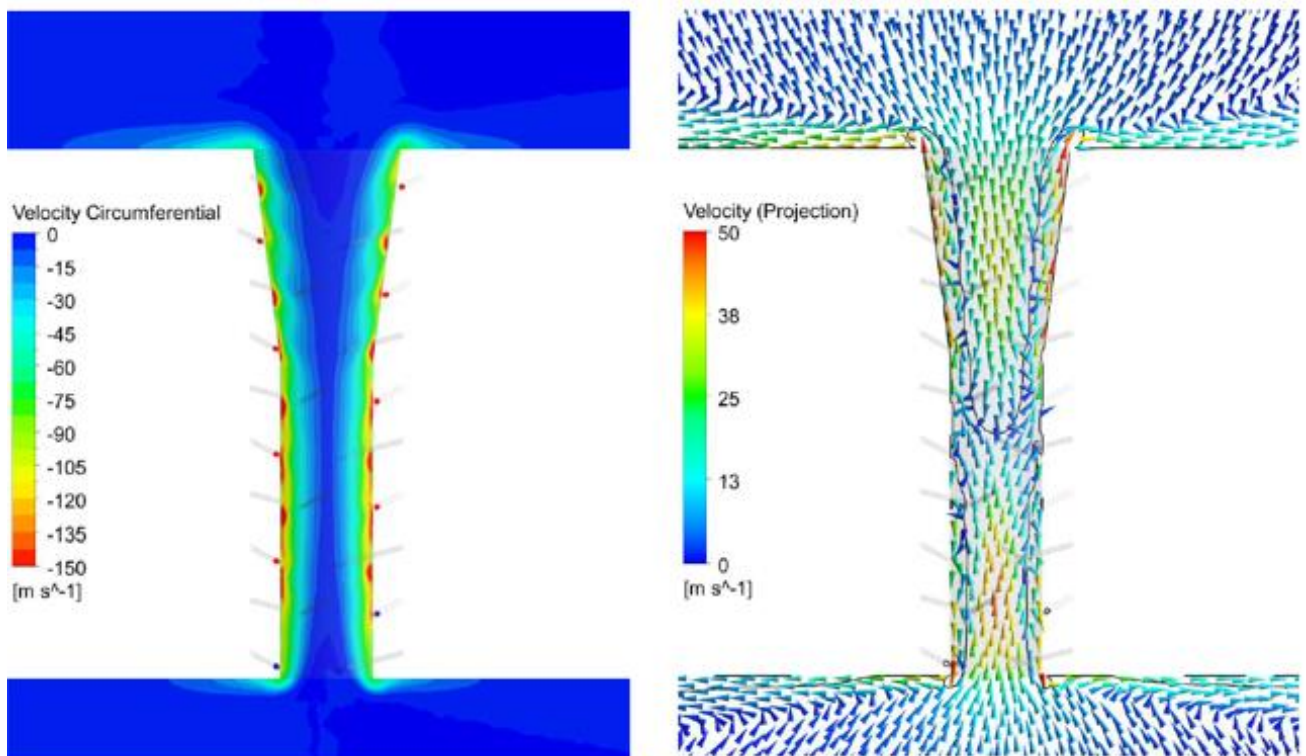


Figure 3.12 Swirl flow stationary CFD simulation (CFX): circumferential velocity and velocity vectors projection with  $\alpha$  equals to  $15^\circ$ .

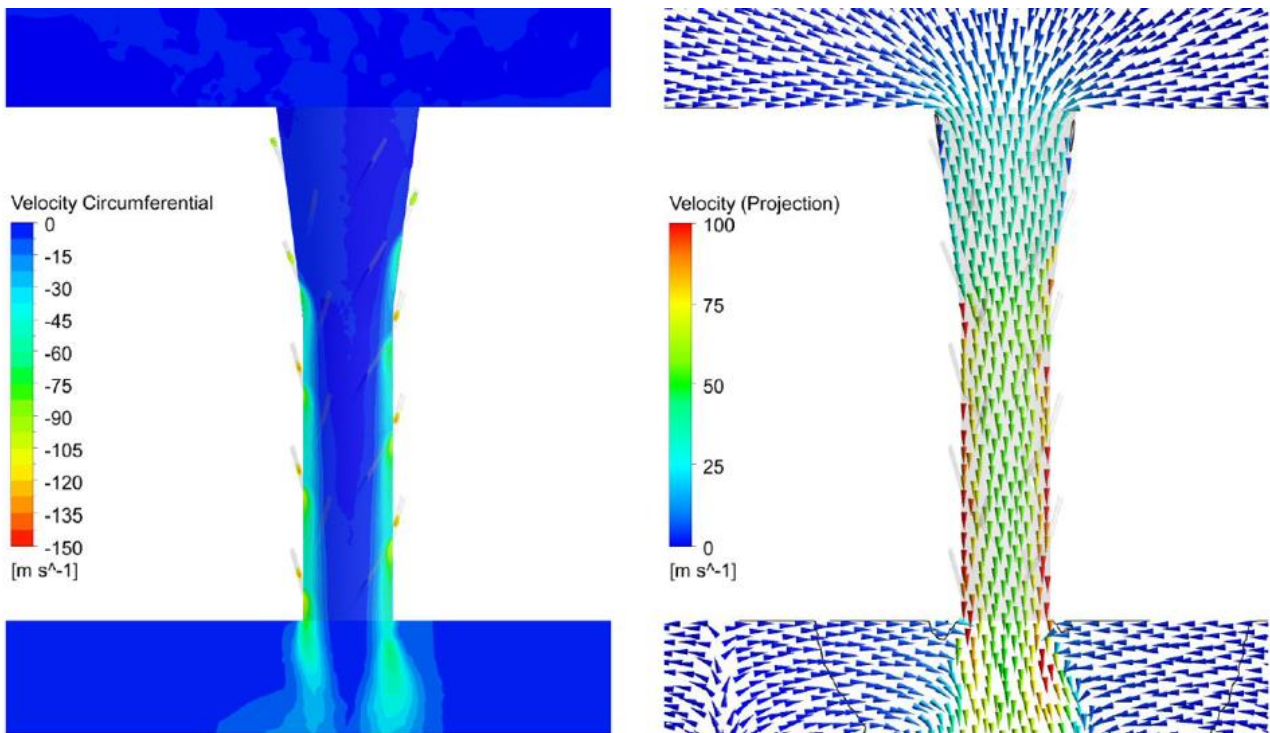


Figure 3.13 Swirl flow stationary CFD simulation (CFX): circumferential velocity and velocity vectors projection with  $\alpha$  equals to  $60^\circ$ .

## 3.4 PRELIMINARY TESTS

### 3.4.1 Testing machine PAM002A

A ten-year-old PAM prototype (PAM002A) installed at a converter factory was used for the preliminary gob pneumatic transport tests because it was the only machine available to start the tests. In the converter factory, there was also a dozen of injection molding plants.

The PAM002A plant is composed of:

- A Plastic System PET dryer (model H5500 PET, see figg. 3.14 and 3.15);
- An AMUT industrial PET single screw extruder with a diameter of 120 mm and an L/D (length/diameter) ratio of 33. Its flow rate goes from 100 to 900 kg/h. A gear pump to stabilize the flow rate, then a static mixer, an elbow curve and, finally, the nozzle follows the extruder;
- An industrial prototype of compression molding machine with all its carrousel and auxiliary plants.

The plant is on two levels: on the mezzanine, there are the PET dryer, the hydraulic power plant, the air dehumidifier and the cooling liquid thermoregulation system. On the floor level, there are the PET extruder and the molding machine with all its carrousel. In figure 3.16 there is a similar plant (PAM002B) to give an idea of plant size and complexity.

The polymer used is a Cleartuf P82™ of M&G group and it is a food grade PET copolymer resin based on terephthalic acid. Its high clarity and sparkle make it well suited for the production of bottles and other containers by conventional single and two stage processing machines. Moreover, it is a high molecular weight grade for general use in manufacturing containers. Its intrinsic viscosity (I.V.) is  $0.80 \pm 0.02$  (dl/g). Moreover, its melting point is  $249^\circ\text{C}$  and the acetaldehyde (AA) content declared by the producer is lower than 1 ppm.



Figure 3.14 PAM002A: PET dryer on mezzanine.

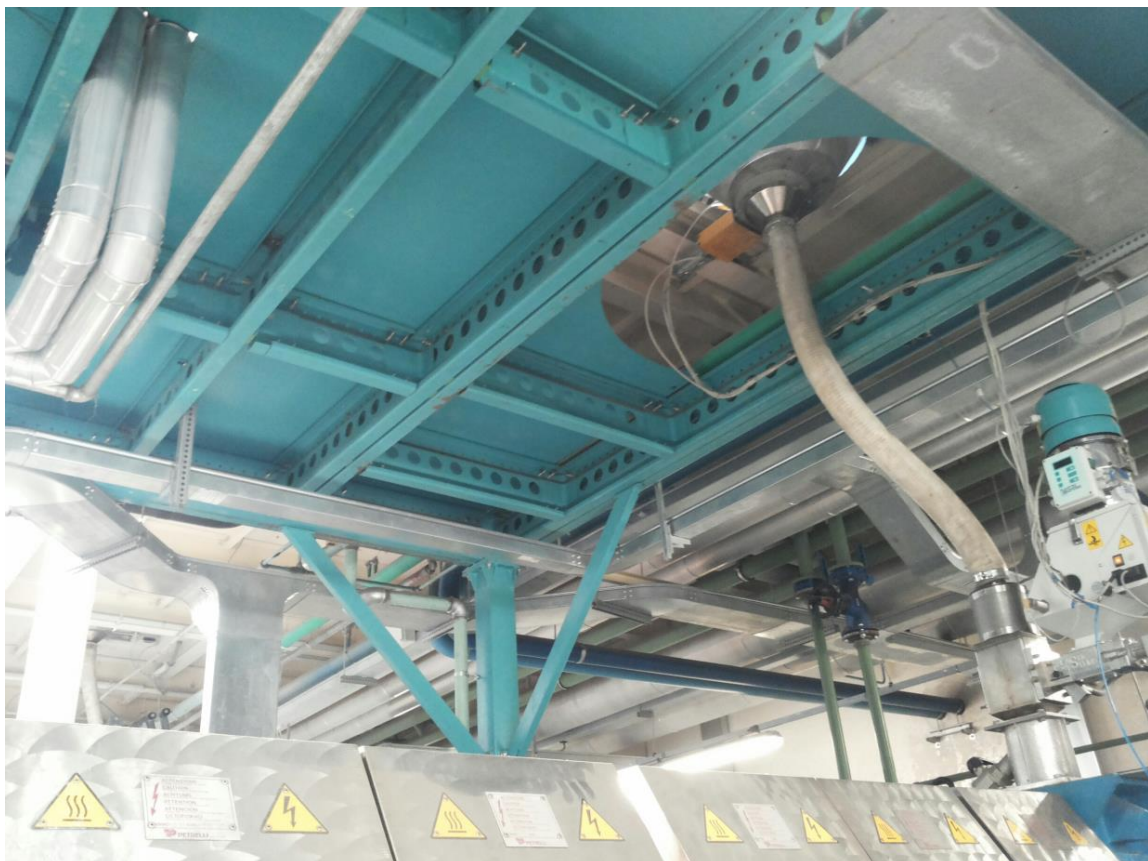


Figure 3.15 PAM002A: pipe from PET dryer to extruder inlet.



Figure 3.16 PAM002B: preform compression molding machine plant.

The PET dehumidification procedure took place in the Plastic System drier at 160 °C for four hours before the beginning of the tests in the morning. Melt temperature after the nozzle was between 270 and 275 °C. The flow rate used in the tests was between 150 and 200 kg/h because the tests were done molding a preform of approximately 9.5 g. Acetaldehyde measurements on the preforms according to the Petes method resulted in an average value of 11.2 ppm at 150 kg/h and 10.5 ppm at 200 kg/h, which is in accordance with literature [5, 6] since the residence time is reduced. The same preform on PAM003 results in an AA content lower than 4 ppm starting from the same AA content in the pellets. The reason for the higher AA content is the higher diameter, length and profile of PAM002A extruder screw compared to PAM003 one. The former is in fact optimised for higher flow rate compared to the latter.

The aim of the tests is to find a handling tool solution for an industrial compression molding machine. That is why an old industrial plant was used. In fact, compared to a new industrial plant it has:

- No differences in PET dehumidification and extrusion process;
- No differences in die swelling conditions due to different PET flow rate;

- Same industrial time process;
- The possibility to check the final product, that is the preform, to see if there are any defects related to the cutting or handling process.

Moreover, the advantages of doing them at a converter factory are:

- PET raw material is exactly the same as the one used for the close injection plants;
- Time saving for PET loading in the dryer since it is automatic. For endurance tests (several hours of continuous production) it means almost 2 hours per day.

However, an industrial machine has also some disadvantages:

- No degrees of freedom, for example on handling tool trajectory and motion laws;
- High material and energy costs compared to a lab plant.

Furthermore, since the machine was a very old prototype and had almost no maintenance in the last months before the start of the tests, most of the time it was impossible to do tests due to failures. Nevertheless, it was useful to get expertise in problem solving from the hydraulic field to the pneumatic, mechanical and electric, basically almost all the technical issues which can happen in such a complex plant. To sum up, there were no alternatives to PAM002A, apart from a small-scale plant which was used for the tests described in chapter 4.

After the first preliminary tests showed promising results, a new testing machine started to be designed to widen the test scenario. Details are in a dedicated paragraph 3.7.

Going back to PAM002A, the machine layout around the handling zone (fig. 3.17) is very similar to the one shown in fig. 3.4, showed again below to help the following discussion.

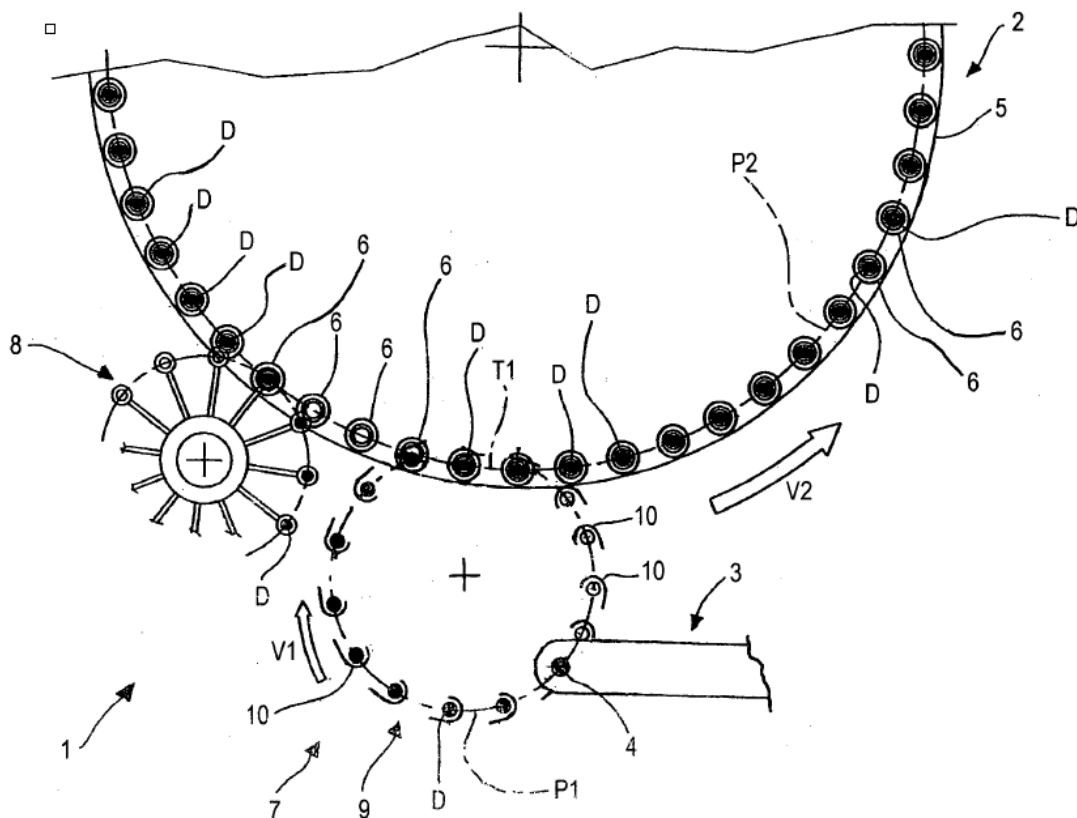


Figure 3.4 Transferring and molding carrousel layout in a preform compression molding machine [1].

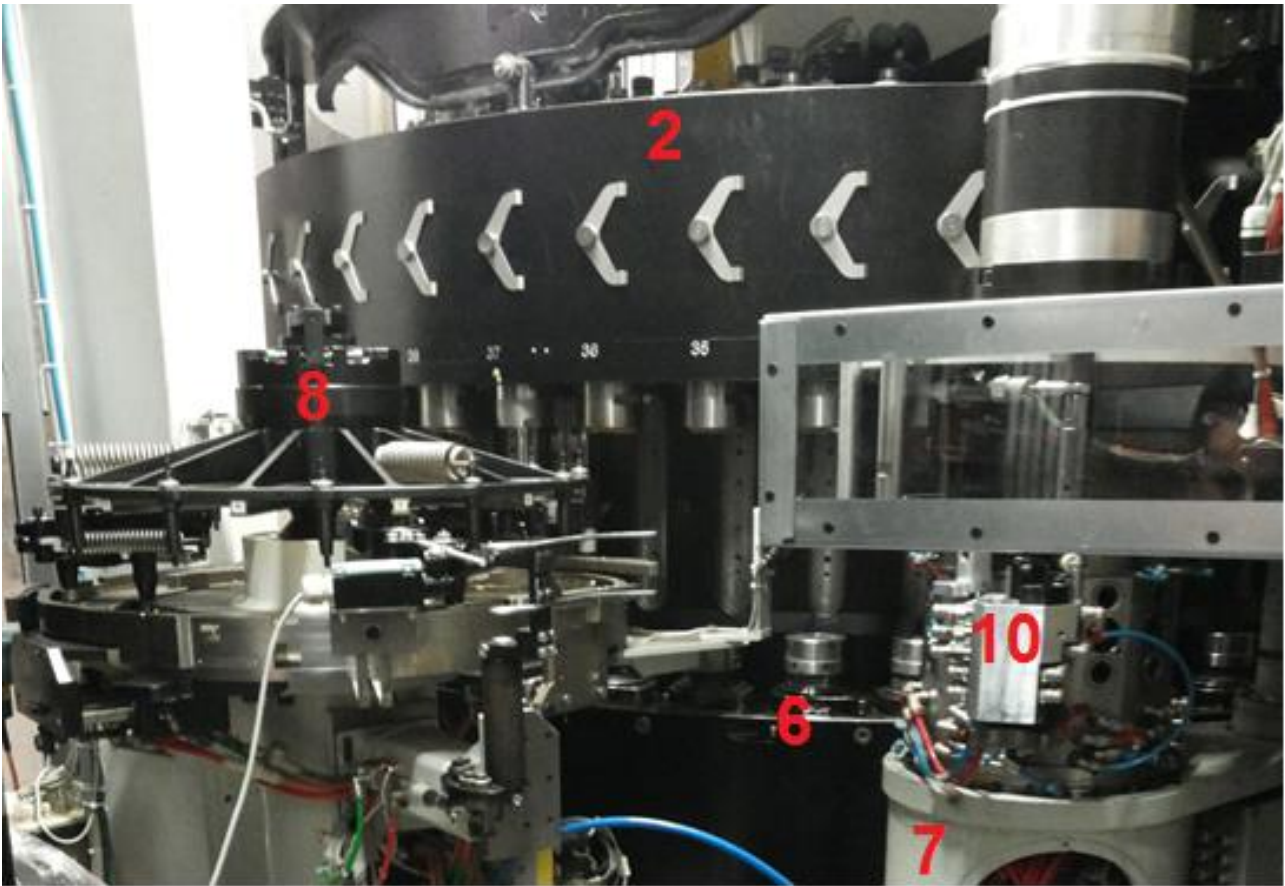


Figure 3.17 PAM002A: transferring (7), molding (2) and preform extraction carrousels (8) seen by row 1 in figure 3.4.

In figure 3.4, the component 4 is the nozzle where the gob is generated by molten PET blade cutting. Component 7 is the molding carousel on which there are several handling tools (components 10). Component 2 is the molding carousel, with several mold cavities (components 6), while component 8 is the preform extraction carousel.

For pneumatic transport tests, just one handling tool (fig. 3.17) was mounted, mainly for two reasons:

- Costs saving: since handling tool geometry was still to be defined, all the modifications are done on only one component;
- Carousel air flow rate and pipes were not enough to feed all the previous handling tools.

Tests were done with the support of a high-speed camera to monitor the cutting zone, gob loading on handling tool after cutting, and gob insertion in the mold. Moreover, air flow rate/pressure measuring systems were used to regulate swirl flows and the temperature of the melt was measured using a thermocouple.

The angle between the nozzle and the cavity mold is very wide in PAM002A. Without the swirl flow, the gob, only by means of gravity, will exit from the handling tool much earlier with respect to the angular position where the handling tool reaches the cavity. This was true also with the previous handling system [1], which had a mechanical system in contact with the gob to stop the gob fall.

Values of air flow rates and their angular phases are not described in this thesis due to SACMI intellectual property policy.

### 3.4.2 Swirl pipe manufacturing

Design work was done to create the geometry simulated with CFD in real components. Moreover, the swirl pipe had to be installed in a handling tool assembled in the testing machine PAM002A. The device was designed with the possibility to host or not (fig. 3.18) the recess (see paragraph 3.2).

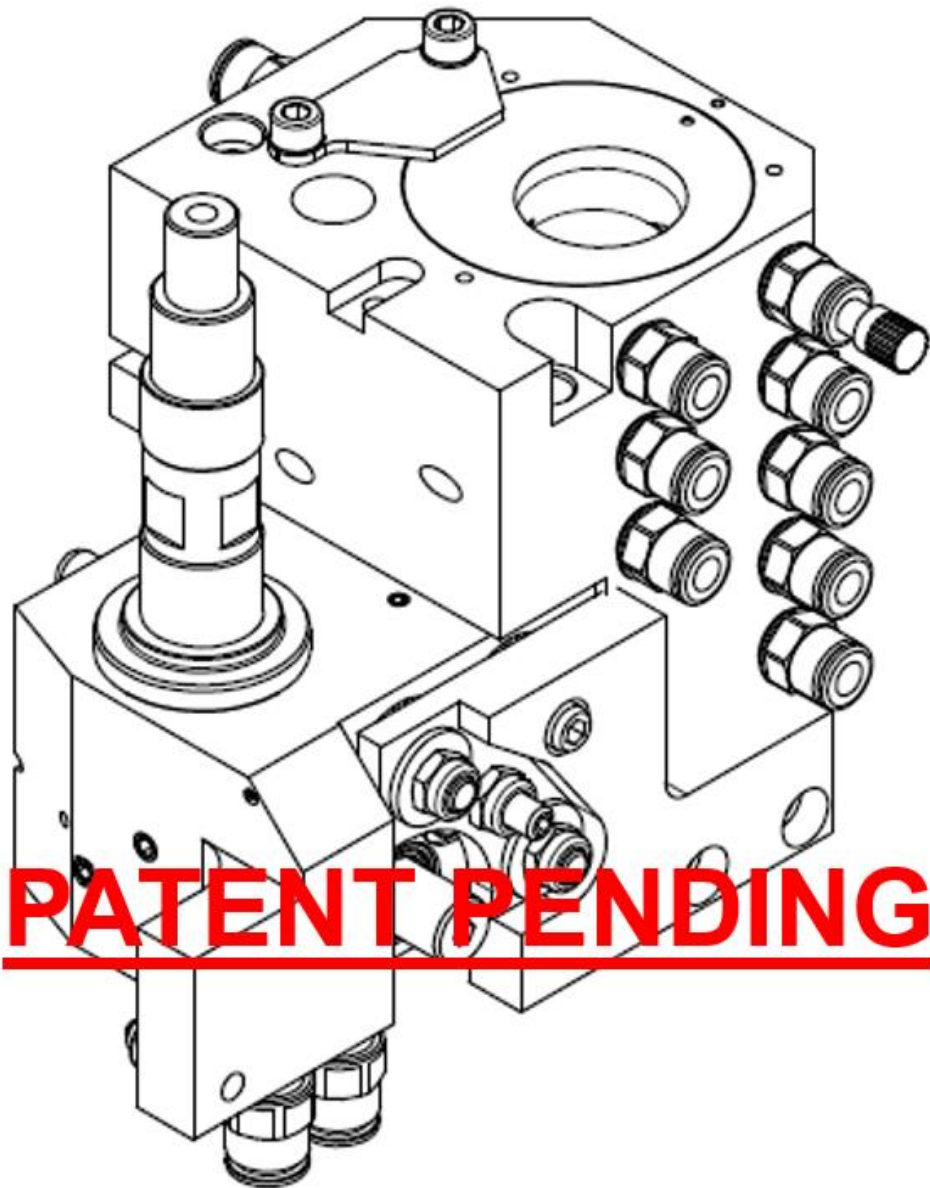


Figure 3.18 PAM002A: handling tool for gob pneumatic transport.

Not all machine tools are good at producing deep holes: high precision is required. The aim was to test the swirl pipe in the closest conditions as possible to those of the CFD simulations. Once validated, it will be checked if such a precision is really necessary for the application. It is worth mentioning a metrology technique used here to check holes straightness: the industrial computed tomography scanning. The metallic component is put inside a camera and irradiated by X-rays. The output file is then elaborated by a software, for example GOM Inspect © to check geometrical tolerances. In this way, a good machine tool was chosen and its precision was characterized. Fig. 3.19 reports a case of the first line holes with a significant straightness error compared to the others. This information helped setting the right machine tool parameters, validating the use of some manufacturing tricks, to significantly reduce the error. The exact values and tolerances of mechanical components are not described due to SACMI intellectual property policy.

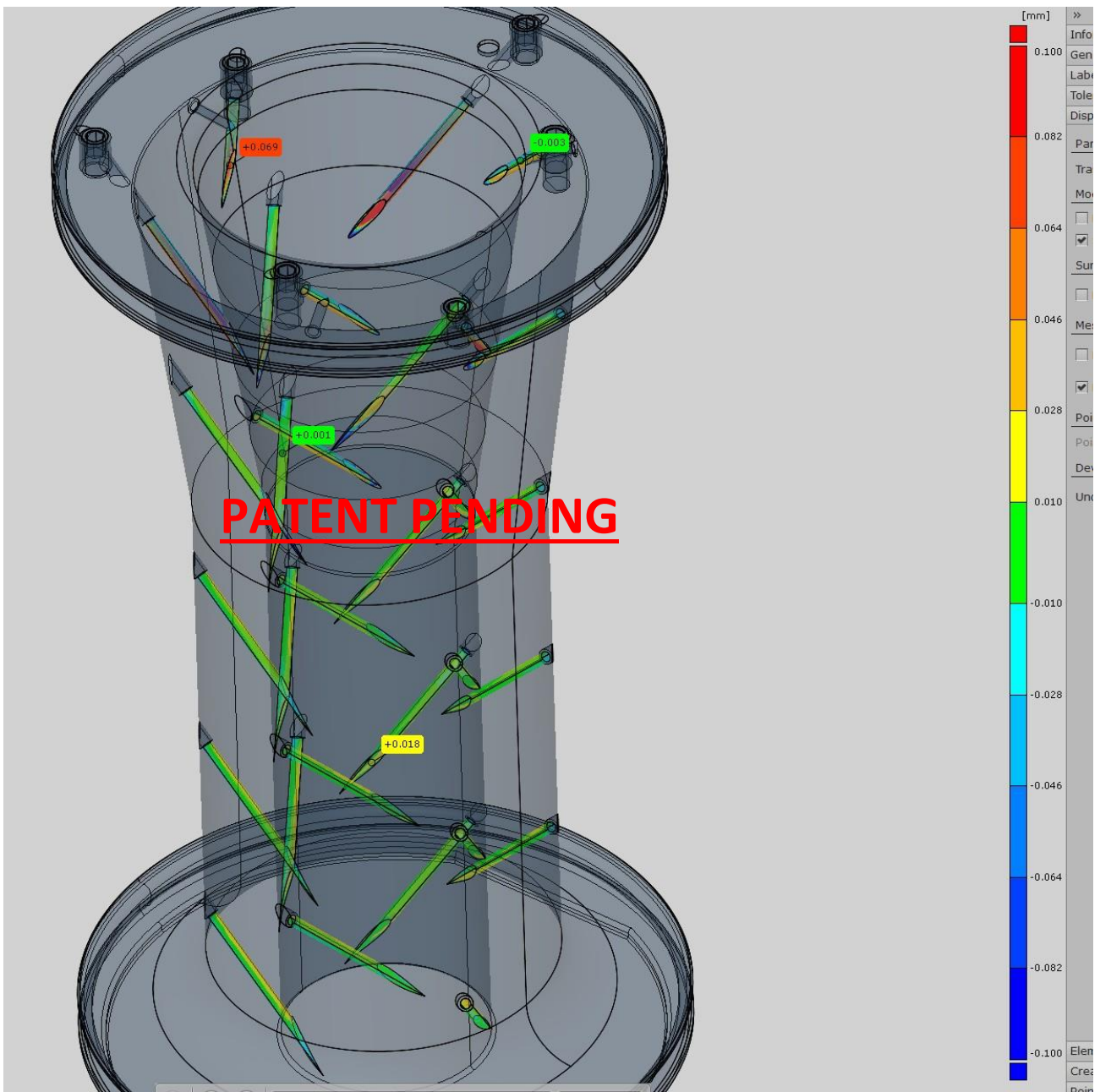


Figure 3.19 Swirl pipe tomography scan elaborated with the software GOM Inspect ©.

### 3.4.3 Gob accelerated ( $\alpha = 60^\circ$ )

The first pipe tested was the solution with  $\alpha = 60^\circ$ . The recess is not necessary (fig. 3.20) since swirl flow exerts a suction power that attracts the gob inside the pipe, as assumed in the introduction at pag.4. Tests showed that suction can adjust the gob which would have led to incorrect loading with present technology. The gob is accelerated by the air flow and for given pressure values reproducibility tests were performed. These tests consist in letting many gobs fall to the ground after passing through the handling tool and evaluating the trajectory reproducibility from the shape of the resulting PET "hill" which, for example, is shown in Figure 3.21. In the top and central part of the hill PET is still melt. The results of the tests for swirl flow with  $\alpha = 60^\circ$  were good. Figure 3.22 reports a graph with the average angle between gob cutting and the start of gob exiting from handling tool and its standard deviation with pressure variation. This test was performed with high speed camera and with a carrousel angular speed correspondent to a productivity of 500 preforms per minutes (ppm). For each pressure value, at least six tests were performed and analyzed.

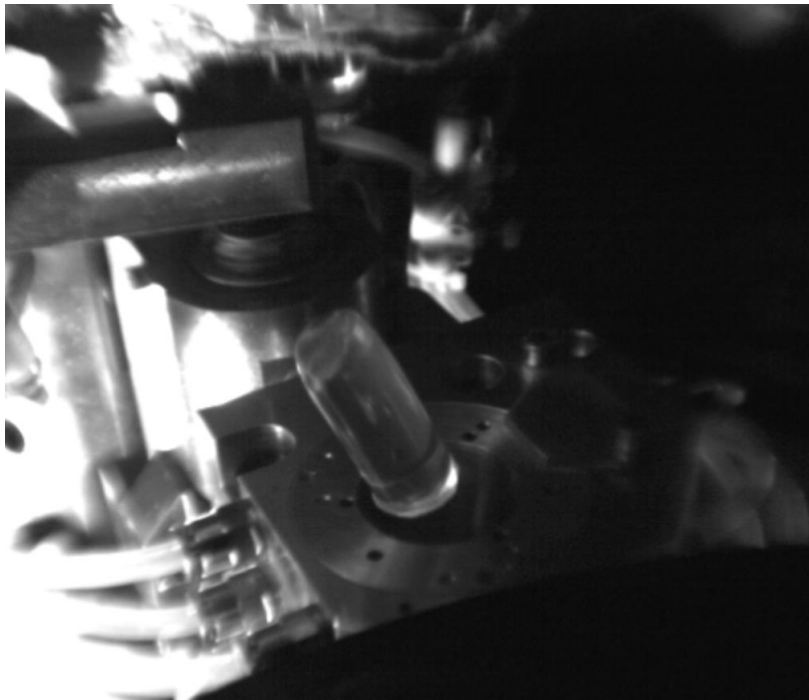


Figure 3.20 Gob loading with  $\alpha = 60^\circ$  swirl pipe.



Figure 3.21 Test on handling tool gob trajectory repetitiveness.

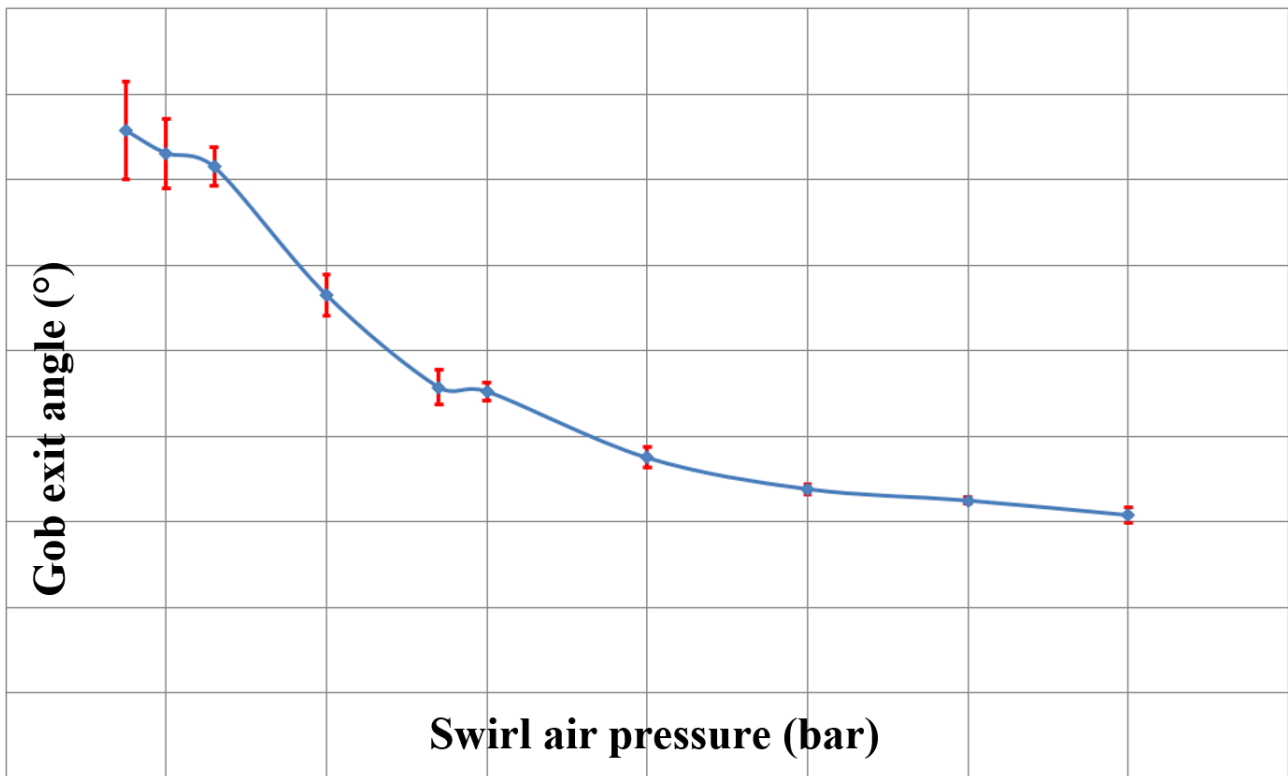


Figure 3.22 Average angle between gob cutting and start gob exiting from handling tool and its standard deviation for  $\alpha = 60^\circ$ . The values on x and y axes are not illustrated due to SACMI intellectual property policy.

The angle variation with pressure is high and the repetitiveness good. This correlation between pressure and exit angle could be very useful to handle the increase of adhesiveness. Machine automation can be set in order to adjust swirl air pressure as soon as gob-transferring time starts changing. Unfortunately, PAM002A layout did not allow to test gob insertion in cavity with this kind of swirl pipe angle. On the contrary, it will be possible with the new testing machine (see paragraph 3.7).

### 3.4.4 Gob floating ( $\alpha = 15^\circ$ )

The surprising result with  $\alpha = 15^\circ$  is that the gob is floating, spinning on itself in a range of positions along the pipe axis, function of the flow rate (fig. 3.23). This could be related to the preliminary flow simulation (fig. 3.12), where the velocity vector projection in the lower part pointed to the upper part of the pipe.

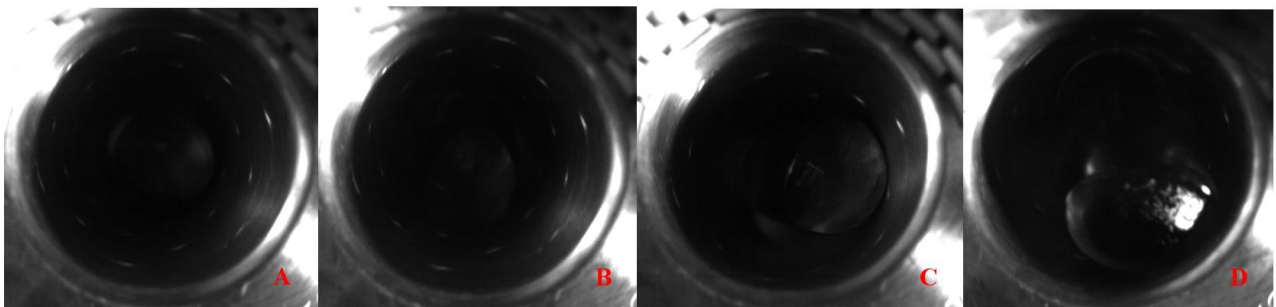


Figure 3.23 Different axial position of the gob depending on swirl flow rate.

Gob floating allowed gob insertion in the cavity and hence preform compression molding. A new kind of test became possible: endurance test on preform compression molding with swirl handling tool. Before repeating the test, the internal pipe surface was cleaned with a commercial multi-purpose cleaner spray and a cloth. The spray is composed of a mixture of heterocyclic nitrogen compounds with glycol ether and alcohols. The exact chemical composition is reported in table 3.1.

Chemical name	Concentration (%)
<i>1-Ethylpyrrolidin-2-one</i>	25÷50
<i>Propan-2-ol</i>	15÷20
<i>1-Methoxy-2-propanol</i>	2,5÷10
<i>2-(3-Methoxypropoxy)propan-1-ol</i>	10÷25

Table 3.1 Chemical composition of cleaning spray for internal pipe surface.

Some parts of the machine were modified to insert additional sensors. A huge experimental work has been done to optimize pipe geometry, temperature, material, superficial roughness.

#### 3.4.4.1 Geometry

With  $\alpha = 15^\circ$  the tests were conducted keeping the C recess on the top part of the handling tool, firstly because the suction power is lower than the case in which  $\alpha = 60^\circ$  but mainly not to change too many variables with respect to what is technically known. Optionally, an upper nozzle can be associated with the duct for expelling the gob from the duct when it is kept floating. Figure 3.24 reports all the pipes (lower half) and their support (higher part on the right) tested during this PhD project.



Figure 3.24 Tested pipes and their supports (the image quality is reduced due to SACMI intellectual property policy).

The starting geometry was the one on figure 3.25, that resulted in few minutes of work after which the gob stuck to the inner part of the pipe. In this paragraph only some geometries are shown, i.e. the ones that gave the best results in terms of gobs transferred without errors. Pipe exiting diameters are almost the same. Finding the proper value was not easy. It is important to keep the gob straight to allow it to enter with precision on mold cavity. But at the same time the gob is not perfectly axial symmetric thus a bit of radial allowance must be given.

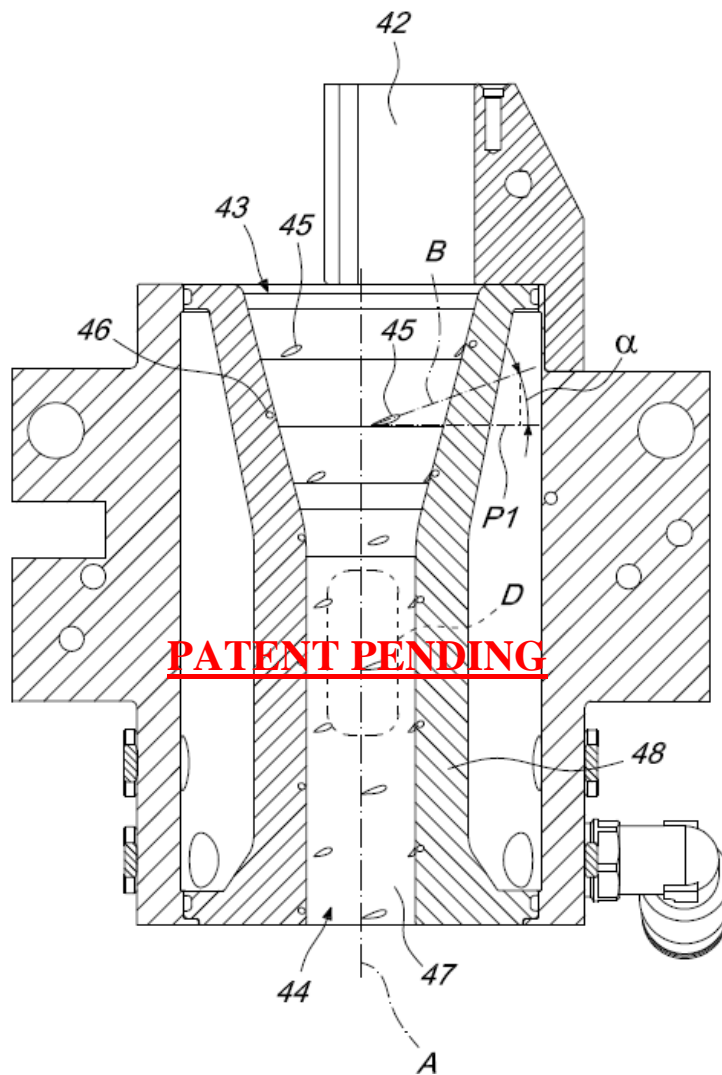


Figure 3.25 First geometry for  $\alpha = 15^\circ$  swirl pipe.

The flow towards the cavity can lead to gob bouncing. If the bounce is too high a defect can be generated on the preform. This inconvenience leads to the adoption of precise pneumatic valves to allow the flow only in precise and repetitive positions. Fig. 3.26 shows an example of test flows cyclogram, which includes also other flows which belong to other swirl pipe geometries.

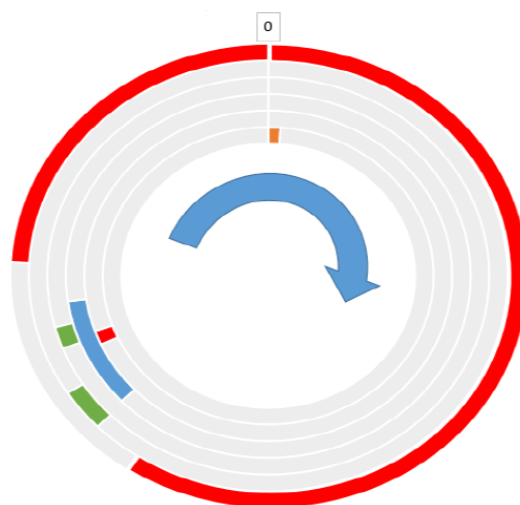


Figure 3.26 Example of swirl pipe flows cyclogram. Details are not illustrated due to SACMI intellectual property policy.

A swirl pipe without the lower cylindrical part (fig. 3.27) resulted in almost 7000 gobs inserted without errors, then errors (i.e. gob exiting with delay) start with a raising frequency until the gob eventually adheres to the pipe. The available transfer time was about 0.22 s.

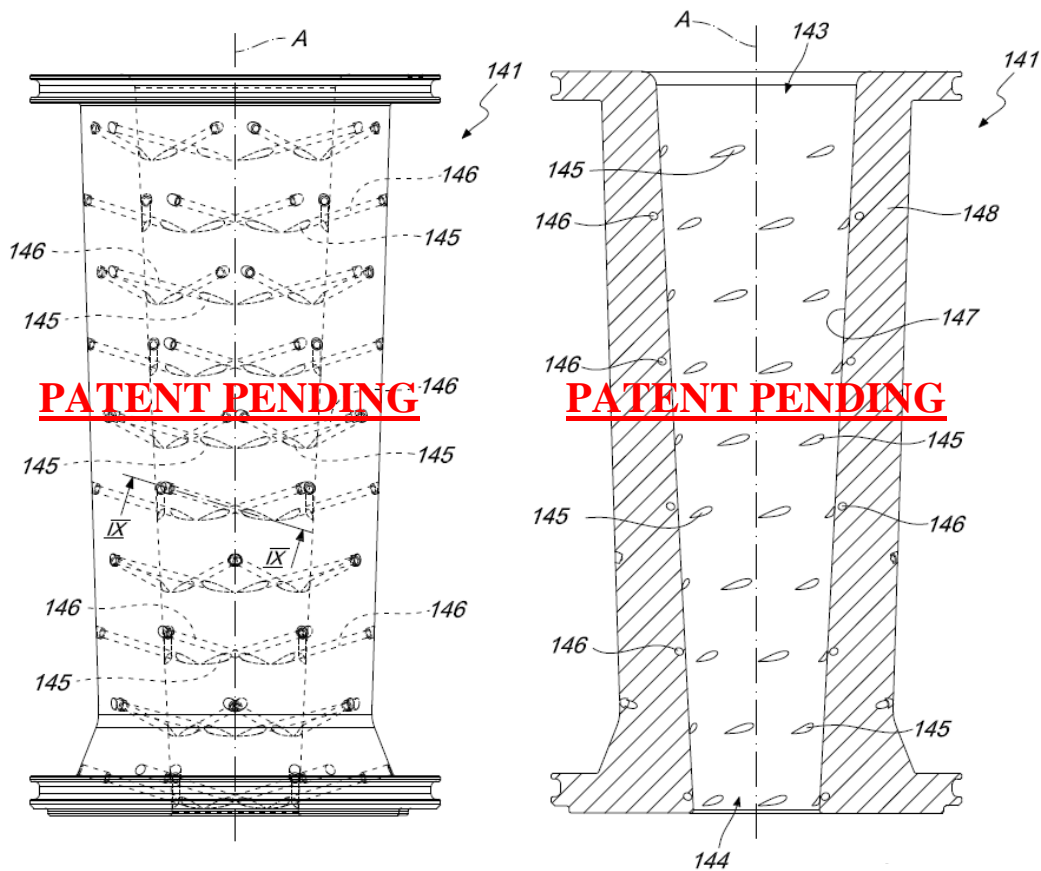


Figure 3.27 Second geometry for  $\alpha = 15^\circ$  swirl pipe.

Advantageously, to increase time without errors an additional air flow can be adopted (fig. 3.30). Around the internal tubular surface of the guiding duct 247 (fig. 3.29) there can be an annular slit 271, for example by way of an annular chamber 272, defined between a bushing 270 and a convex surface blended with the internal tubular surface 247. Such annular chamber 272, can be connected to an independent air flow line, so as to generate a "blade" of air in the direction of the outlet 244. Through the annular slits 271 thus defined, it is possible to make the gob slide better by way of a Coandă effect. The latter, as described by the eponymous Henri Coandă in different patents, is the tendency of a jet of fluid emerging from an orifice to follow an adjacent flat or curved surface and to entrain fluid from the surroundings so that a region of lower pressure develops [7], as shown in fig. 3.28.

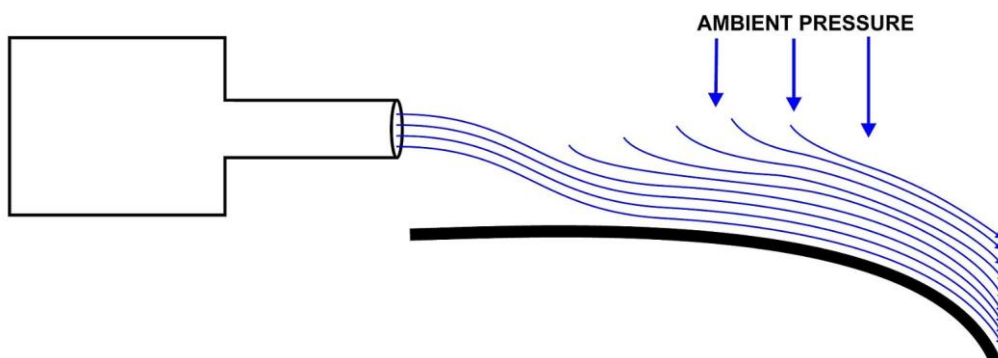


Figure 3.28 Image of a kind of Coandă effect [7].

Gob floats in the frustum part of the pipe, the lower cylindrical part is just a guide for the gob towards the mold cavity.

It took 10 hours of tests to find the proper cyclogram for the swirl pipe in fig. 3.29. Once blow phases were found, without cleaning the pipe, almost 10500 gobs were inserted without errors in 7 hours with an available transfer time of about 0.2 s. During the following 13 hours, there was an average of an error each hour. When 30 hours were reached without cleaning, errors frequency starts increasing with a periodicity of an error every 5 or 6 minutes, while during the last 8 hours the periodicity shortened to an error every 3 minutes, after that the test was stopped. The interesting result was that, for the first time, after more than 40 hours no gob adhered to the pipe, hence there was no unexpected machine stop. The endurance test was repeated and it was confirmed that in 20 hours (after which the test was stopped) there was no gob sticking to the pipe wall.

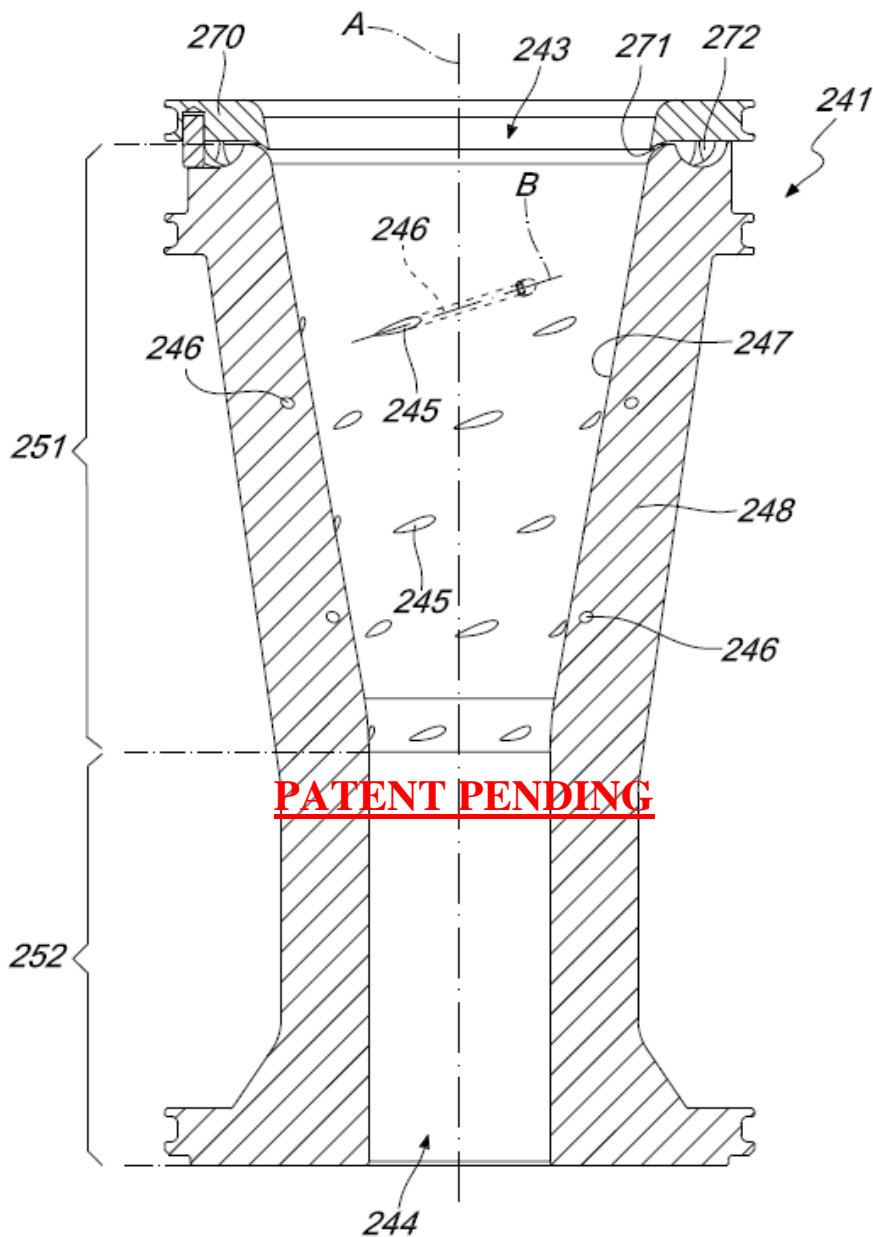


Figure 3.29 Third geometry for  $\alpha = 15^\circ$  swirl pipe.

The distance between the lower part of the handling tool and the upper part of the cavity can be increased to reduce gob bouncing. The limit is when the gob is not sufficiently guided, so it starts touching the higher corner of the cavity mold and this results into a failure in gob transferring.

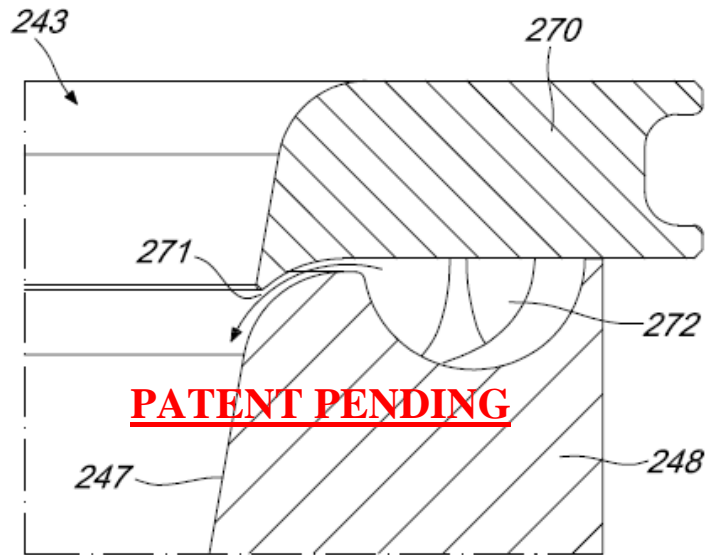


Figure 3.30 Third geometry for  $\alpha = 15^\circ$  swirl pipe: detail view of Coandă effect slit.

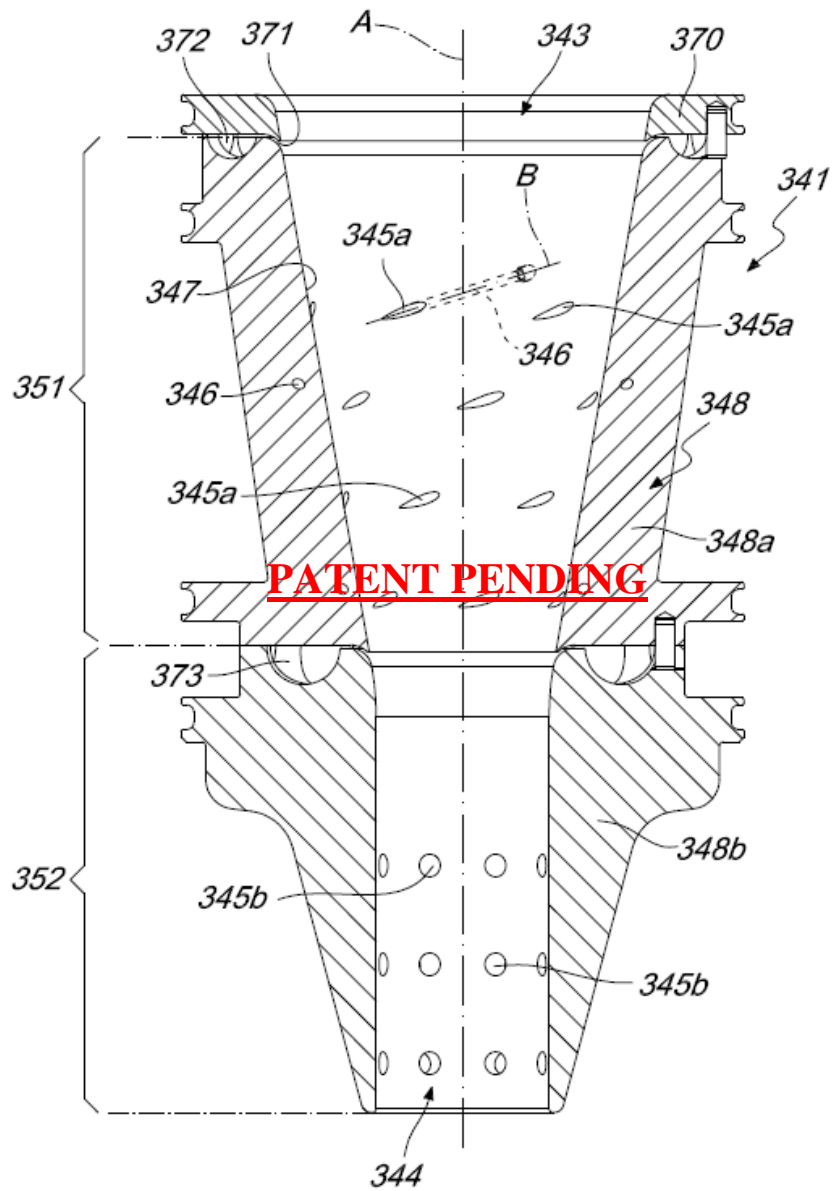


Figure 3.31 Fourth geometry for  $\alpha = 15^\circ$  swirl pipe: Coandă effect double-slit and evacuation holes.

To limit gob bouncing, in the fourth embodiment in figure 3.31, the lower cylindrical part has an external frustum shape to facilitate air evacuation from the cavity. Moreover, an additional improvement is to create a plurality of holes 345b for evacuating the air and reducing thrust on gob in the phase of the gob descent where the thrust is no more necessary.

Another annular chamber (373 of fig. 3.31) and a corresponding annular slit can also be defined in one or more intermediate positions of the guiding duct of the dosed body D, for example between the two monolithic bodies 348a, 348b that form the guiding duct 341.

The first tests with pipe represented in fig. 3.28 are promising. Fig. 3.32 shows a pipe similar to the one of fig. 3.31 assembled on PAM002A testing machine.

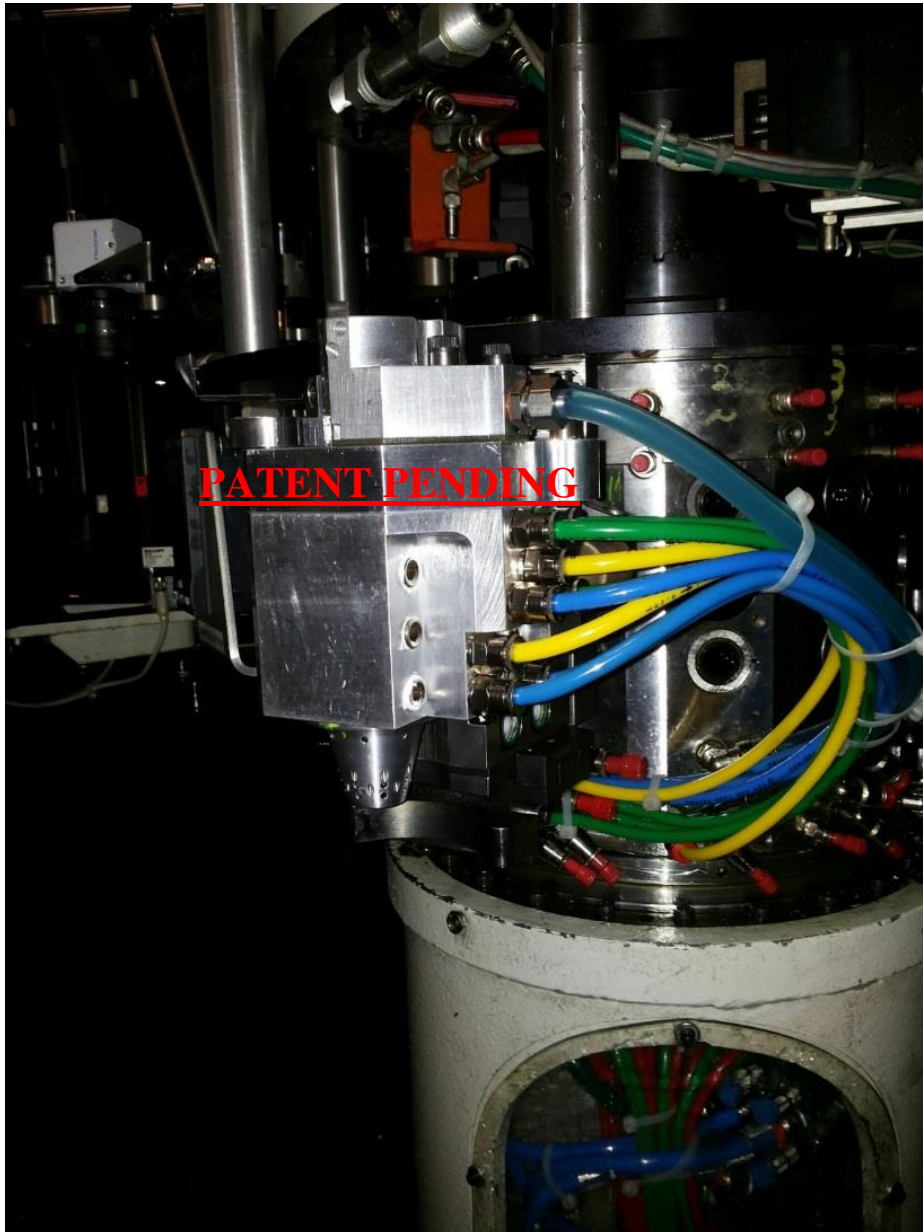


Figure 3.32 Pipe similar to the one of fig. 3.31 assembled on PAM002A testing machine.

Another version of the swirl pipe (fig. 3.33) has the cylindrical part partially constituted by a stack (460) of flat rings. Some of these rings (461, fig. 3.34) have, on at least one of the two flat faces, a plurality of grooves 462 that are adapted to make the air or the fluid fed from outside pass toward the inside of the ring 461. The aim is to reduce adhesiveness in the cylindrical part. The pipe is still to be tested.

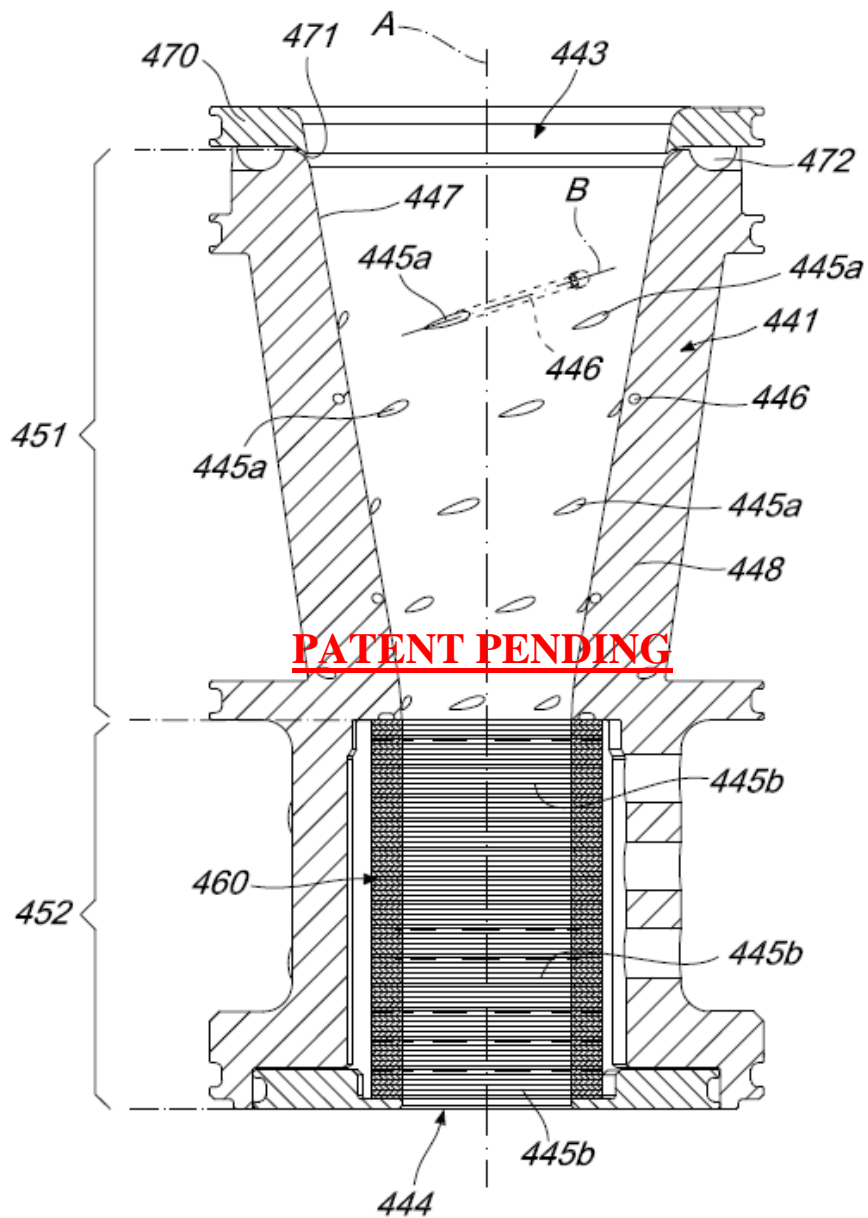


Figure 3.33 Fifth geometry for  $\alpha = 15^\circ$  swirl pipe: plurality of flat rings with grooves for air feeding.

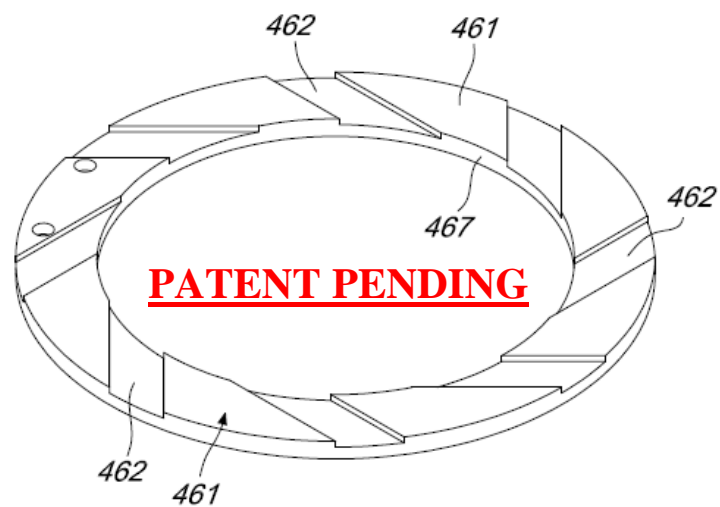


Figure 3.34 Fifth geometry for  $\alpha = 15^\circ$  swirl pipe: detail view of flat ring with grooves.

#### 3.4.4.2 Surface roughness and coatings

Swirl pipe internal surface roughness has a strong impact on PET gob handling tool performances to avoid the bad effects of adhesiveness during the endurance tests. Fig 3.35 reports the result for the same swirl geometry and temperature; the only difference was in the internal surface roughness. The worst behavior was found at very low roughness values, i.e. smooth surface [8]. By increasing Ra (defined in paragraph 2.9), it was possible to find an optimum after which performances declined.

Two food contact anti-adhesion coatings were tested: an industrial three layers poly(tetrafluoroethylene) (PTFE) and a nanoceramic one (thickness lower than 1 micron). The latter showed no improvements compared to the same pipe before coating and, due to the small coating thickness, they share the same roughness. To make PTFE coating adhere to the bulk, the surface was shot peened thus changing surface roughness to much higher values, which, according to fig. 3.35, give worst performance. Moreover, overall coating thickness was variable and much higher than expected by the supplier. It resulted in a very bad performance compared to the same pipe without coating.

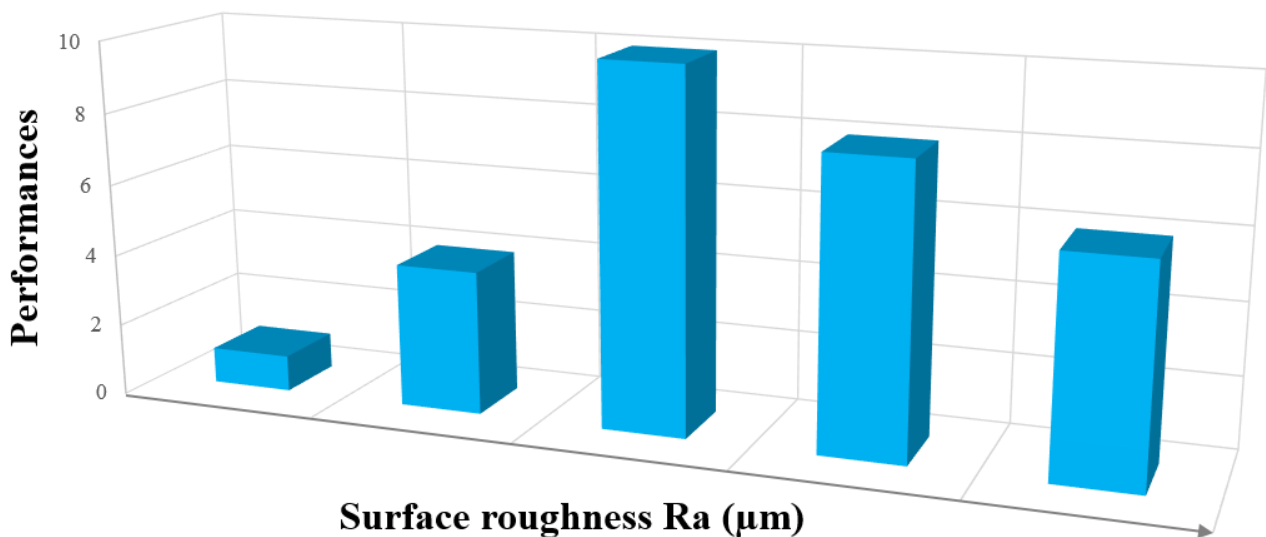


Figure 3.35 PET gob handling tool performances function of its internal average surface roughness. Performances are expressed in a quantitative way that assesses the sticking behavior of the gob on metal surface after many gobs passages (the higher the number, the better the antisticking behavior of the metal surface). The values on x axis are not illustrated due to SACMI intellectual property policy.

#### 3.4.4.3 Temperature

The impact of handling tools temperature on endurance test was studied. Two kinds of swirl handling tools had been designed: one that cools down the swirl pipe, the other that heats it up. The overall temperature testing condition ranged from 10 °C (mold cooling temperature) to 300 °C (a bit higher than molten PET gob temperature). The technical difficulty of the latter was to locally heat up the swirl pipe without a temperature increase on the mechanical components on which the handling tool is assembled. For example, the handling tool radial sliding guides have strict tolerances, so a strong thermal insulation and a proper cooling had to be implemented to avoid guide dimensional growth which will end in a block of the movement and hence in components failure. Finite Element Method (FEM) thermal simulations were done, using Ansys® software, to help the design (fig. 3.36). In figg. 3.36 and 3.37 decimal places are separated with a comma instead of a dot due to the software configuration which follows Italian standard.

Furthermore, the different temperature between the pipe and its box can lead to a higher radial dimensional growth of the first which could end in plastic deformation of the guiding diameter. Even in this case thermal FEM simulations can help design proper diameter dimensions, which are different for stainless steel and aluminum alloy due to their different coefficients of thermal expansion and hence different radial variation (fig. 3.37) at the same temperature difference.

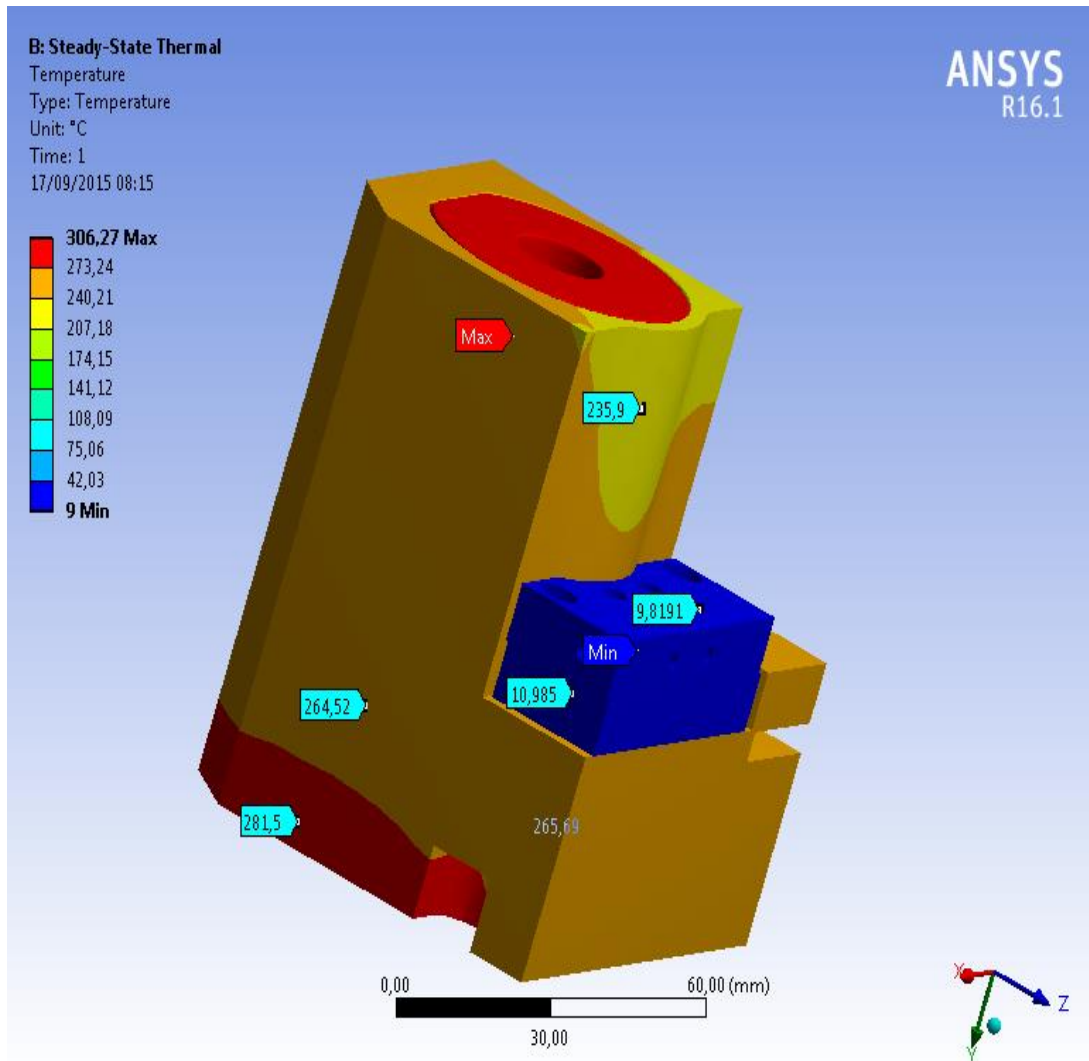


Figure 3.36 Temperature plot of a FEM simulation to optimize heated pipe thermal insulation.

It is important to underline that the pipe is assembled at room temperature and then it is heated. Gob transferring carousel was not designed to carry hot liquid to the handling tool. What is more, as previously mentioned, it is important that high temperature is just inside the handling tool parts in contact with the gob to prevent mechanical failures. Therefore, as showed in fig. 3.39, the swirl pipe is heated locally by a thermo-resistance assembled on its external surface. This apparently seems easy, but it is fundamental to remember that the handling tool is on a rotating system where electrical power is brought through a rotating joint. Fig. 3.38 shows how an electrical rotating joint is made: the rotating part has several conductive rings (function of the number of the electrical signals/power lines required) covered by a gold layer. Each ring is continuously touched by a spring connected to the fixed part to transmit signal/power. In fig. 3.38 the ring number 14 ("#14") is heavily damaged and also the other rings have the gold layer partially abraded. The power cannot be too much since the PAM002A transferring carousel joint is not designed to support a high electrical current as the latter would lead to an excessive heating due to Joule effect. Nevertheless, the voltage cannot be too high due to existing electrical insulation.

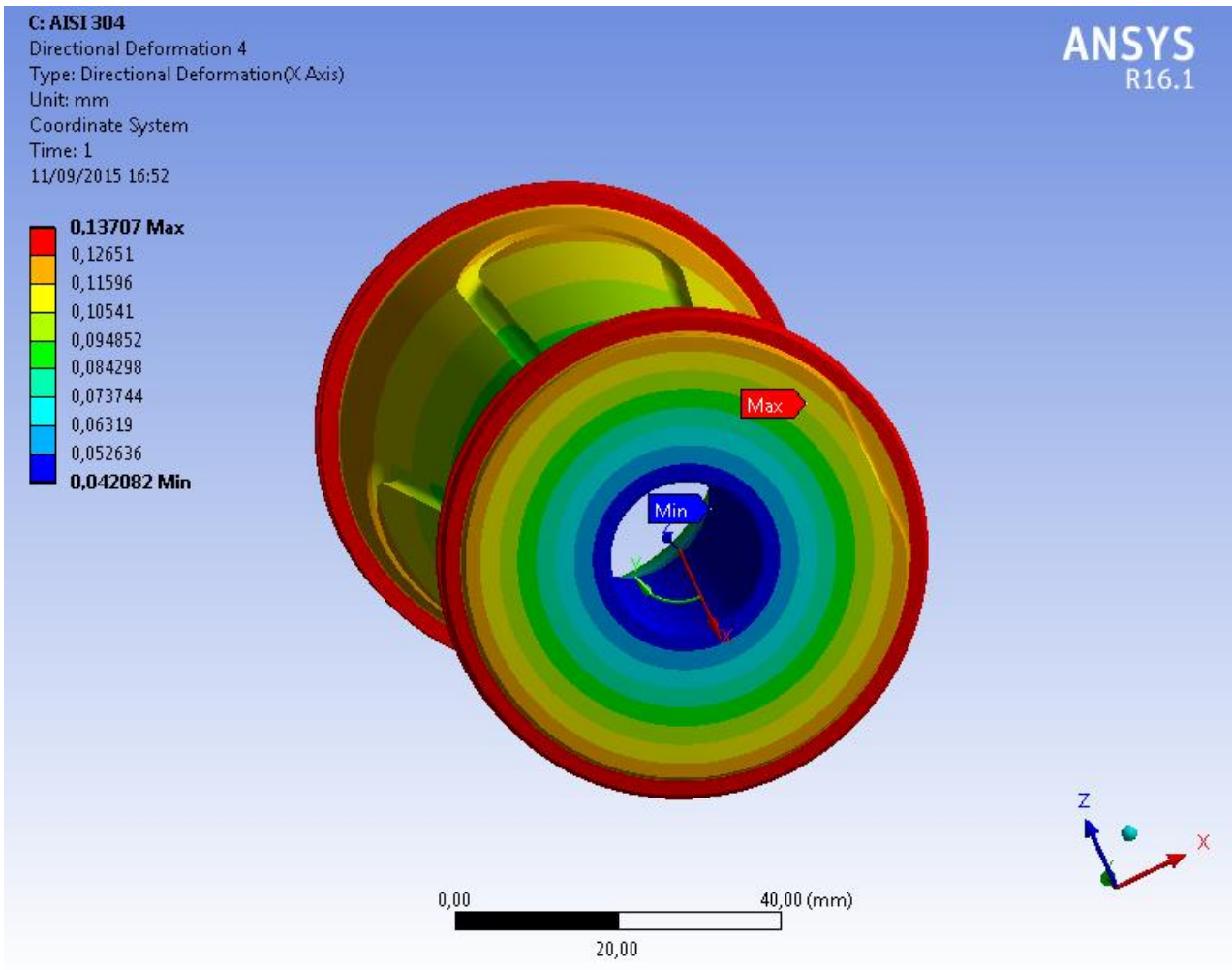


Figure 3.37 Heated swirl pipe: radial deformation due to high temperature.

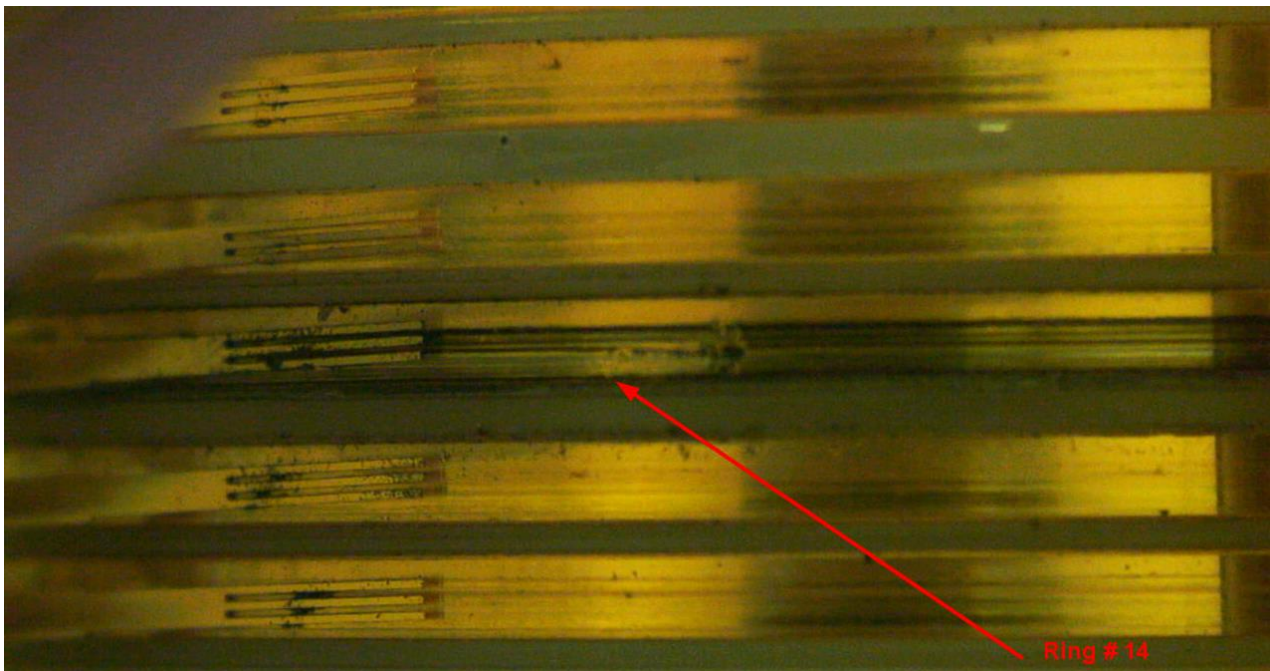


Figure 3.38 Inner part of an electric rotating joint.

The assembling of the thermo-resistance on the external face of the swirl pipe is not easy. It is important to guarantee a homogenous thermal profile without interfering with small inlet ducts. Fig. 3.39 shows a picture of the heated swirl pipe with also a sensor to check the temperature value.



Figure 3.39 Picture of heated swirl pipe with heating thermo-resistance and thermocouple.

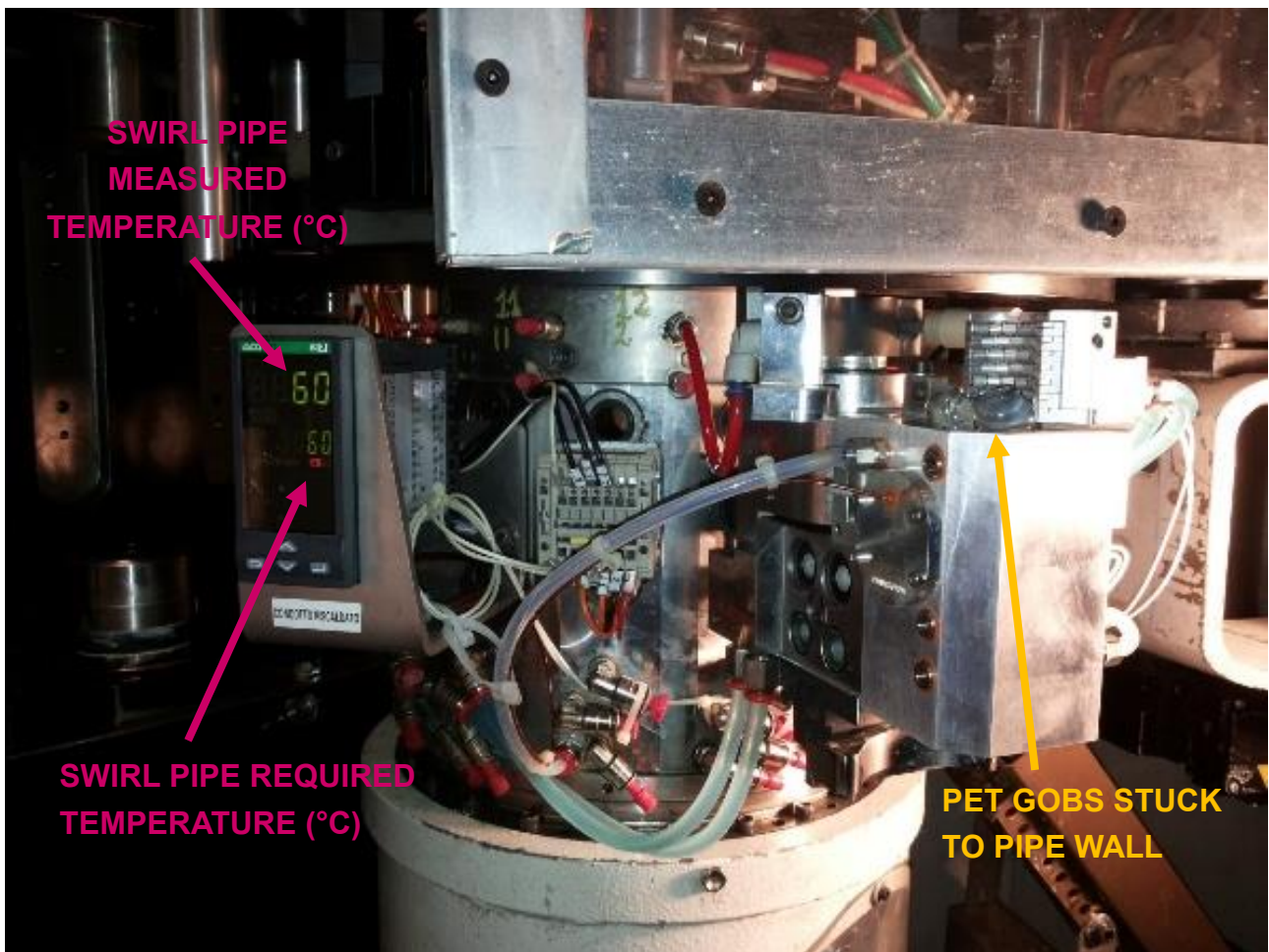


Figure 3.40 Picture of heated swirl pipe with heating thermo-resistance and thermocouple.

The temperature sensor chosen is a Pt100 miniaturized sensing resistor (1.2 x 1.6 mm) with an accuracy of  $\pm 0.35$  °C at 100 °C. For reasons due to the assembling process the sensor was inserted in the cylindrical part of the pipe, at a distance of 1 mm from the inner wall. Moreover, air seals require particular heat resistance not reached with a usual NBR (Nitrile butadiene rubber) blend which is usually guaranteed till 100 °C. A patented perfluoro-elastomer was used because its working temperature can reach about 315 °C. A commercial sealing paste for high temperature was used to seal the holes where the cables enter the handling tool (fig. 3.40). Finally, a PID (proportional integral derivative) thermoregulation controller regulates the temperature required and allows the operator to easily change it. Fig. 3.40 shows the testing equipment on PAM002A transferring carousel. The picture was taken after performing a test at 60 °C on an AISI 316 swirl pipe. The test resulted in the gob stuck to the pipe wall after almost 20 gob loadings as fig. 3.41 shows. After the first gob stuck, the following ones accumulated on the upper part as shown in fig. 3.40 until the machine was stopped.

Fig. 3.41 shows the results of high temperature tests on two pipes with the same geometry but two different materials: AISI316 (stainless steel) and EN-AW-6082-T6, an aluminum alloy.

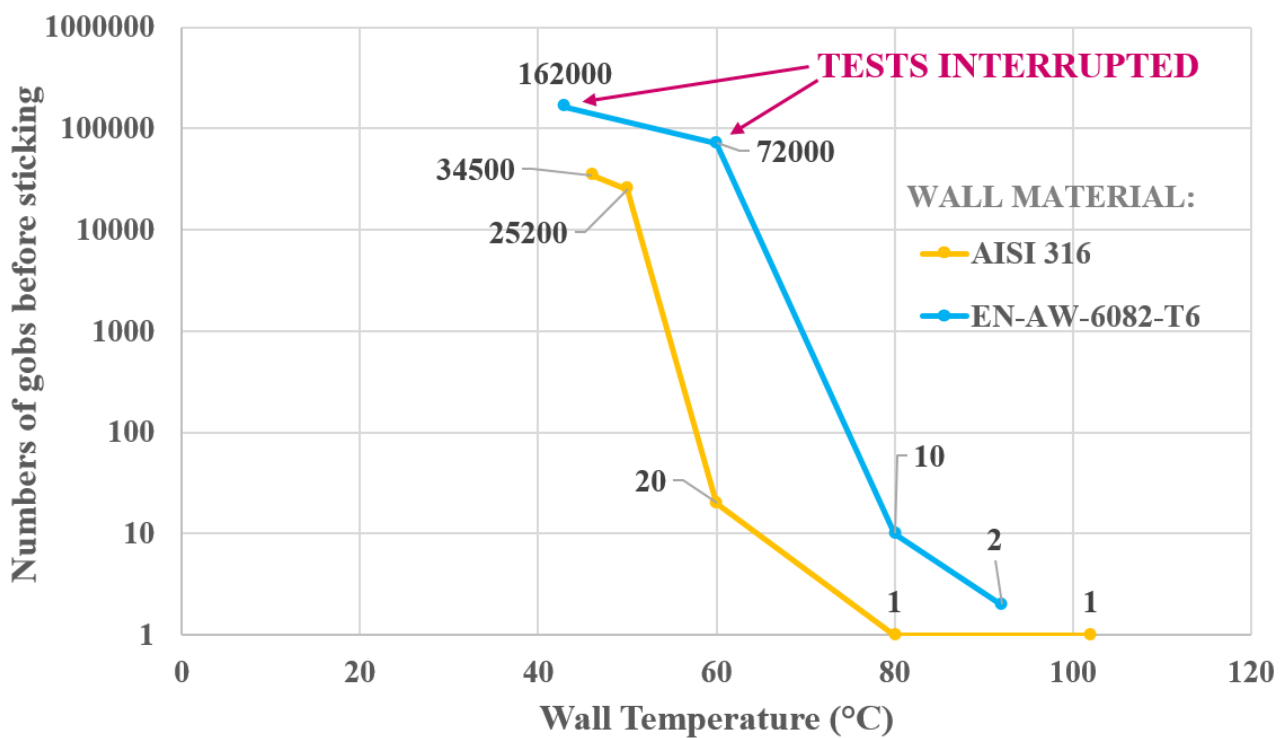


Figure 3.41 High temperature endurance tests results.

It is important to underline that, even if the temperature sensor is very precise, its position is quite far from the zone where the gob stuck during the tests. The temperature values are not to be taken as absolute values but rather to be used for comparative analyses and to search for a trend. Moreover, the supplier made an error in roughness manufacturing, which results in different values: for stainless steel, it is close to the lower one of fig. 3.35, while for aluminum alloy it is close to the third one which gave the best results. For this reason, results for temperature equal to or lower than 50 °C were not considered. The different behavior is attributable to the difference in roughness as seen for similar temperature (around 40 °C) using the same pipe material. The results for higher temperature (i.e. equal to or higher than 60 °C) are surprising because a new phenomenon was observed: as temperature increased, a temperature value was reached where the first gob stuck on the cleaned pipe. The temperature at which the gob stuck after one, maximum two passages, was higher for aluminum

compared with stainless steel. This phenomenon does not seem ascribable to the difference in roughness. It is interesting to note that sticking temperatures are closed to PET glass transition temperature ( $T_g$ ) which is about 80 °C [6]. The phenomenon, molten PET - metal stickiness after a contact time of the order of  $10^{-3}$  s, is not described in the existing literature, as seen in chapter 2. It will be further developed in chapter 4.

Pipe wall temperature values from 10 °C to 45 °C did not show any significant impact on endurance tests. Pipe cooling was obtained through cooling water at 9 °C already present in the previous PAM002A handling tool. A valve regulated water flow rate, hence pipe wall temperature measured in the same zone of heated swirl pipe.

#### 3.4.4.4 Preform quality

To validate a PET gob handling tool, it is fundamental to check the quality of the machine final product. This is a preform, if the preform compression molding machine is a stand-alone, or a bottle, if the machine is coupled with a blowing one performing a single stage process (as shown in chapter 1).

The first tested swirl pipes generated on the gobs the defect shown in fig. 3.42. This issue was solved by eliminating sharp edges.



Figure 3.42 Gob with defect after passage through swirl pipe.

Fig. 3.43 shows a gob taken out from the cavity mold just before the mold closes. The gob has a higher diameter compared to the one of fig. 3.42 because it took the shape of the cavity mold. It is interesting to observe the PET flow lines that have a torsional orientation around the gob axis and in concordance with swirl air streamlines.



Figure 3.43 Gob passed through swirl pipe and taken out from the cavity mold.

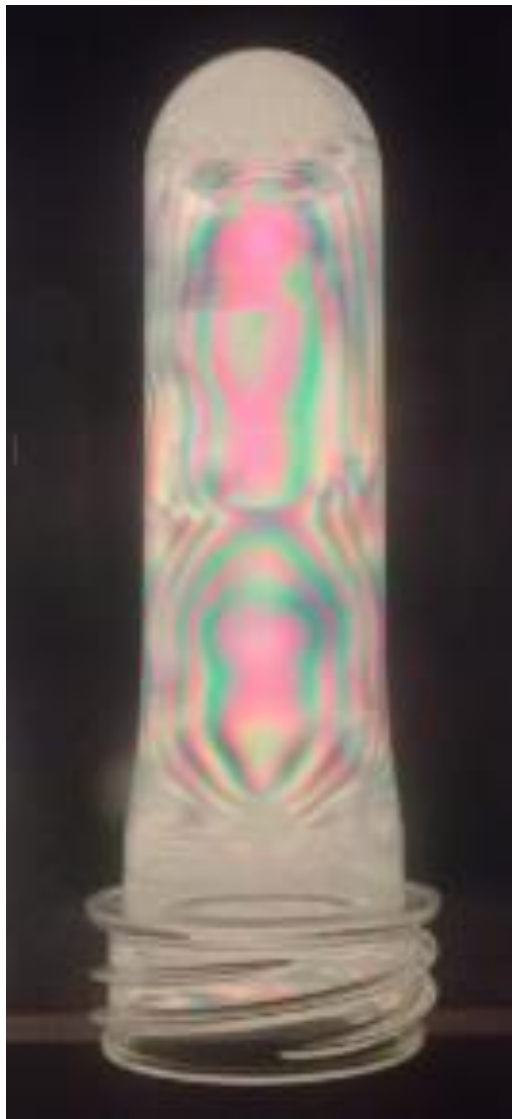


Figure 3.44 Polarized light on a preform whose gob passed through swirl pipe.

Finally, fig. 3.44 shows a preform obtained using a swirl pipe handling tool. It is illuminated with polarized light that can highlight preform problems related to drying, degraded materials, bubbles, moisture and erroneous process conditions. Polarized light it is also indispensable for highlighting tensions within the preforms [6]. Preform in fig. 3.42 shows an axial symmetric distribution of tension lines which, according to SACMI Lab and compression molding testing customer experience, will make preforms result in bottles of good technical quality. Some preforms present defects, but it is not possible to assess if they were generated by the swirl pipe. It is more likely that they were generated by water leakages or other causes related to the absence of maintenance in some part of the machine. Further tests must be done to better understand the topic.

### 3.5 CONSIDERATIONS ON ADHESIVENESS

Adhesiveness, as previously explained, increases if the surface has already been in contact with PET. The tests showed that pipes surface could be regenerated cleaning it with a commercial spray whose composition is reported in table 3.1 (see page 18). Geometry, additional flows and surface roughness can raise anti-adhesion performances but do not eliminate adhesiveness effects that, at present state of art, come out after about 10000 gob passages.

Temperature seems not to have impact on PET-metal adhesiveness if its value stays below 45 °C. At this temperature, it seems there is no significant differences among stainless steel, aluminum or an anti-stickiness nanoceramic coating if they all have the same roughness.

Touching with a fingertip then inner part of the pipe when adhesiveness effects start happening, a feeling of slightly sticky surface occurs compared to cleaned one. From the optical point of view the surfaces look similar and they have the same size (measures with 0.005 mm precision). It was not possible to analyze the inner part of the pipe with Fourier Transform Infrared Spectroscopy (FTIR), a technique to identify organic and sometimes inorganic material, without cutting a part of the pipe and hence probably eliminating the tracks of interest or introducing new elements. Differently, the knife that cuts the gob has a flat surface and it is cleaned with a much lower frequency compared to the handling tool. There is hence the time necessary to accumulate much more material and to see the deposition of a visible white thin layer in addition to the powder (see fig. 2.1). Powder and layer were analyzed with FTIR. Fig. 3.45 compares the spectra of the white thin layer on the gob cutting knife (red) and of the PET (green): the match is very good.

It is known [5] that during polycondensation reaction (fig. 3.46) under vacuum with catalyst, two or more BHET molecules (fig. 3.47) can react by closing on themselves and forming for example Ethylene Terephthalate Cyclic Dimers (fig. 3.48) with the release of two ethylene glycol molecules. These cyclic dimers, or generally cyclic oligomers, do not have OH groups. They hence have a higher volatility compared to their non-cyclic equivalent ones, even if they have almost the same molecular weight. OH groups increase molecules boiling temperature because they can create hydrogen bonds, so it is no more correct to use the term polymer boiling point, because, at high temperature, degradation occurs before boiling could happen. PET made in industrial reactors has a polydispersity index higher than three, as shown in fig. 3.49 [5]. According to Rieckmann and Völker [5] PET contains about 2 – 3% of oligomers, which can occur as linear or cyclic molecules. Cyclic oligomers that are inside the polymer gob could vaporize and condense on pipe wall that is cold, compared to gob temperature (about 270 °C). This could be an explanation for the adhesiveness increase after many gob passages.

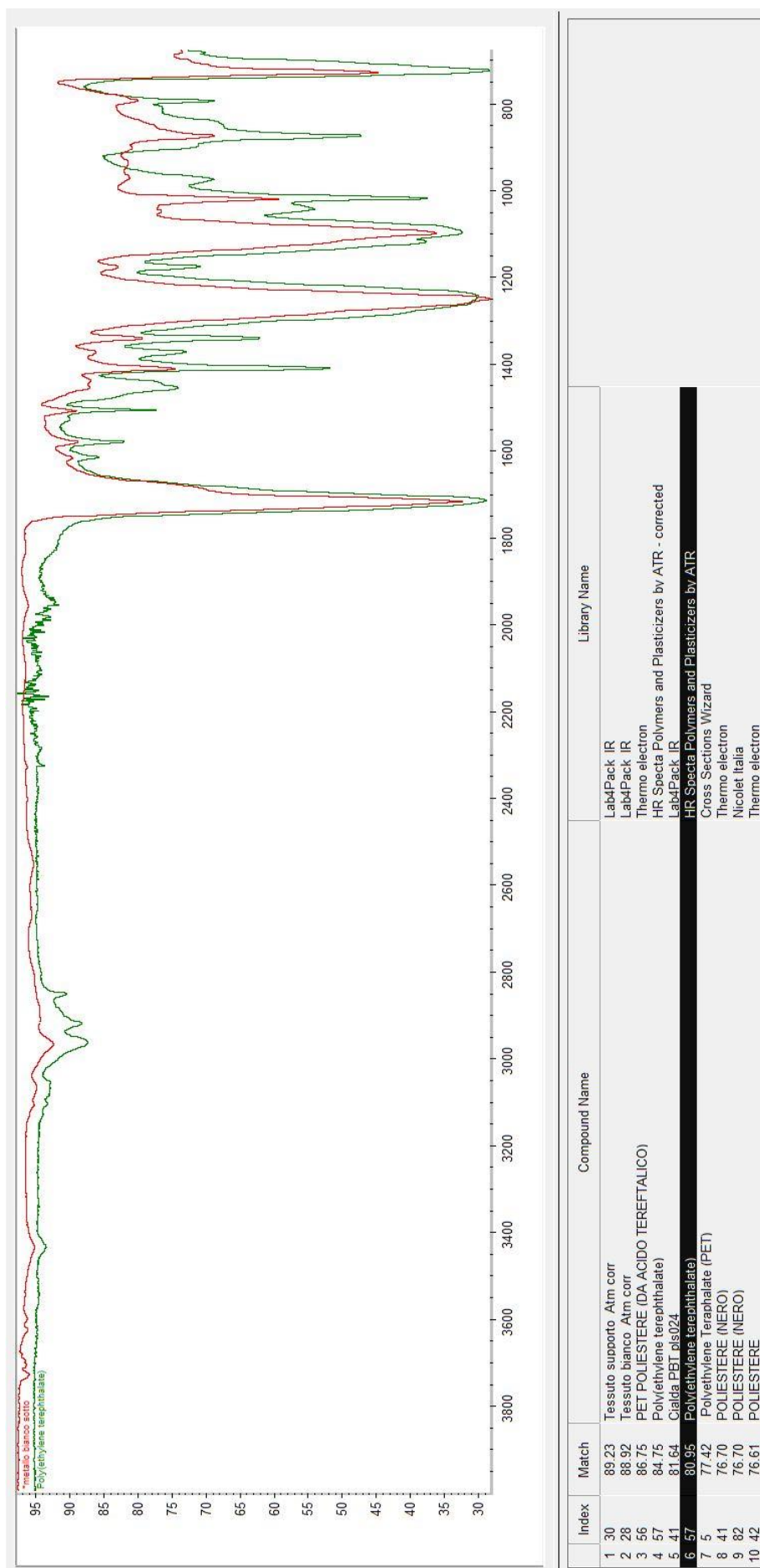


Figure 3.45 FTIR spectra of white layer deposited on gob cutting knife (red) and of PET (green).

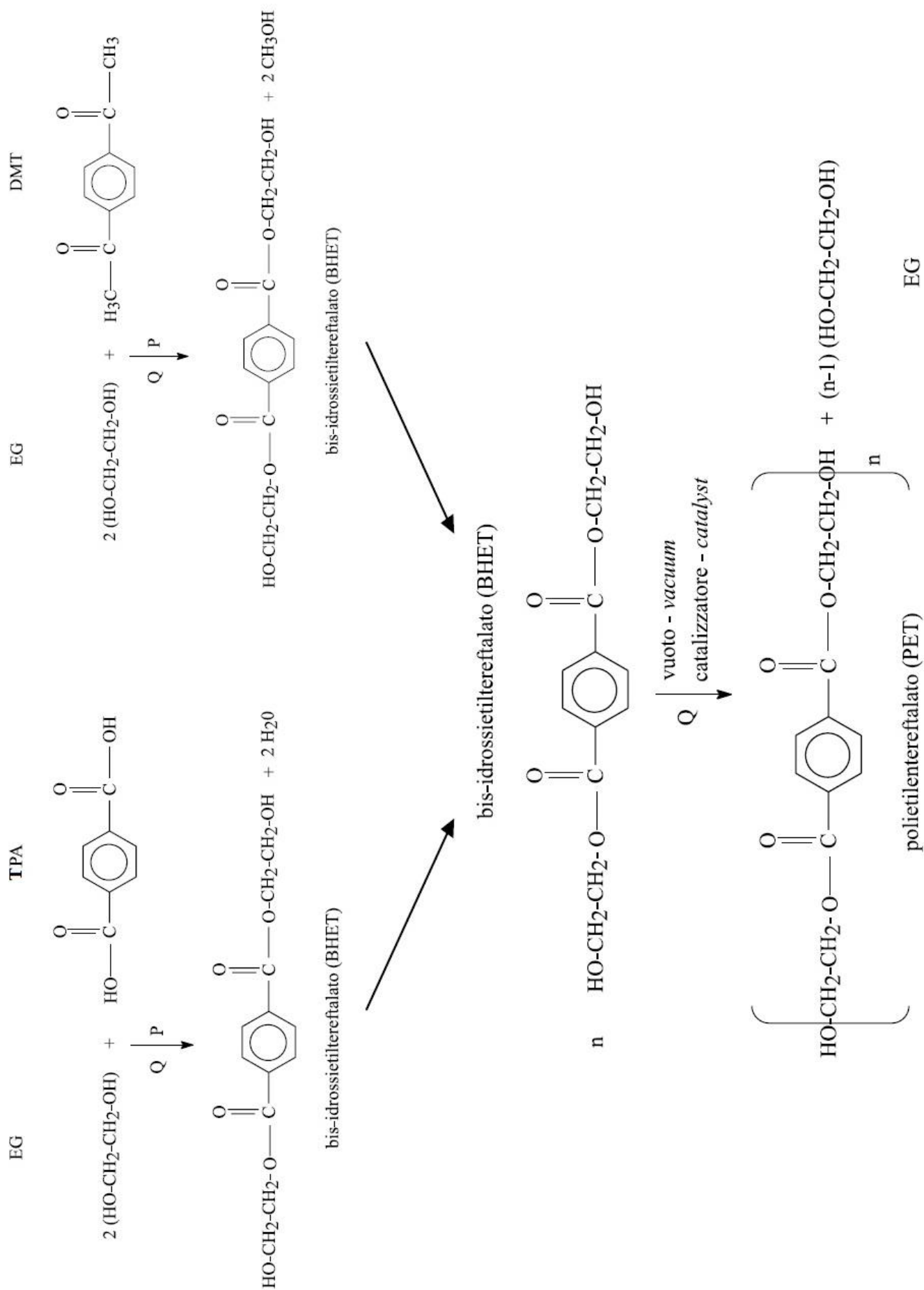


Figure 3.46 PET polycondensation reaction starting from EG/TPA and EG/DMT [6].

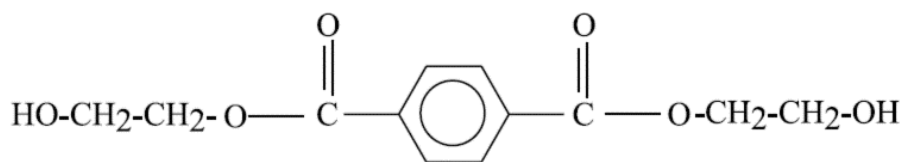


Figure 3.47 BHET molecule.

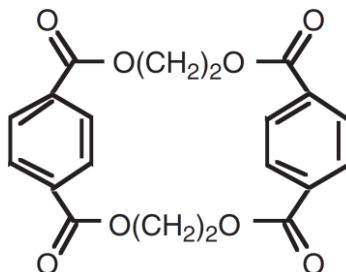


Figure 3.48 Ethylene Terephthalate Cyclic Dimer.

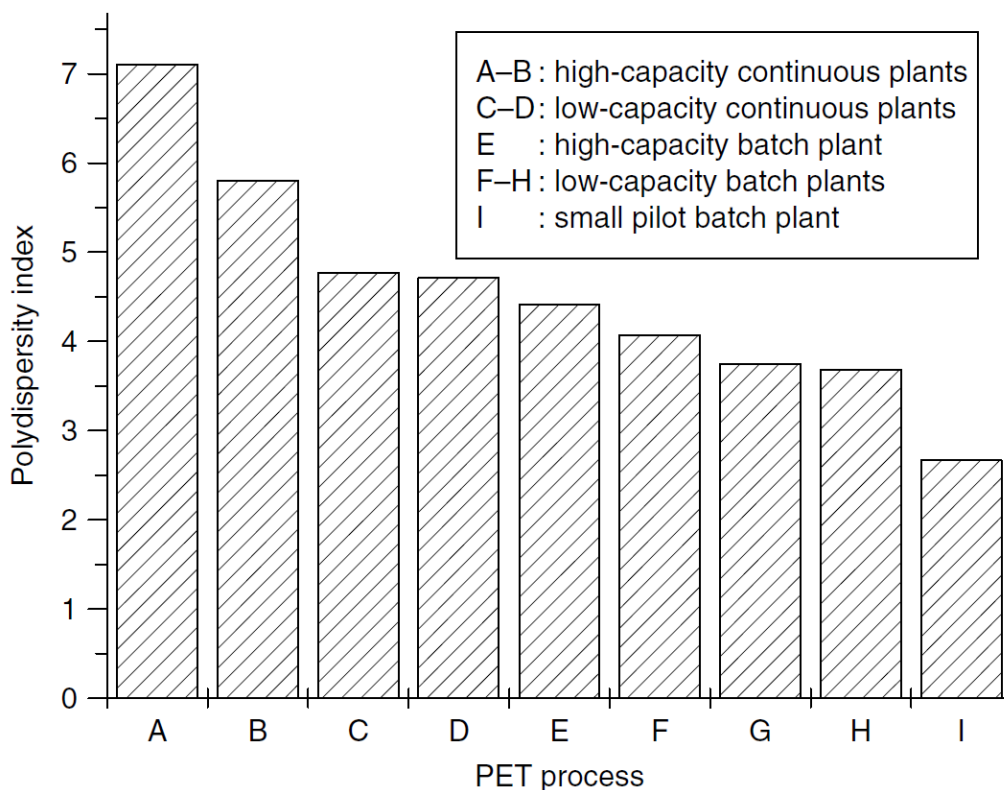


Figure 3.49 Polydispersity index for different PET processes and reactor sizes <sup>1</sup> [5].

<sup>1</sup> Reprinted from Th. Rieckmann and S. Völker, *Poly(Ethylene Terephthalate) Polymerization – Mechanism Catalysis, Kinetics, Mass Transfer and Reactor Design* ch.2 pp. 29-115 in *Modern Polyesters: Chemistry and Technology of Polyesters and Copolyesters*, J. Scheirs, T.E. Long, Ed., John Wiley & Sons, Ltd, Copyright (2003), with permission from John Wiley & Sons Ltd, The Atrium, Southern Gate, Chichester, West Sussex PO19 8SQ, England. All Rights Reserved. No part of this publication may be reproduced, stored in a retrieval system or transmitted in any form or by any means, electronic, mechanical, photocopying, recording, scanning or otherwise, except under the terms of the Copyright, Designs and Patents Act 1988 or under the terms of a license issued by the Copyright Licensing Agency Ltd, 90 Tottenham Court Road, London W1T 4LP, UK, without the permission in writing of the Publisher. Requests to the Publisher should be addressed to the Permissions Department, John Wiley & Sons Ltd, The Atrium, Southern Gate, Chichester, West Sussex PO19 8SQ, England, or emailed to [permreq@wiley.co.uk](mailto:permreq@wiley.co.uk), or faxed to (+44) 1243 770620. This publication is designed to provide accurate and authoritative information in regard to the subject matter covered. It is sold on the understanding that the Publisher is not engaged in rendering professional services. If professional advice or other expert assistance is required, the services of a competent professional should be sought.

### 3.6 IMPROVED CFD SIMULATIONS

Preliminary gob handling tests with a swirl flow on a real preform compression molding machine showed that it is worthy to continue the developments. Once validated, improved CFD simulations of the phenomenon could help understanding how to increase swirl pipe efficiency. Moreover, once reached the desired performances, simulations could reduce costs and testing time of new pipes design. Different preforms have different gob dimensions so it is necessary to have a dedicated swirl pipe for each kind or family of preforms.

The first improved simulation was without gob. The aim is to better simulate swirl flow and then find  $\alpha$  limit value below which gob floats and above which gob accelerates.

The second improved simulation was with gob. The aim was to check if it is possible to simulate the phenomenon and validate it by comparing the simulation resulting video with the high-speed camera video.

The simulations were done with the help of PROTESA, a company of SACMI group.

#### 3.6.1 Simulation without gob

As previously mentioned, the aim was to find  $\alpha$  limit value below which gob floats and above which gob accelerates. At the same time, small gob axial movements while it floats seemed ascribable to instabilities in swirl flow which are also described in literature [9, 10]. The software chosen for the simulation is AcuSolve™. It allows a parametric management of the model. In particular, it is possible to easily change  $\alpha$  angle value in CAD 3D software, without setting again the other parameters of the simulation, which results in time saving.

The first simulation was done with  $\alpha$  equal to  $15^\circ$  to compare and calibrate the model with the preliminary simulation done with CFX. It was a stationary one, as previously done with CFX. The simulation did not converge. Acusolve™ has two convergence criteria: residuals and residuals derivative. It declares a simulation as steady when both the criteria are respected. In the present simulation the residual derivatives continue changing because the flow continues moving. This means that preliminary CFX simulation result (fig. 3.50) is just one of the possible simulation solutions but it is not stable.

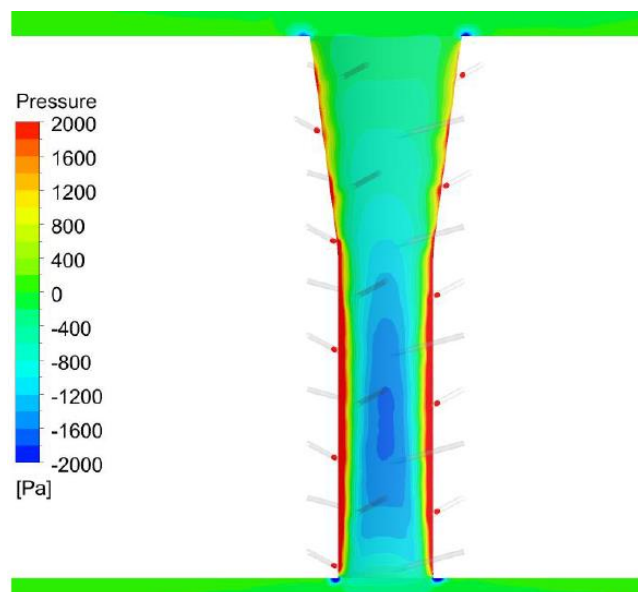
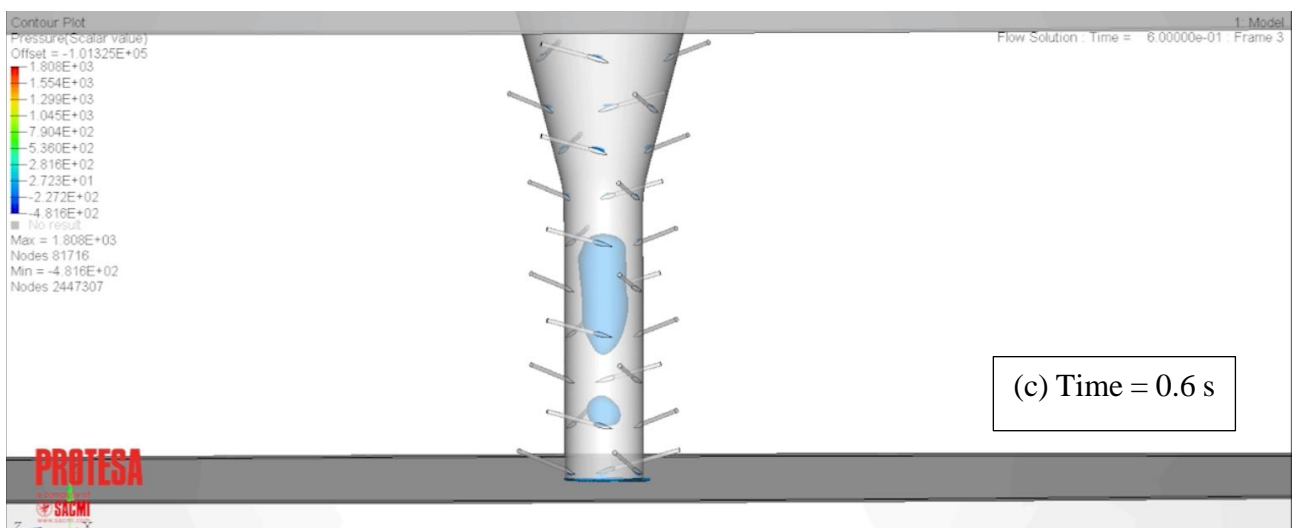
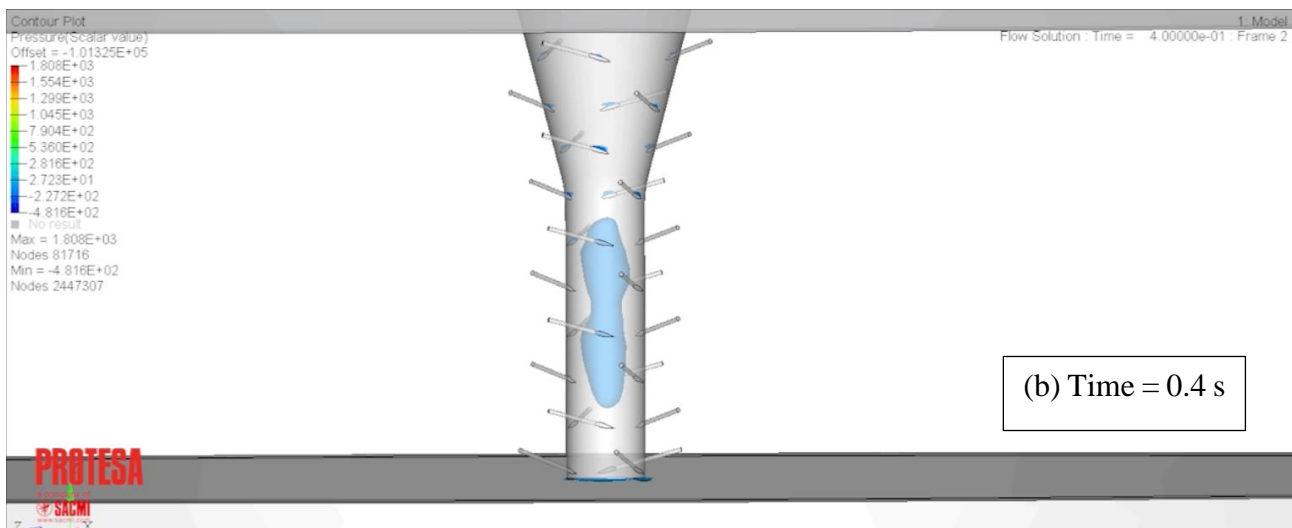
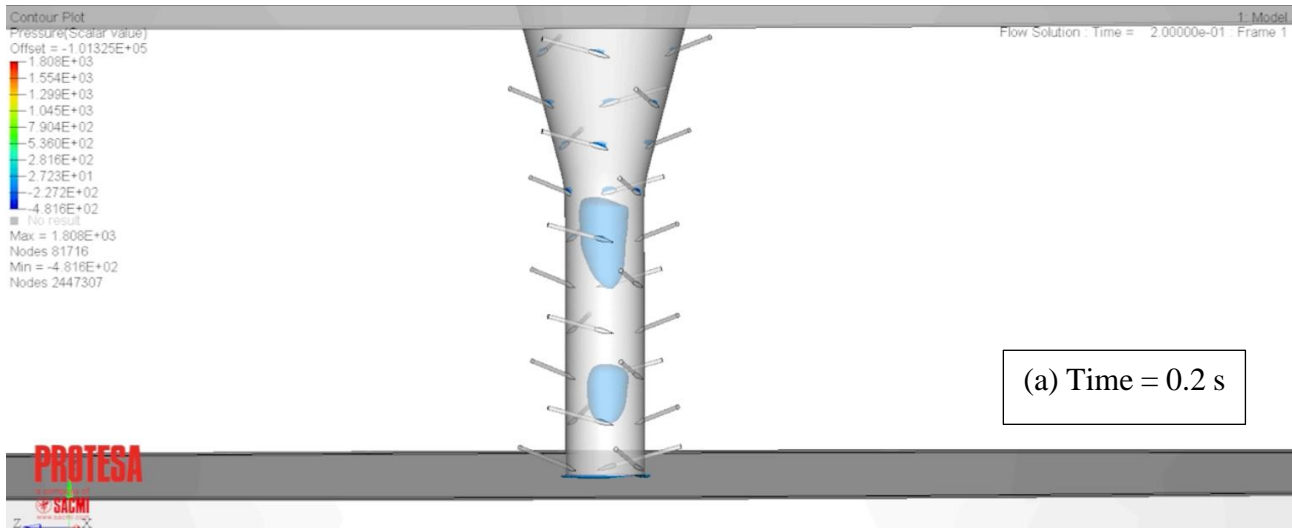


Figure 3.50 Swirl flow stationary CFD simulation (CFX): relative static pressure for  $\alpha = 15^\circ$ .

A transient simulation was then done with AcuSolve™ to better examine these flow instabilities. The integration step was set equal to 0.01 s and 3 seconds of the process were simulated. Several flow instabilities were shown. The main one is the negative pressure bubble which moves along the axial direction. Fig. 3.51 shows four different positions assumed by an isosurface at - 90 Pa with time passing. To save simulation time the inlet flow rate through each inlet pipe was reduced by 80 %. This is the cause of the difference in pressure absolute values between fig. 3.50 and fig. 3.51.



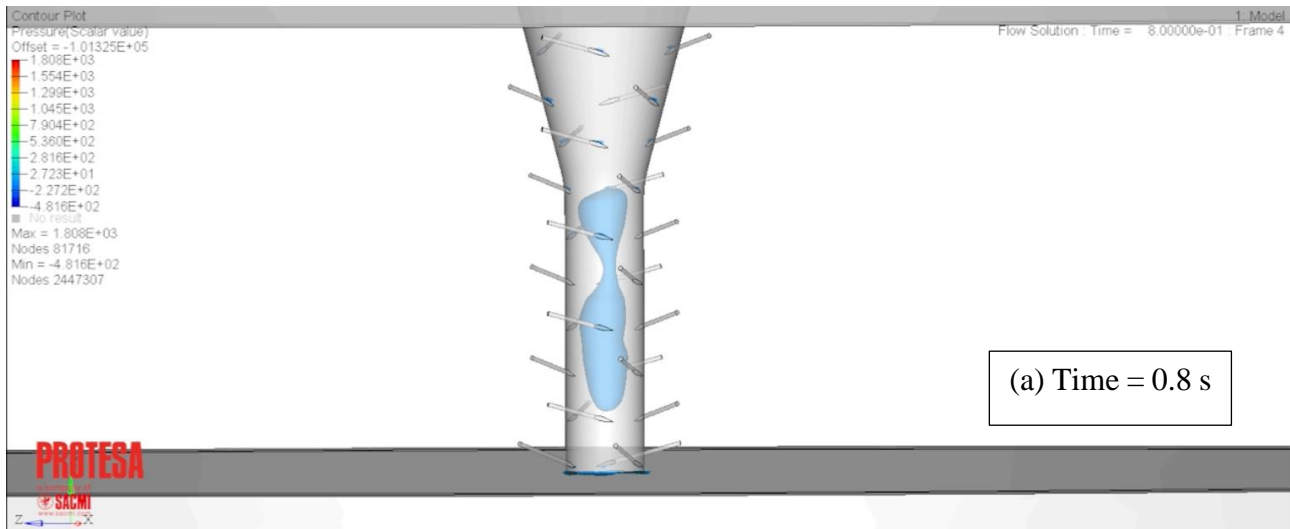


Figure 3.51 (a), (b), (c), (d) Swirl flow transient CFD simulation (AcuSolve™): relative static pressure  $\alpha = 15^\circ$ .

It is important to underline that the results of this simulation can significantly vary depending on the turbulence model adopted. AcuSolve™ uses a modified Spalart-Allmaras that emphasizes non-stationary behavior.

Simulations to find the  $\alpha$  limit value below which gob floats and above which gob accelerates are still to be done.

### 3.6.2 Simulation with gob

Simulating PET gob pneumatic handling it is not easy at all. The approaches to the topic are essentially three and are listed below:

- a) Fluid–structure interaction (FSI) approach, i.e. the interaction of some movable or deformable structures with an internal or surrounding fluid flow [11]. Simulation would be defined both inside a CFD software as concerns the air (considered as Newtonian fluid) domain, and inside a FEM software as concerns the deformable solid (PET gob) domain. Calculation process would be iterative: CFD software evaluates forces on solid/fluid interface and transfers them as loads to the FEM software. FEM software deforms the solid according to the received loads and transfers the resulting displacements to the CFD code that updated forces. The process is iterative within the same time step. The accuracy is high but the level of technical criticality is high too. Calculation time is also high and seems not compatible with design time.
- b) Six degrees of freedom (DOF) approach. Simulation is entirely defined within CFD software. Air is considered as Newtonian fluid and PET gob as a rigid body with inertial properties. CFD software need gob external surface (in contact with air) on which aerodynamic forces are evaluated to solve rigid body (6 DOF) equations. Some software already have collisions, friction and non-interpenetration models. The accuracy is medium. Gob is seen as a not deformable body.
- c) Multiphase approach. Simulation is entirely defined within CFD software. Both air and PET are modelled as fluids. In particular, air as Newtonian fluid and PET as non-Newtonian fluid. PET gob is considered as a "drop" in an air field and its movement is the result of forces acting on it (aerodynamic, weight, inertia) through a multiphase Eulerian approach. The accuracy is medium-low and it depends on grid refinement.

Six degrees of freedom approach was chosen, because it seemed the best compromise between accuracy and time/difficulty. The simulation was done with the commercial software FLOW-3D, which already have collisions, friction and non-interpenetration models. Gob is modelled as a rigid body with six degrees of freedom in a CFD air domain. Collisions are assumed as completely elastic and air as an incompressible fluid. The simulated swirl pipe is similar to the one of fig. 3.31 except for the middle Coandă slit. The handling tool is simulated still, neglecting transferring carousel angular speed. The first modelled step was gob floating with  $\alpha$  equal to  $15^\circ$ . The gob was put in the position of fig. 3.52 before starting the simulation. Fig. 3.53 shows mesh setting.

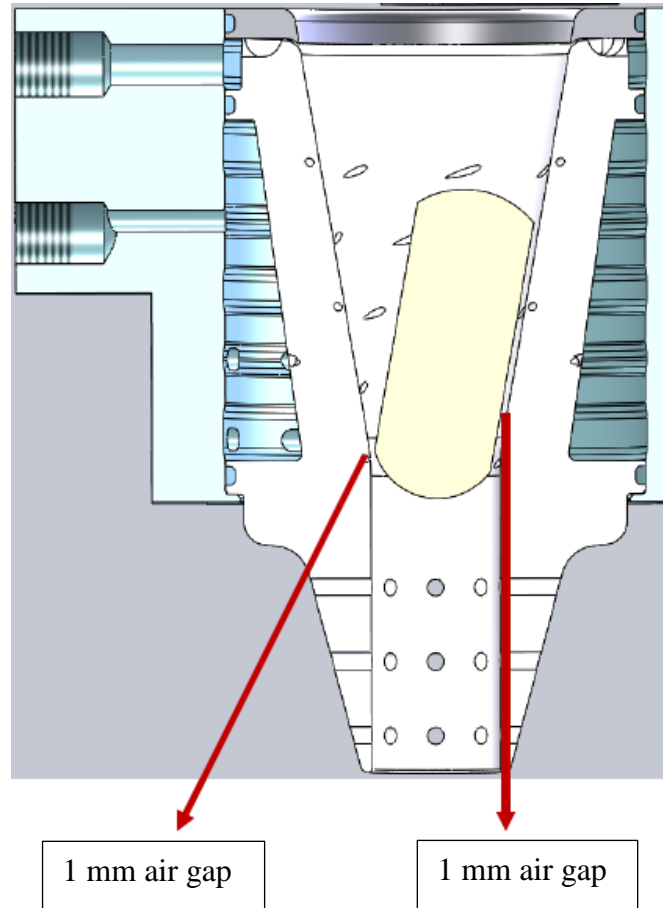


Figure 3.52 Swirl flow transient CFD simulation with gob (FLOW-3D): starting conditions.

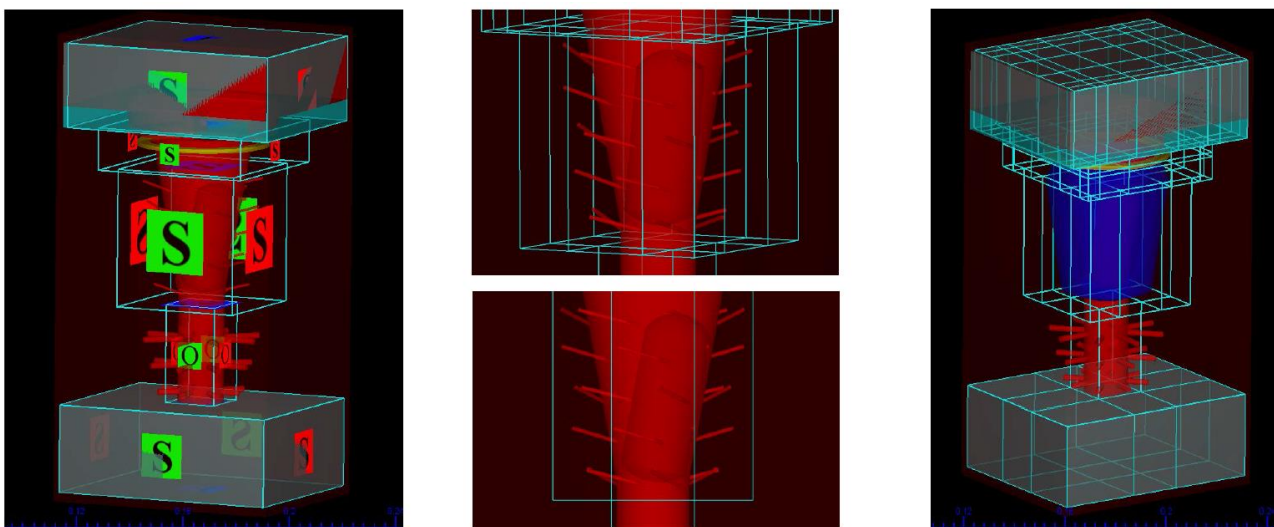


Figure 3.53 Swirl flow transient CFD simulation with gob (FLOW-3D): mesh setting.

The results were encouraging. After few hundredths of seconds, when simulation starting transient can be considered as finished, the gob almost reached the height it had in the test on the machine, with similar small axial oscillations. Fig. 3.54 shows a moment of simulation video. Moreover, fig. 3.55 is taken from a video that compares from a top view the gob rotation during simulation with a real gob rotation in a video made with a high-speed camera at 2000 frame per second (fps). The rotation is almost the same, so gob floating it is validated. The other steps of the swirl pipe handling cycle are still to be simulated.

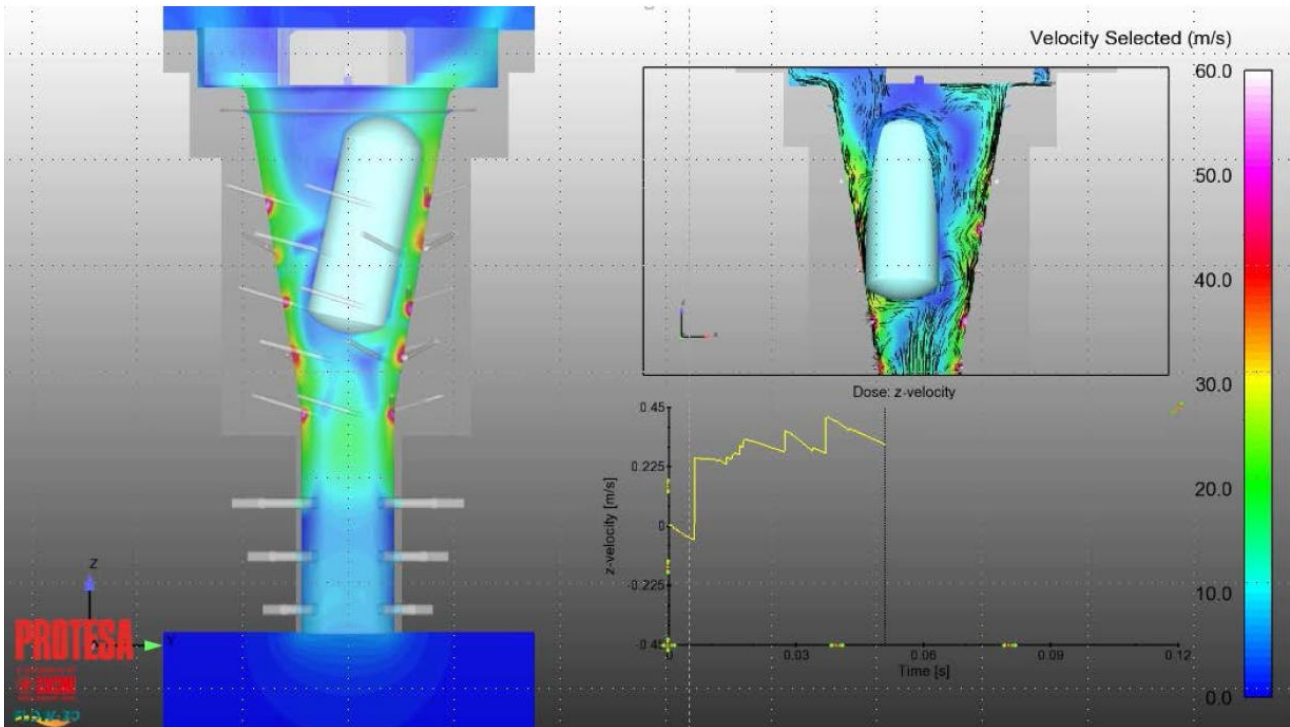


Figure 3.54 Swirl flow transient CFD simulation with gob (FLOW-3D): gob floating position after 0.05 seconds (real time) the simulation started.

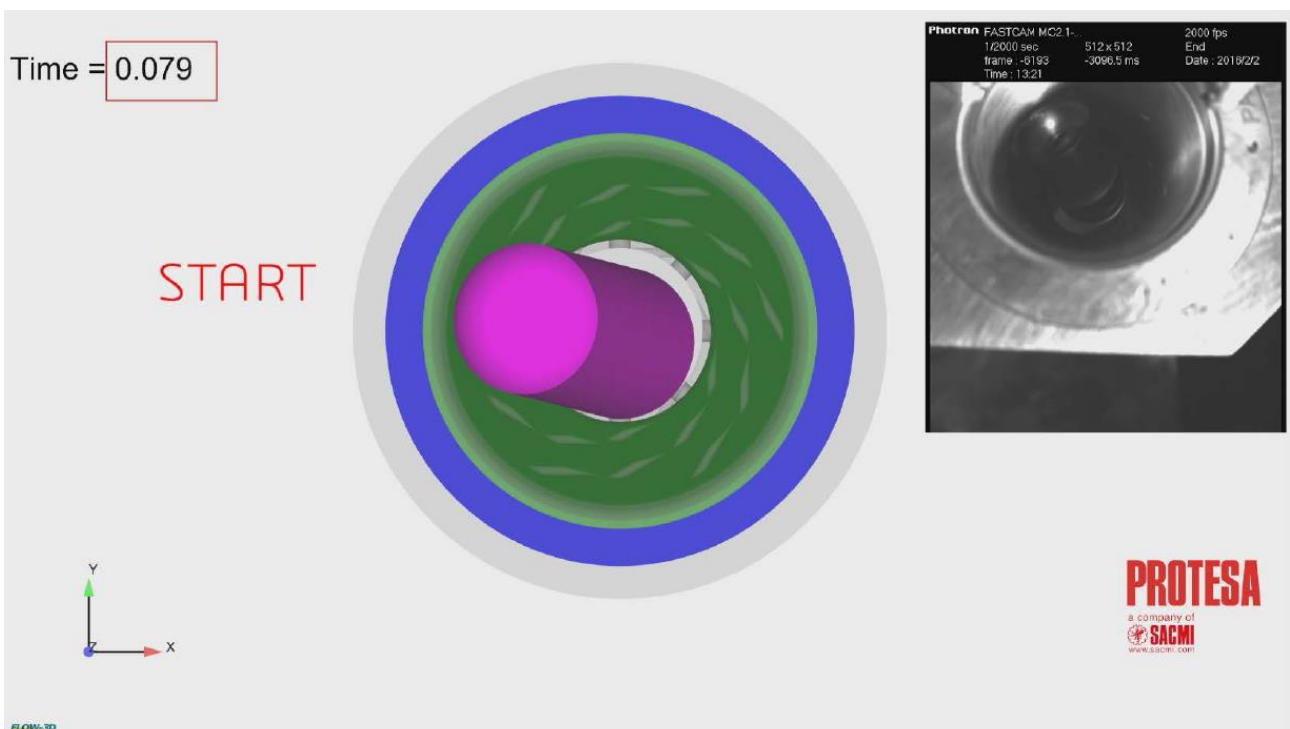


Figure 3.55 Swirl flow transient CFD simulation with gob (FLOW-3D) compared to real process.

### 3.7 NEW TESTING MACHINE

PAM002A has several limitations. Due to the wide angle between the nozzle and the cavity mold, it is not possible to test the gob accelerating swirl pipe with the gob transferring to cavity or it is necessary to keep the gob floating for about two seconds before transferring it to the cavity without a real advantage in doing it.

Fig. 3.56 shows a part of a simplified preform compression machine layout. B corresponds to the nozzle, c to the first coupling point of the gob transferring carrousel (red) with the molding one (yellow), d to the last one.

It is difficult to know a priori which are the optimum angles "bc" or "cd". Is "bc"- "cd" the better trajectory or do other handling tool trajectory shapes, different from the circle one, behave better? What about motion laws? For example, is it advantageous to slow the speed under the nozzle to help gob loading?

In PAM003 (SACMI compression molding prototype machine which follows PAM002A and PAM002B) the position of b can be regulated, but regulation takes almost 1 or 2 weeks of works, so it is hard to consider this regulation useful for several handling tests.

The idea was to design a testing machine (PAMLAB) that allows to test every kind of trajectory and motion law (see example in fig. 3.57) to help answer the questions raised above. To do this, two couples of linear axes can be used:

- M1 - M2 to replicate every kind of handling tool trajectory and motion law;
- M4 - M5 to replicate every kind of molding carrousel trajectory and motion law;

M3 is the motor of the cutting device.

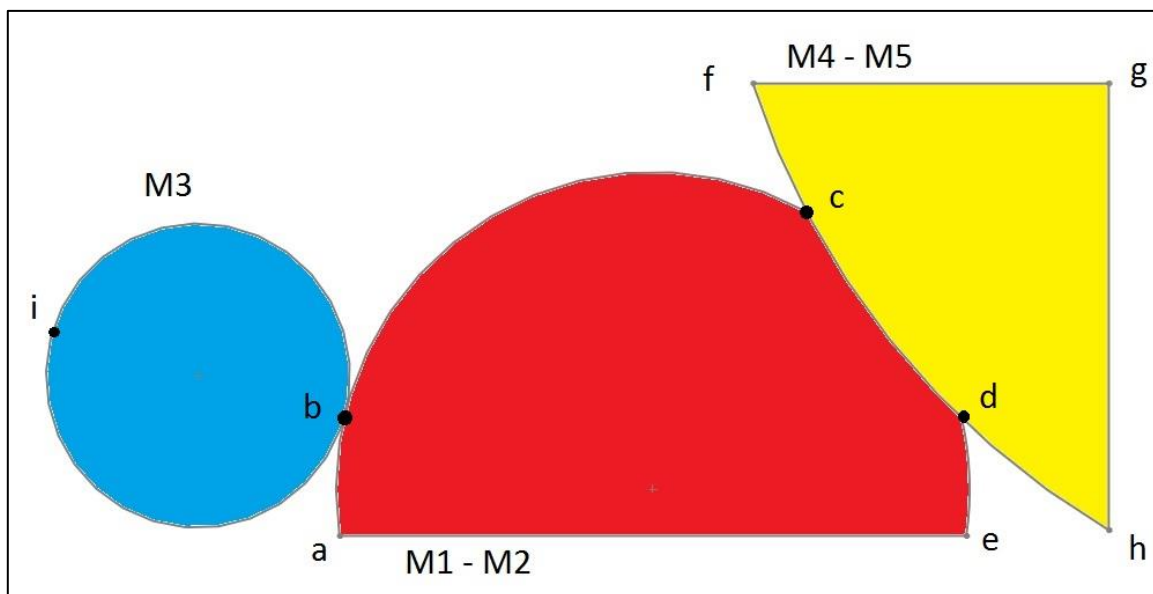


Figure 3.56 Typical layout of gob handling zone of a preform compression molding machine.

In a preform compression molding machine the relative position of the handling tool and cavity is very precise due to mechanical coupling. It is important to keep such precision, not to reject some solutions that in the industrial machine would work but in the testing machine they result in gob transferring failures due to coupling imprecisions. As mentioned in the previous paragraph, a frequent kind of transferring error is gob touching the upper corner of the cavity. To meet this precision

requirements the couple of linear axes were obtained through synchronous linear motors. In this way, the error between handling tool axis and cavity mold axis is lower than 0.1 mm in each working condition (high speed, low speed). Moreover, each synchronous linear motor has a good acceleration (maximum  $65 \text{ m/s}^2$ ) and a maximum speed of 4.6 m/s. Each couple of axes height can be regulated manually. Fig. 3.58 shows the 3D model of the testing machine and its extruder

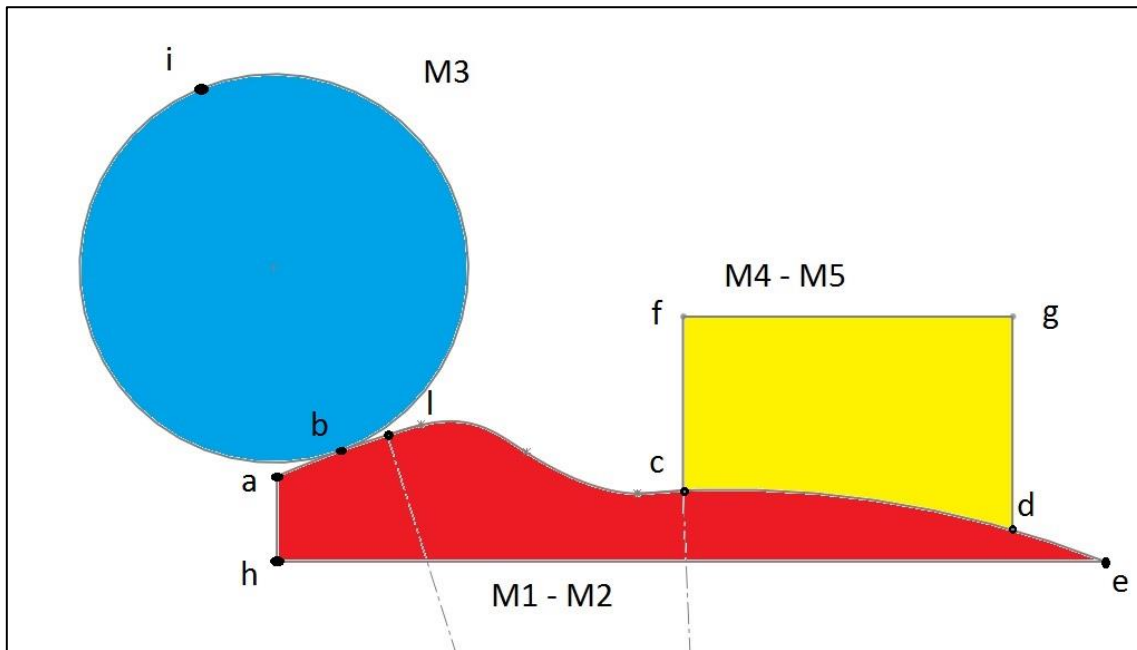


Figure 3.57 Possible gob handling zone layout on a preform compression molding machine.

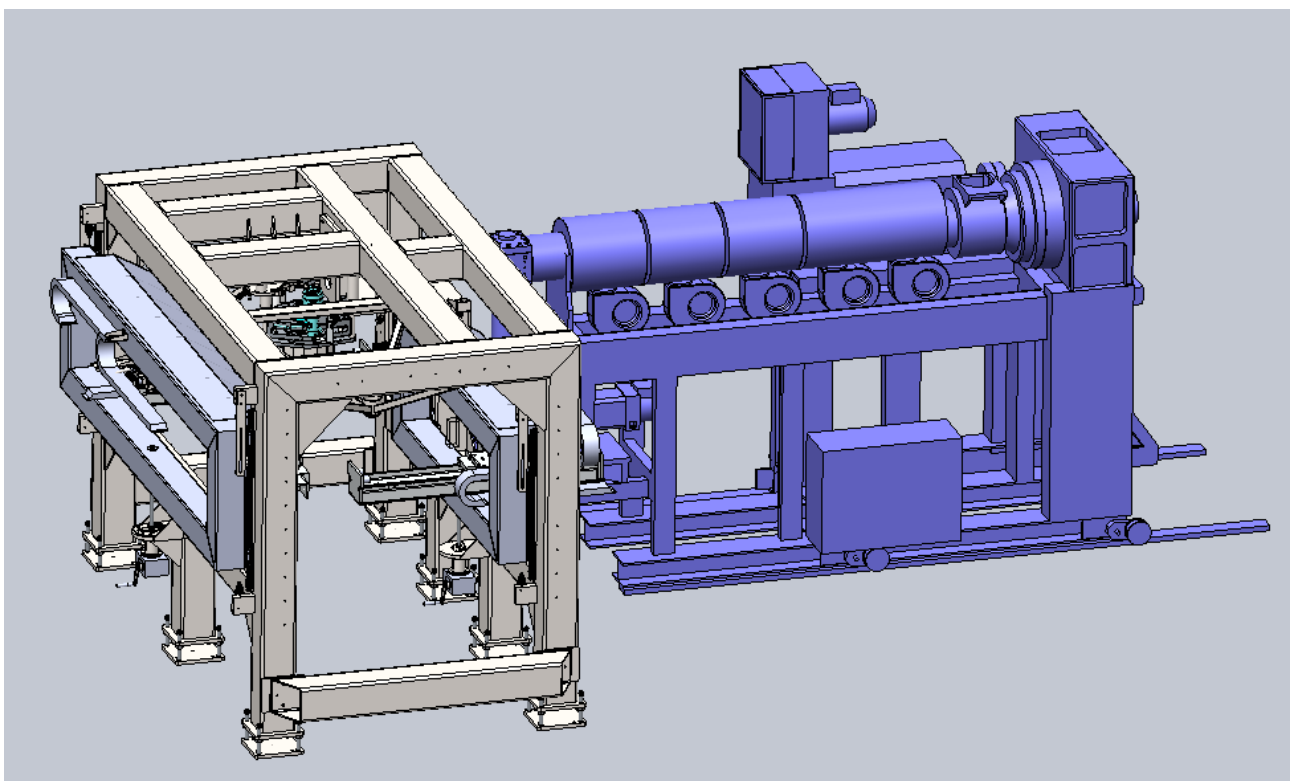


Figure 3.58 PAMLAB and extruder 3D model.

The handling tool and cavity are cooled. Furthermore, an electric device with a maximum power of 1 kW can be installed in the handling tool. In addition to that, there are several cables ready for additional electric sensors (temperature, flow rate, humidity, etc.).

Some precision air valves allow many puffs on the handling tool with different starts, ends, durations, and feed pressures. It is hence possible to complete tests on gob pneumatic handling through a swirl pipe.

The PET extruder is an industrial unit. Its extrusion screw has a diameter of 100 mm and its flow rate goes from 60 to 600 kg/h. As in PAM002A tests, PET dehumidification, PET extrusion process, die swelling conditions and dehumidification in the working area are the same as those on a preform compression molding industrial machine, making the test results more reliable.

Moreover, the testing machine is designed to perform cutting tests with several kinds of blades and a wider range of cutting speeds with respect to the tests already done.

The limit of the testing machine is that there is no feedback on preform or bottle quality. PAMLAB must be considered as a tool to make an initial selection between various solutions. It allows a huge reduction in tests time and costs: what on an industrial machine would require months of work on PAMLAB can be done in few days.

PAMLAB was designed to respect the safety code of SACMI which is usual stricter than what is imposed by the Italian laws. At the same time, PAMLAB was designed to perform endurance tests and hence it can work continuously for all the hours required. The scrap containers, which must be changed every working hour, it can be moved while the machine is working. Proper sensors and protective devices allow the technicians to work in safe conditions.

Fig. 3.59 shows PAMLAB mezzanine with PET dryer and air dryer with their electric panels. Under the mezzanine there is PET extruder and behind its electrical panel. The testing machine was still to be mounted. Fig. 3.60 shows the PAMLAB layout where only what is under the mezzanine is represented.



Figure 3.59 PAMLAB mezzanine and extruder.

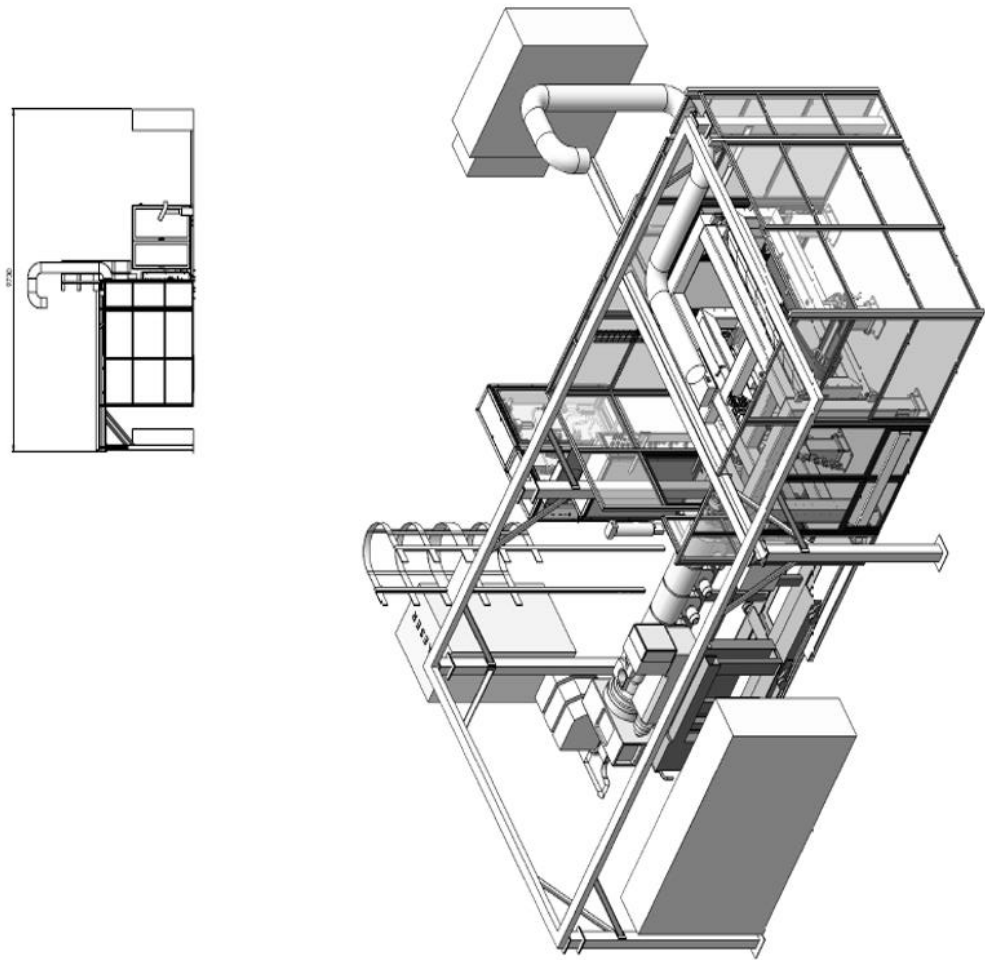
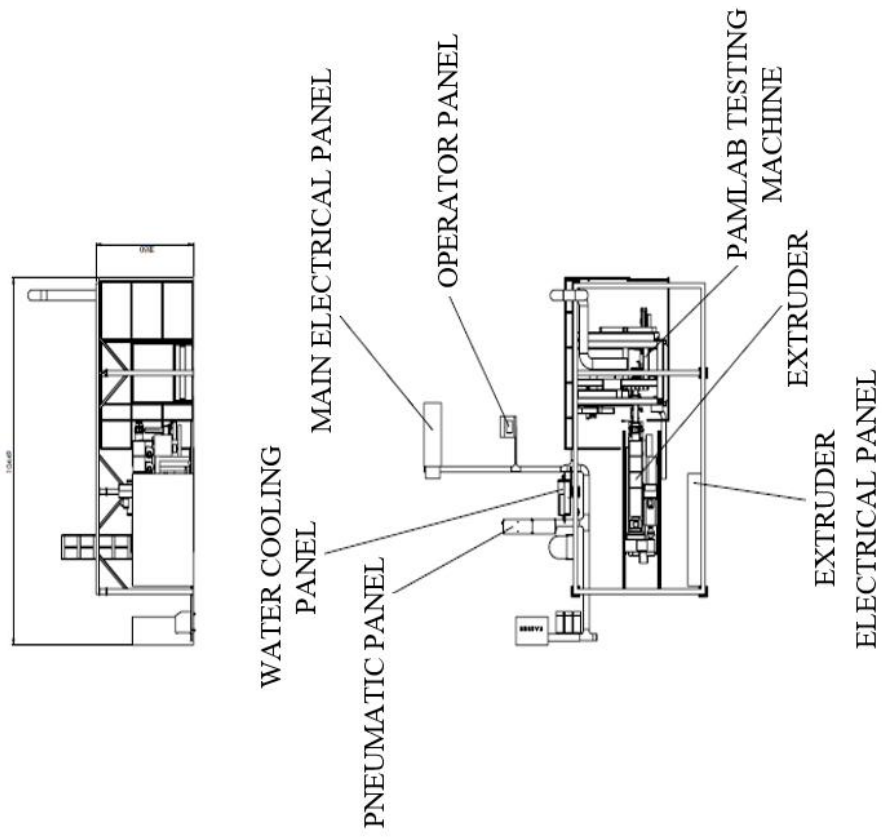


Figure 3.60 PAMLAB layout (only the part under the mezzanine).

At the date of writing, PAMLAB has been assembled and, before connecting it with the extruder, the synchronous couples of axes movement was tested successfully. Functional tests with PET are still to be done. Fig. 3.61 shows designers that control PAMLAB final assembling after positioning it under the mezzanine. Men's figures are shown to give an idea of the testing machine size.



Figure 3.61 Designers control PAMLAB final assembling.

### 3.8 FUTURE DEVELOPMENTS

The first tests on a new PET gob handling technique gave promising results. They have to be completed and a new testing machine is almost ready for this purpose. This machine can only give a pre-validation on an endurance gob handling test without transferring errors. Once handling tool best configurations are found, its technological validation tests must be done by producing preforms and bottles on an industrial machine.

Simulations to find the  $\alpha$  limit value below which the gob floats and above which the gob accelerates are still to be done. A pre-validated transient CFD model without gob is ready for them.

CFD simulation with gob was validated with respect to the floating phase of the handling cycle with  $\alpha$  equal to  $15^\circ$ . The other steps of the handling cycle are still to be simulated. These simulations are very demanding in terms of time and number of cores and RAM required. Anyway, they are fundamental because they could reduce costs and testing time of new preform/bottle swirl handling tool pipe design.

After many cycles, the handling tool must be cleaned since its adhesiveness increases probably due to cyclic oligomers condensation on pipe walls. To reduce the operators' costs, it will be strategic to

find and test cheap and safe ways to clean the handling device periodically and automatically. This must be done in accordance with HACCP (Hazard analysis and critical control points). Some possible technical solutions are not reported here due to SACMI intellectual property policy.

### 3.9 REFERENCES

- [1] G. Cavina, F. Parrinello, Z. Zuffa, "*Apparatus for transferring objects WO 2009/027777*", 2009.
- [2] K. Takeuchi, T. Kurosawa, K. Ichikawa, N. Hirota, *EP 1849573*, 2013.
- [3] Y. Asano, N. Hirota, J. Nagao, K. Watanabe, *EP 1985430*, 2012.
- [4] Y. Asano, N. Hirota, J. Nagao, K. Watanabe, *EP 2404732*, 2017.
- [5] Th. Rieckmann and S. Völker, *Poly(Ethylene Terephthalate) Polymerization – Mechanism Catalysis, Kinetics, Mass Transfer and Reactor Design* ch.2 pp. 29-115 in *Modern Polyesters: Chemistry and Technology of Polyesters and Copolyesters*, J. Scheirs, T.E. Long, Ed., John Wiley & Sons, Ltd, 2003.
- [6] M. Camerani, *PET AND ITS PREFORMS Handbook*, SACMI, 2008, ISBN 88-7586-132-3.
- [7] [https://en.wikipedia.org/wiki/Coand%C4%83\\_effect](https://en.wikipedia.org/wiki/Coand%C4%83_effect), viewed on 12/10/2017. Image by Cruithne9 (Own work) [CC BY-SA 4.0 (<https://creativecommons.org/licenses/by-sa/4.0/>)], via Wikimedia Commons.
- [8] J.N. Israelachvili and D. Tabor, *Proc. Roy. Soc*, 1972, **A 321**, p. 435.
- [9] C.A. Montavon, H. Grotjans, I. S. Hamill, H. W. Phillips and I. P. Jones, AEA Technology Engineering Software, *Mathematical Modelling And Experimental Validation Of Flow In A Cyclone*, BHR Conference on Cyclone Technologies Warwick, 2000.
- [10] Witt, P.J., Mittoni, L.J., Wu, J., Shepherd, I.C., *Validation of a CFD Model for Predicting Gas flow in a Cyclone*, CHEMECA99, Newcastle, Australia, 1999.
- [11] H. J. Bungartz, M. Schäfer Eds., *Fluid-structure Interaction: Modelling, Simulation, Optimization*, Springer-Verlag, 2006.

## Chapter 4

# THE EFFECT OF METAL TEMPERATURE ON MOLTEN PET - METAL ADHESIVENESS FOR SHORT TIME CONTACT

### 4.1 INTRODUCTION

As explained in chapter 3, PET gobs can stick to the metal handling tool wall even after a very short contact time, of the order of 0.001 s. Fig. 4.1 (it is fig. 3.41 reported again below to help the following discussion) shows the effect of the temperature on short contact time adhesiveness. The change of behavior of the molten PET gob adhesiveness beyond a certain temperature is impressive. Moreover, there is a difference between aluminum and stainless steel. Existing literature, cited in chapter 2, seems not to deal with adhesiveness for such a short contact time. This chapter illustrates an innovative test to assess the effect of metal wall temperature on PET adhesiveness for a very short contact time.

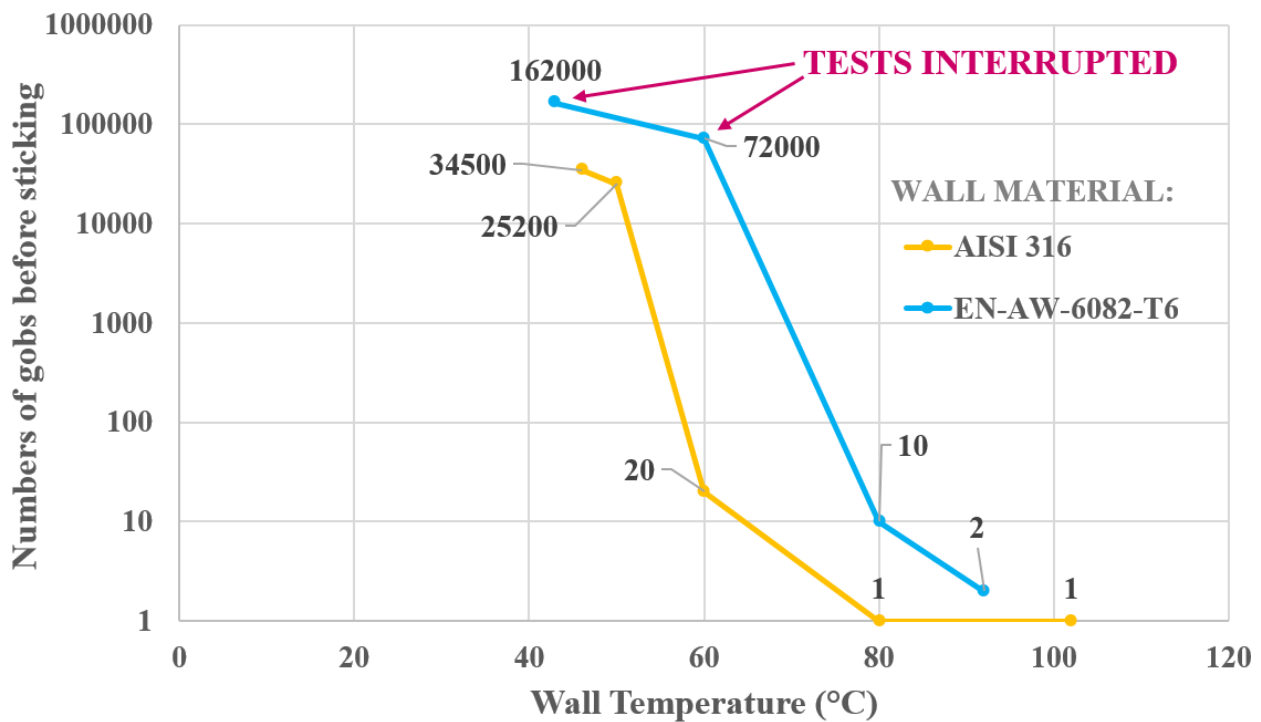


Figure 4.1 High temperature endurance tests results.

### 4.2 TEST DESIGN

#### 4.2.1 Test goals

The aim of swirl pipe endurance tests on an industrial machine prototype (PAM002A) was to find a stable and long-lasting handling tool solution against molten PET gob adhesiveness that increases with gob passages. In chapter 3, it was assumed that the main cause of increased adhesiveness is probably the deposition of PET cyclic oligomers on the metal wall. As wall metal temperature

increases, PET oligomers adhesiveness should decrease since the driving force of oligomers condensation on colder metal wall declines. Nevertheless, this did not happen. On the contrary, with an increase in the metal surface temperature, adhesiveness rose rapidly until the gob stuck at the first contact with a cleaned metal surface.

A new test was designed to investigate this new and unknown phenomenon. The test consists in analyzing PET gob adhesiveness during a single short contact time (about  $10^{-3}$  s) with a cleaned surface of an aluminum alloy (EN AW-6082-T6) and of stainless steel (AISI 316) with similar roughness. Tables 4.1 and 4.2 respectively illustrate the chemical composition and the physical properties of the two materials.

In particular the aims of the test are:

1. To verify that as metal temperature increases, the adhesion between molten PET and the metal plate considerably rises resulting in the gob sticking to the metal;
2. To find the "adhesion threshold temperature" or the range of temperatures starting from which the gob sticks to the metal;
3. To verify that the adhesion threshold temperature or range of temperature is a function of the material by comparing stainless steel AISI 316 and aluminum alloy EN AW-6082-T6 and to give an explanation for it;
4. To verify if below the adhesion threshold temperature, the adhesion decreases as temperature declines, or if it is an on-off mechanism.

Chemical component	EN AW-6082-T6		AISI 316	
	% min	% max	% min	% max
Al		98 (approx.)		
C				0.08
Cr		0.25	16	18
Cu		0.1		0.75
Fe		0.5		70 (approx.)
Mg	0.6	1.2		
Mn	0.4	1		2
Mo			2	3
Ni			10	14
Other each		0.05		
Other total		0.15		
P				0.04
S				0.03
Si	0.7	1.3		1

Table 4.1 Comparison of chemical composition between EN AW-6082-T6 and AISI 316 [1].

	EN AW-6082-T6	AISI 316
Elastic modulus (GPa)	70	186
Thermal conductivity (W/(mK)) at 23 °C	170-220	16.3
Coefficient of thermal expansion (1/(10 <sup>6</sup> K)) at 23 °C	23.4	16-18
Specific heat (J/(kg K))	896	502

Table 4.2 Comparison of physical properties between EN AW-6082-T6 and AISI 316 [1], [2].

## 4.2.2 Testing machine



Figure 4.2 Testing machine (MONOPAM).

The machine used for the test is MONOPAM: a prototype of preform compression molding machine with a single molding cavity, already available in SACMI laboratory. This machine consists of:

- A PIOVAN PET dehumidification plant, model DP620, composed of a dehumidification tower DPM605 and a hopper C10I;
- A single screw PET extruder with a screw diameter of 25 mm, an L/D ratio of 21 and 4 zones with independent thermal heating through electric resistances;
- An oleo-dynamic syringe to accumulate the PET coming from the extruder and to push it quickly so that the same die swelling as that of an industrial machine occurs after the nozzle;
- A rotating blade that separates gobs of desired weight. The cutting speed is not indicated here due to SACMI secrecy policies.

The remaining parts of the machine (handling tool, mold and post cooling systems) were disassembled or deactivated to adapt the machine for the adhesiveness tests as illustrated in fig. 4.3, i.e. to make the gob hit a metal plate. Two possible positions have been found for the metal plate: A and B as shown in fig. 4.3. Moreover, the metal plate (back view in fig.4.4) has 6 degrees of freedom to help find the better gobs trajectory and motion law. Plate thermo-resistance, temperature sensor and PID thermoregulation controller are of the same type as those used for high temperature tests on swirl pipe (see paragraph 3.4.4.3). In particular, it seems important to underline that temperature sensors on metal plates are miniaturized sensing resistors with an accuracy of  $\pm 0.35$  °C at 100 °C (see paragraph 3.4.4.3). They are positioned at 1 mm from the gob contact plane but, unluckily, not

in the position where, after initial test settings (see paragraph 4.4), it was found convenient that the gobs would hit. This position was unknown a priori. The exact temperature in the contact zone was measured with a contact thermocouple, only when the tests were completed (see paragraph 4.5.3) not to alter the surface characteristics. Between the plate and its support there is layer of thermal insulating material to keep the plate temperature homogeneous.

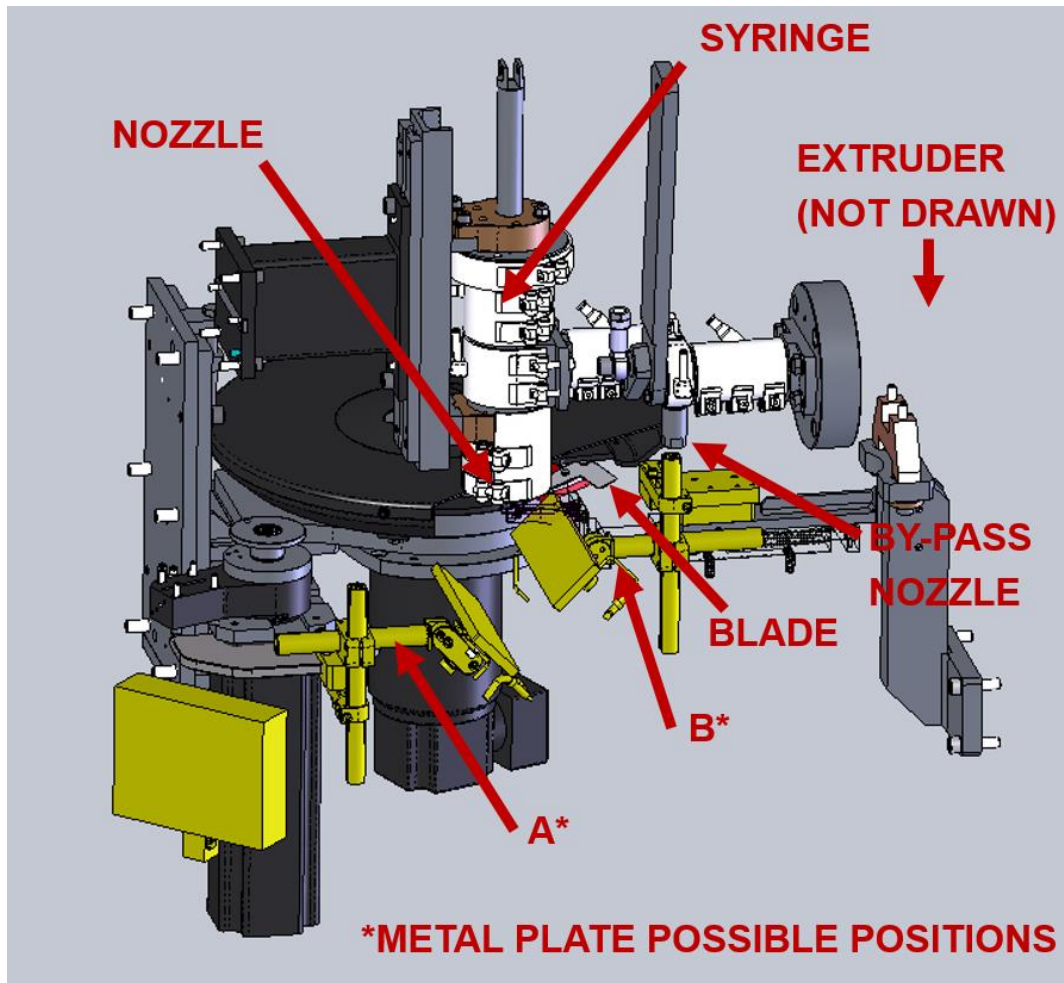


Figure 4.3 Testing machine: details of cutting zone.



Figure 4.4 Metal plate: back view.

### 4.2.3 Test equipment

A list of the equipment used for the test is reported in the following paragraphs.

#### 4.2.3.1 Infrared Camera

The model used is a FLIR T440 (see fig. 4.5). It is a high performance infrared camera with an optical camera on board to simultaneously take both thermal and optical images. This tool helps recognizing the location of the object observed as shown in fig. 4.6 and 4.7. The accuracy of the temperature measurements is calibrated within  $\pm 2\text{ }^{\circ}\text{C}$  or  $\pm 2\%$  of reading. There is also the possibility to perform measurement correction for reflected ambient temperature and emissivity correction.



Figure 4.5 Infrared camera.

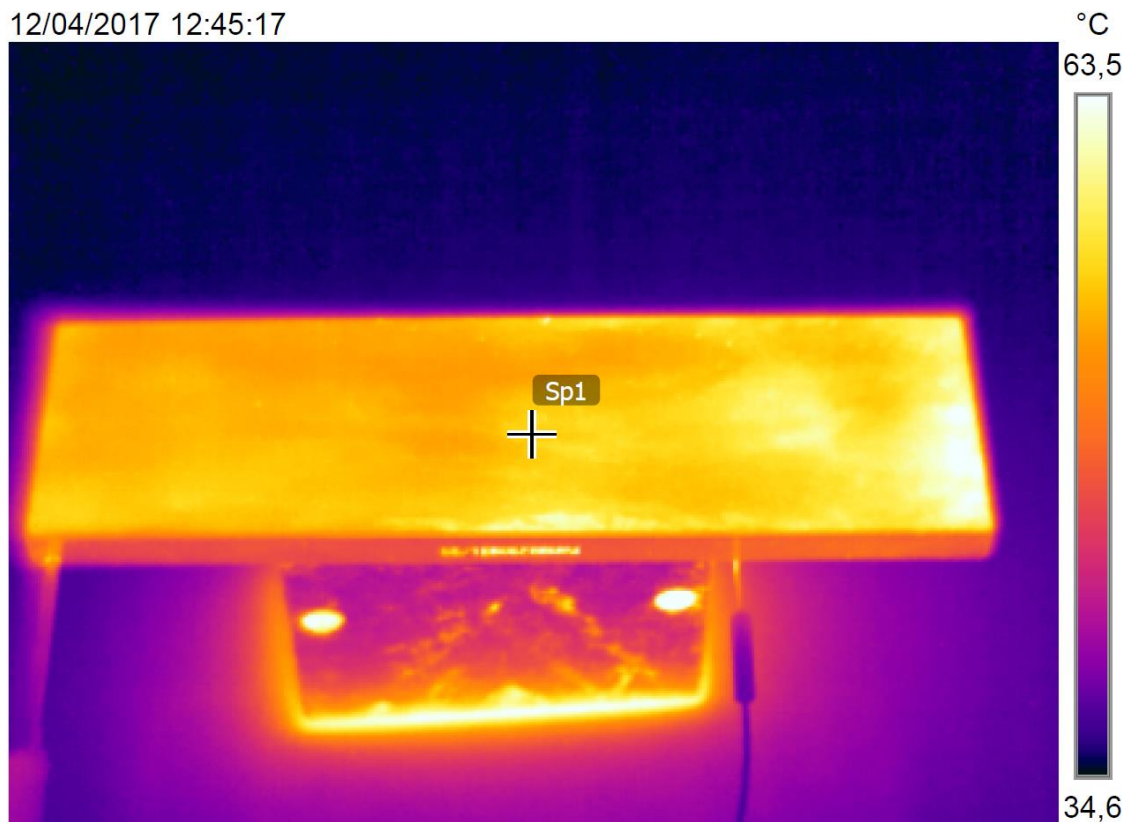


Figure 4.6 Plate image taken with infrared camera. Point Sp1 temperature is equal to  $56.4\text{ }^{\circ}\text{C}$ .

12/04/2017 12:45:17



Figure 4.7 Same image of fig.4.6 taken in the same instant with on board optical camera.

#### 4.2.3.2 High speed video recording camera

The model used is a Photron FASTCAM-ULTIMA APX, whose maximum frame rate is 120000 frames per second (fps). The system is composed by the head with a sensor and lens (fig. 4.9), the control unit, where the video is temporary stored, and a laptop (fig. 4.8) The function of the latter is to watch the video at different playback speeds, select only the frames of interest and save the file. An increase of lamps is required when rising the frame rate.



Figure 4.8 Laptop and control unit of the high speed camera used for tests.

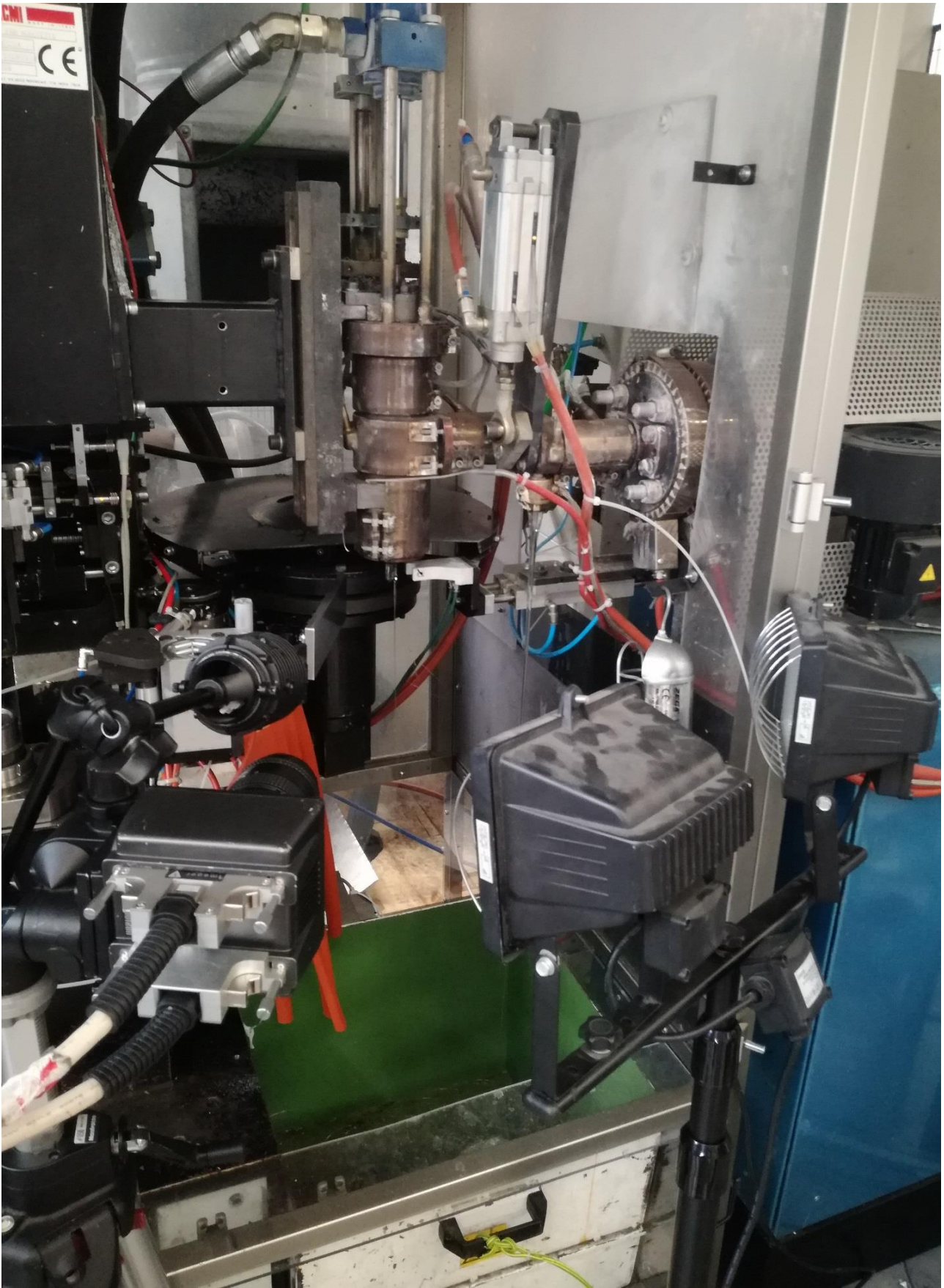


Figure 4.9 Head of the high speed camera with lamps placed before tests started.

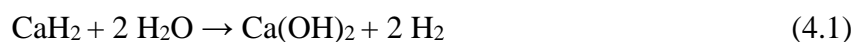
#### 4.2.3.3 PET hygrometer

There are many ways to measure PET moisture content [3]. The water content has a great influence on the quality of the finished product. For this test, the AQUATRAC® system by Brabender Messtechnik was used (fig. 4.10).



Figure 4.10 Pet pellets hygrometer.

The moisture content in PET dried for a compression molding process is lower than 50 ppm. The accuracy of such measurements is in the range  $\pm 10$  ppm. The measuring volume mainly consists of the sample container, which contains the samples (PET pellets just taken out from PET drier) and the reagent (calcium hydride) which is placed in a mesh base inserted above the sample (see fig. 4.11). Once the container is sealed and locked, the vacuum pump decreases the pressure below 10mbar in approximately 30 seconds. The sample container is then heated up to 160 °C. The water desorbed reacts with calcium hydride and generates hydrogen gas according to the following equation:



The gas pressure is proportional to the water content in the sample and is monitored by means of a piezoelectric transducer. AQUATRAC® calculates the ratio of pressure to sample weight. Then it displays the result in terms of H<sub>2</sub>O content, both as a percentage and in parts per million (ppm). Volatiles other than water do not react with the reagent and condense, therefore they do not influence the reading. The partial pressure in the gas system is zero; therefore, the total water content is accurately measured. Furthermore, the test is not affected by the presence of oxygen and no carrier gas is needed. This measurement takes about 40 minutes to be completed.



Figure 4.11 PET hygrometer detail: reagent ( $\text{CaH}_2$ ) placed in a mesh based above the sample container.

The reagent has to be changed every about fifteen measurements. The sample container is filled to the top level and weighted once, since PET pellets density is almost the same. The weight is then typed in the instrument. This results in a time saving between PET pellets extraction from PET drier (fig.4.12) and vacuum creation. It is important that this time is the lowest possible to prevent PET from absorbing water from the atmosphere.



Figure 4.12 PET dryer hopper: by opening a shutter PET pellets are taken out from the lower part of the hopper for humidity content measurements.

#### 4.2.3.4 Thermometer with thermocouples

It is important to monitor the temperature of the PET that exits from the extruder and this could be done with an immersion thermocouple. The chosen one, combined with the available thermometer, has an accuracy of  $\pm 1\text{ }^{\circ}\text{C}$  and a repetitiveness of  $\pm 0.2\text{ }^{\circ}\text{C}$  from  $250\text{ }^{\circ}\text{C}$  to  $300\text{ }^{\circ}\text{C}$ . Moreover, as it will be explained in paragraphs 4.2.4 and 4.5.3 it is important to characterize the plate temperature through a contact thermocouple that, combined with the aforementioned thermometer, has an accuracy of  $\pm 1\text{ }^{\circ}\text{C}$  and a repetitiveness of  $\pm 0.2\text{ }^{\circ}\text{C}$  from  $0$  to  $150\text{ }^{\circ}\text{C}$ . Both the thermocouples and the thermometer are shown in fig. 4.13.



Figure 4.13 Contact and immersion thermocouples with thermometer.

#### 4.2.3.5 Air hygrometer

The air hygrometer used in the test is a RS 1360A (fig.4.14). Its resolution is  $0.1\%$  and  $0.1\text{ }^{\circ}\text{C}$ . Its accuracy on humidity is  $\pm 5\%$  RH (at  $10$  to  $30\%$  RH) and  $\pm 3\%$  RH (at  $30$  to  $95\%$  RH), while on temperature it is  $\pm 0.8\text{ }^{\circ}\text{C}$ . It was set to measure air dew point ( $^{\circ}\text{C}$ ) and air relative humidity (%).



Figure 4.14 Air hygrometer.

The air hygrometer was placed as close as possible to the plate (fig. 4.15).



Figure 4.15 Air hygrometer position during tests.

#### 4.2.4 Plate heating transient time

It is important to see the equilibrium temperature profile on the plate and the time required to reach this equilibrium. Two different data sets are then required. It is possible, with a FEM software, such as Ansys®, to simulate the heating transient (fig.4.16) and the thermal profile at equilibrium (fig.4.17). Figures 4.16 and 4.17 are just indicative.

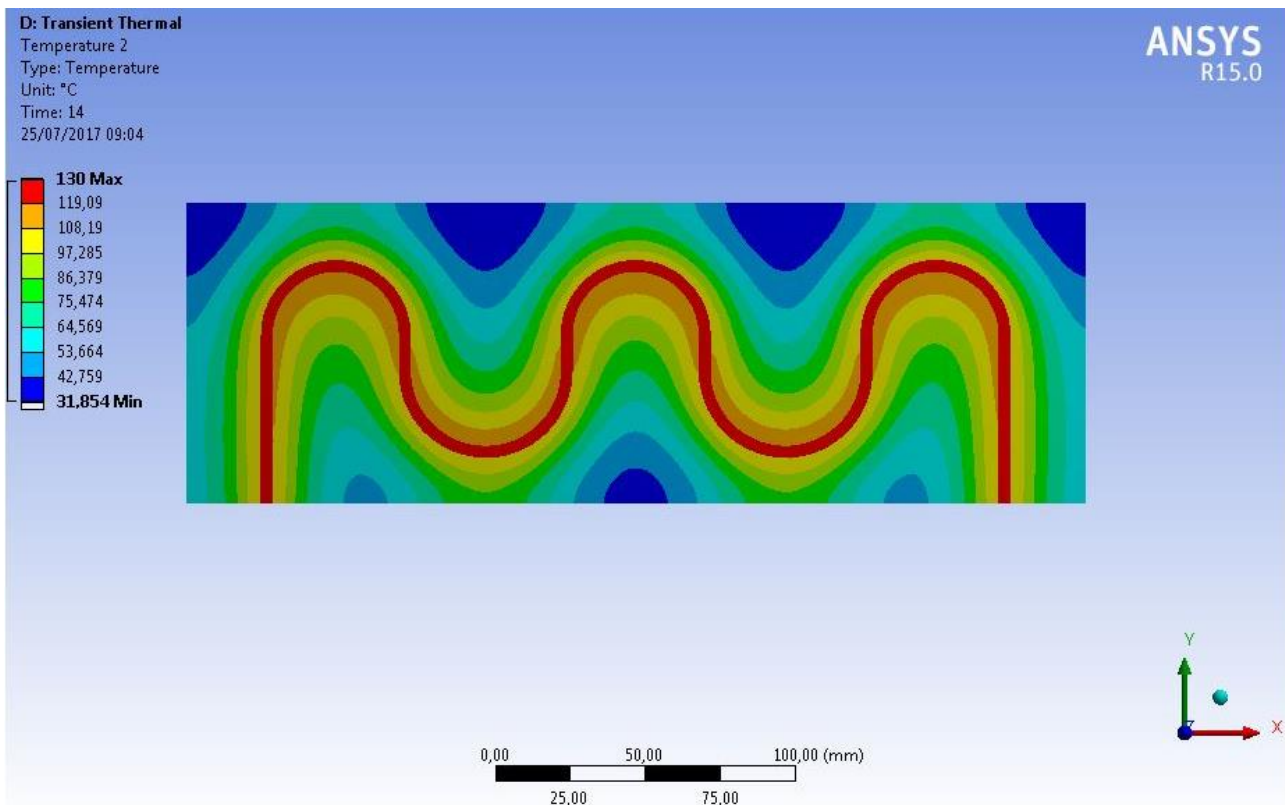


Figure 4.16 Indicative transient thermal simulation on steel plate.

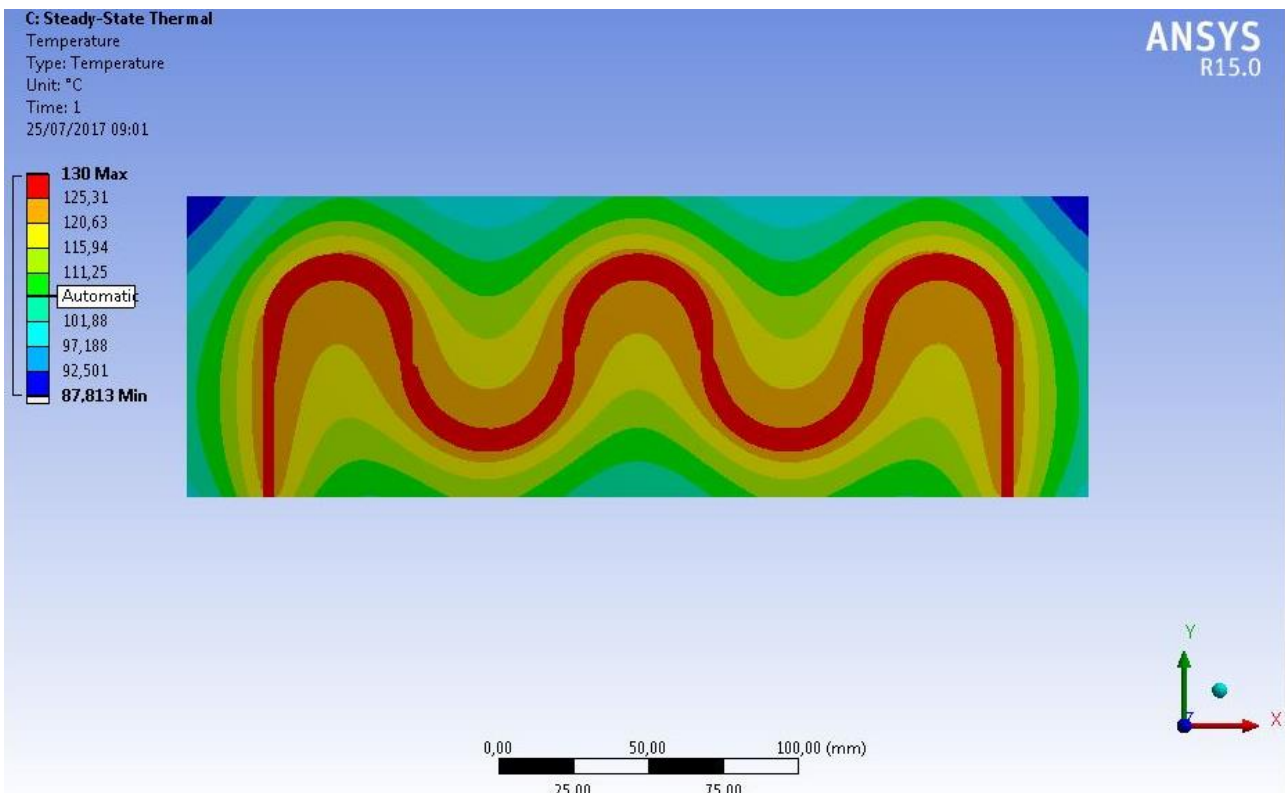


Figure 4.17 Indicative steady state thermal simulation on steel plate.

To have a precise FEM result it is important to know material and heat exchange coefficients with high accuracy. It will take a long time and experimental measurements to validate the simulation. The testing plate has a reflective surface, so, to take a realistic temperature measurement with an infrared camera, the emissivity factor ( $\epsilon$ ) has to be corrected and validated with an experimental measure. The

preferable way, to be sure of the exact temperature of the plates in the gob contact point, is to take measurements with the contact thermocouple. These measurements were done at the end of the tests not to alter the contact surface (see paragraph 4.5.3). In this way, the first data required at the beginning of the paragraph was obtained. About the second one, i.e. the time required to reach the equilibrium, it can easily be measured with an infrared camera since the temperature absolute values are not important. Taking plate pictures with the infrared camera when the plate was assembled on the machine was quite difficult, because of tight space, light reflections and heat coming from the other components (extruder, nozzle) (see fig.4.18) that could false the measurement.

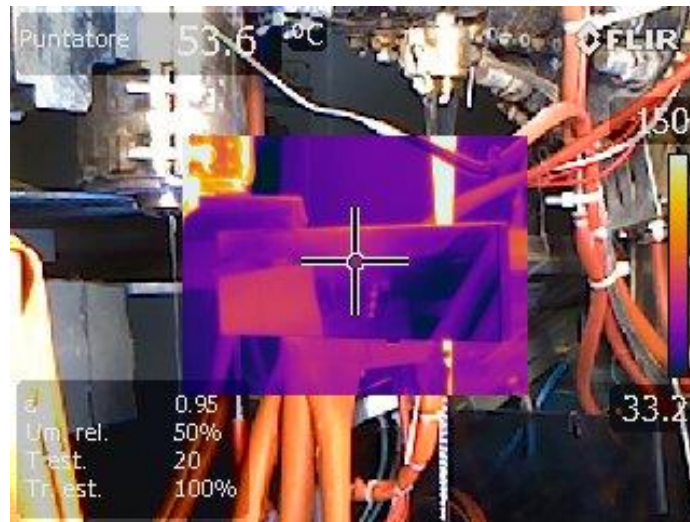


Figure 4.18 Composed image (infrared and visible spectra) of plate assembled on the machine.

The metal plate was hence put on a desk. In figg.4.19, 4.20, 4.21, 4.22 there is an example of the test done on steel without thermal insulation in order to emphasize the behavior.

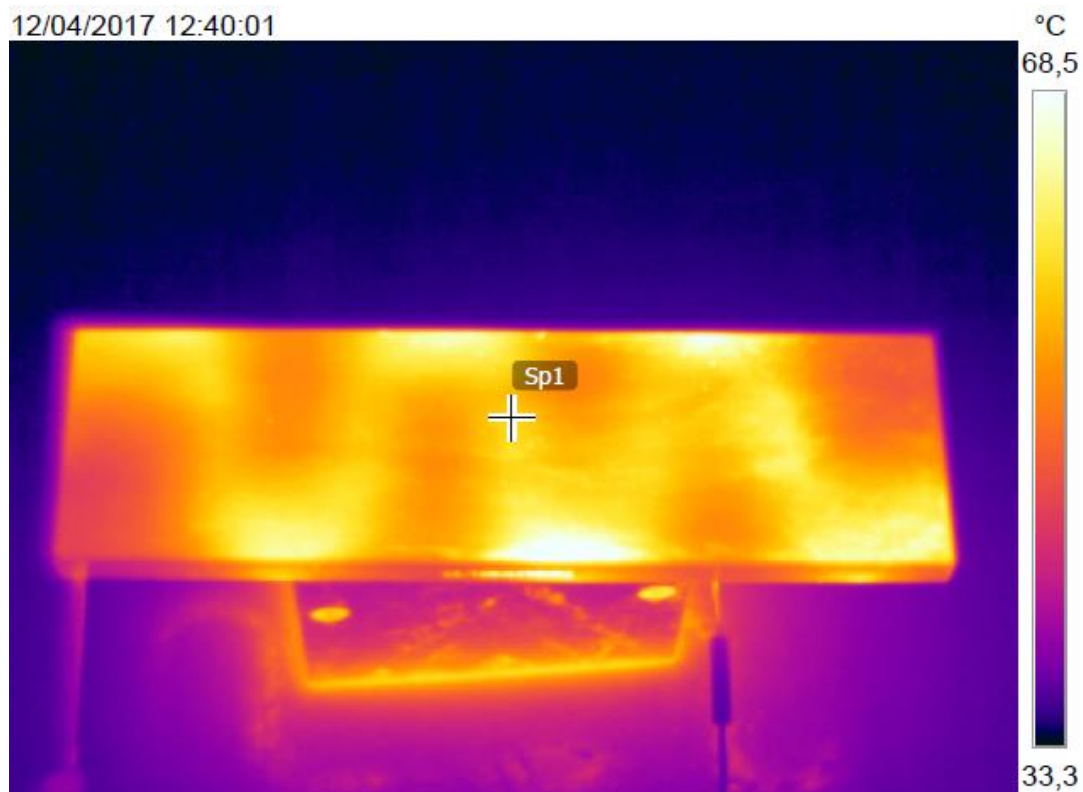


Figure 4.19 Plate infrared picture at 12:40:01. Point Sp1 temperature is equal to 59 °C.

Tests on aluminum and steel plates with insulation and different temperature steps were done. It was found that, when the required temperature measured by the PID thermocouple is reached, it takes 5 minutes to achieve the plate equilibrium and start the tests.

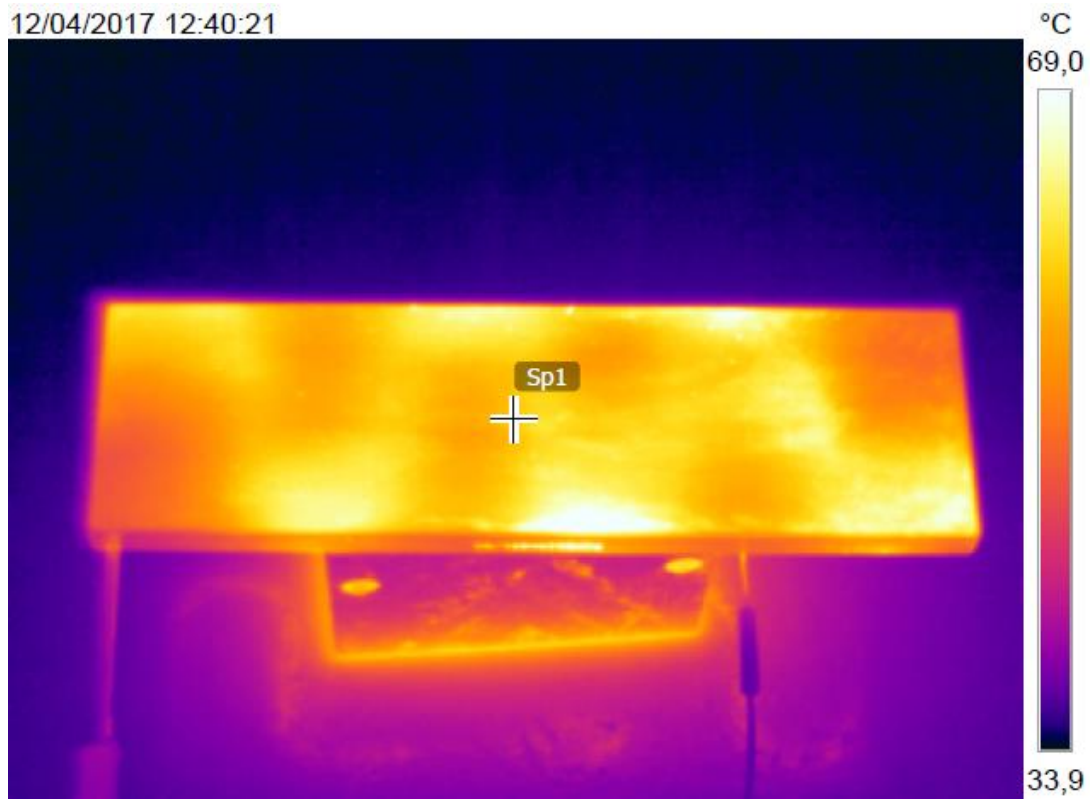


Figure 4.20 Plate infrared picture at 12:40:21. Point Sp1 temperature is equal to 59.7 °C.

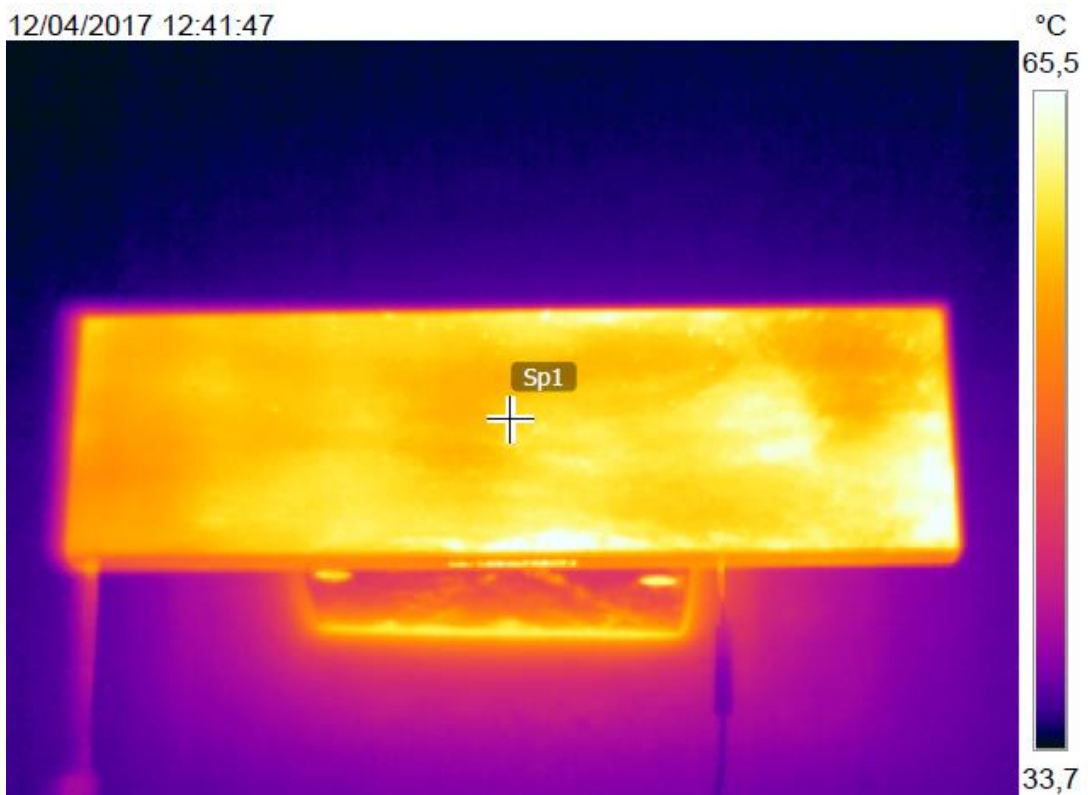


Figure 4.21 Plate infrared picture at 12:41:47. Point Sp1 temperature is equal to 58.8 °C.



Figure 4.22 Plate infrared picture at 12:45:09. Point Sp1 temperature is equal to 56.1 °C.

#### 4.2.5 Polymer properties and dehumidification parameters

**PPK™ FR** resin is a food grade PET copolymer resin based on terephthalic acid. Its high clarity and sparkle make it well suited for the production of bottles and other containers by conventional single- and two-stage processing machines. It is a high molecular weight grade for general use in manufacturing containers. Its intrinsic viscosity (I.V.) is  $0.80 \pm 0.02$  (dl/g) according to ASTM D4603:03. Moreover, its melting point is 249 °C and the acetaldehyde (AA) content declared by the producer is lower than 1 ppm.

The PET dehumidification procedure took place in the Piovan drier at 160 °C for four hours before the beginning of the tests in the morning. PET amount in the drier was enough for all day tests.

#### 4.2.6 Test methodology

The plate was accurately cleaned before starting each test. The aim was to eliminate tracks of previous contact. The cleaning methodology was the same adopted for endurance swirl pipe tests (see paragraph 3.4.4): a commercial multi-purpose cleaner spray (its chemical composition is described in table 3.1) and a clean soft cloth (not to alter the plate surface). After the plate temperature sensor attained the required temperature, it took five minutes to allow all the plate surface to reach the equilibrium temperature, according to the test done in paragraph 4.2.4. Table 4.3 is the template for the data collected during tests. For each single test, date (expressed in the form "day/month/year" and not "month/date/year" as a precaution to avoid mistakes since the technicians that helped conduct the tests were Italian), hour, plate temperature were registered. Gob contact behavior was recorded through a color in the cell below the question "Did gob bounce?". The color was green when gob bounced, while red when gob stuck. Moreover, also the following parameters were collected:

- Blade cutting speed (it was just a check, because this parameter should be set at the beginning of the test and kept constant);

- Gob weight when the gob stuck (except for a few cases);
- Minimum and maximum extrusion screw engine electrical absorption (kW/100) (the unit of measurement is divided by 100 as it is in machine software to avoid technicians' mistakes);
- Extruder inlet (named zone 1) temperature (°C);
- Air dew point (°C);
- Air relative humidity (%).

The third and fourth parameters were registered because, according to SACMI technicians' experience, they could help monitor macro differences on PET dehumidification conditions. In particular, extruder inlet temperature helps the interpretation of extrusion screw electrical absorption. If this temperature decreases, frictions rise and this results in higher engine absorption, which is not due to difference moisture content in PET pellets. On the other hand, an important decrease in the engine absorption associated with no variation in the extruder inlet temperature could mean a degradation of the polymer. This could be a useful piece of information since PET pellets humidity measurements through Aquatrac are discontinuous, which means that it is not possible to detect short period variations. Melt PET temperature and PET humidity were measured every five gobs due to the time required for the measurements. For MONOPAM architecture, the measure of melt PET temperature can be taken only at by-pass nozzle exit (fig. 4.23) where there is a continuous flow. The continuous flow gives time to the thermocouple hot joint to reach the equilibrium with flow temperature, and to the technician to find the center of the flow where the temperature is usually higher.

Furthermore, for each test, a video at 2000 fps was recorded. The video includes gob cutting and bouncing till the gob exits from the video area or a few frames after the gob sticks.

The tests were planned day by day having the test goals in mind (see paragraph 4.2.1) and considering that there was a limited number of tests available. The leading idea was that it was better to have few information with a good level of confidence than a large set of data (for example on many temperatures) but difficult to interpret. For example, after the first three days of tests, it became clear that there was a range of temperature at which the gob could, apparently randomly, stick or bounce. Hence the aim of each day was to find the lowest temperature at which all gobs stuck and the highest temperature at which all gobs bounced. This meant repeating tests at the same plate temperature lots of times on different days and at different hours of the day. The goal was to increase the number of samples and have a confirmation that what had previously seen was not at random or related to the concomitance of other parameter values. The minimum temperature interval between the tests was set equal to 5 °C as a compromise between the time available and the PID regulation precision. Sometimes, due to a lack of time, some temperatures were not investigated and the minimum temperature interval between the tests was 10 °C. Apart from a few exceptions, each day, for each temperature selected, at least five tests were performed to have a minimum sample for statistic considerations.

Test number	Test date	Test hour	Plate temperature	Did gob bounce?	Blade cutting speed	Gob weight	PET pellets humidity	Min and Max electrical absorption extrusion screw		Extruder inlet (zone 1)	Melt temperature	Air dew point	Air relative humidity
			(°C)		(m/s)	(g)	(ppm)	(kW)/100	(kW)/100	(°C)	(°C)	(°C)	(%)
<i>(insert PLATE MATERIAL here)</i>													

Table 4.3 Template for data collected during tests.

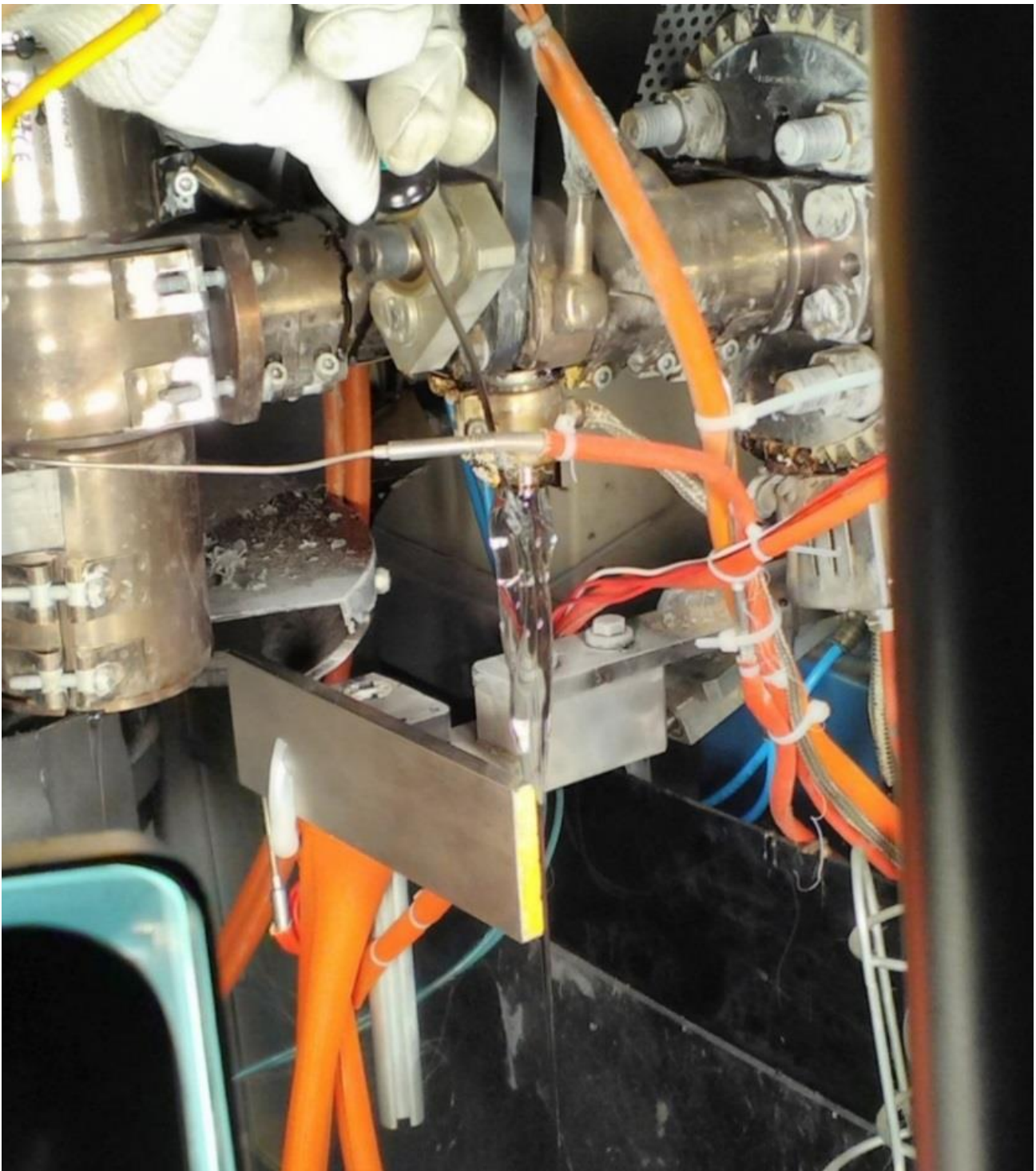


Figure 4.23 Melt temperature measurement.

## 4.3 METAL SURFACES CHARACTERIZATION

### 4.3.1 Roughness

Handling tool endurance tests showed an important contribution of surface roughness, as explained in paragraph 3.4.4.2. Literature on mold reducing adhesion attests that roughness is an important parameter even on a single adhesion contact test, where the contact lasts some hours [4], see paragraph 2.9. The aim of the present test is not to find the best roughness, but to have almost the same roughness

on the two metal plates. Anyway, to do the test in conditions closer to the industrial ones, an industrial rough surface is preferred to a polished one. Since the elastic modulus of the two materials is different, materials react differently to plastic deformations. To lose memory of the milling phase (made with same cutting parameters) the two plates are polished. The surfaces were then sandblasted and polished again to round the peaks. The process was optimized to have almost the same level of roughness as shown in figg. 4.24 - 4.25 that have the same scale. The scale value is not reported due to SACMI intellectual property policy.

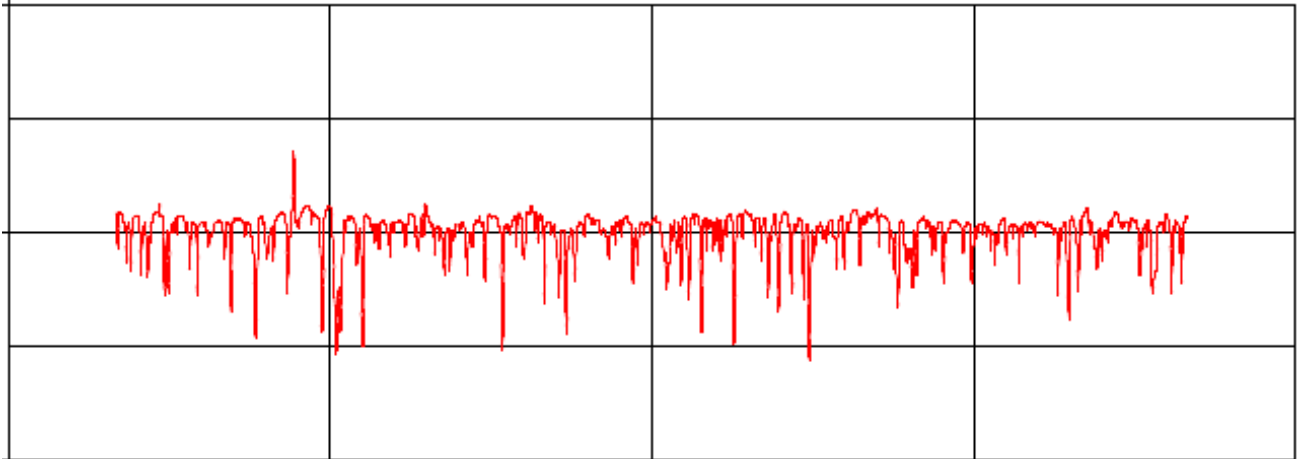


Figure 4.24 2D roughness measurement of EN AW-6082 T6 plate. The scale value is not reported due to SACMI intellectual property policy.

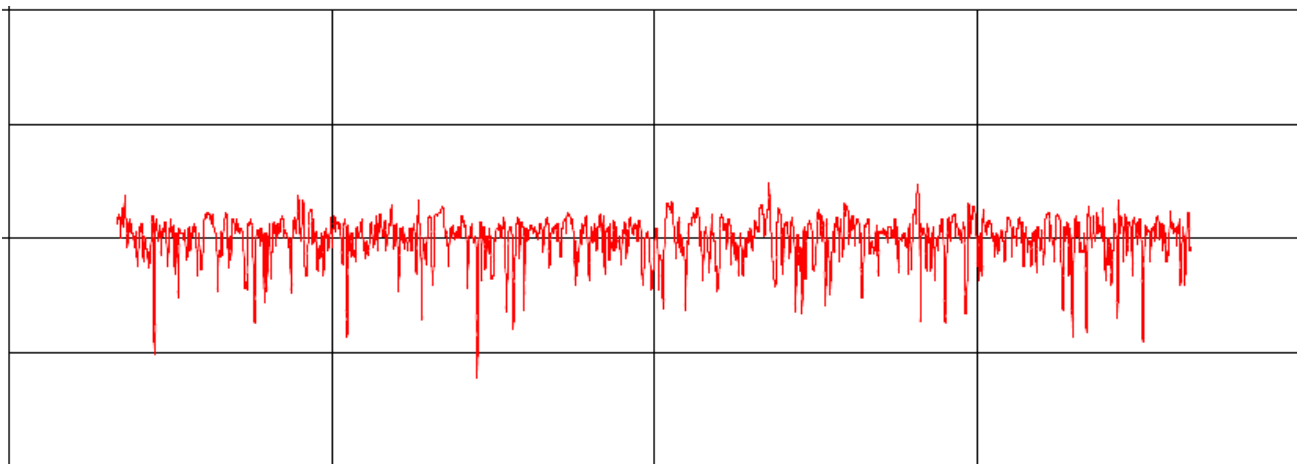


Figure 4.25 2D roughness measurement of AISI 316 plate. The scale value is not reported due to SACMI intellectual property policy.

Roughness and morphology controls were also done with a HOMMEL-ETAMIC nanoscan 855 (see fig. 4.26). Measurements of surface morphology were also done by Shalnov at al. [4] with the aid of an Atomic Force Microscope (AFM) in their research on surface modification to reduce the plastic sticking in the forming process. Nanoscan 855 uses an innovative and technologically advanced opto-mechanical measuring system. Tactile workpiece scanning is transmitted to an optical scale by a high-precision mechanical pick-up which is then interpreted by a laser interferometer. It has a high precision with a resolution of 0.6 nm. Figg, 4.27 and 4.28 show the 3D surface morphologies of the two plates with the same scale. The latter is not indicated due to SACMI intellectual property policy. Nanoscan measurements confirmed that roughness and morphology of the plate in EN AW-6082-T6 and AISI 316 are similar.

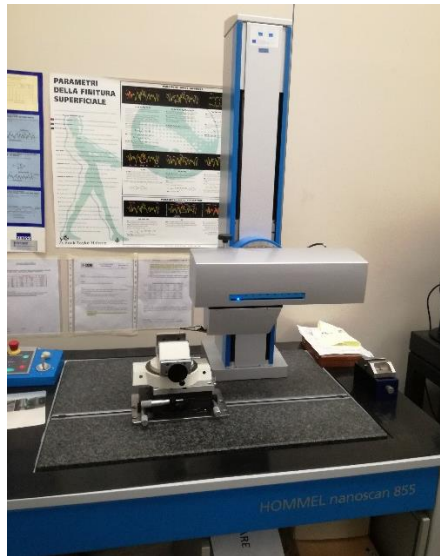


Figure 4.26 HOMMEL-ETAMIC nanoscan 855.

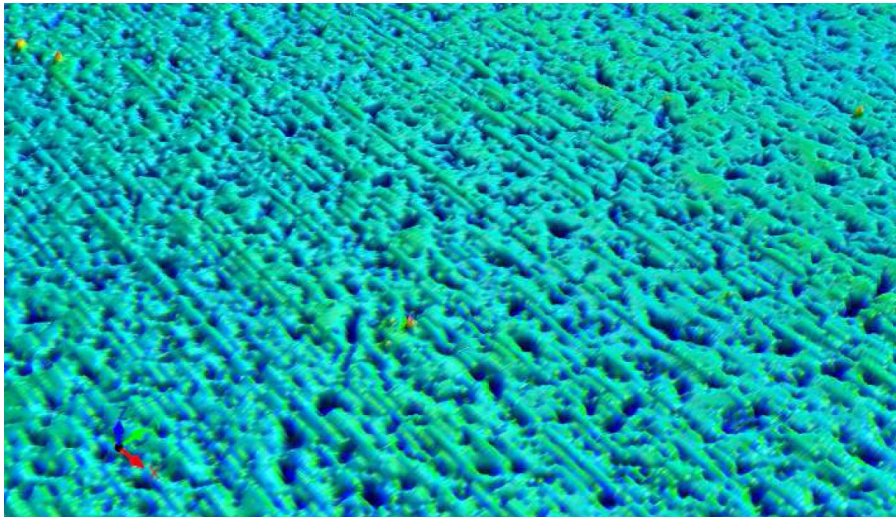


Figure 4.27 3D roughness measurement of EN AW-6082-T6 plate. The scale not indicated due to SACMI intellectual property policy.

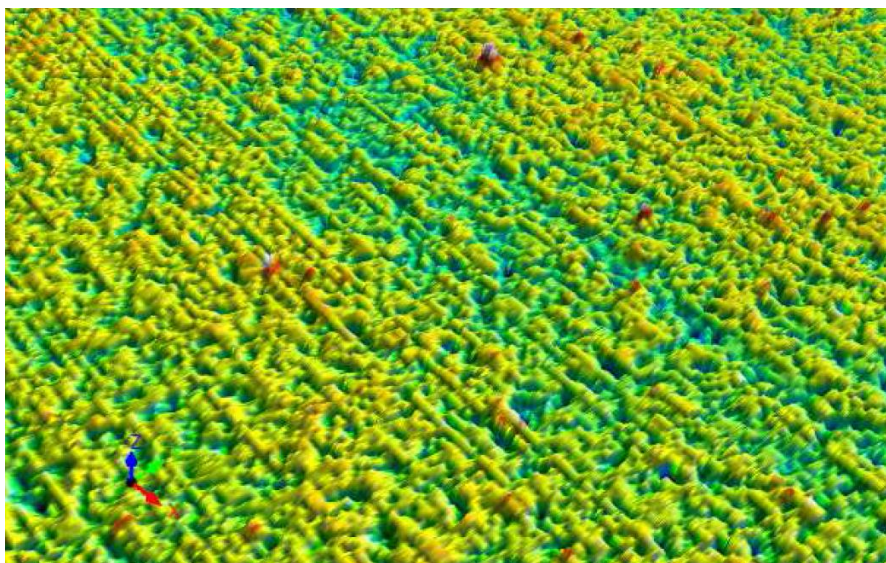


Figure 4.28 3D roughness measurement of AISI 316 plate. The scale not indicated due to SACMI intellectual property policy (same scale as fig. 4.27).

### 4.3.2 Contact angle tests

The surface free energy (SFE) can be considered as a way to assess the chemical attitude of the surface to create polar or disperse bonds as it was illustrated in paragraph 2.4. A study of short-time contact adhesiveness between different materials could not neglect an investigation on materials surface free energies. As described in paragraph 2.4, SFE is normally measured indirectly with the help of sessile drop contact angles with at least two liquids with known disperse and polar parts of the surface tension, wherein at least one of the liquids must have a polar part higher than 0.

#### 4.3.2.1 Instrument

The instrument used for the contact angle tests is a KRUSS DSA30S, which has a measurement range of contact angle from  $0^\circ$  to  $180^\circ$  and a software-based resolution of  $0.01^\circ$ . The accuracy is of  $0.3^\circ$  and it is instrument-based. The instrument can perform sessile drop and captive bubble tests of several types: advancing, receding, static, dynamic and tilting. It has several fitting methods, i.e. the mathematical function used to describe the curvature of the drop shape. The instrument has already implemented the Owens-Wendt-Rabel-Kaelble (OWRK) method in its software to get surface free energy from contact angle measurements [5, 6, 7, 8] and the surface tension values (polar and dispersion components) of many liquids.

#### 4.3.2.2 Plates samples

The samples were two small plates (see drawing in fig. 4.29), one of AISI 316 (PAM0029A059) and one of EN AW-6082-T6 (PAM0029A061). In each small plate, one face was polished (side named 1B), while the other one (side named 1A) was finished in the same way of the adhesiveness test metal plates. The resulting roughness was checked with both the 2D profilometer and the nanoscan. Investigation of roughness influence on wettability performed by Kubiak et al. [9] pointed out the importance of topographical parameters in 2D and 3D morphology analysis. Both surfaces resulted as very similar to adhesiveness test plates. It was decided to test both the surfaces of each plate for future analyses of roughness influence on contact angle. There are several theories about it, e.g. Wenzel's one [10] or the one of Cassie and Baxter [11].

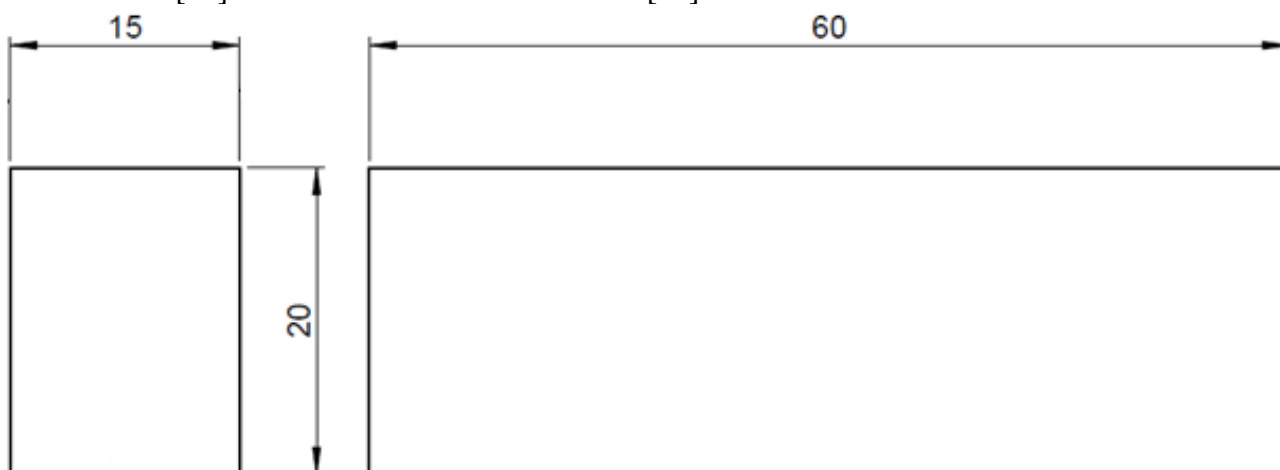


Figure 4.29 Plate drawing for contact angle sessile drop test. Dimensions are expressed in mm.

#### 4.3.2.3 Liquid tested

As mentioned at the beginning of paragraph 4.3.2 and, more in detail, in paragraph 2.4, two liquids are required. According to literature, distilled water [15, 4] was chosen as polar liquid, in particular bidistilled one. The supplier datasheet illustrates that such a water meets specifications for water type 2 according to ISO:3696:1987 "Water reagent for use in laboratory analysis". As other liquid, two

possible ones were taken into consideration: diiodomethane ( $\text{CH}_2\text{I}_2$ ) with a purity  $\geq 98.5\%$  and hexadecane. Table 4.4 illustrates the surface tension and molecular weight values of liquids used in the contact angle tests.

Compound	Molecular Formula	CAS Number	Molecular weight [12]	Surface Tension at 20 °C ( $\text{mJ/m}^2$ )		
				Total	Dispersion	Polar
Diiodomethane	$\text{CH}_2\text{I}_2$	75-11-6	267.84	50.8 [13]	48.5 [13]	2.3 [13]
Hexadecane	$\text{C}_{16}\text{H}_{34}$	544-76-3	226.44	27.5 [14]	27.5 [14]	0 [14]
Water	$\text{H}_2\text{O}$	7732-18-5	18.02	72.8 [14]	21.8 [14]	51 [14]

Table 4.4 Surface tension and molecular weight values of liquids used in the tests.

#### 4.3.2.4 Test conditions

The tests were done with a static sessile drop technique, according to literature [15]. The used fitting method is the "Ellipse (Tangent-1)" recommended in a range from 10 °C to 120 °C. The syringes used are model SY20 in borosilicate glass produced by Microsyringe. The needle is made of steel apart from some hexadecane tests, where a teflon needle was also used but without success. The liquid adheres to the needle walls and it was very difficult to form a drop. Moreover, the hexadecane drop, initially tested on rough aluminum alloy surface, completely wetted the surface at such a level that the instrument, even changing the fitting method, was not able to fit any contact angle. For these reasons, hexadecane was abandoned in favor of diiodomethane. Fig. 4.30 shows the syringe during the automatic bidistilled water filling phase.

Tests were carried out in a laboratory with a room temperature of about 24 °C and a relative humidity which ranged from 37 to 52 %. This is in accordance with literature, where Kubiak et al. [15] did their tests at a temperature of about 22 °C, and at quasi-constant relative humidity, of about 45 %, while Shalnov et al. [4] did them at about 20 °C and about 40 % of relative humidity. Table 4.5 illustrates the temperature and the relative humidity conditions of the contact angle tests.

		EN AW-6082-T6 (PAM0029A061)		AISI 316 (PAM0029A059)	
		1B (Polished)	1A (Rough)	1B (Polished)	1A (Rough)
Air relative humidity (%)	Bidistilled water	51.3	49.3	50.9	51.4
	Diiodomethane	39	38.7	38.3	37.4
Temperature (°C)	Bidistilled water	24.4	23.8	24.5	24.4
	Diiodomethane	24.6	24.6	24.5	24

Table 4.5 Temperature and relative humidity conditions of contact angle tests.

According to literature [15], before starting each test, the plate surfaces were accurately cleaned with ethanol and a clean cloth. Kubiak et al. [15] also used ultrasounds to perform this task, but ultrasounds were not available in our laboratory.

The chosen water drop volume was equal to 4  $\mu\text{L}$ , within the range where, according to literature [15], the contact angle did not change with the variation of the volume ( $4 \mu\text{L} \pm 0.5$ ). The chosen volume rate of drop creation was equal to 0.75  $\mu\text{L/s}$ . With diiodomethane it is not possible to deposit drops larger than 1.1  $\mu\text{L}$ . This could be due to its lower surface tension compared to water. 1  $\mu\text{L}$  is

the biggest drop volume allowed by diiodomethane with a good volume repetitiveness. Its chosen drop volume creation rate was equal to  $0.3 \mu\text{L/s}$ .

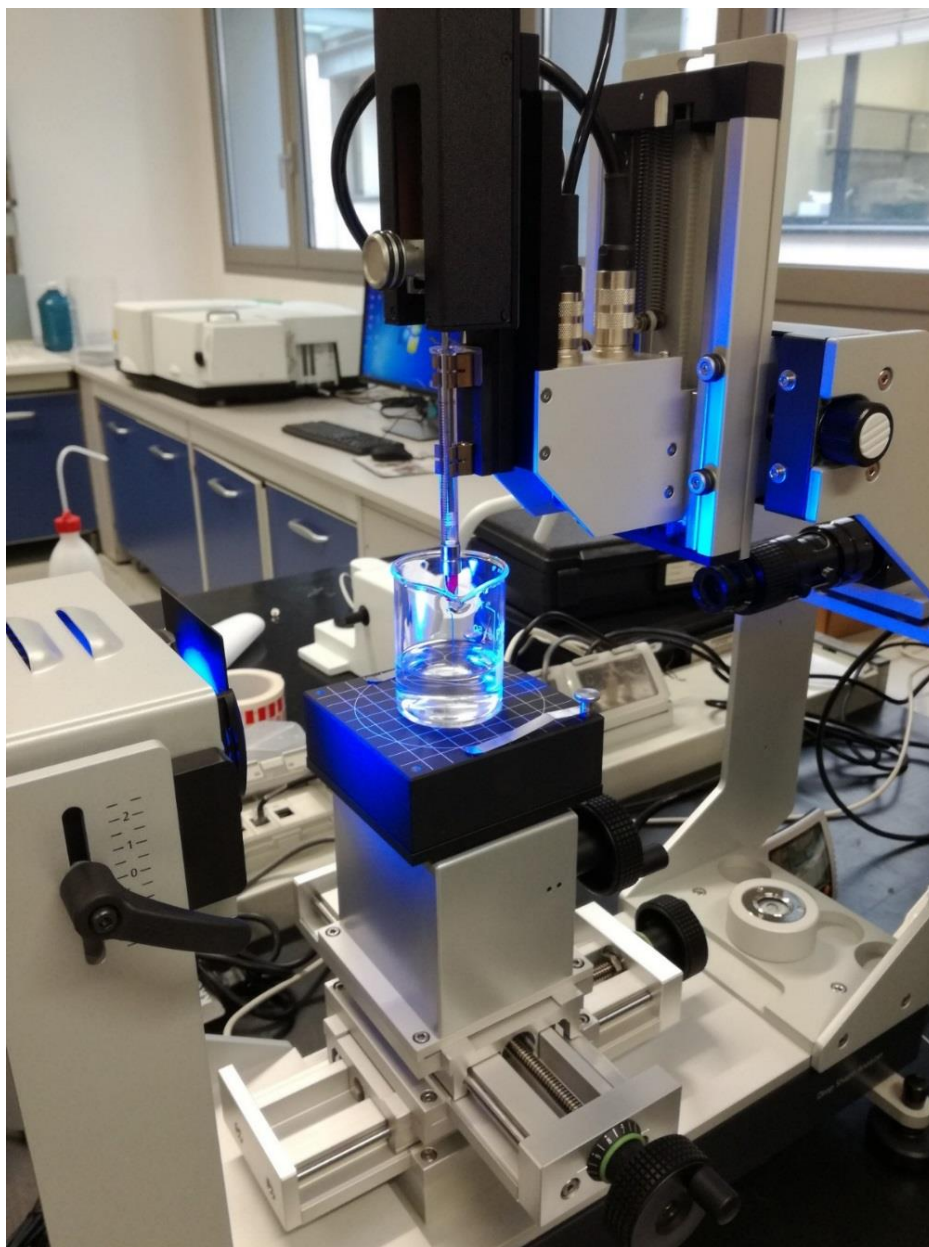


Figure 4.30 Contact angle tests: syringe automatic filling.

Each time the operator, through a regulation screw, manually moved the plate upwards to catch and deposit the liquid drop on the plate itself (see fig. 4.31). The equilibrium contact angles were measured after 20 seconds from water drop depositions, according to Kubiak et al. [15]. The parameters of each test were saved by the instrument software.

Tests were done to have at least seven valid values for each condition. Values that are considerably different (from about  $7^\circ$ ) from the average of the others were not considered, because they probably are the results of dust or local defects on the surface, or even operator's mistakes.

#### 4.3.2.5 Results

Table 4.6 illustrates the results in terms of contact angle and surface free energy resulting from tests on polished and rough surfaces of both EN AW-6082-T6 and AISI 316 plates. The average value is reported together with its maximum and minimum variations. The number of valid tests is in brackets.

		EN AW-6082-T6 (PAM0029A061)		AISI 316 (PAM0029A059)	
		1B (Polished)	1A (Rough)	1B (Polished)	1A (Rough)
<b>Average contact angle (°)</b>	Bidistilled water	79.7 ± 1.9 (7)	72.4 ± 2.1 (8)	79.1 ± 2.5 (7)	69.6 ± 2.9 (8)
	Diiodomethane	42.4 ± 0.6 (8)	42.9 ± 1 (9)	41.9 ± 1.4 (8)	43.1 ± 1.2 (8)
<b>Surface Free Energy (mN/m)</b>	Disperse part	38.4 ± 0.3	38.2 ± 0.5	38.6 ± 0.7	38.0 ± 0.6
	Polar part	3.8 ± 0.6	6.8 ± 0.9	4 ± 0.9	8.1 ± 1.4
	Total	42.2 ± 0.9	45.1 ± 1.5	42.6 ± 1.6	46.1 ± 2

Table 4.6 Contact angle and surface free energy resulting from tests. The number of valid tests is in brackets.

There are no differences between polished surfaces of EN AW-6082-T6 and AISI 316 plates. There is a slight difference (1 mN/m) between rough surfaces of EN AW-6082-T6 and AISI 316 plates and it is entirely due to the polar component of the surface free energy. It is possible to say that the rough surfaces have almost an equal chemical attitude to create polar or disperse bonds.

Tests confirmed that roughness has an impact on surface wettability as illustrated by Kubiak et al. [9].

The next paragraphs illustrate the following data for each of the four surfaces:

- A picture of the water drop on surface;
- A picture of diiodomethane drop on surface;
- A graph showing the single contact angle results for the various tests with the two liquids;
- A surface free tension wetting envelope, i.e. values of polar and total liquid tensions to obtain a contact angle equal to 0 °, so complete surface wettability.



Figure 4.31 Operator manually deposits liquid drop on plate surface.

#### 4.3.2.5.1 AISI 316 rough surface (PAM0029A059-1A)

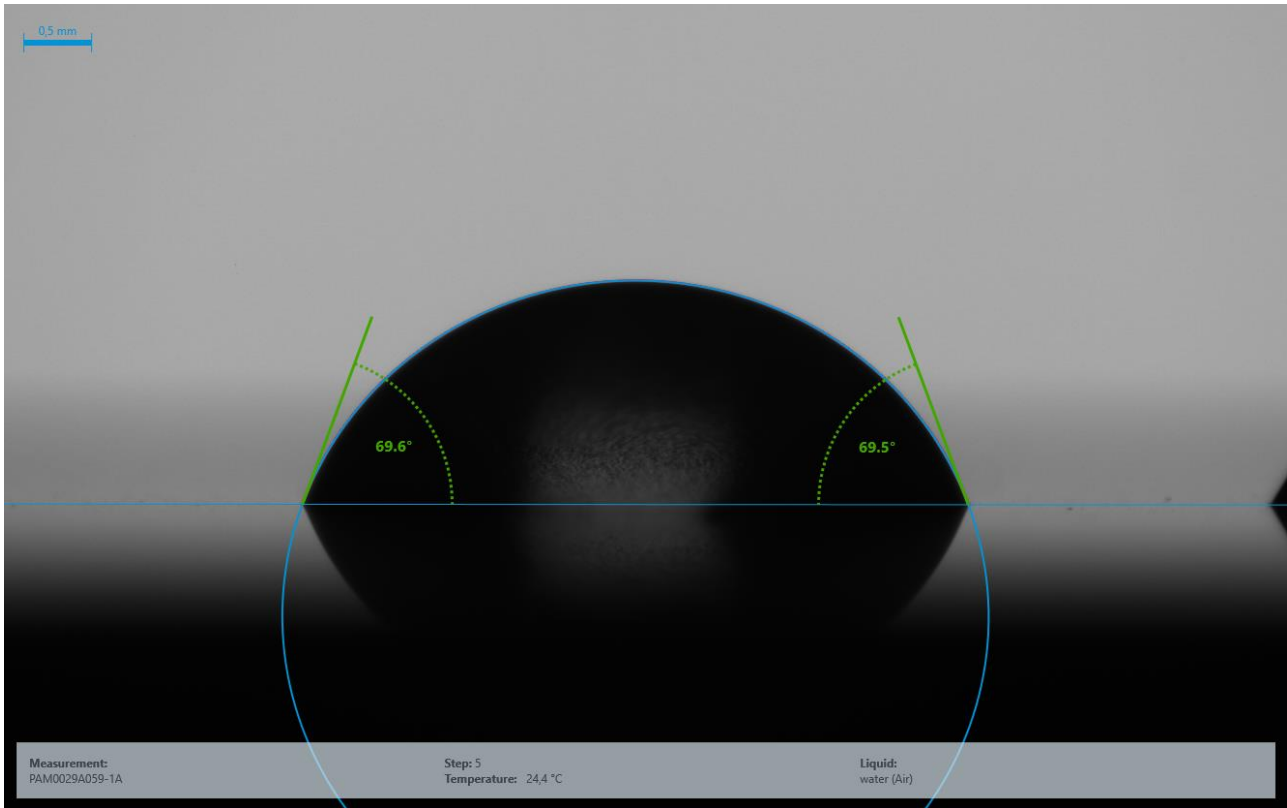


Figure 4.32 Contact angle measurement: water drop on AISI 316 rough surface.

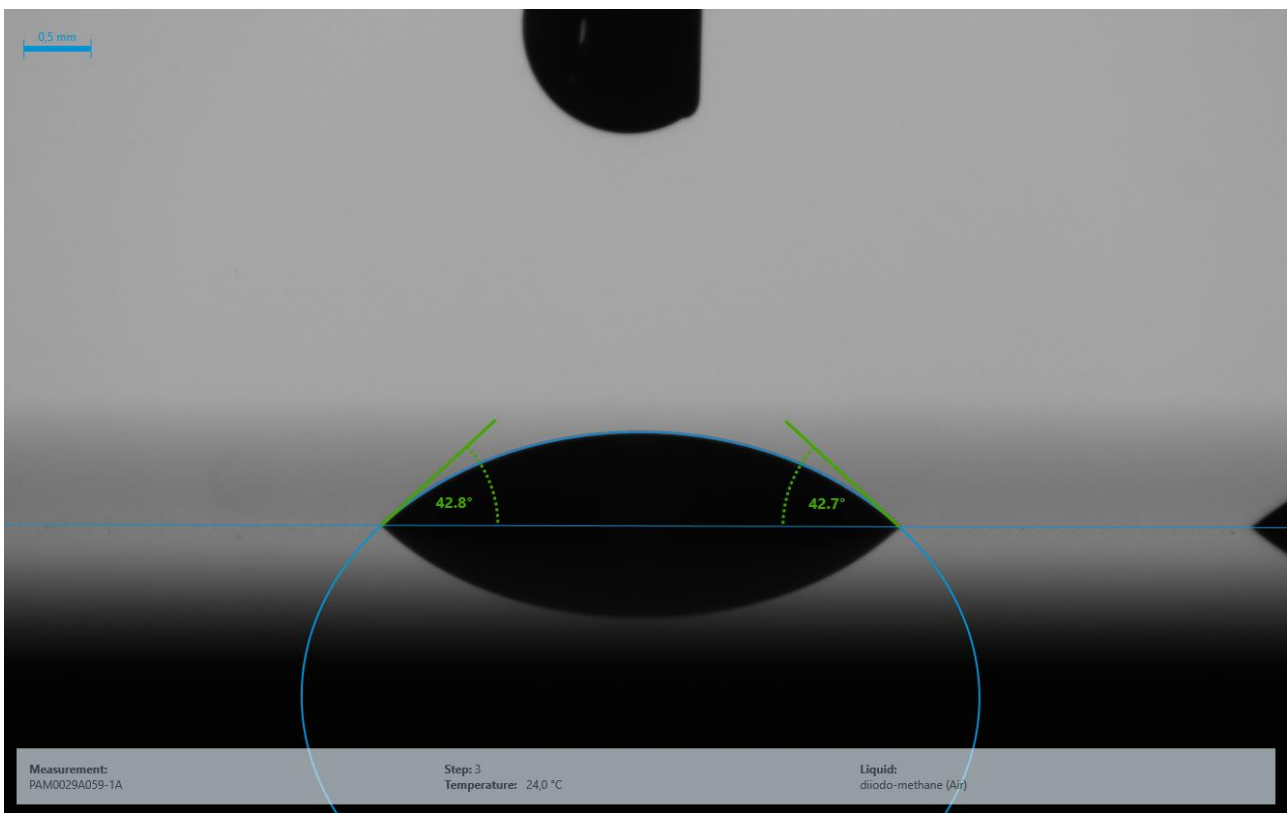


Figure 4.33 Contact angle measurement: diiodomethane drop on AISI 316 rough surface.

### Chart

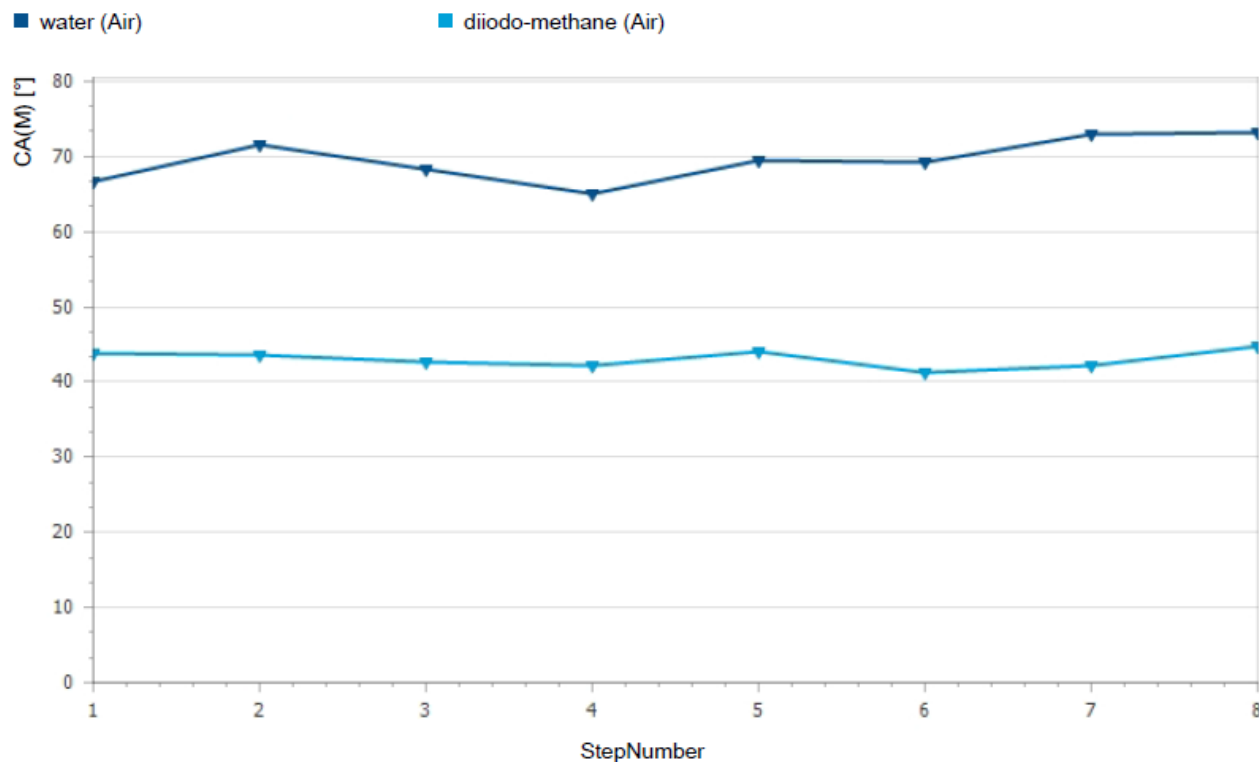


Figure 4.34 Contact angle results of water and diiodomethane on AISI 316 rough surface.

### Wetting envelope

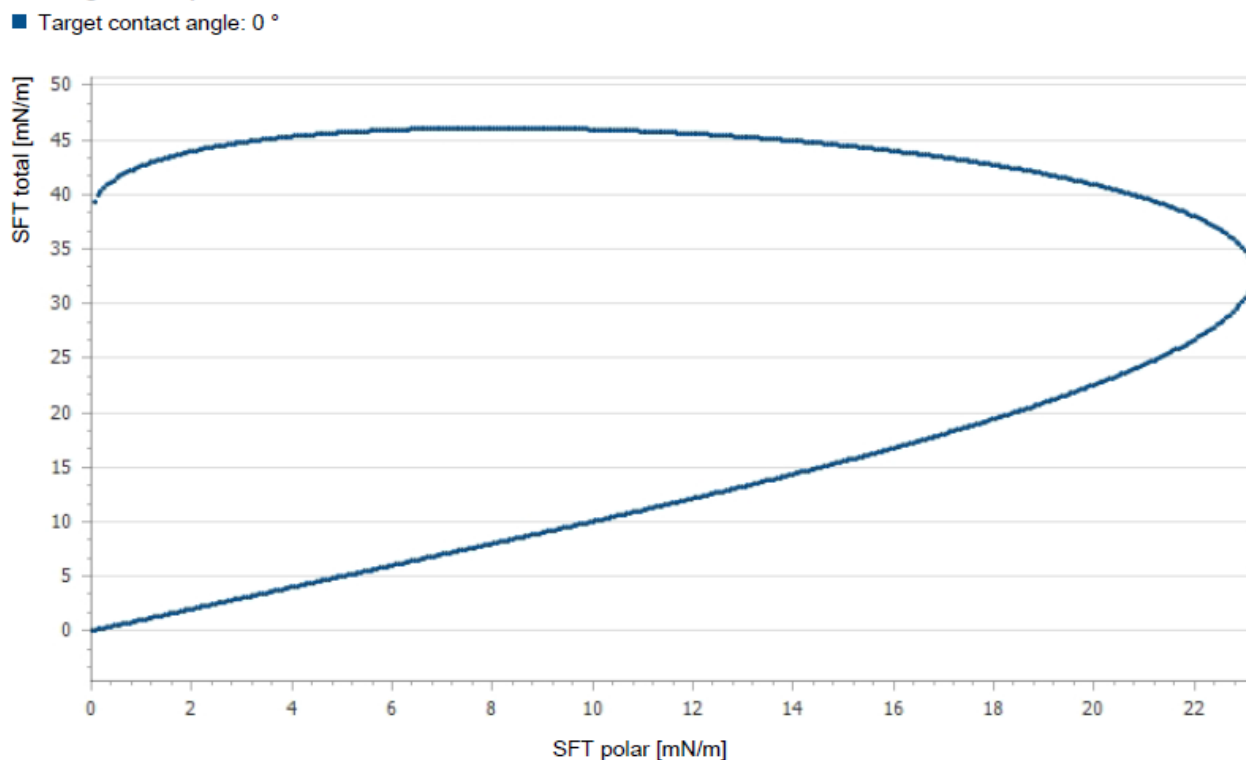


Figure 4.35 Surface free tension wetting envelope of AISI 316 rough surface, i.e. values of polar and total liquid tensions to obtain a contact angle equal to 0 °, so complete surface wettability.

4.3.2.5.2 AISI 316 polished surface (PAM0029A059-1B)

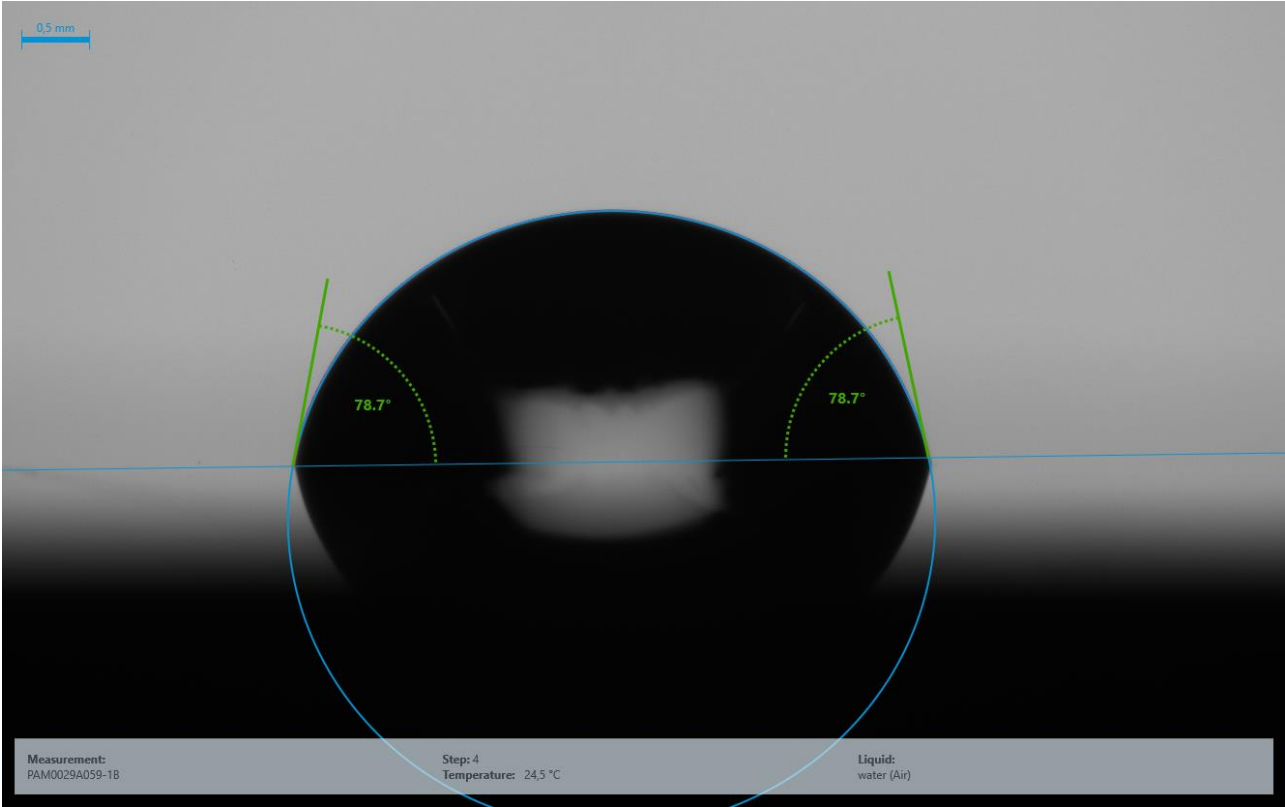


Figure 4.36 Contact angle measurement: water drop on AISI 316 polished surface.

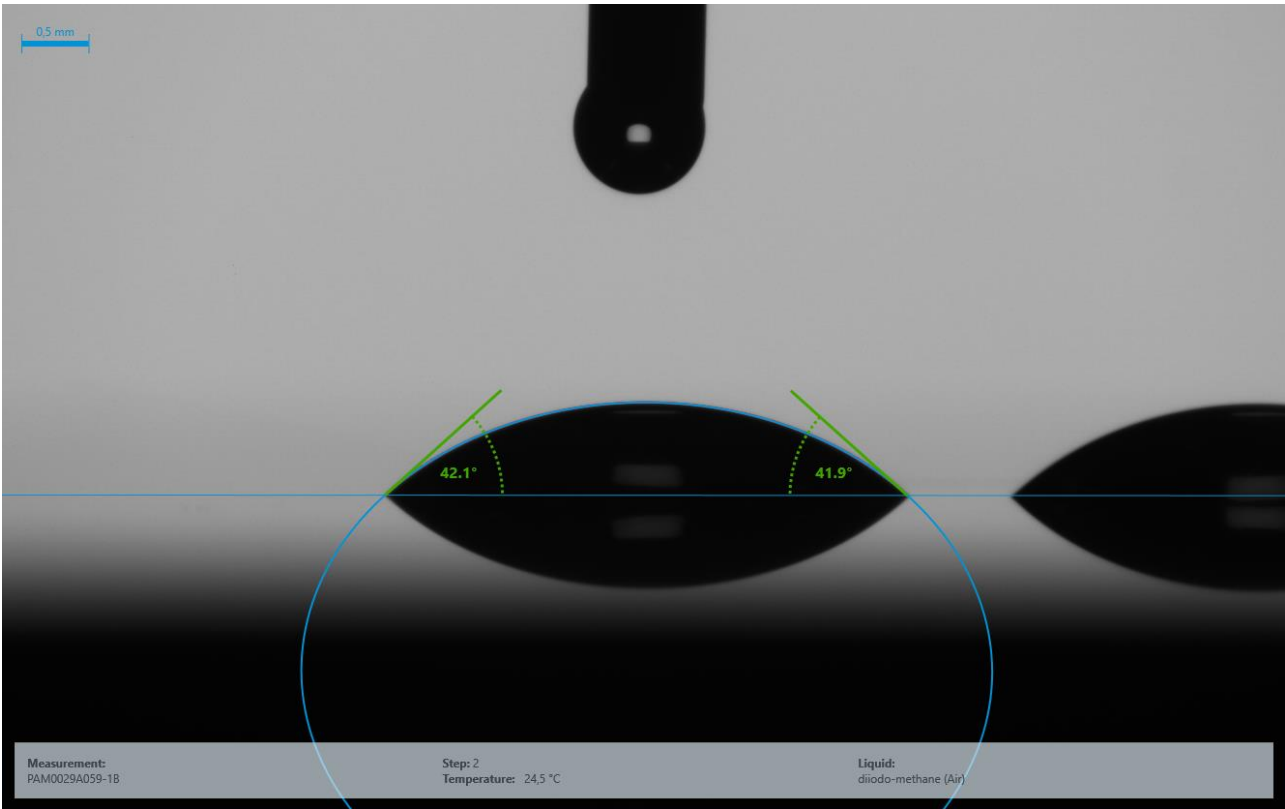


Figure 4.37 Contact angle measurement: diiodomethane drop on AISI 316 polished surface.

### Chart

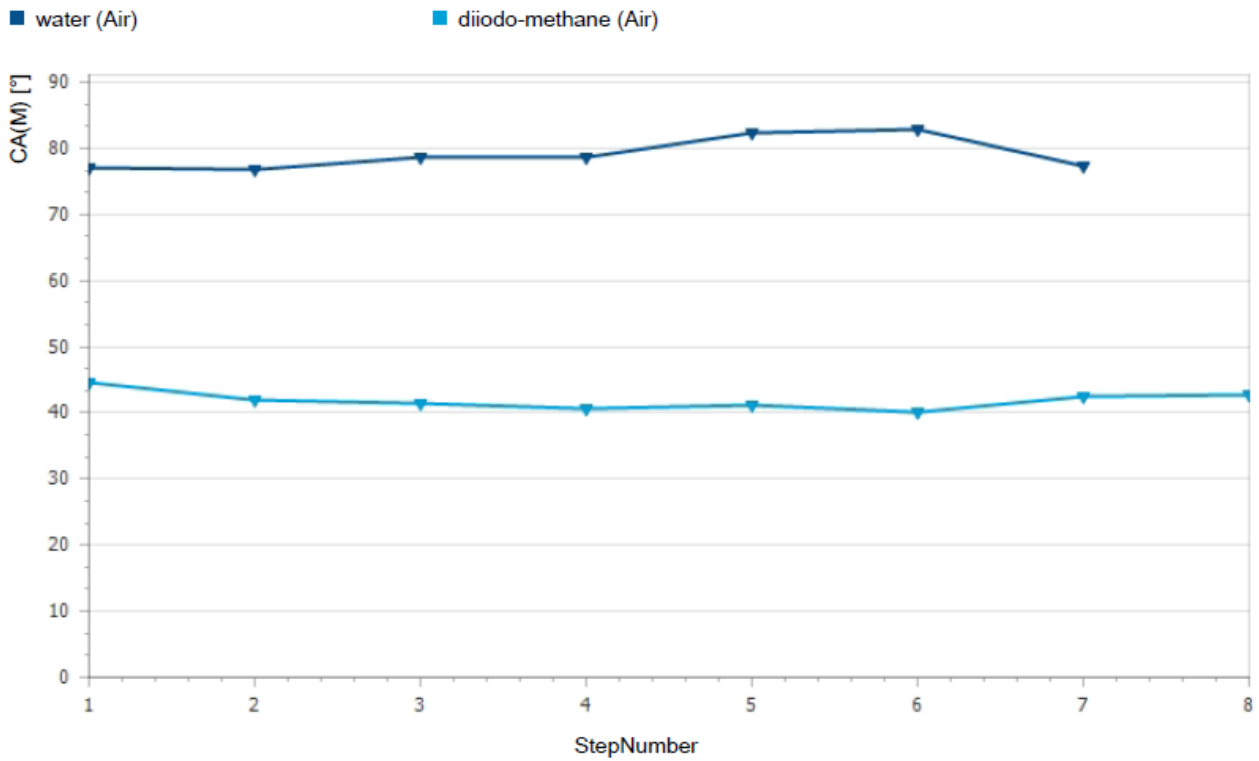


Figure 4.38 Contact angle results of water and diiodomethane on AISI 316 polished surface.

### Wetting envelope

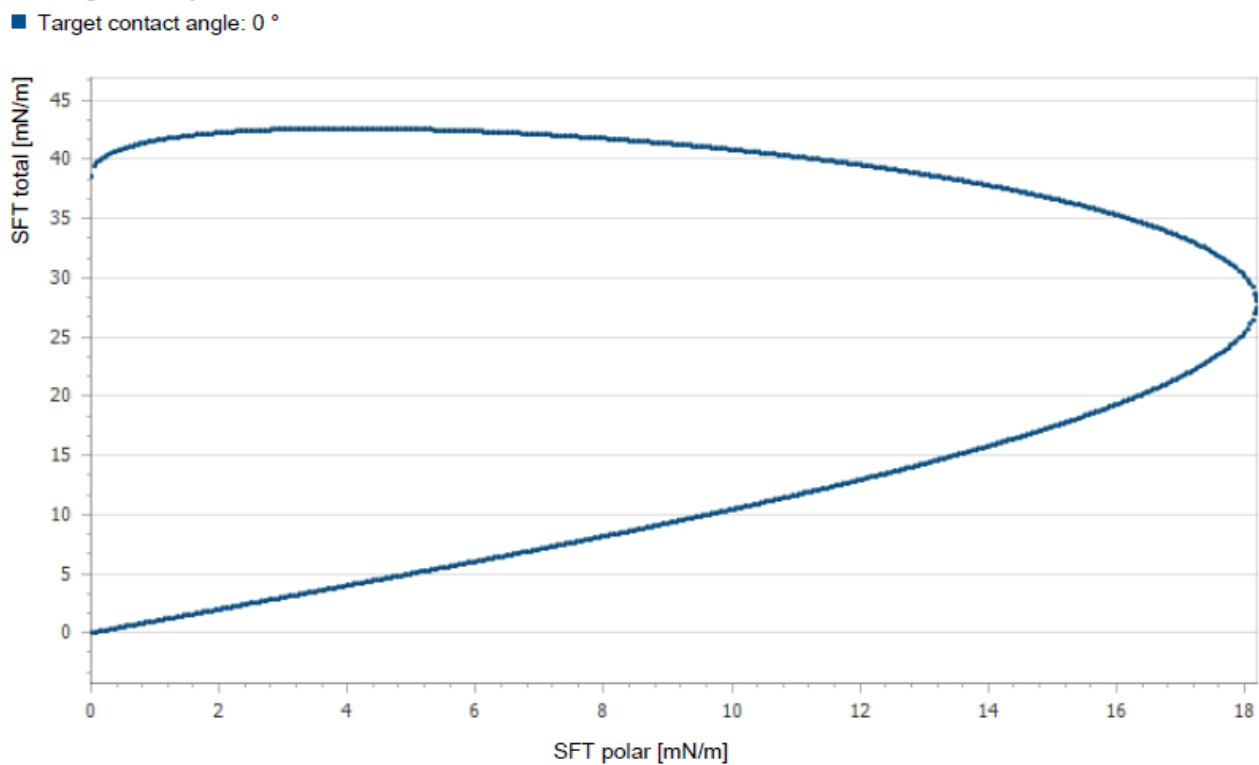


Figure 4.39 Surface free tension wetting envelope of AISI 316 polished surface, i.e. values of polar and total liquid tensions to obtain a contact angle equal to 0°, so complete surface wettability.

#### 4.3.2.5.3 EN AW-6082-T6 rough surface (PAM0029A061-1A)

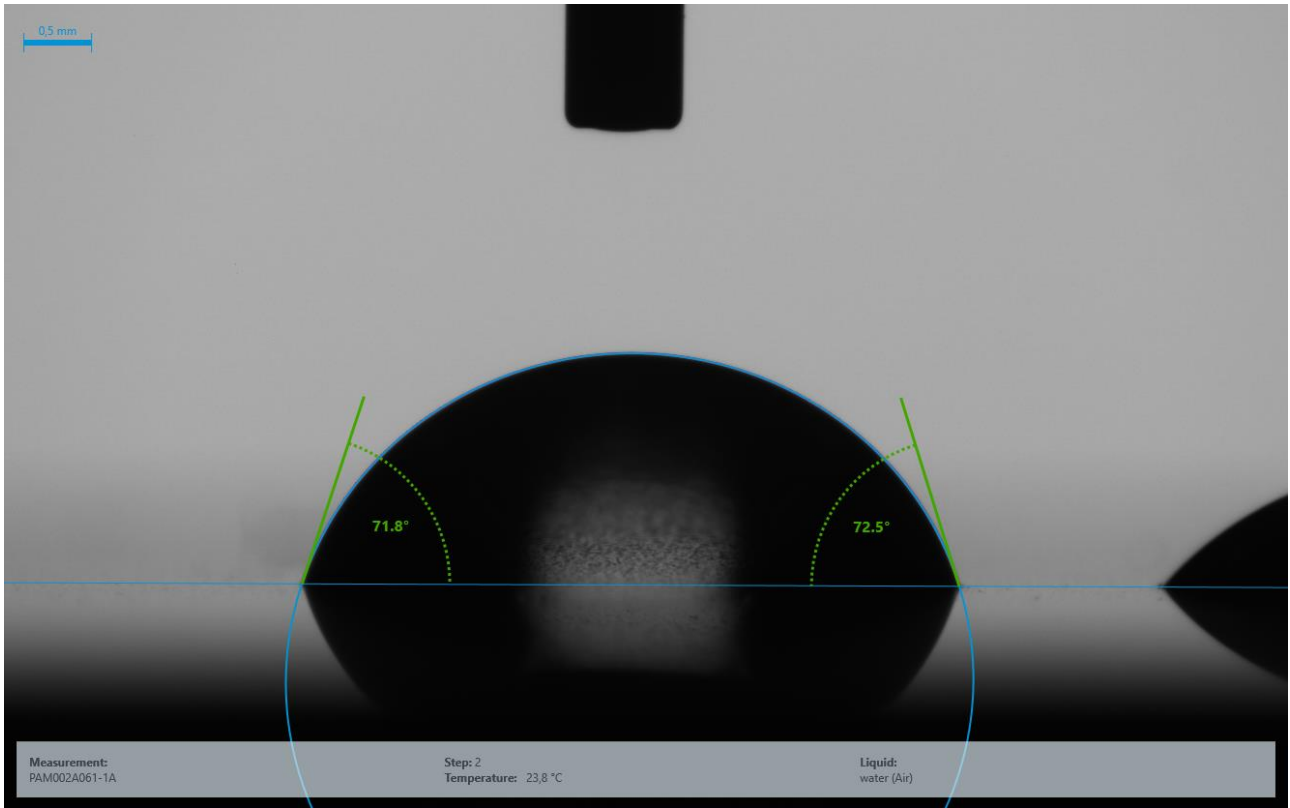


Figure 4.40 Contact angle measurement: water drop on EN AW-6082-T6 rough surface.

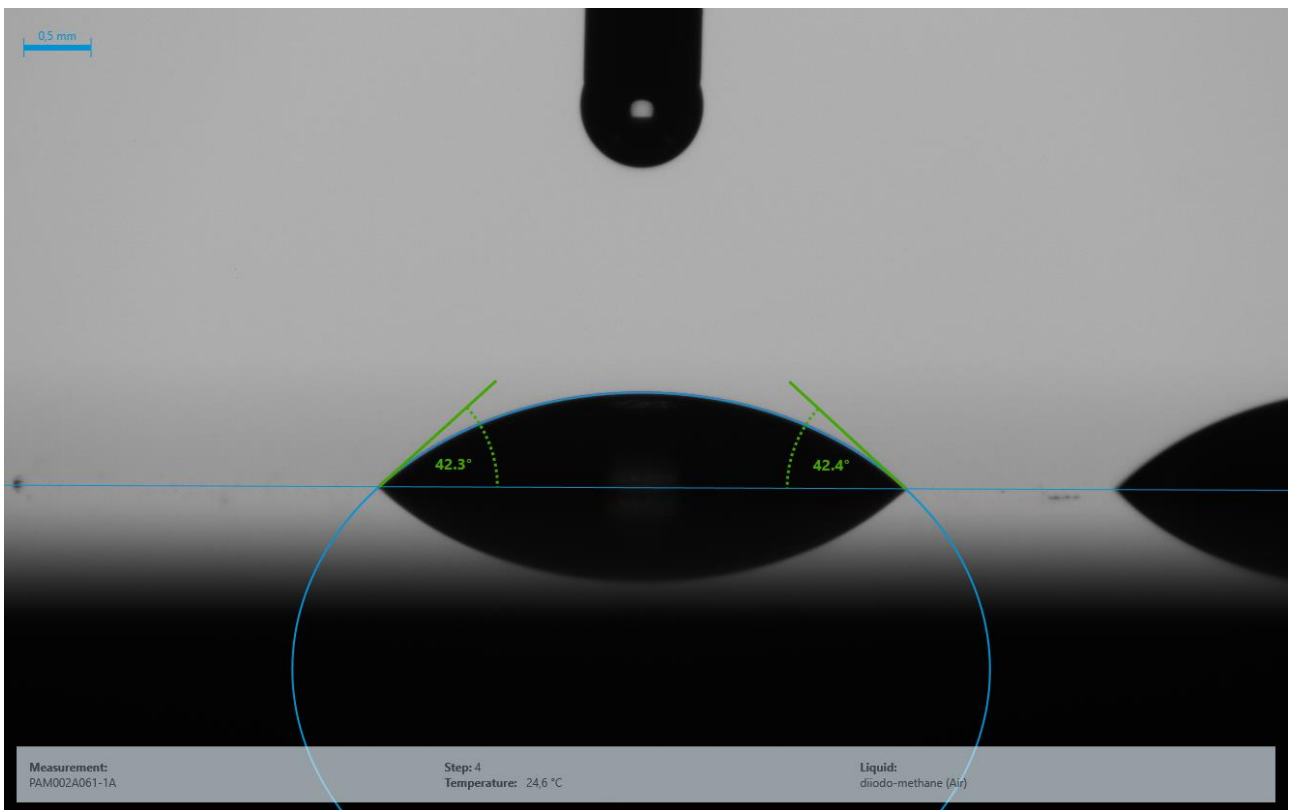


Figure 4.41 Contact angle measurement: diiodomethane drop on EN AW-6082-T6 rough surface.

### Chart

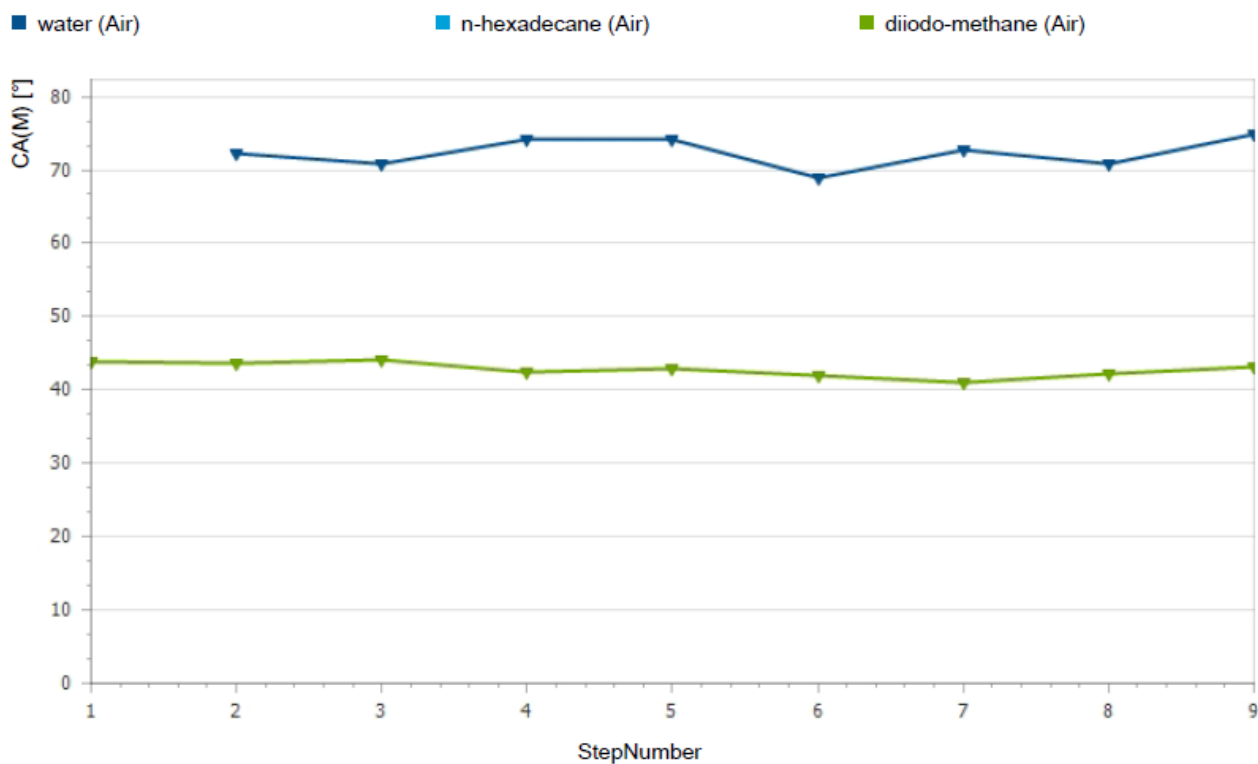


Figure 4.42 Contact angle results of water and diiodomethane on EN AW-6082-T6 rough surface.

### Wetting envelope

■ Target contact angle: 0 °

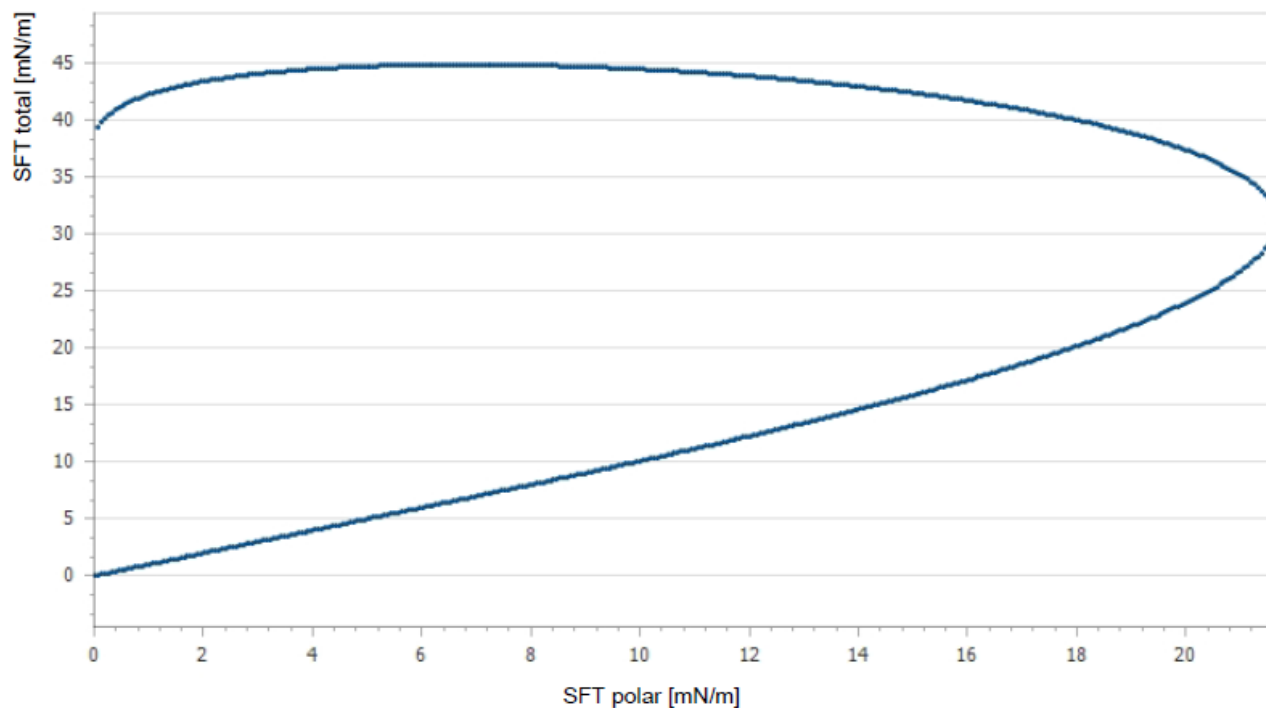


Figure 4.43 Surface free tension wetting envelope of EN AW-6082-T6 rough surface, i.e. values of polar and total liquid tensions to obtain a contact angle equal to 0 °, so complete surface wettability.

#### 4.3.2.5.4 EN AW-6082-T6 polished surface (PAM0029A061-1B)

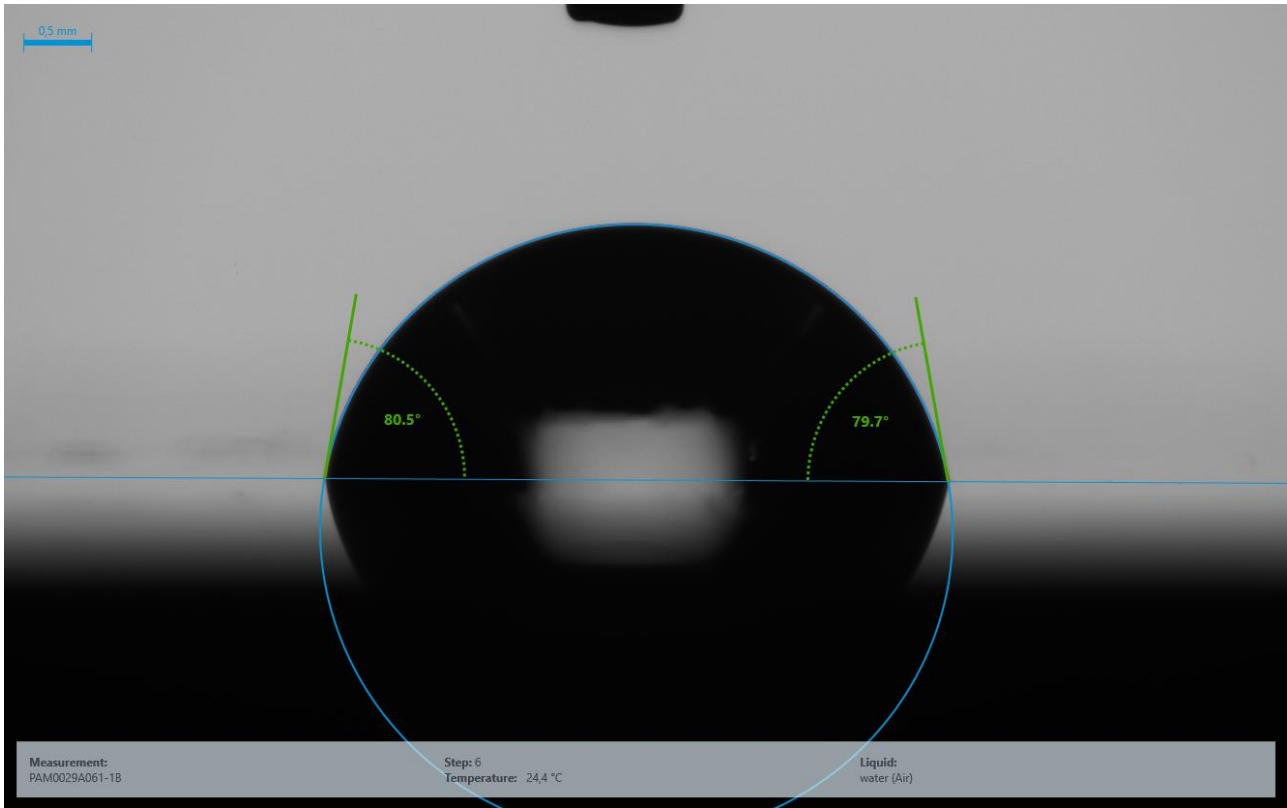


Figure 4.44 Contact angle measurement: water drop on EN AW-6082-T6 polished surface.

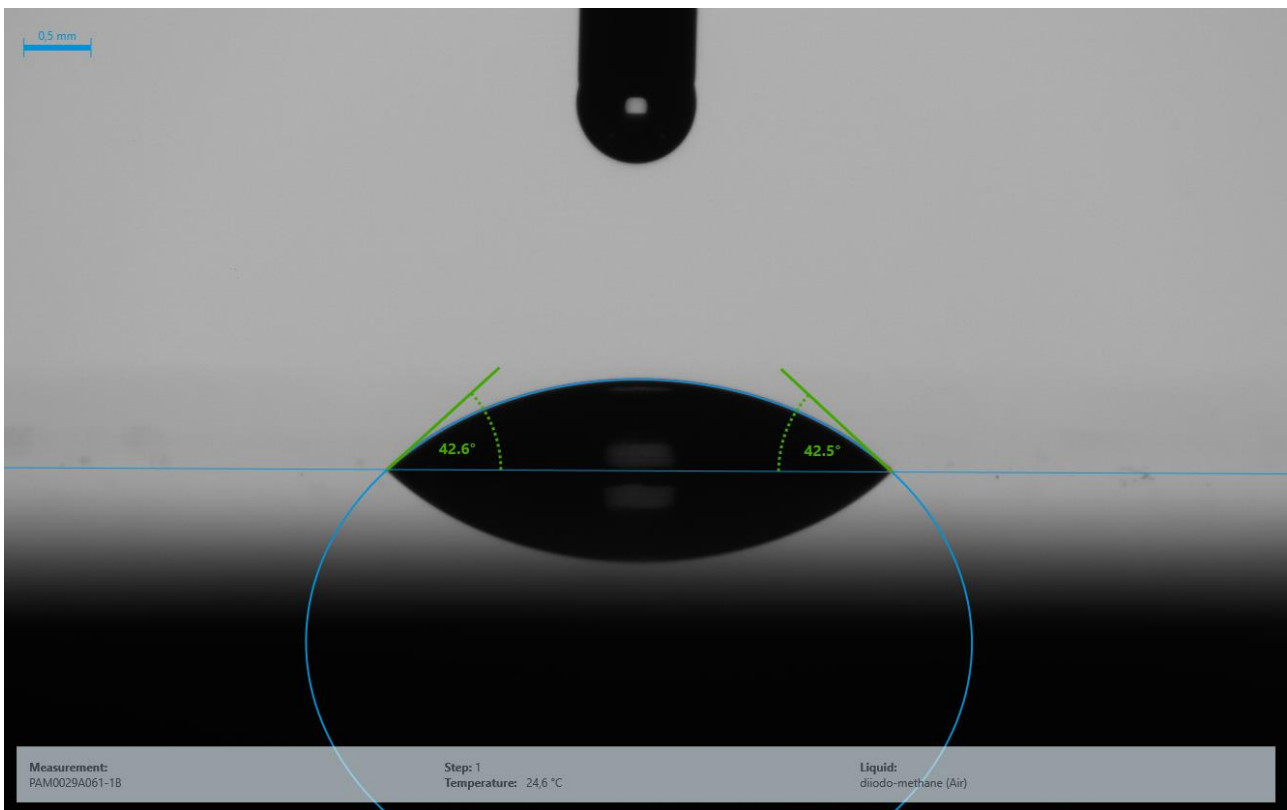


Figure 4.45 Contact angle measurement: diiodomethane drop on EN AW-6082-T6 polished surface.

### Chart

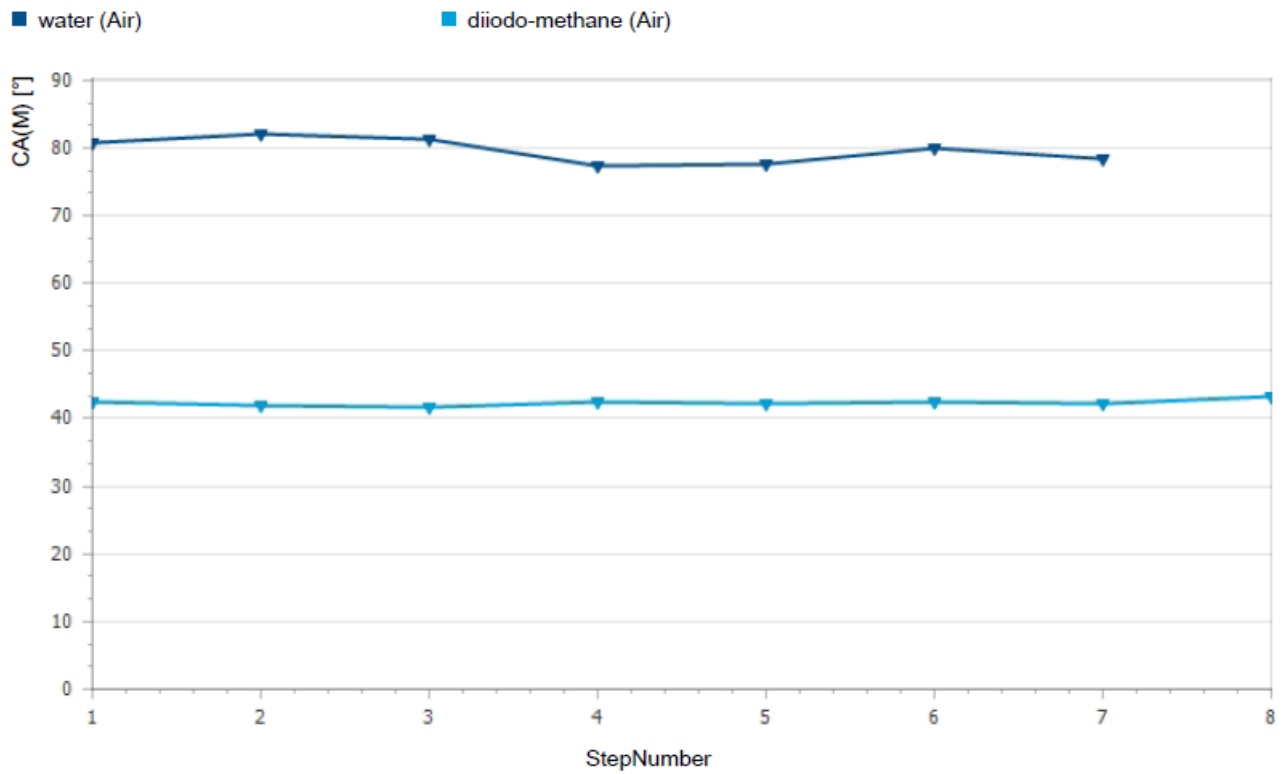


Figure 4.46 Contact angle results of water and diiodomethane on EN AW-6082-T6 polished surface.

### Wetting envelope

■ Target contact angle: 0 °

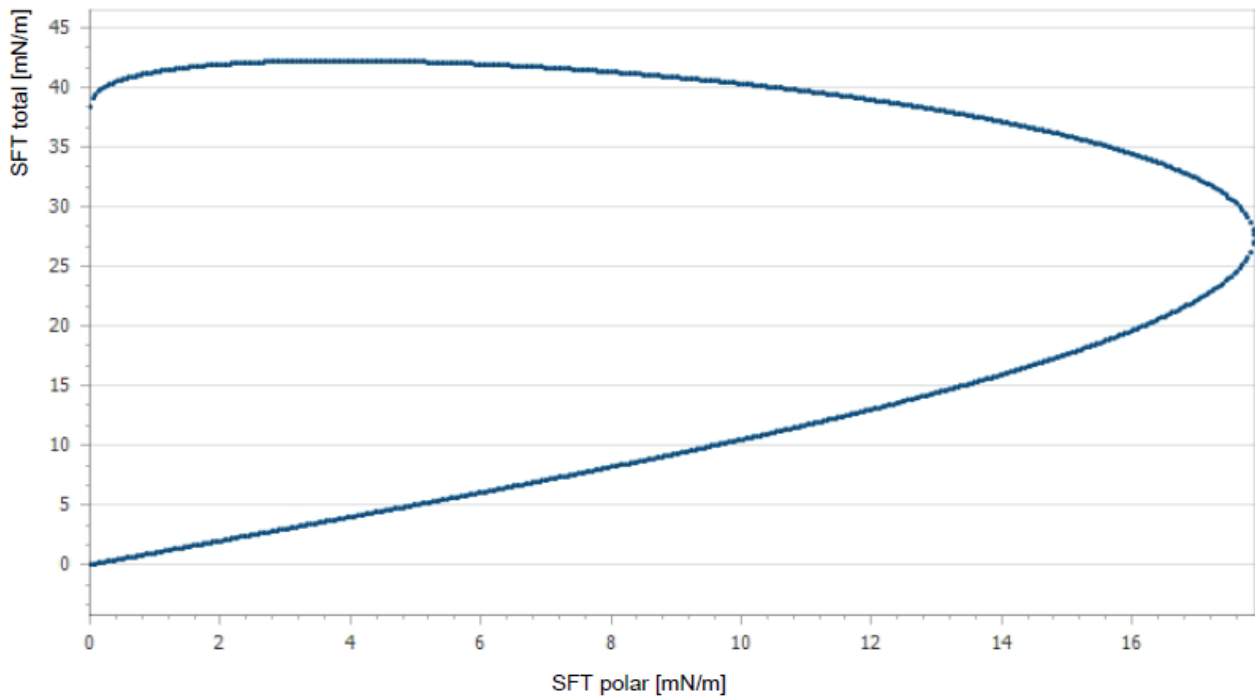


Figure 4.47 Surface free tension wetting envelope of EN AW-6082-T6 polished surface, i.e. values of polar and total liquid tensions to obtain a contact angle equal to 0 °, so complete surface wettability.

## 4.4 MODEL FOR THE ANALYSYS OF ADHESIVENESS VARIATION WITH TEMPERATURE

An aim of the test (chapter 4.2.1) is to verify if below the "adhesion threshold temperature" (if present), the adhesion decreases as temperature declines following some mathematical law, or if adhesion is an on-off mechanism activated at a threshold temperature. In the latter case, adhesion seems to be an on-off mechanism with temperature. To measure adhesion decrease, if present, it would be useful to measure the difference in gob kinetic energy a few instants before and after the gob contact with the plate. The work of adhesion, as defined in chapter 2 (paragraph 2.3), is the work that must be done to separate two adjacent phases - 1 and 2 of a liquid-solid phase boundary - from one another. Assuming to separate the phase of the gob contact with the metal plate in two steps: the first one is the bond creation while the second one is the bond destruction. During the first step the energy should be released and it will result in thermal energy, while during the second step energy should be absorbed, or, in other words, a work must be done (work of adhesion). PET is a viscoelastic material, which means that it has both viscous and elastic characteristics when undergoing deformation. In particular, its elastic behavior is predominant when a load is applied in a very short time [16]. The work of adhesion to separate the PET phase from the metal phase can be considered as given by the elastic energy which the gob accumulated when touching the metal. If this work of adhesion increases, the gob has a lower kinetic energy when leaving the metal. If the work of adhesion oversteps the available elastic/kinetic energy, the bond between gob and plate is not broken. If with subscript 1 all the variables and parameters before gob touches the metal are defined, and with subscript 2 the ones after the gob detaches from the plate, the work of adhesion ( $W_{ad}$ ) can be defined as follows:

$$W_{ad} = \Delta K_{21} = m_g * (v_{G1}^2 - v_{G2}^2) + I_g * (\omega_1^2 - \omega_2^2) \quad (4.2)$$

$m_g$  = gob mass;

$I_g$  = gob moment of inertia (calculated with respect to the axis that passes through the gob center of mass and that is perpendicular to the gob axis);

$v_{G1}$  = velocity of gob center of mass before contact gob-plate;

$v_{G2}$  = velocity of gob center of mass after contact gob-plate;

$\omega_1$  = angular velocity with respect to gob center of mass before contact gob-plate;

$\omega_2$  = angular velocity with respect to gob center of mass after contact gob-plate;

$K$  = gob kinetic energy.

As anticipated, all tests were recorded with a high-speed camera at 2000 fps which is a good compromise between image quality, information obtained and file size. It is important to place the camera orthogonal to the plane where the gob path lies. The software Tracker<sup>®</sup>, a free video analysis and modelling tool, was used to find and analyze the speeds of each videos.

## 4.5 TESTING MACHINE SETTING

The nozzle adopted in the tests had a diameter of 15 mm, which is a common value for beverage preform gobs. The diameter of the melt PET which exits from the nozzle changes with the speed rate, according to the physical phenomenon of the die swelling.

MONOPAM extruder has a lower productivity compared to an industrial machine since it has to fill just one mold while industrial machine usually has 48 ones.

The extruder works continuously. To have a melt die swelling similar to the one of an industrial machine, the melt is accumulated in an oleo-dynamic syringe which pushes it through the nozzle

when the machine has finished to mold the previous preform. A part of the melt remains inside the nozzle and the connecting pipe for a few seconds (preform mold time) then it degrades. Therefore, each time the syringe ejects the melt, the first part of it must be discarded. This is done through a cleaning cut.

It is relevant to note that melt flow stops for 0.45 s between the finish of scrap gob exit and the start of the flow of the "good" gob (measurement taken on test 77). However, previous tests proved that this residence time does not bring relevant problems to the final preform. Anyway, the air dehumidification plant was modified and pipes were brought close to the cutting zone (see left part of fig. 4.48). Orange fire protective sheets were installed to protect plastic pneumatic pipes and electric wires (see figg. 4.48 and 4.49) from the contact with melt PET.

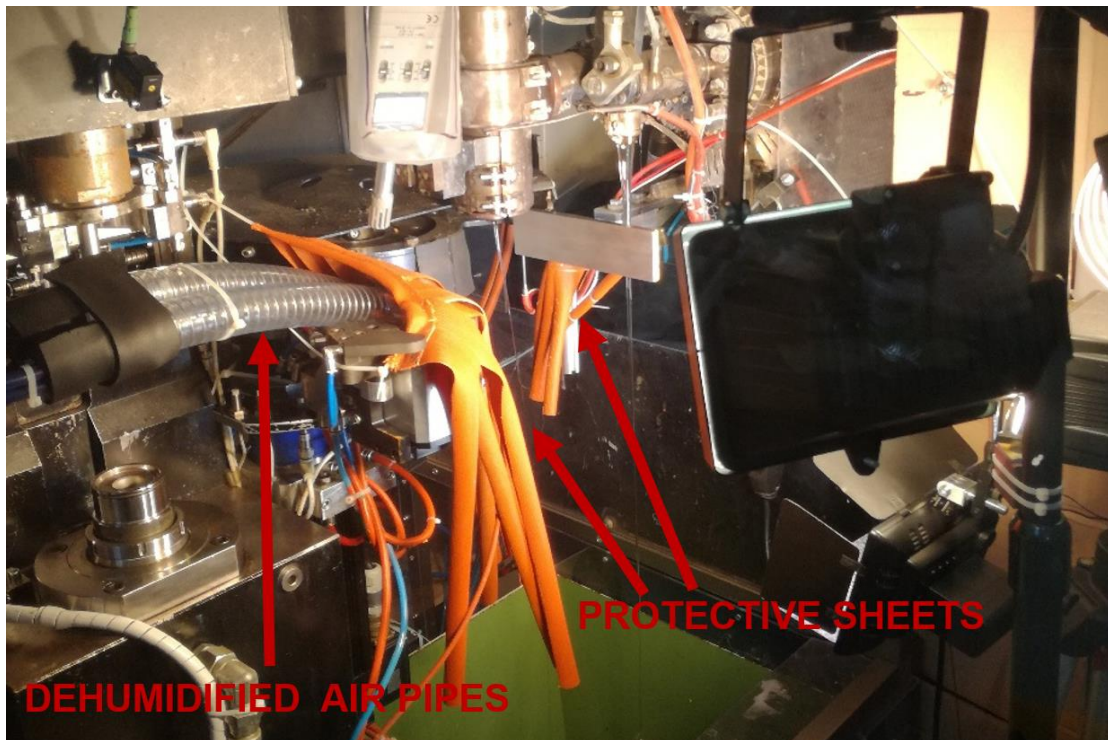


Figure 4.48 Testing machine: protective sheets and dehumidified air pipes.

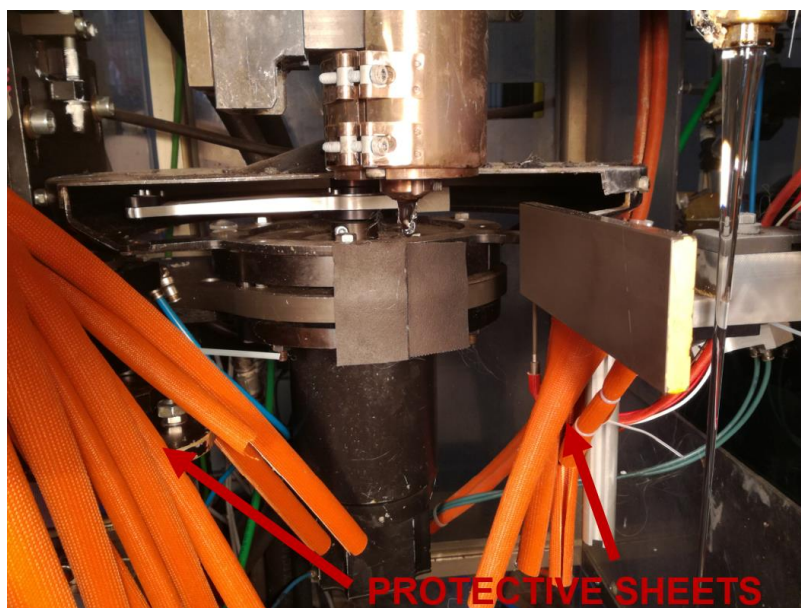


Figure 4.49 Testing machine: protective sheets.

### 4.5.1 Plate position

Initially the plate was placed in position A of fig. 4.3. In this configuration, the movement of the gob during cutting is limited by another plate which is usually adopted in industrial machines. After setting the light, the high-speed camera video showed that in this configuration it is difficult to have a repetitive trajectory and motion law. Fig. 4.50 which shows two steps of a gob bouncing on metal plate in position A.

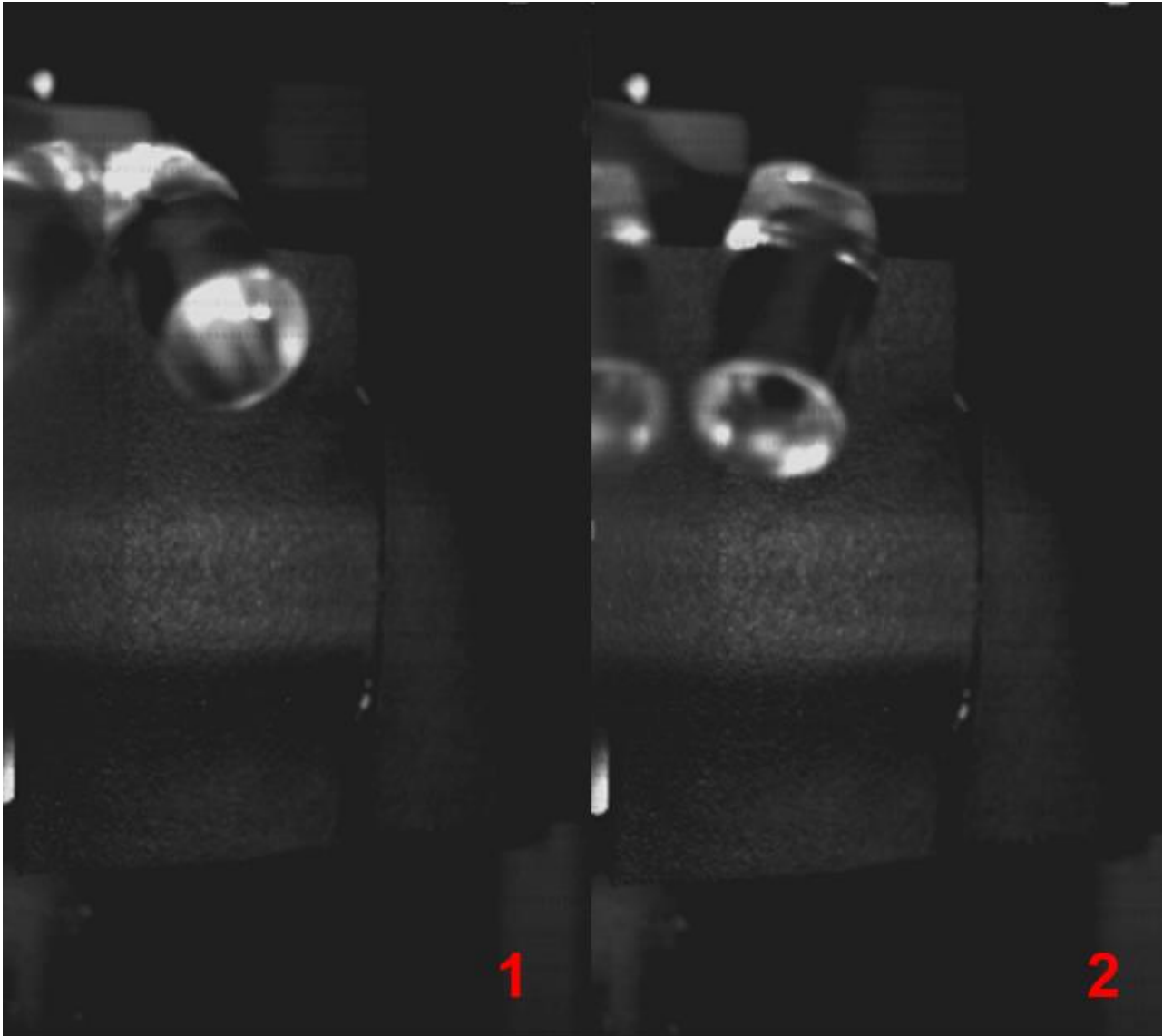


Figure 4.50 Gob bouncing sequence on metal plate in position A.

Thus, the plate was moved to position B of fig. 4.3. For the aim of the test it was important to avoid this scrap gob falling on the metal plate, to keep the plate surface clean. To obtain a scrap gob trajectory different from that of the valid gob, it was decided to work with masses. Starting with a certain mass of the gob and with a certain cutting speed of the knife, the syringe stroke was defined, hence the mass of the scrap gob. In fig. 4.51 six photograms taken from the same video show the scrap gob before cutting, during cutting and after cutting. The metal plate is on the right and the scrap gob did not touch it, so the goal was reached. Finally, the valid gob was cut and hit the plate, see fig. 4.52. The gob trajectory is more repetitive compared with the plate positioned in A.



Figure 4.51 Scrap gob cutting sequence with metal plate assembled in position B.



Figure 4.52 Valid gob bouncing on metal plate in position B.

#### 4.5.2 Gobs size

Gob dimensions and the blade cutting speed were then optimized to increase the repetitiveness of the gobs trajectory and the motion law. The best results were obtained with a gob which weighs about 4 g. Fig. 4.53 shows the moment when the gob impacts on the plate for three different gobs. The time between cut and impact is the same for the three gobs, i.e. 0.0115 s, with a precision of 0.0005 s given by the chosen camera frame rate (2000 fps). The first setting tests showed that the gob contact with the plate, from the instant when it starts touching the plate (of fig. 4.48) until the moment when none of its edge touches the plate, could last  $0.003 \pm 0.0005$  s.

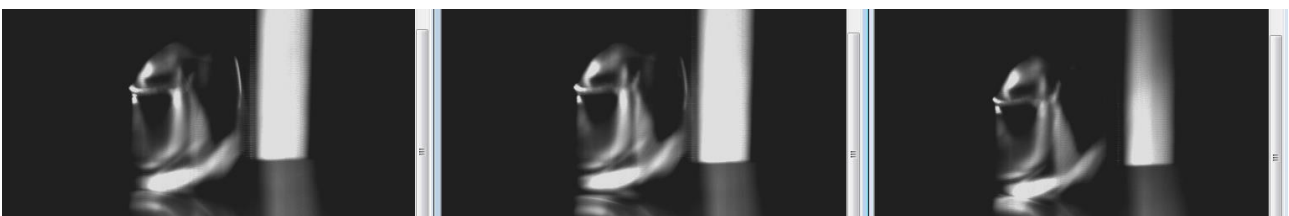


Figure 4.53 Impact on plate of three different gobs.

Fig. 4.54 shows the gob impact sequence. The red line is the trajectory of a gob edge from cutting to impact. The video was elaborated with Tracker<sup>®</sup>. There is an automatic trajectory detector, but it did not work properly due to PET gob transparency and reflections. For each video, the operator manually

selected a point step by step. There is hence a little margin of error. Fig. 4.55 compares the trajectory of three different gobs photographed in three different instants of the impact. Their trajectories are very similar.

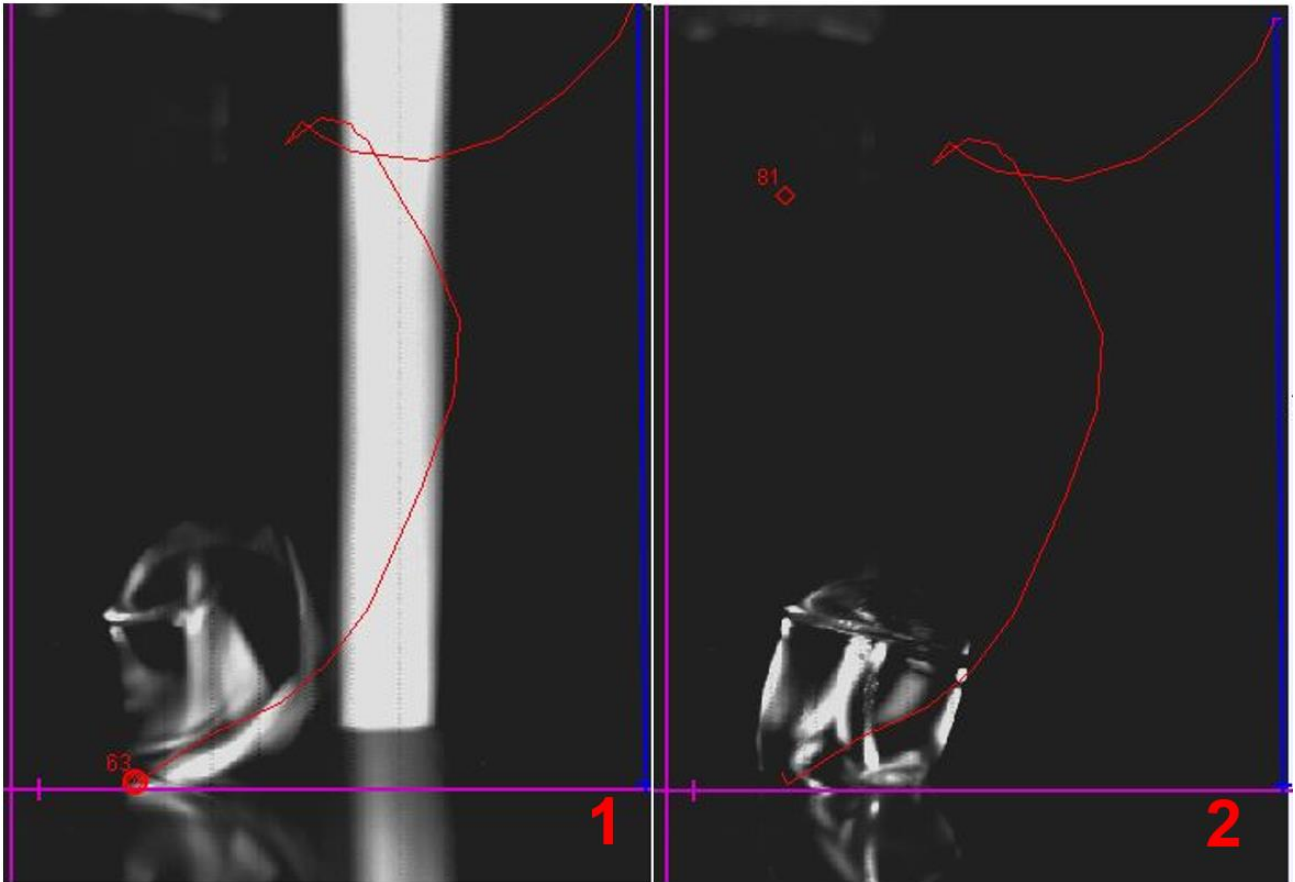


Figure 4.54 Sequence of gob impact on plate.

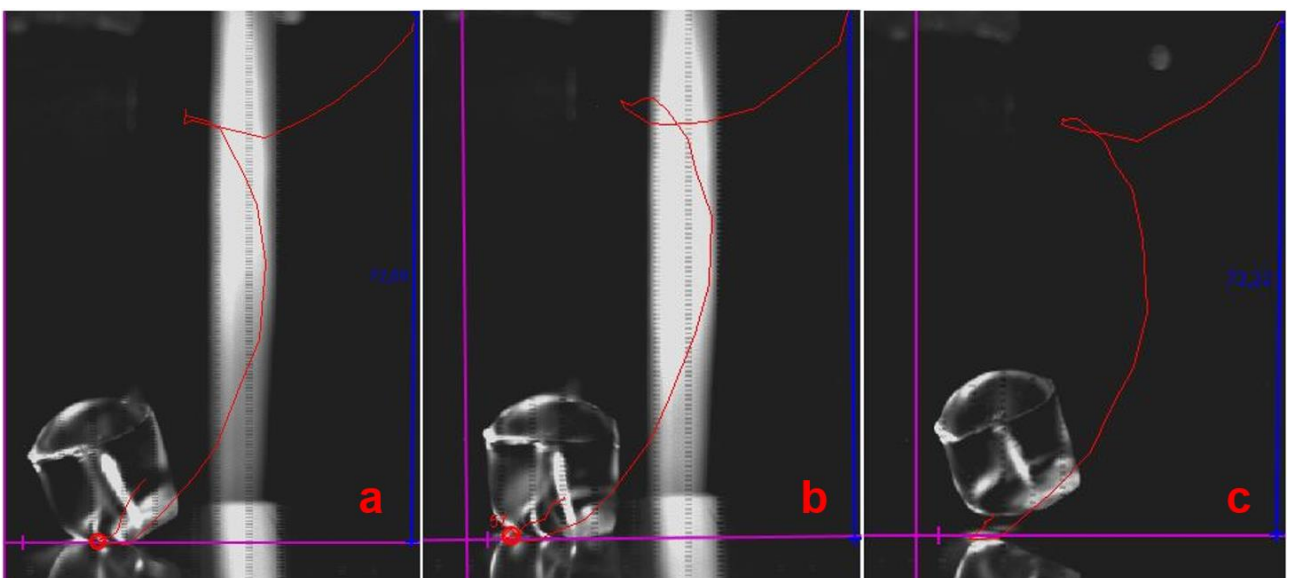


Figure 4.55 Trajectories of three different gobs photographed in three different instants of the impact.

Tracker<sup>®</sup> also has a tool to measure distances, and hence to measure body speed known video framerate. The tool scale was calibrated with a known dimension of a distance between two components close to the gob. The first setting tests illustrated that the speed of gob center of mass

(red arrows of fig. 4.56) at the instant before the impact was around 7 m/s. Gob rotates around its center of mass as its center of mass trajectory shows. The cyan track and the red tracks of figg. 4.54 and 4.55 are analogous, i.e. the trajectory of a gob edge. Fig. 4.56 shows an instant where speed vectors of both the gob center of mass ( $v_a$ , whose value is around 7 m/s) and the gob edge ( $v_b$ , whose value is around 13 m/s) have the same direction. In this particular instant, subtracting the value of  $v_a$  to the value of  $v_b$  it is possible to calculate the relative speed of the gob edge  $v_{ba}$ , whose value is around 6 m/s, with respect to the gob center of mass. Dividing  $v_{ba}$  by the distance between the gob edge and the gob center of mass, the gob angular speed is calculated. Gob dimensions are described in the following pages. There is another way to calculate the gob angular speed, that is by dividing 1s for the time (i.e. number of frames divided by framerate) the gob takes to make a complete round. 20 frames divided by 2000 (framerate) gives 0.01 s. The gob angular speed is about 100 rounds per second or about 600 radians per second, which is quite an impressive value. At the same angular speed the engine of an average class car would quickly break.

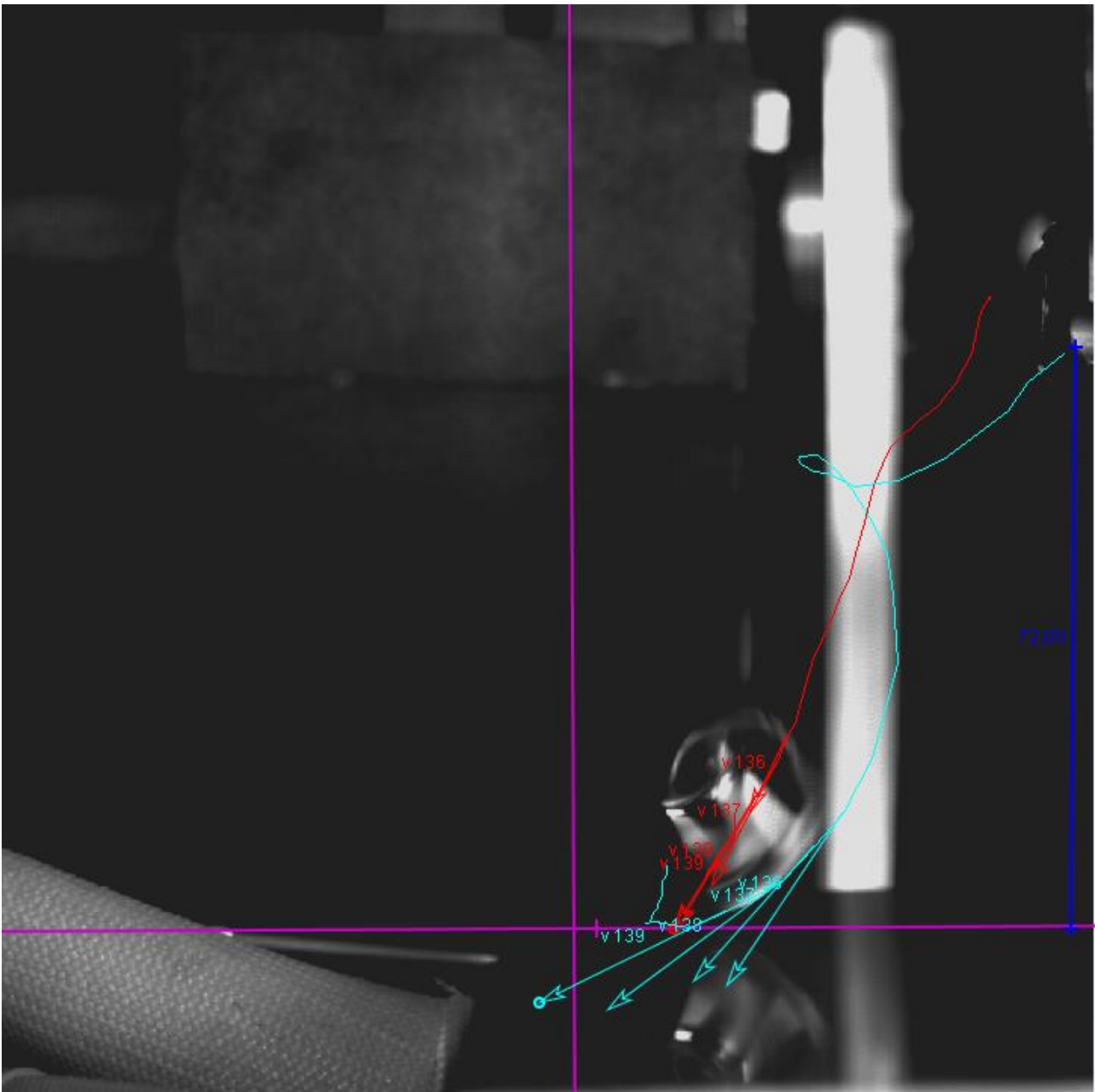


Figure 4.56 Gob before contact with plate (speed measurement with Tracker<sup>®</sup> tool).

Gob dimensions and weight were measured through a dedicated test set up. The plate was disassembled and a basin with water was placed along the gob trajectory (see fig. 4.57), so that gobs could impact on water (see video sequence in fig.4.58).

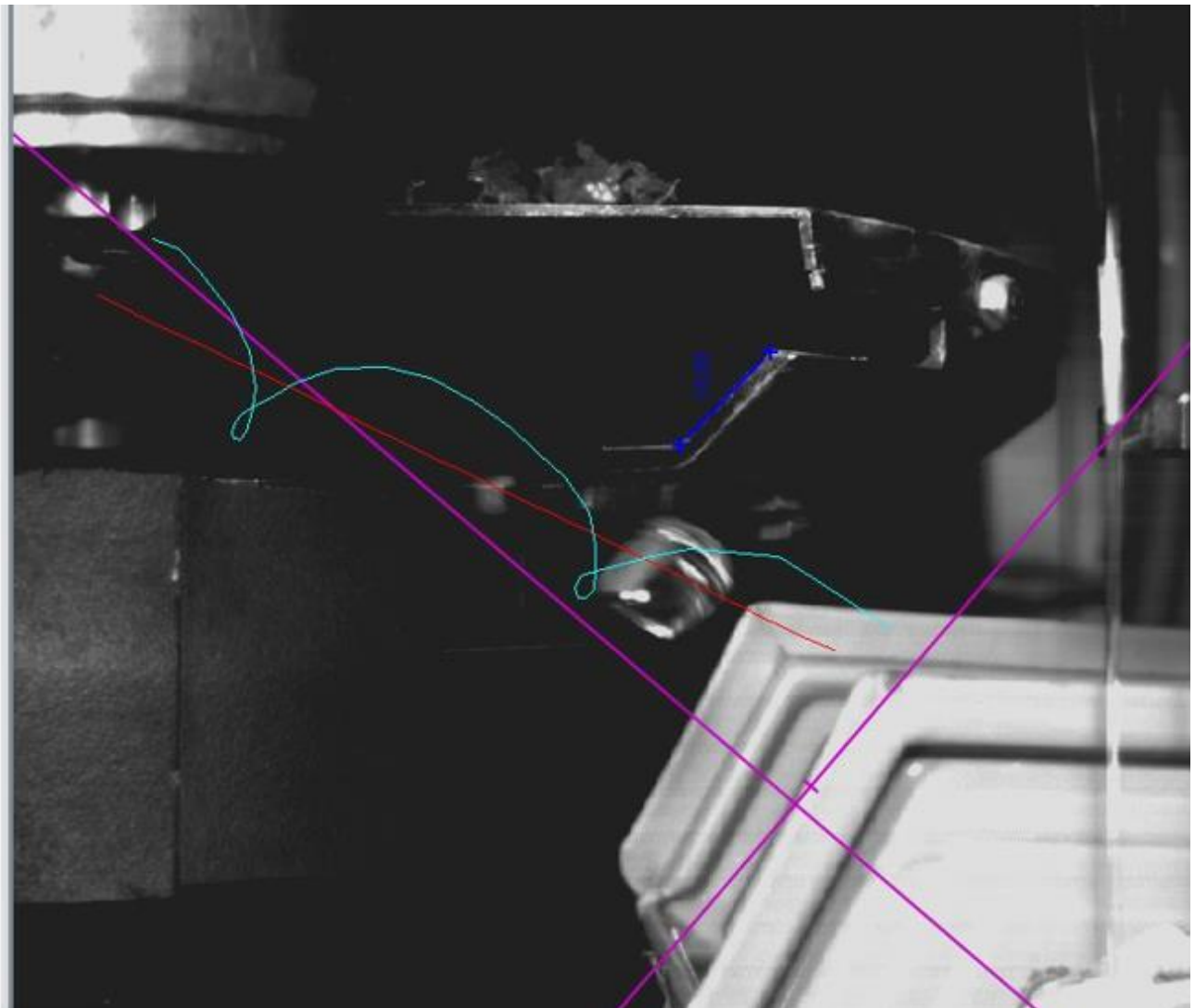


Figure 4.57 Gob trajectory towards the water basin.

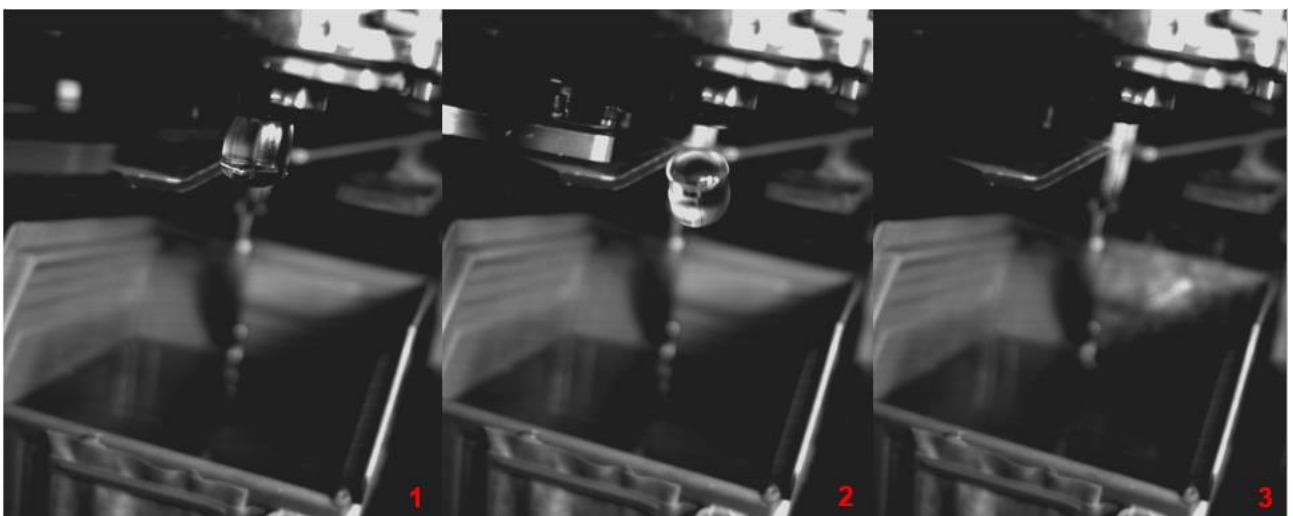


Figure 4.58 Sequence of images from gob cutting to gob entering the water (see water splashes in image 3).

The impact on water helps not to change the gob geometry apart from thermal shrinkages (see PET PVT curves in fig. 4.59). Fig. 4.60 shows the resulting gobs.

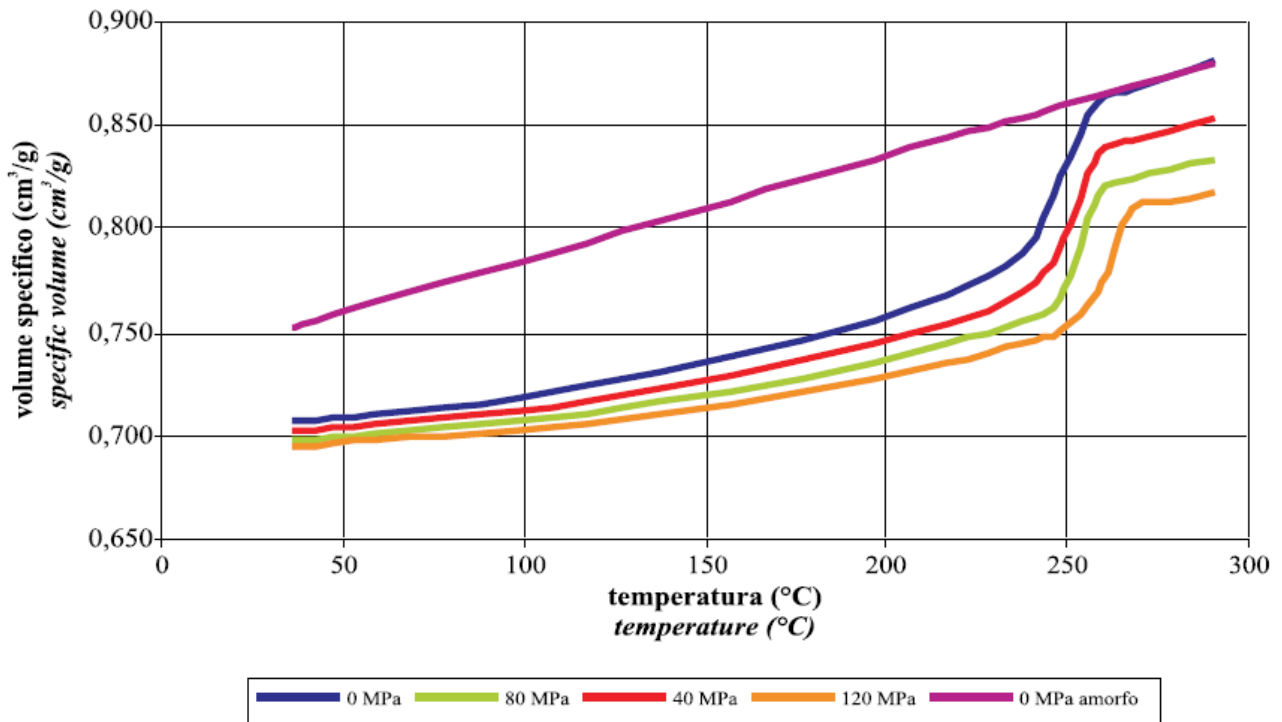


Figure 4.59 PVT curves for a PET sample [3].



Figure 4.60 Gobs that hit water.

Each gob was measured according to scheme of fig.4.61. Measurements of gob dimensions, their average values and their standard deviations are illustrated in table 4.7.

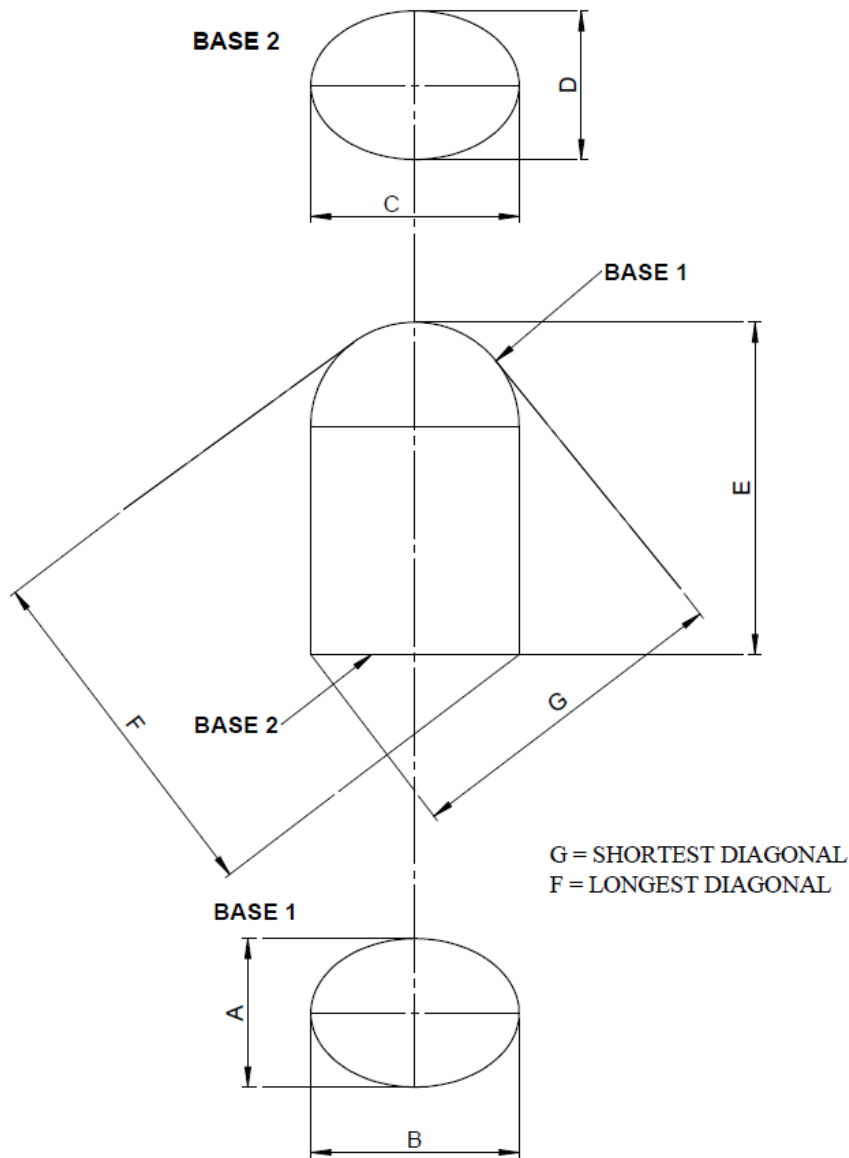


Figure 4.61 Gob measured dimensions.

Gob number	Cold gob parameters									
	Linear dimensions (mm)							Weight (g)	Crystallinity (%)	
	A	B	C	D	E	F	G	Weight (g)	Surface	Core
<i>D1</i>	14.03	17.71	13.52	17.31	19.19	22.04	24.84	4.0487		
<i>D2</i>	14.31	17.58	13.26	17.48	19.24	21.59	24.43	4.0613		
<i>D3</i>	13.43	17.75	13.22	17.23	19.35	21.20	24.59	4.0671	4.2	13.0
<i>D4</i>	13.88	17.58	13.37	17.43	19.21	21.47	23.51	4.0551		
<i>D5</i>	13.87	17.96	13.56	17.34	19.56	21.00	23.58	4.0609	3.7	19.8
<i>D6</i>	13.72	17.61	13.29	17.16	19.45	21.93	25.07	4.0598		
<i>D7</i>	14.07	17.77	13.06	17.54	19.41	20.37	24.14	4.0901		
<i>D8</i>	13.62	17.91	13.19	17.90	19.80	19.86	24.82	4.054		
<i>D9</i>	14.11	17.93	13.23	17.68	19.78	21.53	23.62	4.0653		
<i>D10</i>	13.67	17.64	13.38	17.37	19.85	20.15	24.26	4.0608	6.9	16.7
<i>D11</i>	13.87	17.55	13.61	17.52	19.20	21.28	24.07	4.0608		
<i>Average value</i>	13.87	17.73	13.34	17.45	19.46	21.13	24.27	4.0622	4.9	16.5
<i>Standard deviation</i>	0.25	0.15	0.17	0.21	0.25	0.72	0.54	0.0106	1.7	3.4

Table 4.7 Measurements of gob dimensions, weight and crystallinity.

Dimensional measurements on cold gobs are just indicative due to the huge change of specific volume seen in fig. 4.59. Moreover, due to the cooling conditions, the core of the gob has a higher crystallinity with respect to the surface, i.e. the specific volume varies in different zones of the gob. The crystallinity was measured with a DSC analysis, performed with the same calorimeter and the same conditions described in paragraph 1.5.2.1. Table 4.7 also includes the results of the crystallinity measurements performed on three gobs. As fig. 4.60 shows, thermal retirements are not isotropic, e.g. a section perpendicular to the gob cylindrical axis results in a pseudo-elliptical shape instead of a circular one as it is when PET gob temperature is about 275 °C. As a comparison, measurements were taken also from videos as shown in fig. 4.62. There is an uncertainty of few tenths of mm in the measurement. In the melt state gob diameter is about 16 mm, 1 mm larger than the nozzle diameter due to aforementioned die swelling, while gob length is about 19mm. From gobs measurements and from their specific volume (see fig. 4.59) it is possible to determine the inertia moment of the gob in order to analyze the kinetic energy variations (see paragraph 4.4).

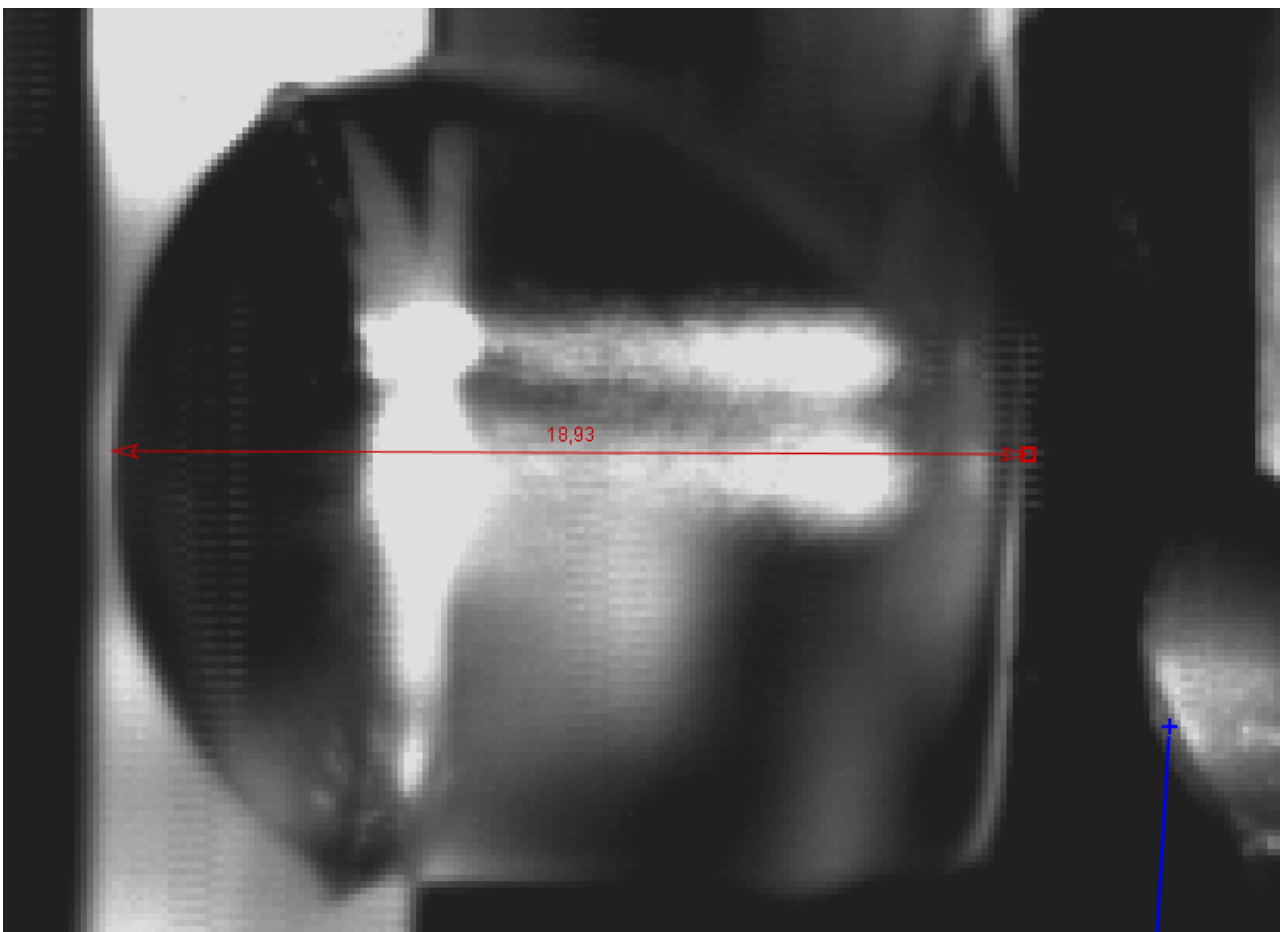


Figure 4.62 Gob length measurement with Tracker<sup>®</sup> tool.

Gobs weight was also measured (see table 4.7). Maximum variations are lower than  $\pm 0.03$  g. As mentioned in paragraph 4.2.6 almost all sticking gobs were measured to check weight influence on adhesiveness (see paragraph 4.6.2.1).

### 4.5.3 Plate thermoregulation characterization

The tests results are described here to facilitate the thesis reading, but measurements were done at the end of the adhesiveness tests no to alter the surface. The gob contact point was measured with the contact thermocouple (see par. 4.2.3.4). During the measurement, the thermocouple was kept in the measuring position with the aid of a clamp, to have a repetitive positioning, and a spring to exert a

constant force on the plate (see fig. 4.63). The aim is to know the exact temperature values (error lower than  $\pm 1.2$  °C) of the plates in the gob contact point for a certain temperature set on the thermoregulation device. Five minutes after the plate temperature sensor reached the temperature required, (see paragraph 4.2.4) five measurements were performed with contact thermocouple. Each measurement considered the maximum and minimum temperature of a thermoregulation cycle. Fig. 4.64 shows the results, i.e. temperature average values and their variations for the two plates as functions of the temperature measured by the plate sensor.

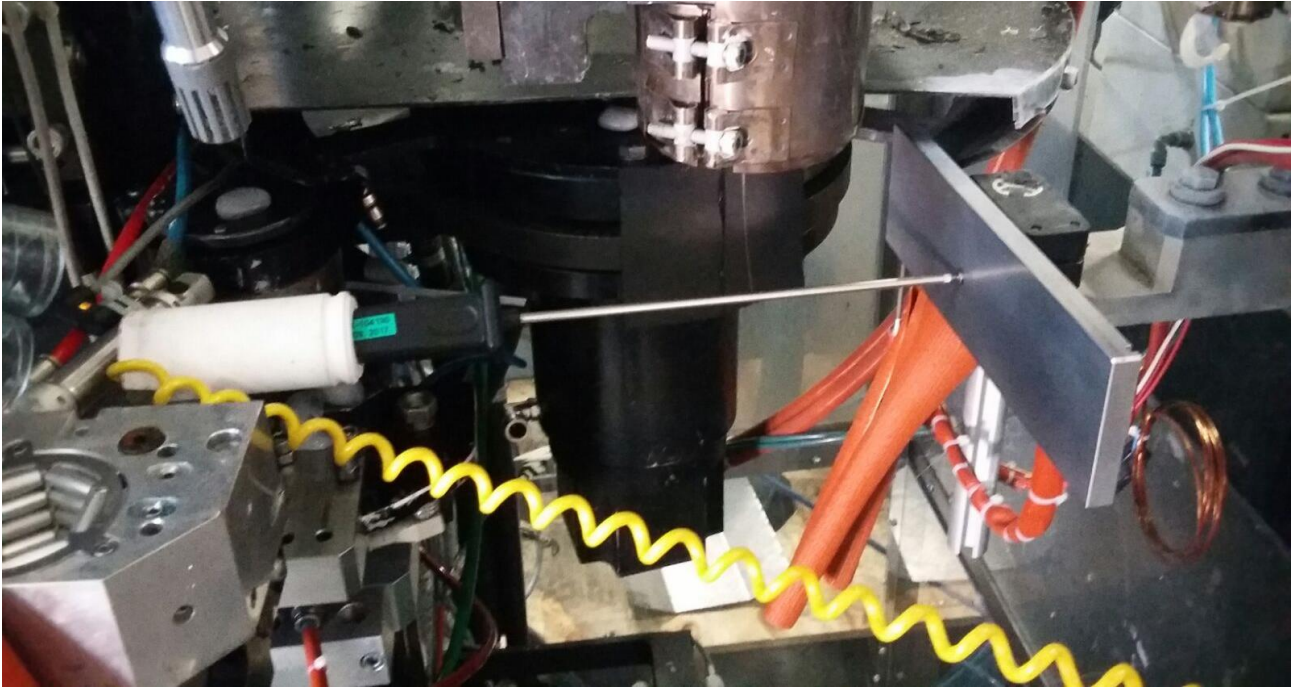


Figure 4.63 Temperature characterization of gob contact point on metal plate.

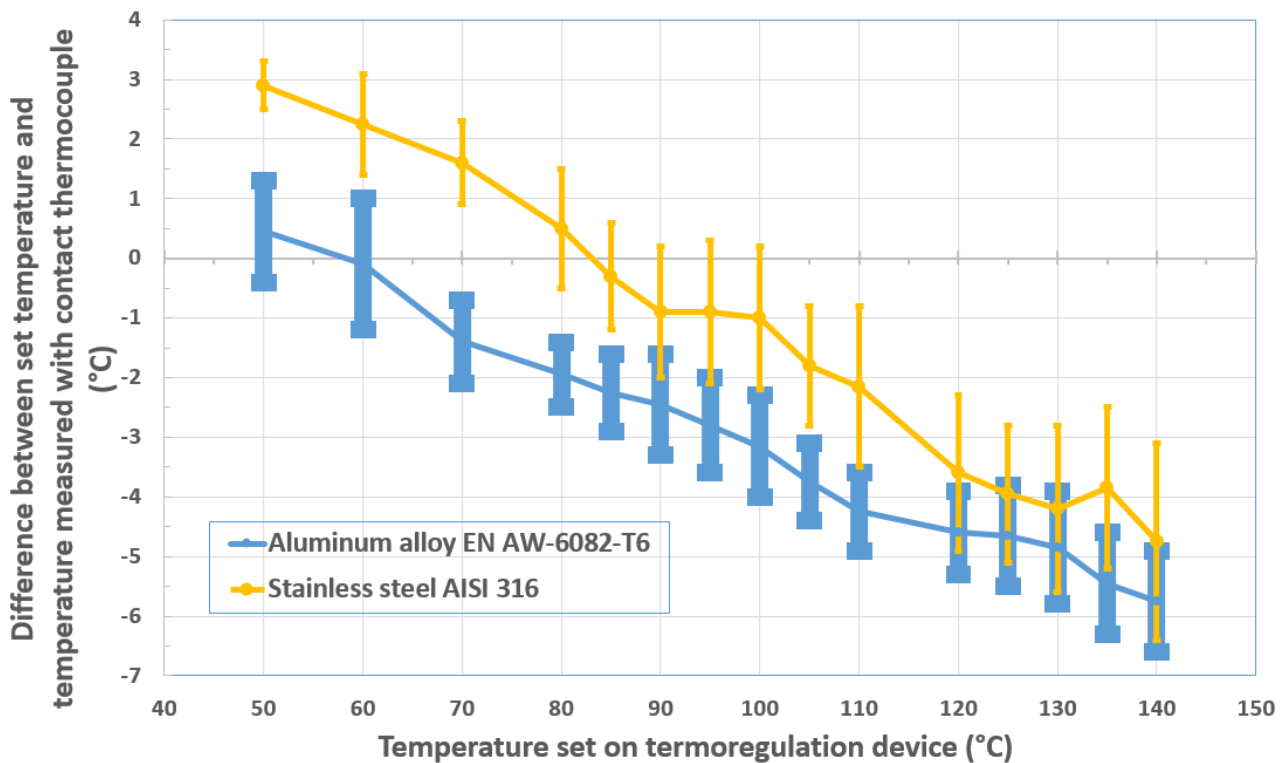


Figure 4.64 Results of temperature characterization of gob contact point on metal plate.

At each temperature, from 50 °C to 140 °C, stainless steel always has a higher temperature compared to aluminum alloy. The difference between the maximum value of stainless steel and the minimum value of aluminum is always lower than 5 °C, while the difference between plates average values is always lower than 3.5 °C.

## 4.6 TEST RESULTS

The test campaign lasted almost three weeks and consisted of 341 valid tests. Among them, 180 were done on stainless steel AISI 316 and 161 on aluminum alloy EN AW-6082-T6, as shown in fig. 4.65. An analysis of more than 50 random videos confirmed the gob trajectory repetitiveness. When tests were completed, the plates roughness and the morphology of the contact zone were checked again. The values were the same measured at the beginning of the test.

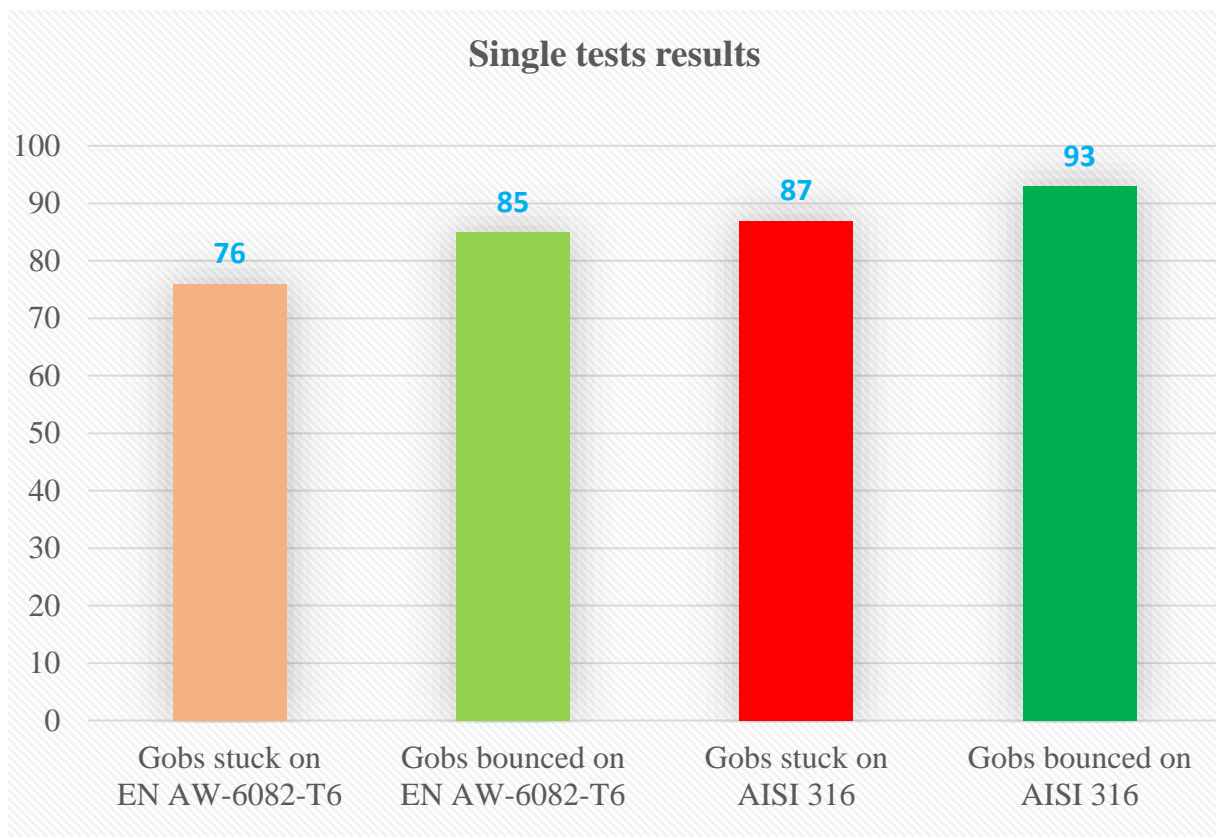


Figure 4.65 Tests results: quantity of gobs stuck and bounced on AISI 316 and EN AW-6082-T6.

### 4.6.1 Effect of plate temperature

Fig. 4.66 illustrates the gobs behavior (after contact with plate) at temperature ranging from 50 °C to 135 °C, separately for aluminum and stainless steel. On x-axis, there are the temperature values measured by the plate sensor and displayed on the thermoregulation device. Yellow arrows highlight a change of behavior in test results. On the y-axis, for each temperature and plate material, there are the number of gobs that bounced and the number of gobs that stuck.

Table 4.8 illustrates, for each temperature required on thermoregulation device, the maximum and minimum temperature measured with contact thermocouple on stainless steel AISI 316 and on aluminum alloy EN AW-6082-T6 plates. The critical temperatures are highlighted in table 4.8 and illustrated more in details in table 4.9 which considers also contact thermocouple and thermometer measuring errors.

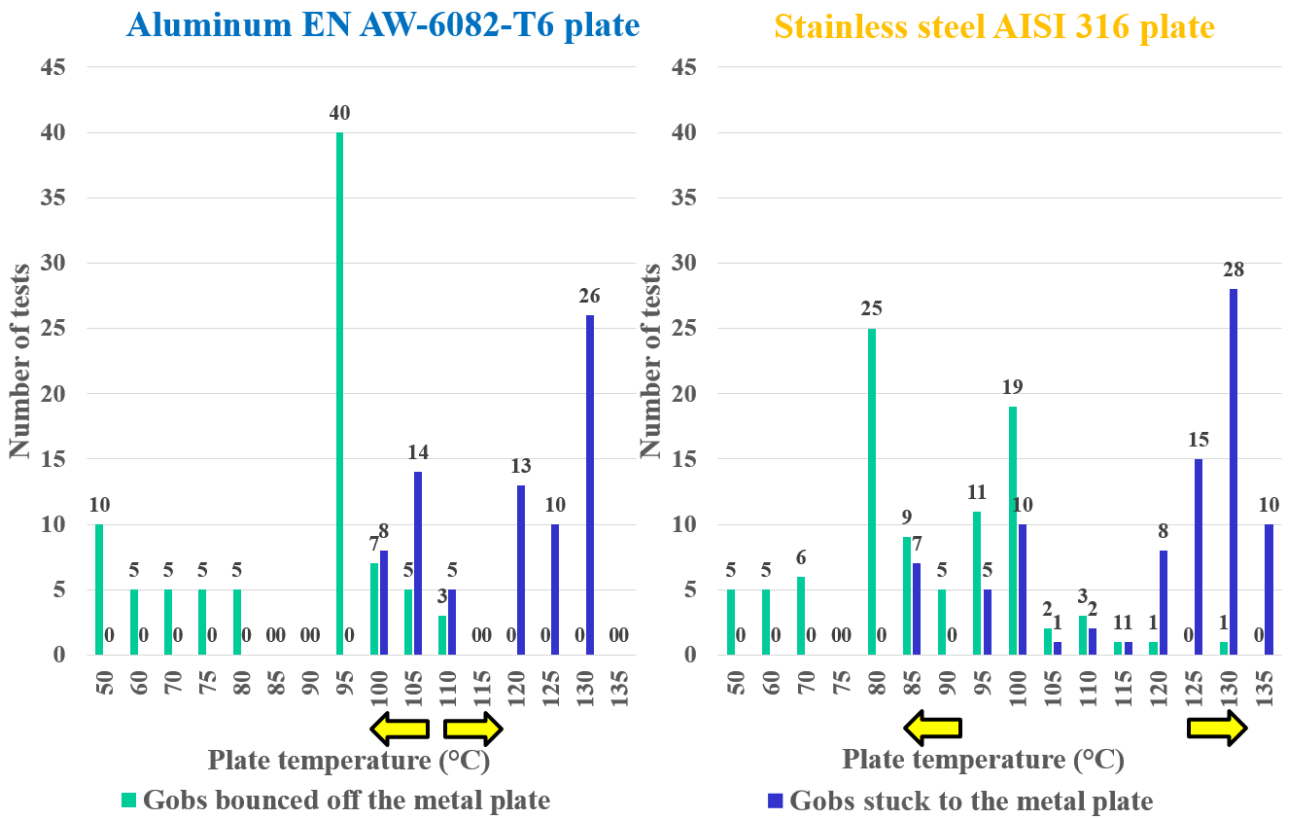


Figure 4.66 Test results: gobs behavior on AISI 316 and EN AW-6082-T6 at different temperatures.

Temperature required on thermoregulation device (°C)	Temperature measured with contact thermocouple (°C)			
	Aluminum alloy EN AW-6082-T6		Stainless steel AISI 316	
	MIN	MAX	MIN	MAX
50	49.6	51.3	52.5	53.3
60	58.8	61	61.4	63.1
70	67.9	69.3	70.9	72.3
80	77.5	78.6	<b>79.5</b>	<b>81.5</b>
85	82.1	83.4	83.8	85.6
90	86.7	88.4	88	90.2
95	<b>91.4</b>	<b>93</b>	92.9	95.3
100	96	97.7	97.8	100.2
105	100.6	101.9	102.2	104.2
110	105.1	106.4	106.5	109.2
120	<b>114.7</b>	<b>116.1</b>	115.1	117.7
125	119.5	121.2	119.9	122.2
130	124.2	126.1	124.4	127.2
135	128.7	130.4	<b>129.8</b>	<b>132.5</b>
140	133.4	135.1	133.6	136.9

Table 4.8 Minimum and maximum temperature measured on plate compared to the required one.

There is a significant difference between stainless steel AISI 316 and aluminum alloy EN AW-6082-T6 plates regarding the highest temperature at which gobs do not stick to metal plate. This difference, as shown in table 4.10, is still remarkable even taking into account the "worst case", i.e. maximum temperature measured on AISI 316 (81.5 °C) and minimum on EN AW-6082-T6 (91.4 °C). The difference is hence of 9.9 °C. Including the maximum value of both repetitiveness errors and accuracy errors of the measuring instrument the minimum value of that difference is 7.5 °C (see table 4.8).

	<b>Highest temperature at which all gobs bounce (°C)</b>	
	<b>Aluminum alloy EN AW-6082-T6</b>	<b>Stainless steel AISI 316</b>
Temperature set on thermoregulation device (°C)	95	80
Highest temperature measured by contact thermocouple (°C)	93	81.5
Lowest temperature measured by contact thermocouple (°C)	91.4	79.5
Average temperature measured by contact thermocouple (°C)	92.2	80.5
Highest temperature measured by contact thermocouple (°C) + maximum accuracy error ( $\pm 1$ °C) + maximum repetitiveness error ( $\pm 0.2$ °C)	94.2	82.7
Lowest temperature measured by contact thermocouple (°C) + maximum accuracy error ( $\pm 1$ °C) + maximum repetitiveness error ( $\pm 0.2$ °C)	90.2	78.3

Table 4.9 Highest temperature at which all gobs bounce considering instrument measuring errors.

<b>Highest temperature at which all gobs bounce: temperature difference between Aluminum alloy EN AW-6082-T6 and Stainless steel AISI 316</b>	
<b>Reference temperature values considered for calculation</b>	<b>Temperature difference value (°C)</b>
Temperature set on thermoregulation device	15
Average temperature measured by contact thermocouple	11.7
Highest temperature difference measured by contact thermocouple	13.5
Lowest temperature difference measured by contact thermocouple	9.9
Highest temperature difference considering also the maximum value of both repetitiveness and accuracy errors	15.9
Lowest temperature difference considering also the maximum value of both repetitiveness and accuracy errors	7.5
<b>Average temperature difference and its tolerance</b>	<b>11.7 <math>\pm</math> 4.2</b>

Table 4.10 Highest temperature at which all gobs bounce: difference between aluminum and stainless steel.

In the other "extreme case", i.e. maximum temperature measured on AISI 316 (79.5 °C) and minimum on EN AW-6082-T6 (93 °C), the difference is hence of 13.5 °C. Considering the maximum value of both repetitiveness and accuracy errors of the measuring instrument the maximum value of that difference is 15.9 °C. The average temperature value of AISI 316 is 80.5 °C while the average value of EN AW-6082-T6 is 92.2 °C so the average difference is 11.7 °C. Finally, regarding the highest temperature at which gobs still bounce, it is higher for EN AW-6082-T6 compared to AISI 316 and that difference of temperature is of 11.7  $\pm$  4.2 °C (see table 4.8).

There is another interesting phenomenon: a difference between EN AW-6082-T6 and AISI 316 in the lowest temperature at which all gobs stick to the plate as shown in table 4.6. The critical temperature is highlighted in table 4.8 and illustrated more in detail in table 4.11 which considers also contact thermocouple and thermometer measuring errors, while table 4.12 illustrates temperature difference. The temperature set on the thermoregulation device is 120 °C for EN AW-6082-T6 (unfortunately there was no time to test also 115 °C) and 135 °C for AISI 316. As regards temperatures measured

with contact thermocouple, the minimum difference (see table 4.10), i.e. maximum temperature on EN AW-6082-T6 (116.1 °C) and minimum temperature on AISI 316 (129.8 °C), is 13.7 °C. Including also the maximum value of both repetitiveness and accuracy errors of the measuring instrument, the minimum value of that difference is 11.3 °C. In the other "extreme case", i.e. maximum temperature measured on AISI 316 (132.5 °C) and minimum on EN AW-6082-T6 (114.7 °C), the difference is hence of 17.8 °C. Considering the maximum value of both repetitiveness and accuracy errors of the measuring instrument, the maximum value of that difference is 20.2 °C.

	<b>Lowest temperature at which all gobs stick (°C)</b>	
	<b>Aluminum alloy EN AW-6082-T6</b>	<b>Stainless steel AISI 316</b>
Temperature set on thermoregulation device (°C)	120	135
Highest temperature measured by contact thermocouple (°C)	116.1	132.5
Lowest temperature measured by contact thermocouple (°C)	114.7	129.8
Average temperature measured by contact thermocouple (°C)	115.4	131.15
Highest temperature measured by contact thermocouple (°C) + maximum accuracy error ( $\pm 1$ °C) + maximum repetitiveness error ( $\pm 0.2$ °C)	117.3	133.7
Lowest temperature measured by contact thermocouple (°C) + maximum accuracy error ( $\pm 1$ °C) + maximum repetitiveness error ( $\pm 0.2$ °C)	113.5	128.6

Table 4.11 Lowest temperature at which all gobs stick considering instrument measuring errors.

<b>Lowest temperature at which all gobs stick: temperature difference between Aluminum alloy EN AW-6082-T6 and Stainless steel AISI 316</b>	
<b>Reference temperature values considered for calculation</b>	<b>Temperature difference value (°C)</b>
Temperature set on thermoregulation device	15
Average temperature measured by contact thermocouple	15.75
Highest temperature difference measured by contact thermocouple	13.7
Lowest temperature difference measured by contact thermocouple	17.8
Highest temperature difference considering also the maximum value of both repetitiveness and accuracy errors	20.2
Lowest temperature difference considering also the maximum value of both repetitiveness and accuracy errors	11.3
<b>Average temperature difference and its tolerance</b>	<b>15.75 <math>\pm</math> 4.45</b>

Table 4.12 Lowest temperature at which all gobs stick: difference between aluminum and stainless steel.

In conclusion, the lowest temperature at which all gobs stick is higher for AISI 316 compared to EN AW-6082-T6 and that difference of temperature is of  $15.75 \pm 4.45$  °C. It is important to underline that this second phenomenon is less remarkable than the first, since only three gobs out of sixty-five stuck on AISI 316 at temperature higher than 110 °C. Since there are no data available on EN AW-6082-T6 at 115 °C, that temperature should not be considered. In this case, there are only two gobs out of sixty-three that stuck at temperature higher than 115°C. The two gobs are test number 72 (120 °C) and test number 380 (130 °C). Table 4.13 and 4.14 respectively illustrate the report of the two

tests. The blade cutting speed is not reported due to SACMI intellectual property policy. Fortunately, the weight of the first gob (380) is known, because it was the last test of the day and the operator had to clean the machine. Since the test had just finished, he knew exactly where the gob fell and was able to register its weight. The latter is lower than the ones of the previous tests at a plate temperature of 130 °C but higher than that of the gob 374, which was done at plate temperature 125 °C. However, it seems that the gob weight does not affect gob adhesiveness, as it will be explained in paragraph 4.6.2.2.

Test number	Test date	Test hour	Plate temperature	Did gob bounce?	Gob weight	PET pellets humidity	Min and Max electrical absorption extrusion screw		Extruder inlet (zone 1)	Melt temperature	Air dew point	Air relative humidity
			(°C)		(g)	(ppm)	(kW)/100	(kW)/100	(°C)	(°C)	(°C)	(%)
<b>AISI 316</b>												
69	04-07-2017	10:10	100				79	87			13	31.1
70	04-07-2017	10:27	110				77	87			12	30.4
71	04-07-2017	10:40	120				71	87			13	31
72	04-07-2017	10:52	120				70	87			12.7	27.3
73	04-07-2017	11:15	130				69	85			12.1	26.1
74	04-07-2017	11:27	130				75	90			11.7	25.4
75	04-07-2017	11:33	130				75	90			12	25.6
76	04-07-2017	11:40	130				82	93			11.8	25.3
77	04-07-2017	11:46	130				75	87			11.4	24.6
	04-07-2017	11:50				26				271		
78	04-07-2017	13:28	125				84	94			11.4	25.9
79	04-07-2017	13:37	125				82	91			12.2	25.1
	04-07-2017	13:44				10						
80	04-07-2017	13:46	125		4.017		78	91			11.2	22.6
81	04-07-2017	13:55	125		4.005		81	91			10.9	22.2
82	04-07-2017	14:01	125		4.03		78	94			11.7	22.4
83	04-07-2017	14:10	120		4.02		77	88			11.2	21
	04-07-2017	14:16				26						
84	04-07-2017	14:18	120		4.021		68	78			11.6	21.6
85	04-07-2017	14:27	120		4.029		55	75			12.7	24.9
86	04-07-2017	14:34	120		4.017		72	86			11.9	23
87	04-07-2017	14:44	120		4.018		68	76			11.5	22.4
88	04-07-2017	15:04	115		4.026		78	98			12.3	23
	04-07-2017	15:16				12						
89	04-07-2017	15:17	110		4.022		65	78			13.5	25.7
90	04-07-2017	15:26	105		4.015		67	83			12.2	22.1
91	04-07-2017	15:33	100				70	91			12.5	22.1
92	04-07-2017	15:37	100				77	86			12.3	21
	04-07-2017	15:42				21						

Table 4.13 Test report of gob 72.

Videos of these two cases were analyzed and they showed no differences that could justify a different behavior compared to the other sixty-one gobs. Fig. 4.67 shows gob trajectory (before plate impact and few instants after it) of test 72, photographing the gob leaving the metal plate after bouncing. The contact (from a gob edge start touching to end of gob edge touching) lasts 0.003 s, so it is the same of other bouncing gobs. Fig. 4.68 shows test 380 gob trajectory, photographing gob leaving the metal plate a few instants after bouncing. The contact lasts from 0.0045 s to 0.005 s, so a 50 % more than the samples. This could be a clue of a limit situation. In fig. 4.68 the trajectory of a gob corner is in cyan (in the previous picture, for example 4.59, it was in red), while the trajectory of the gob center of mass is in red. These two trajectories were tracked for kinetic energy evaluation (see paragraphs

4.4, 4.5.2 and 4.6.4). Fig. 4.69 illustrates gob 378 which had about the same value of the monitored parameters and the same trajectories of gob 380 but stuck to the metal plate ten minutes before gob 380 was cut (see table 4.13).

Test number	Test date	Test hour	Plate temperature (°C)	Did gob bounce?	Gob weight (g)	PET pellets humidity (ppm)	Min and Max electrical absorption extrusion screw		Extruder inlet (zone 1) (°C)	Melt temperature (°C)	Air dew point (°C)	Air relative humidity (%)
							(kW)/100	(kW)/100				
<b>AISI 316</b>												
	12-07-2017	13:55								278		
366	12-07-2017	14:00	100				76	81	250.5		13.8	23.6
367	12-07-2017	14:04	100				84	95	251.8		14	23.1
368	12-07-2017	14:08	100				73	86	249		11.1	21
369	12-07-2017	14:12	100		4.034		84	92	250.2		10.6	19.4
370	12-07-2017	14:17	100				78	87	248		14.4	23.8
	12-07-2017	14:22				19						
	12-07-2017	14:22								277		
371	12-07-2017	14:27	125		4.028		79	85	248.6		12.5	19.6
372	12-07-2017	14:32	125		4.042		79	86	254.6		13.2	22.6
373	12-07-2017	14:37	125		4.039		82	88	246.8		13.6	22.6
374	12-07-2017	14:42	125		4.022		81	87	254.1		15.3	26
375	12-07-2017	14:47	125		4.042		78	84	247		12.8	21.8
	12-07-2017	14:57				21						
	12-07-2017	14:57								278		
376	12-07-2017	15:01	130		4.043		79	87	249.4		13.6	26.1
377	12-07-2017	15:06	130		4.035		82	87	246.8		16.3	27.5
378	12-07-2017	15:11	130		4.037		85	93	247.5		14	23.8
379	12-07-2017	15:16	130		4.042		50	59	251.1		14.2	23.2
380	12-07-2017	15:22	130		4.022		86	98	246.1		14.1	23.3
	12-07-2017	15:40				17						
	12-07-2017	15:40								278		

Table 4.14 Test report of gob 380.

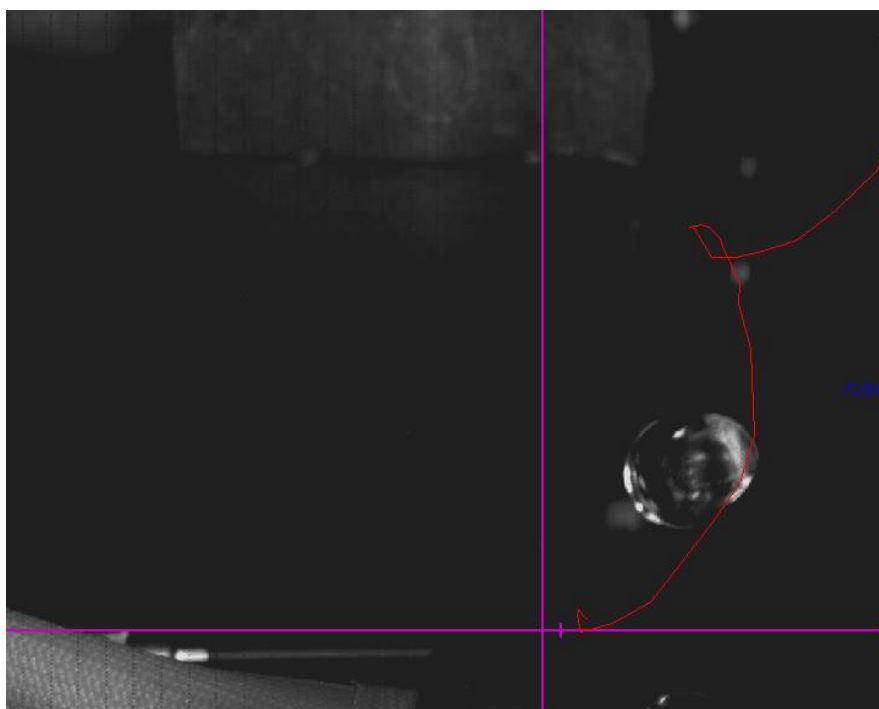


Figure 4.67 Test 72: gob after bouncing on AISI 316 plate at 120 °C.

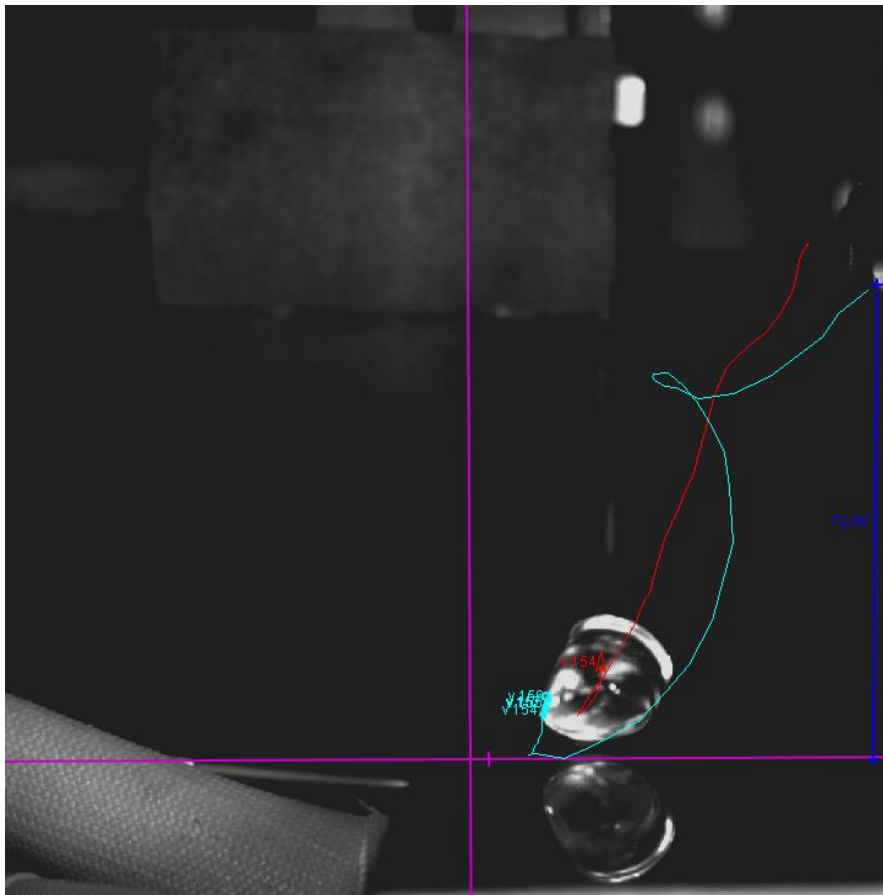


Figure 4.68 Test 380: gob after bouncing on AISI 316 plate at 130 °C.

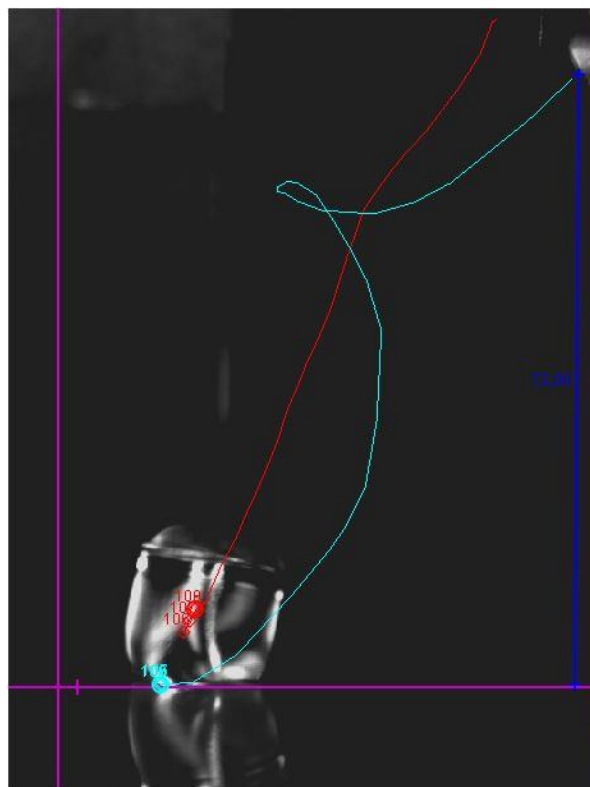


Figure 4.69 Test 378: gob sticking on AISI 316 plate at 130 °C.

A further analysis of different parameters impact on gob 72 is illustrated in paragraph 4.6.2.2.

Before trying to give an explanation for these two phenomena, never described in literature so far, the impact of the other monitored parameters is analyzed.

#### 4.6.2 Influence of monitored parameters variation on adhesiveness

In the previous paragraphs the huge impact of metal temperature on PET adhesiveness was described. Theoretically, there should be no other variables during the test, apart from the plate material, but in an industrial machine all parameters have a range of variation. Table 4.15 shows the maximum and minimum values of the monitored parameters during the test. The pink lines refer only to AISI 316. The light blue lines refer only to EN AW-6082-T6 and the green lines refer to both tests together.

Monitored Parameters	Gob weight	PET pellets humidity	Electrical absorption extrusion screw	Extruder inlet (zone 1)	Melt temperature	Air dew point	Air relative humidity
Unit of measurement	(g)	(ppm)	(kW/100)	(°C)	(°C)	(°C)	(%)
Plate material	<b>STAINLESS STEEL AISI 316</b>						
Max value of parameter	4.079	40	98	256.7	280	17.4	37
Min value of parameter	4.0045	9	40	244.4	271	5.1	14.6
Plate material	<b>ALUMINUM EN AW-6082-T6</b>						
Max value of parameter	4.0869	50	98	255.9	280	15.5	35.8
Min value of parameter	4.0087	6	49	244.3	274	7.1	14.2
Plate material	<b>STAINLESS STEEL AISI 316 and ALUMINUM EN AW-6082-T6</b>						
Max value of parameter	4.0869	50	98	256.7	280	17.4	37
Min value of parameter	4.0045	6	40	244.3	271	5.1	14.2

Table 4.15 Maximum and minimum values of the monitored parameters during tests on different plate materials.

The following tables (4.16 to 4.17) illustrate for each metal plate temperature (measured by plate sensor), starting from 80 °C, the maximum and minimum value of all parameters for tests resulting in gob bouncing and for tests resulting in gob sticking. Results for AISI 316 and EN-AW-6082-T6 are shown separately. In the tables, the date of the tests and the number of the tests done are also indicated. The cutting speed values are not reported according to SACMI intellectual property policy.

	Gob weight	PET pellets humid.	Min and Max electrical absorption extrusion screw		Extr. inlet	Melt	Air dew point	Air rel. hum.	Days of tests	Number of tests
			(kW)/100	(kW)/100						
<b>STAINLESS STEEL AISI 316</b>										
<b>Gob bouncing</b>										
max	n. a.	33	87	96	254.7	278	16.5	31.1	13,14,17 - 07-2017	25
min		10	55	62	245.8	275	5.1	15.3		
<b>ALUMINUM ALLOY EN AW-6082-T6</b>										
<b>Gob bouncing</b>										
max	n. a.	26	86	93	252	n. a.	13.2	24.5	11-07-2017	5
min		24	60	71	245.6		10.6	19.8		

Table 4.16 Parameters variation of tests at plate temperature equal to 80 °C.

	Gob weight	PET pellets humid.	Min and Max electrical absorption extrusion screw		Extr. inlet	Melt	Air dew point	Air rel. hum.	Days of tests	Number of tests
	(g)	(ppm)	(kW)/100	(kW)/100	(°C)	(°C)	(°C)	(%)		
<b>STAINLESS STEEL AISI 316</b>										
<b>Gob bouncing</b>										
max	n. a.	40	91	98	253.9	279	16.3	26.4	3,14,17-07-2017	9
min		18	63	71	246.1	275	6.2	16.1		
<b>Gob sticking</b>										
max	4.0539	40	91	96	253.9	278	15.1	30.2	14,17-07-2017	7
min	4.014	22	57	64	245	277	5.2	14.6		

Table 4.17 Parameters variation of tests at plate temperature equal to 85 °C.

In tables 4.17, 4.20 and 4.21, which respectively correspond to a plate temperature of 85 °C, 100 °C and 105 °C, there is no significant difference between sticking and bouncing gobs as regards the registered parameters.

	Gob weight	PET pellets humid.	Min and Max electrical absorption extrusion screw		Extr. inlet	Melt	Air dew point	Air rel. hum.	Days of tests	Number of tests
	(g)	(ppm)	(kW)/100	(kW)/100	(°C)	(°C)	(°C)	(%)		
<b>STAINLESS STEEL AISI 316</b>										
<b>Gob bouncing</b>										
max	n. a.	26	84	92	247.6	280	14.4	37	05-07-2017	5
min		9	81	85	247.6	280	13.7	29.2		

Table 4.18 Parameters variation of tests at plate temperature equal to 90 °C.

	Gob weight	PET pellets humid.	Min and Max electrical absorption extrusion screw		Extr. inlet	Melt	Air dew point	Air rel. hum.	Days of tests	Number of tests
	(g)	(ppm)	(kW)/100	(kW)/100	(°C)	(°C)	(°C)	(%)		
<b>STAINLESS STEEL AISI 316</b>										
<b>Gob bouncing</b>										
max	n. a.	35	83	91	254.8	280	14.7	35.9	3,5,12-07-2017	11
min		9	54	60	246.4	277	9.5	19.6		
<b>Gob sticking</b>										
max	4034	20	82	86	253.1	277	16.8	30.6	13-07-2017	5
min	4.0165	16	56	65	247.1	277	15.2	27		
<b>ALUMINUM ALLOY EN AW-6082-T6</b>										
<b>Gob bouncing</b>										
max	n. a.	50	87	98	255.9	278	15	35.8	5,6,7,10,11-07-2017	40
min		20	0.58	0.67	244.9	278	7.6	14.2		

Table 4.19 Parameters variation of tests at plate temperature equal to 95 °C.

At plate temperature of 95 °C, see table 4.19, on AISI 316, the only differences in the monitored parameters between sticking and bouncing is that the latter has a slightly higher air dew point.

Further considerations on this point are in paragraph 4.6.2.2.

	Gob weight	PET pellets humid.	Min and Max electrical absorption extrusion screw		Extr. inlet	Melt	Air dew point	Air rel. hum.	Days of tests	Number of tests
	(g)	(ppm)	(kW)/100	(kW)/100	(°C)	(°C)	(°C)	(%)		
<b>STAINLESS STEEL AISI 316</b>										
<b>Gob bouncing</b>										
max	n. a.	23	84	95	252.2	279	14.4	34	3,4,5,12-07-2017	19
min		12	63	70	246.2	271	9.6	19.2		
<b>Gob sticking</b>										
max	4.0397	26	86	92	254.8	277	15.5	33.6	3,5,12,13-07-2017	10
min	4.0145	22	59	65	244.4	274	9.2	19.4		
<b>ALUMINUM ALLOY EN AW-6082-T6</b>										
<b>Gob bouncing</b>										
max	n. a.	24	85	95	254.8	280	13.3	25.8	5,10,11-07-2017	7
min		17	60	67	245.5	278	10.6	19		
<b>Gob sticking</b>										
max	5.6095	28	82	90	253.5	277	13.2	24.4	5,10,11-07-2017	8
min	4.0244	26	59	67	245.6	277	9.8	18.2		

Table 4.20 Parameters variation of tests at plate temperature equal to 100 °C.

	Gob weight	PET pellets humid.	Min and Max electrical absorption extrusion screw		Extr. inlet	Melt	Air dew point	Air rel. hum.	Days of tests	Number of tests
	(g)	(ppm)	(kW)/100	(kW)/100	(°C)	(°C)	(°C)	(%)		
<b>STAINLESS STEEL AISI 316</b>										
<b>Gob bouncing</b>										
max	n. a.	23	81	87	254.1	275	12.2	31.3	4,5-07-2017	2
min		21	74	85	254.1	275	12	21.6		
<b>Gob sticking</b>										
gob 90	4.0147	n. a.	67	83	n. a.	n. a.	12.2	22.1	04-07-2017	1
<b>ALUMINUM ALLOY EN AW-6082-T6</b>										
<b>Gob bouncing</b>										
max	n. a.	28	85	93	253.6	280	11.9	24.3	06-07-2017	5
min		24	54	63	245.5	275	10.7	20.4		
<b>Gob sticking</b>										
max	4.0517	33	84	92	253.3	277	11.4	27.1	6,7-07-2017	14
min	4.0087	16	49	58	245.5	276	7.8	15.1		

Table 4.21 Parameters variation of tests at plate temperature equal to 105 °C.

At plate temperature of 110 °C, table 4.22, on EN-AW-6082-T6, the only differences in the monitored parameters between sticking and bouncing is that the former has a slightly higher air dew point. On AISI 316 it is the contrary as it will be illustrated in paragraph 4.6.2.2.

	Gob weight	PET pellets humid.	Min and Max electrical absorption extrusion screw		Extr. inlet	Melt	Air dew point	Air rel. hum.	Days of tests	Number of tests
	(g)	(ppm)	(kW)/100	(kW)/100	(°C)	(°C)	(°C)	(%)		
<b>STAINLESS STEEL AISI 316</b>										
<b>Gob bouncing</b>										
max	n. a.	n. a.	77	87	251.8	275	12.5	30.4	4,5-07-2017	3
min			75	81	251.8	275	11.9	21.7		
<b>Gob sticking</b>										
max	4.0387	12	76	81	n. a.	n. a.	13.5	25.7	04-07-2017	2
min	4.0215	12	65	78			13.1	23.1		
<b>ALUMINUM ALLOY EN AW-6082-T6</b>										
<b>Gob bouncing</b>										
max	n. a.	31	72	80	255.3	278	14.3	25.2	05-07-2017	3
min		17	66	75	246.2	274	12.6	23.2		
<b>Gob sticking</b>										
max	4.0628	20	80	90	255.1	278	10.7	18.9	07-07-2017	5
min	4.0173	16	52	61	247.5	276	8.1	14.8		

Table 4.22 Parameters variation of tests at plate temperature equal to 110 °C.

	Gob weight	PET pellets humid.	Min and Max electrical absorption extrusion screw		Extr. inlet	Melt	Air dew point	Air rel. hum.	Days of tests (and hour)	Number of tests
	(g)	(ppm)	(kW)/100	(kW)/100	(°C)	(°C)	(°C)	(%)		
<b>STAINLESS STEEL AISI 316</b>										
<b>Gob bouncing</b>										
gob 99	n. a.	n. a.	74	83	n. a.	n. a.	11.6	20.2	04-07-2017 (16:17)	1
<b>Gob sticking</b>										
gob 88	4.026	12	78	98	n. a.	n. a.	12.3	23	04-07-2017 (15:04)	1

Table 4.23 Parameters variation of tests at plate temperature equal to 115 °C.

	Gob weight	PET pellets humid.	Min and Max electrical absorption extrusion screw		Extr. inlet	Melt	Air dew point	Air rel. hum.	Days of tests	Number of tests
	(g)	(ppm)	(kW)/100	(kW)/100	(°C)	(°C)	(°C)	(%)		
<b>STAINLESS STEEL AISI 316</b>										
<b>Gob bouncing</b>										
gob 72	n. a.	n. a.	70	87	n. a.	n. a.	12.7	27.3	04-07-2017	1
<b>Gob sticking</b>										
max	4.0294	26	81	89	251.9	275	13	31	4,5-07-2017	8
min	4.0171	23	55	75	245.6	275	11.2	21		
<b>ALUMINUM ALLOY EN AW-6082-T6</b>										
<b>Gob sticking</b>										
max	4.043	19	87	95	253.2	280	12.8	24.6	5,6,7-07-2017	13
min	4.0169	6	57	67	244.3	274	7.6	15.7		

Table 4.24 Parameters variation of tests at plate temperature equal to 120 °C.

Table 4.23 illustrates tests at plate temperature of 115 °C: one gob stuck, one gob bounced. The tests were done on the same day at 73 minutes of distance. Among the registered parameters, it seems there are no significant differences that could justify the gob different behavior.

	Gob weight	PET pellets humid.	Min and Max electrical absorption extrusion screw		Extr. inlet	Melt	Air dew point	Air rel. hum.	Days of tests	Number of tests
	(g)	(ppm)	(kW)/100	(kW)/100	(°C)	(°C)	(°C)	(%)		
<b>STAINLESS STEEL AISI 316</b>										
<b>Gob sticking</b>										
max	4.0531	26	84	94	254.6	278	16.5	27.3	4,12,13-07-2017	15
min	4.0045	10	53	61	246.7	277	10.9	19.6		
<b>ALUMINUM ALLOY EN AW-6082-T6</b>										
<b>Gob sticking</b>										
max	4.0517	24	84	90	254	278	13.1	24.2	10,11-07-2017	10
min	4.0316	17	53	60	245.3	277	10.8	18.7		

Table 4.25 Parameters variation of tests at plate temperature equal to 125 °C.

	Gob weight	PET pellets humid.	Min and Max electrical absorption extrusion screw		Extr. inlet	Melt	Air dew point	Air rel. hum.	Days of tests	Number of tests
	(g)	(ppm)	(kW)/100	(kW)/100	(°C)	(°C)	(°C)	(%)		
<b>STAINLESS STEEL AISI 316</b>										
<b>Gob bouncing</b>										
gob 380	4.0223	17	86	98	246.1	278	14.1	23.3	12-07-2017	1
<b>Gob sticking</b>										
max	4.0572	33	88	95	254.9	278	16.3	27.7	3,4,5,12,13,14,17-07-17	28
min	4.0129	14	40	48	244.9	275	5.2	15.1		
<b>ALUMINUM ALLOY EN AW-6082-T6</b>										
<b>Gob sticking</b>										
max	4.0869	28	84	94	255.5	280	15.5	29.9	5,6,7,10,11 - 07-2017	25
min	4.0122	21	56	68	245.5	274	7.1	14.7		

Table 4.26 Parameters variation of tests at plate temperature equal to 130 °C.

At plate temperature equal to 130 °C, between the monitored parameters, there is no significant difference that could explain why gob 380 bounced and the others did not.

	Gob weight	PET pellets humid.	Min and Max electrical absorption extrusion screw		Extr. inlet	Melt	Air dew point	Air rel. hum.	Days of tests	Number of tests
	(g)	(ppm)	(kW)/100	(kW)/100	(°C)	(°C)	(°C)	(%)		
<b>STAINLESS STEEL AISI 316</b>										
<b>Gob sticking</b>										
max	4.079	20	90	96	252	278	17.4	28.3	13,17-07-2017	10
min	4.0109	17	60	72	245.1	277	5.8	17		

Table 4.27 Parameters variation of tests at plate temperature equal to 135 °C.

Table 4.27 illustrates that, at high plate temperature (135 °C), a huge difference in air dew point did not affect PET gob adhesiveness to the metal plate.

#### 4.6.2.1 Gob weight

One hundred and fifty gobs were weighed. The graph below (fig.4.70) shows gobs distribution in order of weight. Gob 351 (5.6095 g) has not been included otherwise the zoom on y-axis should have been reduced of at least 20 times. The almost linear trend shows that, from 4.01 g to 4.054 g, the probability to have a gob in that interval of weight is almost equally distributed.

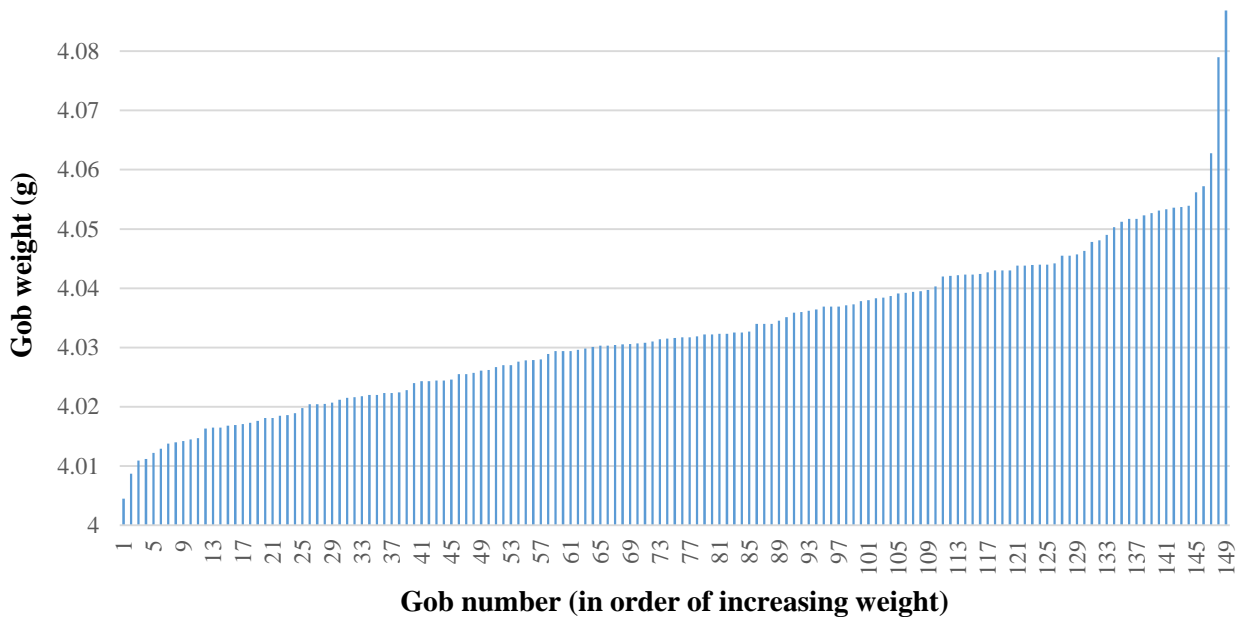


Figure 4.70 Gob weight distribution.

The heaviest gobs in fig.4.70 are 290 (4.0628 g), 422 (4.079 g) and 304 (4.0869 g). The lightest weights 4.0045 g. Table 4.28 shows average gob weight and standard deviation for three different sample compositions.

Sample composition	Average gob weight (g)	Gob weight standard deviation (g)
150 gobs	4.0433	0.1294
149 gobs (test 351 is not included)	4.0328	0.0132
146 gobs (tests 290, 422, 304, 351 are not included)	4.0319	0.0117

Table 4.28 Average gob weight and its standard deviation for three different sample compositions.

Test 351 resulted in gob sticking to the aluminum plate, as shown in table 4.29. Table 4.30 shows the weights of the sticking gobs which were cut almost five hours earlier than gob 351. In this interval of time all the gobs bounced so it was not possible to weigh them. The minimum weight of the gob in table 4.30 is 4.0322 g and its maximum is 4.0478 g, so these values are not at the graph (fig. 4.70) extremities. The video of gob 351 was checked and compared with the video of the following test, where the gob 352 stuck and with that of the preceding one where gob 350 bounced. The pictures (taken by videos) of gobs before cutting clearly demonstrate that gob 351 is much longer than 352 (see fig. 4.71). Fig. 4.72 shows the comparison between gob 351 and gob 350. The size difference is quite evident too.

Test number	Test date	Test hour	Plate temperature (°C)	Did gob bounce?	Gob weight (g)	PET pellets humidity (ppm)	Min and Max electrical absorption extrusion screw		Extruder inlet (zone 1) (°C)	Melt temperature (°C)	Air dew point (°C)	Air relative humidity (%)
							(kW)/100	(kW)/100				
<b>AISI 316</b>												
349	11-07-2017	14:54	80				81	90	248.3		10.6	19.8
350	11-07-2017	15:00	80				86	93	252		11.2	21.9
	11-07-2017	15:05				26						
	11-07-2017	15:05								*		
351	11-07-2017	15:09	100		5.6095		69	76	253		13.2	24.4
352	11-07-2017	15:15	100		4.0537		59	67	246.3		11.4	21
353	11-07-2017	15:19	100		4.0533		80	85	248.6		11.5	21.9
354	11-07-2017	15:24	100				60	67	246.5		11.9	22.1
355	11-07-2017	15:29	100		4.0317		63	70	248.3		11.6	22.7
	11-07-2017	15:32				24						
	11-07-2017	15:32								*		
356	11-07-2017	15:45	125		4.0319		69	78	250.1		12.2	22.9
357	11-07-2017	15:50	125		4.0438		74	82	246.8		12.3	22.8
358	11-07-2017	15:55	125		4.0364		76	84	253.2		12.4	24

\* Immersion thermocouple was unavailable

Table 4.29 Part of a daily test report including the heaviest gob (351).

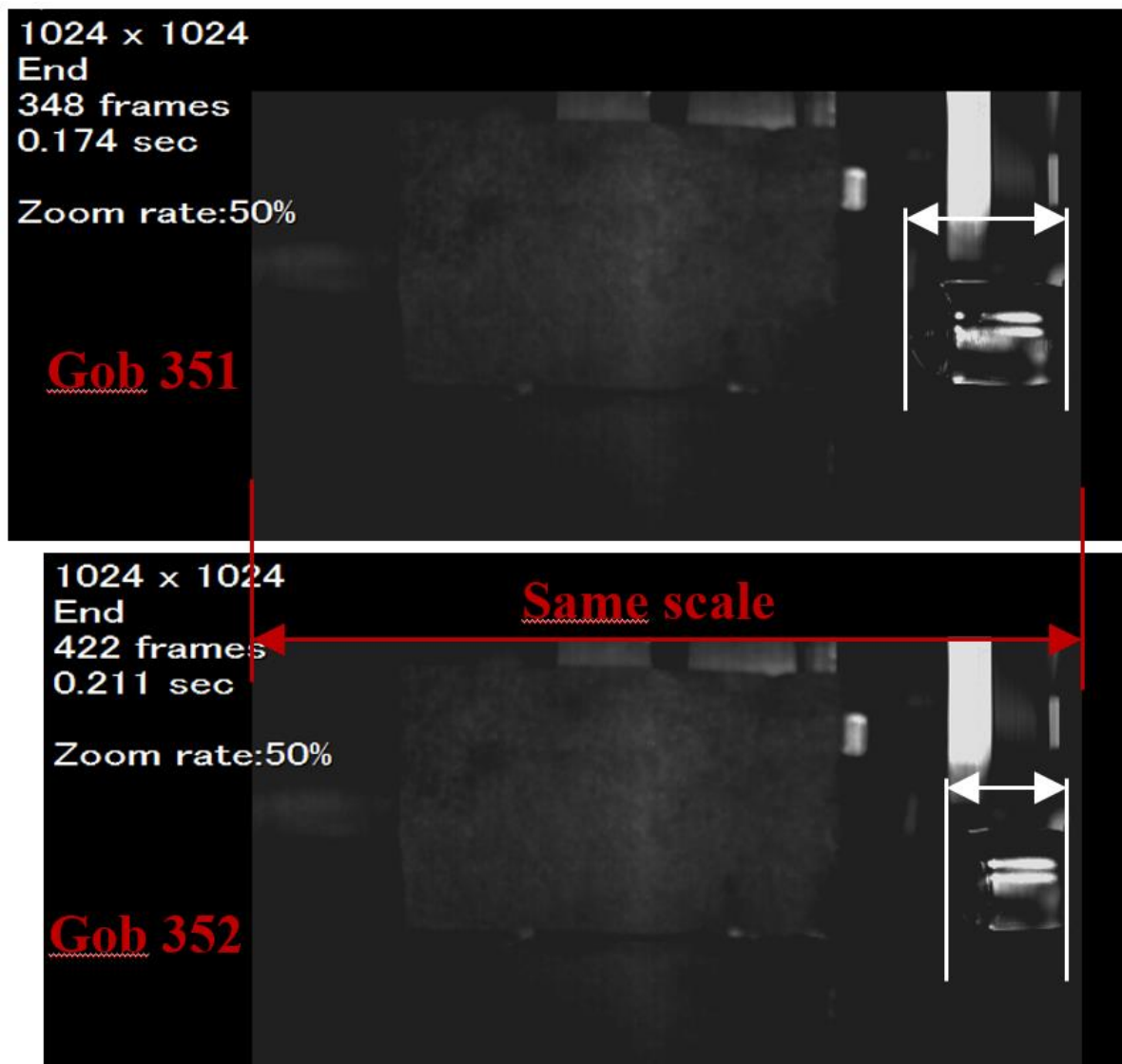


Figure 4.71 Comparison between gob 351 (top image) and gob 352 (bottom image).

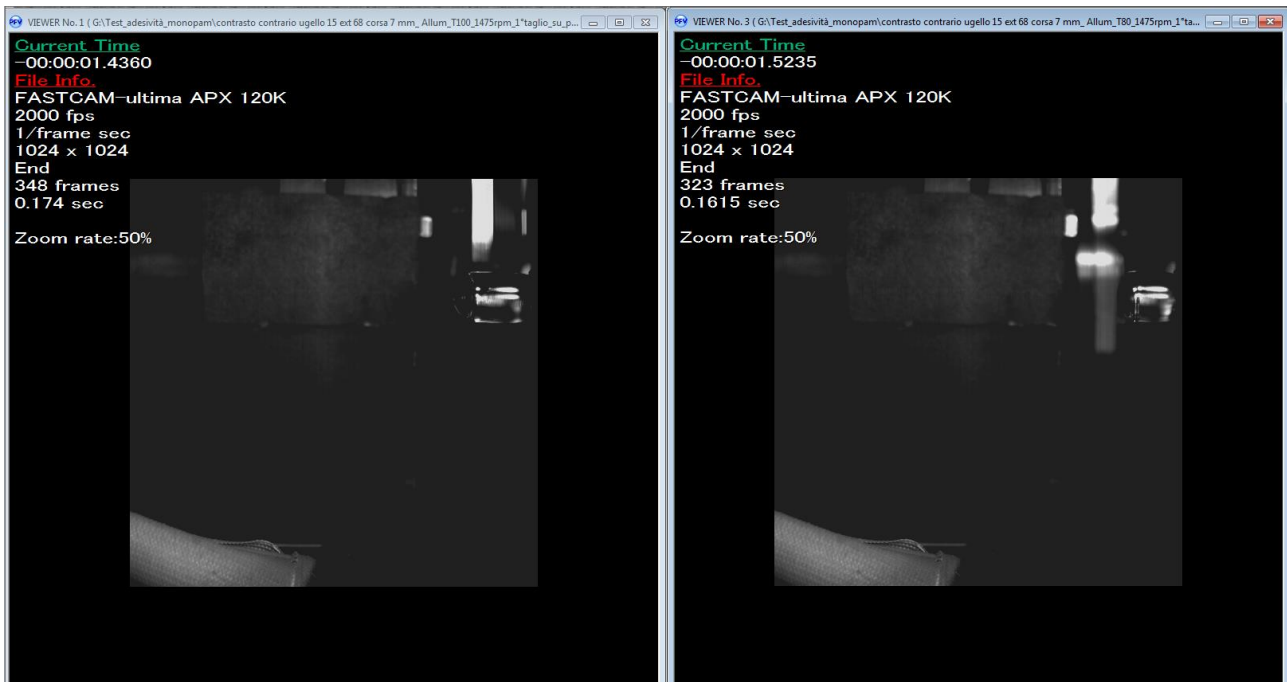


Figure 4.72 Comparison between gob 351 (on the left) and gob 350 (on the right).

Test number	Test date	Test hour	Plate temperature	Did gob bounce?	Gob weight	PET pellets humidity	Min and Max electrical absorption extrusion screw		Extruder inlet (zone 1)	Melt temperature	Air dew point	Air relative humidity
			(°C)		(g)	(ppm)	(kW)/100	(kW)/100	(°C)	(°C)	(°C)	(%)
<b>EN-AW-6082-T6</b>												
	11-07-2017	10:10				22						
	11-07-2017	10:10								277		
326	11-07-2017	10:14	130		4.038		82	87	252.4		14	27.7
327	11-07-2017	10:22	130		4.0478		70	78	246.2		13.8	25.8
328	11-07-2017	10:26	130		4.0322		80	87	251.7		15.5	29.2
329	11-07-2017	10:31	130		4.0384		81	89	245.8		14.2	29.9
330	11-07-2017	10:38	130		4.0362		74	84	255.5		13.8	25.9
	11-07-2017	12:54				25						

Table 4.30 Part of a daily test report including the sticking gobs just before the heaviest one (351).

Other videos were checked, particularly those of the "sticking/non-sticking" temperatures, i.e. temperatures at which gobs showed an ambivalent behavior. For what can be appreciated by videos, all gobs dimensions were equal. The cause of gob 351 big size is hence not clear, the more probable explanation could be an isolated software error of the prototypal machine. Anyway, despite a weight 40 % higher than the average, the sticking behavior was the same as the following two gobs at the same test conditions. Therefore, it seems that the biggest variations in gobs weight do not affect the gobs contact behavior with the metal plate.

Another proof of the previous sentence is the behavior of the heaviest gobs described as follows:

- Gob 351, as previously said, stuck on EN-AW-6082-T6 plate at 100 °C like the following two ones. Gob 354 (always EN-AW-6082-T6 plate at 100 °C) bounced but comparing the videos with the previous two ones (see fig.4.73), the cause seems not its weight, since gobs size look similar. On the contrary, size difference between gob 354 and gob 351 is quite evident, as shown in picture 4.74.
- Gob 304 stuck like all other gobs on EN-AW-6082-T6 plate at 130 °C.
- Gob 422 it stuck like all other gobs on AISI 316 plate at 135 °C.

- Gob 290 stuck on EN-AW-6082-T6 plate at 110 °C like the four previous gobs.

To sum up, the heaviest gobs show a behavior similar to the average weighted gobs at the same plate temperature and material.



Figure 4.73 Comparison between gob 354 (on the left) and gob 352 (on the right).



Figure 4.74 Comparison between gob 354 (on the left) and gob 351 (on the right).

#### 4.6.2.2 Water content

Since PET is a polycondensation polymer and since polycondensation is an equilibrium reaction, heating PET in the presence of water can reverse the reaction, i.e. hydrolytic depolymerization can occur. That is why literature recommends accuracy in PET dehumidification before extrusion and a water content in PET lower than 50 ppm [3]. This is the highest level that was measured by PET hygrometer during a test on the EN AW-6082-T6 plate, while on AISI 316 the highest level measured was 40 ppm. Values of PET pellets water content measured during tests seem not to influence gob adhesiveness. An example are tests on EN AW-6082-T6 at plate temperature equal to 110 °C where the PET pellets of the sticking gobs have between 16 and 20 ppm of water content, while those of the bouncing ones have between 17 and 31 ppm of water content.

As far as the air humidity is concerned, fig. 4.75 illustrates air dew point effects on the behavior of gob-metal plate contact on AISI and EN AW-6082-T6 plates at different plate temperatures.

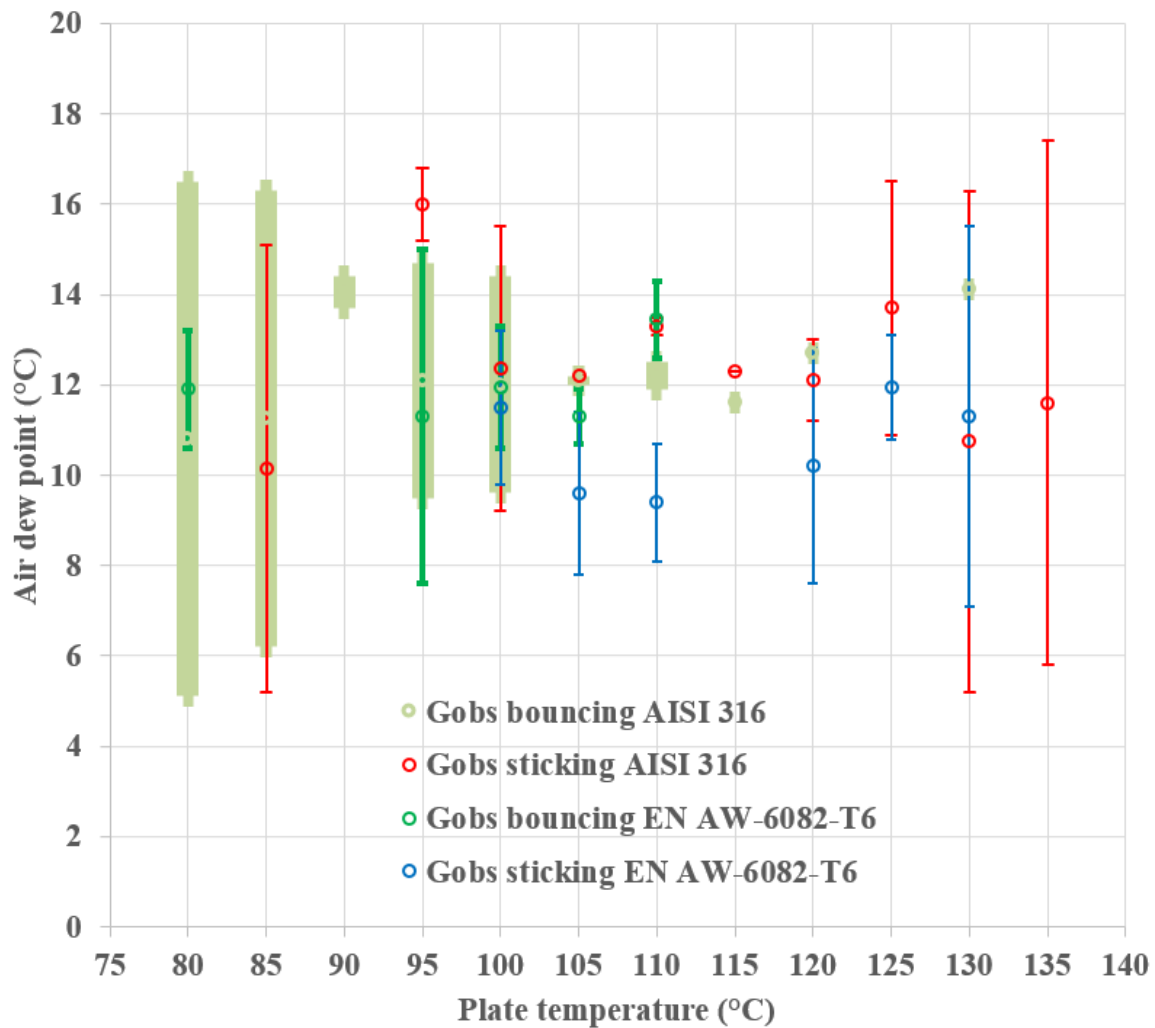


Figure 4.75 Range of gobs sticking and bouncing air dew point at different plate temperature and material.

Below are some considerations on certain plate temperatures:

- T = 85 °C. No significant difference between sticking and non-sticking. On AISI 316, air dew point higher than 15.1 °C results in bouncing.
- T = 95 °C. On AISI 316, air dew point higher than 15.2 °C results in sticking.
- T = 110 °C. On EN AW-6082-T6, air dew point higher than 12.6 °C results in gob bouncing, while lower than 10.7 results in gob sticking. On AISI 316 it is almost the contrary.
- T = 120 °C. Monitored parameters values of gob 72 (air dew point = 12.7 °C), which bounced on AISI 316 plate, showed no differences compared to the ones of the other eight gobs that stuck to it (see tables 4.24 and 4.31). Anyway, from test videos it seems that at this temperature a lower dew point favors the adhesiveness. Gob 71 was tested with an air dew point of 13 °C. After contact (see sequence in fig. 4.76, each image is 0.001 s after the previous one), it started bouncing but it did not lose the contact with the plate making a half round and finally sticking with an edge to the metal plate, as shown in fig. 4.77. Gob 123, which also bounced on AISI 316 at the same plate temperature and which was tested with air dew point equal to 12.8 °C, behaved in a similar way as shown in fig. 4.78. On the other hand, gob 83 (see fig. 4.79) tested with an air dew point equal to 11.2 °C resulted in a

complete sticking on the plate without signs of bouncing. Fig. 4.80 shows gob 257 which stuck perfectly on EN-AW-6082-T6 plate at 120 °C and an air dew point value of 12.8 °C.

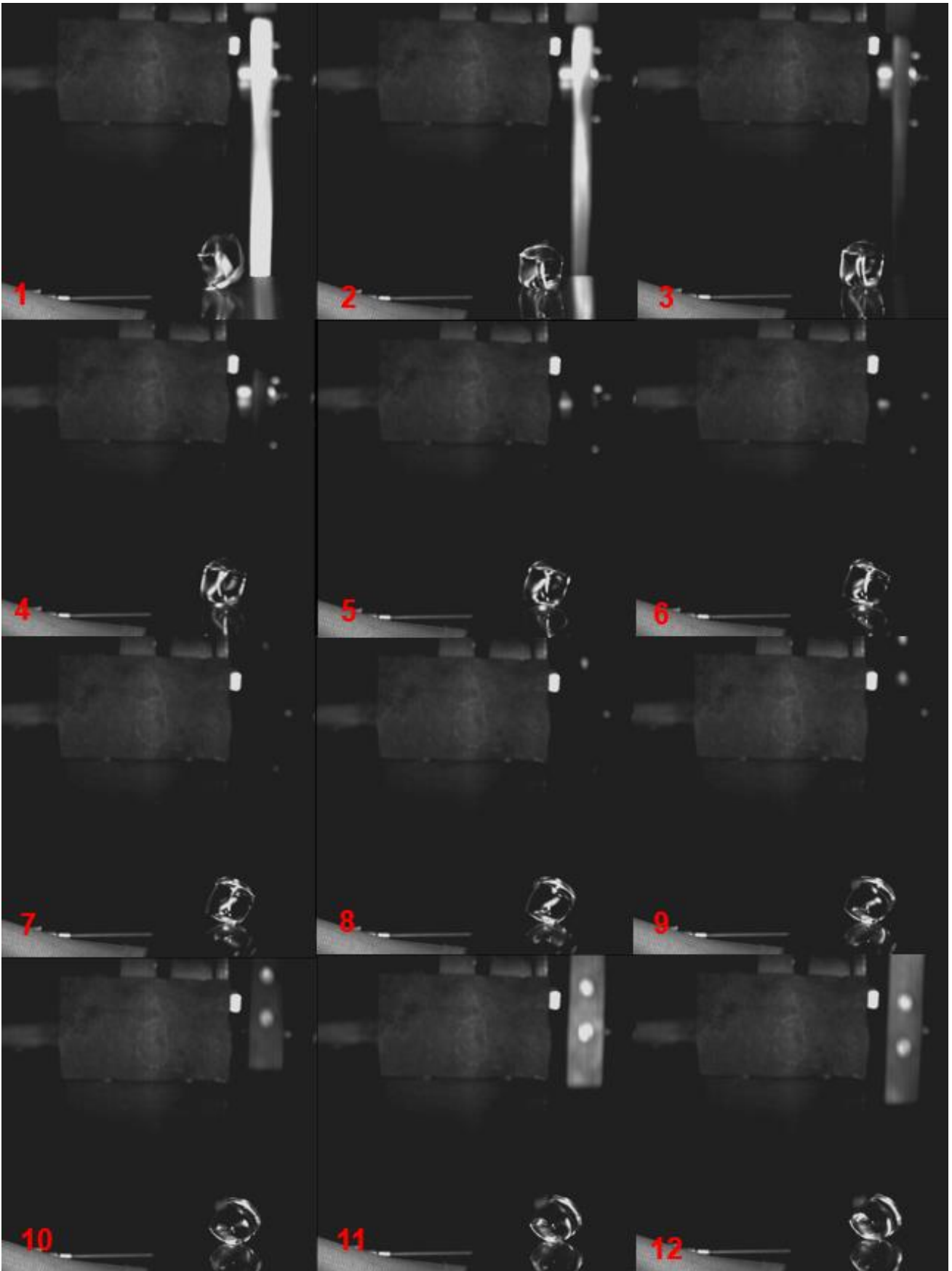


Figure 4.76 Gob 71 contact video sequence: each picture follows the previous one of 0.001 s.



Figure 4.77 Gob 71 makes a half round on the plate before sticking to it. The image was taken few milliseconds after figure 4.76.



Figure 4.78 Test 123: gob sticking on AISI 316 plate at 120 °C (air dew point 12.8 °C).

Test number	Test date	Test hour	Plate temperature	Did gob bounce?	Gob weight	PET pellets humidity	Min and Max electrical absorption extrusion screw		Extruder inlet (zone 1)	Melt temperature	Air dew point	Air relative humidity
			(°C)		(g)	(ppm)	(kW)/100	(kW)/100	(°C)	(°C)	(°C)	(%)
<b>AISI 316</b>												
71	04-07-2017	10:40	120		n.a.		71	87			13	31
72	04-07-2017	10:52	120				70	87			12.7	27.3
83	04-07-2017	14:10	120		4.0204	26	77	88			11.2	21
84	04-07-2017	14:18	120		4.0212		68	78			11.6	21.6
85	04-07-2017	14:27	120		4.0294		55	75			12.7	24.9
86	04-07-2017	14:34	120		4.0171		72	86			11.9	23
87	04-07-2017	14:44	120		4.0176		68	76			11.5	22.4
	05-07-2017	10:56				23						
	05-07-2017	11:23								275		
123	05-07-2017	11:37	120		4.027		71	81	251.9		12.8	26.1
124	05-07-2017	11:40	120		4.0198		81	89	245.6		12.7	25.7
<b>EN-AW-6082-T6</b>												
	05-07-2017	15:46								274		
218	05-07-2017	16:11	120		4.0181	6	84	92	246.2		12.6	22.9
219	05-07-2017	16:14	120		4.043		83	95	245.9		12.7	22.8
220	05-07-2017	16:19	120		4.0378		76	85	252.5		12.5	22.9
	06-07-2017	15:45				16						
	06-07-2017	15:45								280		
256	06-07-2017	15:53	120		4.0169		57	67	252.8		12.6	24.6
257	06-07-2017	15:58	120		4.0276		83	91	246.5		12.8	22.5
258	06-07-2017	16:03	120		4.0244		81	91	244.8		11.8	20.9
259	06-07-2017	16:08	120		4.0327		73	80	251.2		11.3	20.5
260	06-07-2017	16:15	120		4.024		78	91	249.8		12	20.5
	07-07-2017	12:10				19						
	07-07-2017	12:10								276		
281	07-07-2017	12:22	120		4.022		69	76	253.1		8.6	19.4
282	07-07-2017	12:38	120		4.0325		75	84	253.2		8.2	17
283	07-07-2017	13:45	120		4.0186		82	92	253.1		7.6	15.7
284	07-07-2017	13:52	120		4.0315		82	90	246.5		9.7	18.4
285	07-07-2017	13:59	120		4.0325		87	95	244.3		8.2	16.8

Table 4.31 Collage of tests reports at plate temperature equal to 120 °C.



Figure 4.79 Test 83: gob sticking on AISI 316 plate at 120 °C (air dew point 11.2 °C).



Figure 4.80 Gob 257 (EN-AW-6082-T6, T plate = 120 °C, air dew point 12.8 °C).

Fig. 4.75 and table 4.27 illustrate that, at high temperature (135 °C), a huge difference in air dew point did not affect gob adhesiveness.

In conclusion, analyzing collected data, it seems not possible to formulate a rule on air humidity influence on PET gob adhesiveness to metal plate.

#### 4.6.2.3 Conclusion

In the previous paragraphs, the effects of gob weight and water content in PET pellets and moisture in air on PET gob adhesiveness to metal plates were analyzed.

The measured values of minimum and maximum extrusion screw engine electrical absorption and of the extruder inlet zone temperature seem not to have any influence on test results.

Another variable is the date of the tests. It could be argued that, even if many parameters were monitored, other non-monitored ones could differ from day to day. On 5<sup>th</sup> July 2017, both AISI 316 at 90, 95, 100, 105, 110, 120, 130 °C plate temperatures and EN-AW-6082-T6 at 95, 100, 110, 120, 130 °C plate temperatures were tested, as shown in tables from 4.18 to 4.26. A different behavior of the two materials were still confirmed.

We can conclude that, for a given plate material, all monitored parameters, but plate temperature, did not to have any effects on PET gob adhesiveness to the metal plate.

### 4.6.3 Adhesiveness below sticking temperature

The phenomenon is firstly approached with the model illustrated in paragraph 4.4, i.e. evaluating adhesion behavior below sticking temperature through an analysis of gob kinetic energy variation. When gob bounces its rotation axis is no more parallel to the camera axis, but it becomes parallel to the horizontal purple line in the lower part of fig. 4.81. Therefore, it is difficult to evaluate the angular speed after contact. For a first evaluation, the analysis was limited to only the first component (the translational one) of the kinetic energy in the equation (4.2) illustrated in paragraph 4.4. In particular the change in speed of gob center of mass (mm/s) was analyzed.

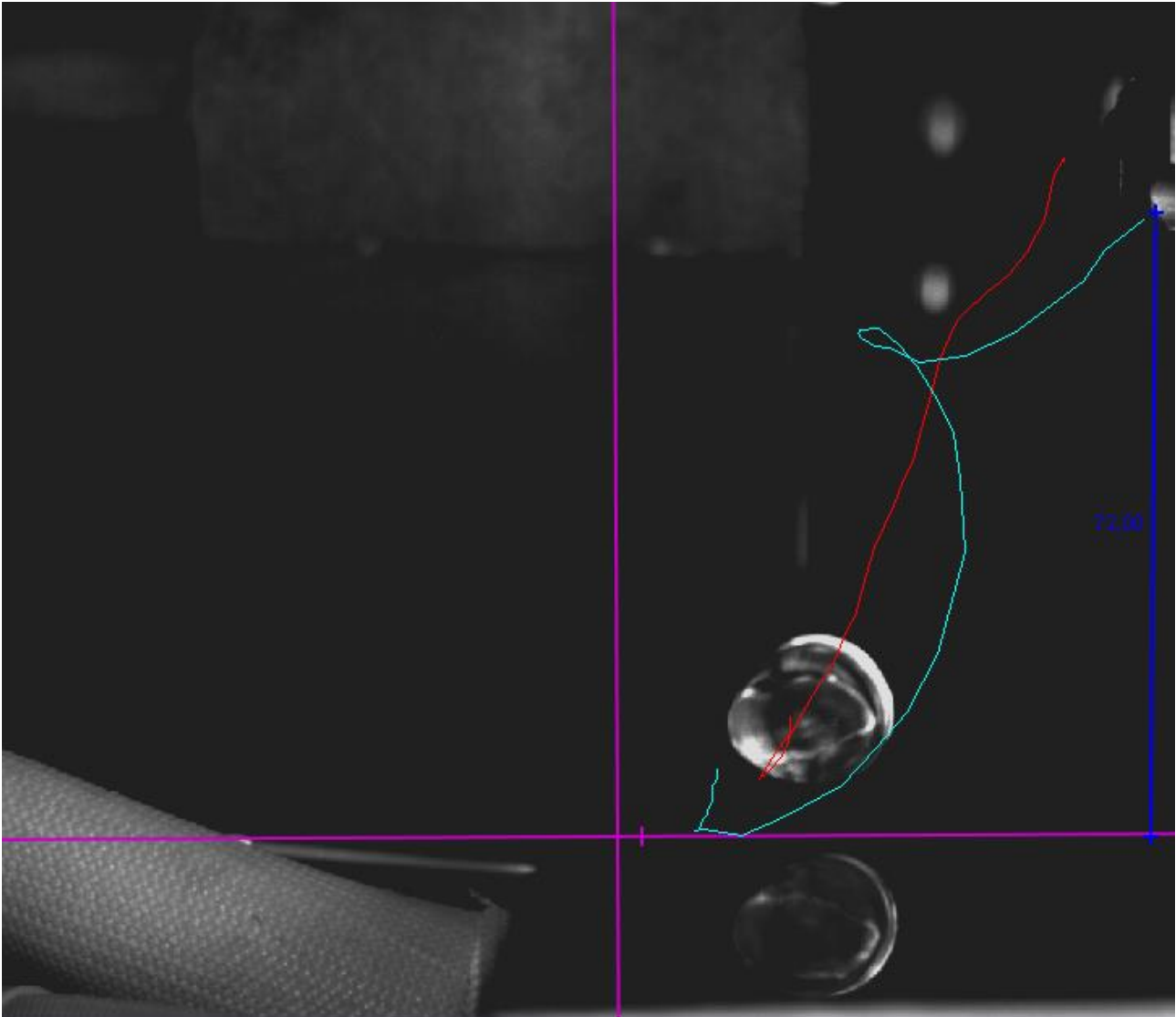


Figure 4.81 Gob after bouncing on plate (gob points trajectories traced with Tracker<sup>®</sup> tool).

With Tracker<sup>®</sup> (see fig. 4.56) the last 5 speed values before contact and the first 5 speed values after contact were measured. Measurements values were not satisfying, because standard deviation was very high. Therefore, each video was elaborated again manually by the operator trying to be more accurate in putting the tracking point in the exact gob center of mass, for each time step. Only three speed values before and after the contact were carefully taken because of the time required. This kind of analysis was done in the temperature range where gob metal adhesion did not occur to verify if below the adhesion threshold temperature, the adhesion decreases as temperature declines, or if it is an on-off mechanism. The extreme values of the range of temperatures where there are no gobs sticking to plate were firstly analyzed, in order to emphasize the phenomenon. The results, shown in

fig. 4.82, tend to confirm the second hypothesis. The graph in fig. 4.82 represents for different temperatures and plate materials the average gob speed before contact with plate (bright color) and the average gob speed after the contact (soft color) with their standard deviation. Blue data are about EN-AW-6082-T6 plate, while red ones are about AISI 316 one. Each point consists in a sample of 5 gobs. For AISI 316 two samples were illustrated at 80 °C. The difference is relevant, and of the same level of the difference with samples at 50 °C. About EN-AW-6082-T6 it seems that the work of adhesion is higher at low plate temperature but considering its standard deviation and the grade of uncertainty in speed data collection with Tracker<sup>®</sup> it is possible to say that there are no appreciable differences.

Adhesion seems hence an on-off mechanism which is activated beyond a certain temperature which is different between EN-AW-6082-T6 and AISI 316.

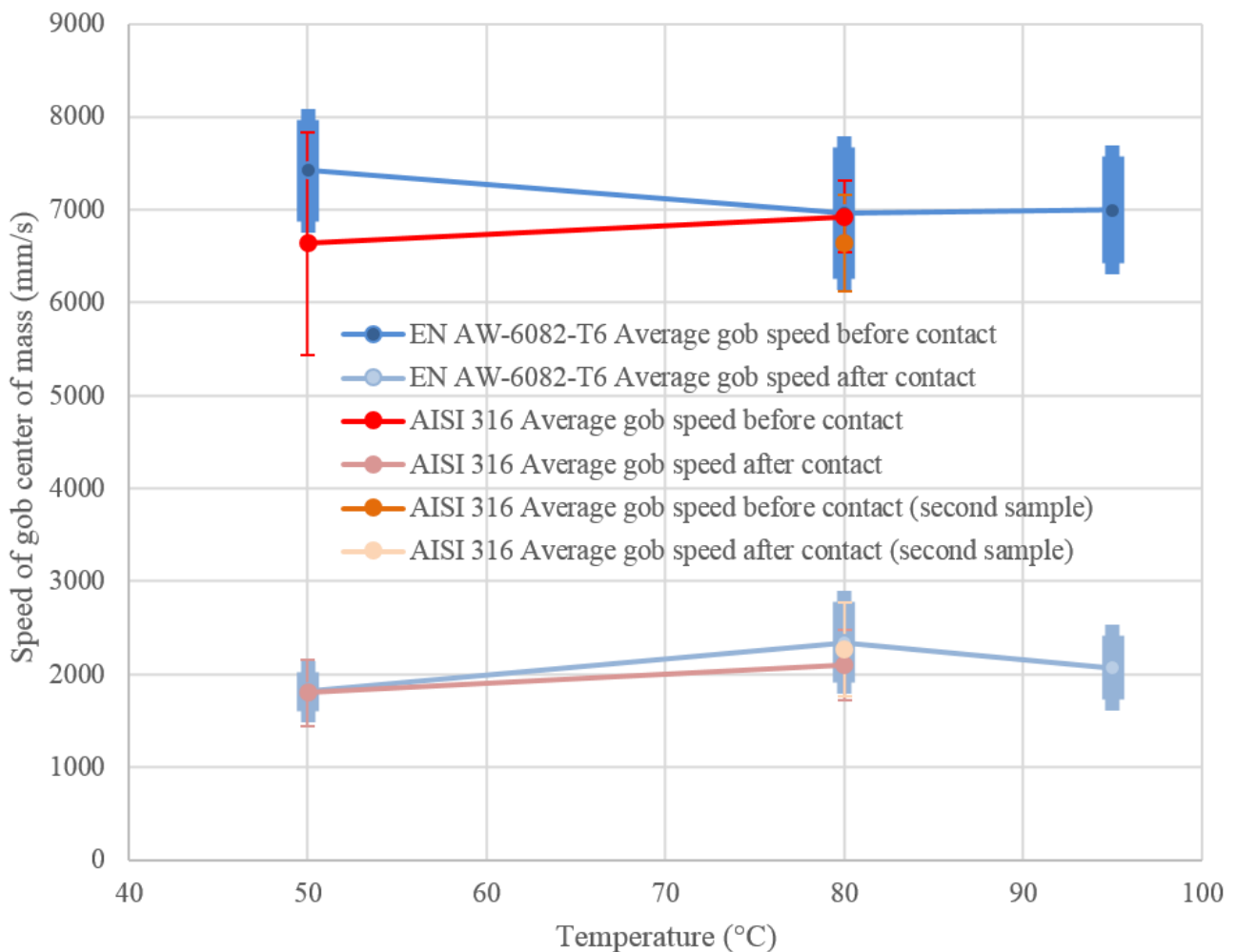


Figure 4.82 Average gob speed before contact with plate (bright color) and after the contact (soft color).

Moreover, as it was done for kinetic energy evaluations, an analysis of gob contact time (defined at the beginning of paragraph 4.5.2) was done on samples at the extreme values of the range of temperatures where there are no gobs sticking to plate. The contact time found in paragraph 4.5.2, i.e.  $0.003 \pm 0.0005$  s, has been confirmed both on AISI 316 (table 4.32) and on EN-AW-6082-T6 (table 4.33). There are no differences between 50 °C and 80 °C for stainless steel, nor between 50 °C and 95 °C for aluminum alloy. This is another proof for adhesion as an on-off mechanism.

Test number	Test date	Test hour	Plate temperature (°C)	Did gob bounce?	Gob weight (g)	PET pellets humidity (ppm)	Min and Max electrical absorption extrusion screw		Extruder inlet (zone 1) (°C)	Melt temperature (°C)	Air dew point (°C)	Air relative humidity (%)	Contact time (number of frames)	Video framerate (Hz)	Contact time (s)
							(kW)/100	(kW)/100							
<b>AISI 316</b>															
	17-07-2017	11:40				22									
	17-07-2017	11:40							278						
466	17-07-2017	11:45	85	4.042	4.042		90	94	252.8	5.2	14.6	-	2000	-	
467	17-07-2017	11:49	85	4.046	4.046		84	92	245	5.7	15.8	-	"	-	
468	17-07-2017	11:55	85				79	83	246.1	6.2	16.1	6	"	0.003	
469	17-07-2017	11:57	85				85	88	246.2	6.4	16.5	6	"	0.003	
470	17-07-2017	12:02	85				83	89	249.7	7.6	18	6	"	0.003	
	17-07-2017	12:05				22									
	17-07-2017	12:05							278						
	17-07-2017	13:21				26									
	17-07-2017	13:21							277						
471	17-07-2017	13:25	80				84	91	251.4	5.1	15.7	6	2000	0.003	
472	17-07-2017	13:30	80				55	62	248.7	5.8	15.7	6	"	0.003	
473	17-07-2017	13:34	80				81	89	252.7	5.2	15.4	6	"	0.003	
474	17-07-2017	13:39	80				87	96	254.7	5.9	15.3	6	"	0.003	
475	17-07-2017	13:44	80				86	88	247.3	6.5	16.2	6	"	0.003	
	17-07-2017	13:46				10									
	17-07-2017	13:46							277						
	13-07-2017	09:07				40									
	13-07-2017	09:07							277						
381	13-07-2017	09:14	50				67	72	245.5	15.3	31.7	6	2000	0.003	
382	13-07-2017	09:18	50				83	89	246.6	16.2	31.4	6	"	0.003	
383	13-07-2017	09:23	50				78	83	256.7	13.7	25.8	6	"	0.003	
384	13-07-2017	09:27	50				84	89	250.4	13.9	25.9	6	"	0.003	
385	13-07-2017	09:36	50				82	89	246.8	13.8	24.5	6	"	0.003	
	13-07-2017	09:45				27									
	13-07-2017	09:45							278						

Table 4.32 Analysis of gob contact time on AISI 316 plate.

Test number	Test date	Test hour	Plate temperature (°C)	Did gob bounce?	Gob weight (g)	PET pellets humidity (ppm)	Min and Max electrical absorption extrusion screw (kW)/100	Extruder inlet (zone 1) (°C)	Melt temperature (°C)	Air dew point (°C)	Air relative humidity (%)	Contact time (number of frames)	Video framerate (Hz)	Contact time (s)
	11-07-2017	09:44				50								
	11-07-2017	09:44							278					
321	11-07-2017	09:49	95				74	247.9		13.6	35.8	6	2000	0.003
322	11-07-2017	09:54	95				71	250.3		13.8	25.8	6	"	0.003
323	11-07-2017	09:59	95				83	255.2		14.1	29	6	"	0.003
324	11-07-2017	10:02	95				75	252.1		15	30.1	6	"	0.003
325	11-07-2017	10:07	95				81	252.3		14.9	29.2	6	"	0.003
	11-07-2017	10:10				22								
	11-07-2017	10:10							277					
	11-07-2017	14:25				24								
	11-07-2017	14:25							n. a.					
346	11-07-2017	14:35	80				80	245.6		11.6	21.8	6	2000	0.003
347	11-07-2017	14:41	80				60	251.8		13.2	24.5	6	"	0.003
348	11-07-2017	14:49	80				80	250.1		11.4	21.1	6	"	0.003
349	11-07-2017	14:54	80				81	248.3		10.6	19.8	6	"	0.003
350	11-07-2017	15:00	80				86	252		11.2	21.9	6	"	0.003
	11-07-2017	15:05				26								
	11-07-2017	15:05							n. a.					
	11-07-2017	12:54				25								
	11-07-2017	12:54							n. a.					
331	11-07-2017	13:03	50				79	252.6		12.1	27.8	6	2000	0.003
332	11-07-2017	13:08	50				71	253.1		11.8	24.2	6	"	0.003
333	11-07-2017	13:13	50				81	248		11.3	23.7	6	"	0.003
334	11-07-2017	13:18	50				83	252.4		11.7	23.2	6	"	0.003
335	11-07-2017	13:22	50				69	252.2		11	22.8	6	"	0.003
	11-07-2017	13:24				15								
	11-07-2017	13:24							n. a.					

Table 4.33 Analysis of gob contact time on EN AW-6082-T6 plate.

## 4.7 SHORT CONTACT TIME ADHESIVENESS MODEL

Molten PET gobs were made with the same grade of PET which was dehumidified in the same plant according to a certain procedure to achieve a water content lower than 50 ppm and finally were extruded by the same extrusion screw with the same operating parameters. The melt exiting from the nozzle had about the same temperature and was mechanically cut to obtain gobs of about the same weight.

Two metal plates were made of different materials (i.e. AISI 316 and EN-AW-6082-T6) but with the same surface roughness and about the same surface free energy.

These gobs hit the metal plate with almost the same trajectory and motion law, showing different behaviors depending on the plate temperature and on the plate material. In particular, below a certain temperature, which is clearly different between AISI 316 and EN-AW-6082-T6, gobs never adhered.

Analyses on gob speed, before and after cutting, show no differences within the examined range of temperatures where gob never adhered. Analyses of gob contact time with plate lead to the same results.

On the other hand, above another certain temperature, which appears different between AISI 316 and EN-AW-6082-T6, gobs always adhere. In between there is a temperature range where gob behavior could result in adhesion and it seems not possible to relate it to some of the monitored parameters.

Previous observations led to think that a mainly on-off mechanism with an activation threshold for PET adhesiveness on the aforementioned metal surfaces is acting.

Gobs contact time with metal is about 0.003 s and, in such a short time, the interaction taking place in conventional plastic to metal adhesion (contact time of the order of seconds) cannot occur. Moreover, the chemical attitude of the surfaces to create polar or disperse bonds are almost equal.

Temperatures at which gobs start adhering to metal plates are about 80 °C for AISI 316 and about 92 °C for EN-AW-6082-T6. It is interesting to note that these temperatures are close to PET glass transition temperature ( $T_g$ ) which is about 80 °C [3]. It is known that above  $T_g$  polymer chains acquire some mobility. As seen in chapter 2, mechanical interlocking is one of the main adhesion mechanism between polymer and metal. Its adhesion strength could increase with temperature because the latter enhances chains mobility [17]. Moreover, mechanical interlocking is a function of contact surface roughness, but the ones of the two plates are almost equal.

A metal physical property shown in table 4.2 could help understand the phenomenon.

EN AW-6082-T6 has a thermal conductivity which is an order of magnitude higher than AISI 316 one and three order of magnitude higher than PET one [3]. The superficial layer of PET gob in contact with metal plate is quickly cooled down, even below  $T_g$ , since the heat inside the gob takes too much time to transfer on the gob surface and to keep it warm. PET surface equilibrium temperature is lower when it is in contact with EN AW-6082-T6 because it can dissipate heat ten times faster compared to AISI 316.

A lower temperature on PET surface layer at the same plate temperature could be the reason of the different behavior between EN AW-6082-T6 and AISI 316. For example, at a plate temperature of 92 °C, on AISI 316 PET chain mobility is enough to generate mechanical interlocking, while on EN AW-6082-T6 it is not.

The reason why at a temperature equal or higher than 115 °C all forty-nine gobs stuck on EN AW-6082-T6 plate, while, on AISI 316 one, a gob bounced at about 116 °C and another one at about 126

°C out of sixty-three ones is not clear yet. The reason could be just statistical, or chemical, or maybe related to the different coefficients of thermal expansion of the two plates. Future developments of this thesis work could be a deeper investigation of this phenomenon.

#### 4.8 REFERENCES

- [1] <http://www.totalmateria.com/page.aspx?ID=Home&LN=EN>, viewed on 12/10/2017.
- [2] <http://www.goodfellow.com/E/Stainless-Steel-AISI-316.html>, viewed on 12/10/2017.
- [3] M. Camerani, *PET AND ITS PREFORMS Handbook*, SACMI, 2008, ISBN 88-7586-132-3.
- [4] K.V. Shalnov, K. Uemura and Y. Ito, *Consideration on Surface Modification of Steel Dies to Reducing the Plastic Sticking in the Forming Process*, Tribology Online, 2012, **7** (3), pp. 190-200.
- [5] <https://www.kruss.de/services/education-theory/glossary/>, viewed on 12/10/2017.
- [6] D. H. Kaelble, *Dispersion-Polar Surface Tension Properties of Organic Solids*, J. Adhesion, 1970, **2**, pp. 66-81.
- [7] D. Owens; R. Wendt, *Estimation of the Surface Free Energy of Polymers*, J. Appl. Polym. Sci, 1969, **13**, pp. 1741-1747.
- [8] W. Rabel, *Einige Aspekte der Benetzungstheorie und ihre Anwendung auf die Untersuchung und Veränderung der Oberflächeneigenschaften von Polymeren*, Farbe und Lack, 1971, **77**, (10), pp. 997-1005.
- [9] K.J. Kubiak, T.G. Mathia, M.C.T. Wilson, *Methodology for metrology of wettability versus roughness of engineering surfaces*, Proceedings of 14th Congrès International De Métrologie, Paris, 2009.
- [10] R.N. Wenzel, *Ind. Eng. Chem.*, (1936), **28**, p. 988.
- [11] A.B.D. Cassie, S. Baxter, *Trans. Faraday Soc.*, 1944, **40**, p. 546.
- [12] David R. Lide, ed., *CRC Handbook of Chemistry and Physics, 85th Edition*, CRC Press, Boca Raton, FL, 2004.
- [13] C. J. van Oss, *Interfacial Forces in Aqueous Media, 2nd Edition*, CRC Press, Boca Raton, FL, 2006.
- [14] J.R. Dann, *J. Adhnsn. Sci. Tech.*, 2007, **21**, p. 961.
- [15] K. J. Kubiak et al., *Wettability versus roughness of engineering surface*, Wear, 2010, **271**, pp. 523-528.
- [16] N. Grizzuti, *Reologia dei materiali polimerici: scienza ed ingegneria*, Edizioni Nuova Cultura, Roma, 2012, ISBN: 9788861348165
- [17] K. Ramani and B. Moriarty, *Thermoplastic Bonding to Metals Via Injection Molding for Macro-Composite Manufacture*, Polym. Eng. Sci., 1998, Vol. **38** (5).

## Chapter 5

### CONCLUSIONS

This thesis is about the research done on the handling of molten Poly(ethylene terephthalate) (PET) cylinders for preform compression molding and it has been developed in collaboration with SACMI, a world leading company in packaging, ceramics machines and plants manufacturing.

PET is the world's most common and best-known polyester and in 1973 its use for the production of shatterproof beverage bottles was patented. PET converter demand is rising over years (see paragraph 1.1).

The current industrial technology to make preforms is the injection (see paragraph 1.3): molten PET is pumped in closed molds which have a preform shape. This technology has several constraints, namely a minimum preforms thickness and a high PET temperature.

An alternative technology to make preforms is compression molding (see paragraph 1.4). In this technology, molten PET exits from a vertical axis nozzle whose dimensions vary according to preform geometry and mass. After the nozzle, a rotating blade cuts a cylinder of molten PET called "gob". The gob is then handled and put inside an open mold cavity. The closing of the mold gives the gob a preform shape.

Compression molding is a cutting-edge technology which could start a revolution in the beverage field, since it allows an important saving of raw materials, i.e. plastic, which, for natural water, is the greatest part of the cost of the final product, i.e. the bottle (see paragraph 1.5).

Secondly, rotative compression molding machine allows a high productivity in a single-stage process plant. Single-stage means that bottles are made directly from PET pellets, without cooling down the preform and then heating it up again. This results in a huge energy saving and better bottles quality compared to the benchmark on the market which is the double-stage injection and blowing.

Thirdly, compression molding prevents the majority of defects on preforms which are related to the presence of the injection point (see paragraph 1.5.3).

Finally, it allows a strong decrease in the production of Acetaldehyde (AA) (see paragraph 1.5.8), which is highly undesirable because it modifies the water taste.

However, as shown in paragraph 3.1, compression technology presents some big challenges, above all the handling of the molten PET gob, which strongly limits the industrial use of this technology. Direct experience in this field proves that molten PET adhesiveness with metals increases with gob passages.

Academic literature does not deal with this topic, while there are many patents on it (see paragraph 3.2). However, none of them seems to have completely solved the issue and that is one of the main reasons why nowadays there are no industrial preform compression molding machines on the market.

In this thesis, a new way to handle the PET gob has been presented (chapter 3), i.e. a gob pneumatic transport, which is now patent pending. The idea was to avoid or at least reduce the contact between the gob and the handling device surface. Moreover, the possibility to slow or accelerate the gob speed by changing air pressure/flow rate seemed to be interesting. An air flow could also create a field of forces able to actively guide the preform. Swirl flow, or cyclone, was analyzed for its characteristics:

no direct air injection on the gob (low risk of gob local deformation) and a theoretical gob stabilization effect due to rotation (like it happens to a bullet in a gunmetal).

Some preliminary computational fluid dynamics (CFD) simulations (paragraph 3.3) were done without the gob, because modelling the gob without introducing some simplifying assumptions is very complex and time demanding. Moreover, it is important to do some experiments to validate the simulation. The preliminary simulations were done with two attempted angle  $\alpha$  values, where  $\alpha$  is a characteristic swirl flow parameter.

A ten-year-old PAM prototype (PAM002A) installed at a converter factory was used for the preliminary gob pneumatic transport tests because it was the only industrial machine available to start the tests (see paragraph 3.4.1). It was important to conduct tests in an industrial plant to have the same PET dehumidification and extrusion process, die swelling conditions, gob handling time and finally the possibility to check the quality of the final product, i.e. the preform.

Research was done on how to design and manufacture a swirl pipe geometry close to the one simulated with CFD and on how to install it as a handling tool in the testing machine (see paragraph 3.4.2).

The first pipe tested was the solution with  $\alpha = 60^\circ$  (see paragraph 3.4.3). Swirl flow effectively exerts a suction power that attracts the gob inside the pipe. That suction can avoid an incorrect gob loading which would occur with present gob handling technology. Gob handling reproducibility tests show a good correlation between air pressure and gob exit angle which could be very useful to automatically handle the aforementioned increase of adhesiveness after many gob passages.

The surprising result with  $\alpha = 15^\circ$  (see paragraph 3.4.4) is that the gob is floating, spinning on itself in a range of positions along the pipe axis, which are a function of the flow rate. Gob floating allowed gob insertion in the cavity and hence preform compression molding. A new kind of test became possible: endurance test on preform compression molding with swirl handling tool. Before repeating the test, the internal pipe surface was cleaned with a commercial multi-purpose cleaner spray and a cloth. The spray is composed of a mixture of heterocyclic nitrogen compounds with glycol ether and alcohols. Some parts of the machine were modified to insert additional sensors. A huge experimental work has been done to mainly optimize pipe geometry, surface roughness and temperature. Another testing parameter was the combination of several kinds of flows with a certain flow rate and with a certain angular phase. As a matter of fact, air flow towards the cavity can lead to gob bouncing. If the bounce is too high a defect can be generated on the preform. This inconvenience leads to the adoption of precise pneumatic valves to allow the air flows only in precise and repetitive positions.

Handling tool reliability grew from few preforms made before gob stuck to swirl pipe, to thousands of gobs handled without errors. Geometry, additional flows and surface roughness can raise anti-adhesion performances but do not eliminate adhesiveness effects that, at present, come out after about 10000 gob passages. Such a result makes this solution very interesting for its application on an industrial compression molding machine.

Pipe wall temperature values from  $10^\circ\text{C}$  to  $45^\circ\text{C}$  did not show any significant impact on endurance tests. The results for higher temperature are surprising because as temperature increased, a temperature value was reached where the first gob stuck on the cleaned pipe. The temperature at which the gob stuck after one, maximum two passages, was higher for aluminum alloy EN-AW-6082-T6 compared with stainless steel AISI316. It is interesting to note that sticking temperatures are closed to PET glass transition temperature. The phenomenon, molten PET-metal stickiness after a contact time of the order of  $10^{-3}$  s, is not described in the existing literature, as seen in chapter 2. It is analyzed in chapter 4.

Preforms made with swirl pipe handling tool (fig. 3.44) show an axial symmetric distribution of tension lines which, according to SACMI Lab and compression molding testing customer experience, will make preforms result in bottles of good technical quality (see paragraph 3.4.4.4). Some preforms present defects, but it is not possible to prove if they were generated by the swirl pipe or by other causes related to the absence of maintenance in some parts of the machine during former years.

Some considerations on adhesiveness are in paragraph 3.5. Adhesiveness, as previously explained, increases if the surface has already been in contact with PET. Touching with a fingertip the inner part of the pipe when adhesiveness effects start happening, a feeling of a slightly sticky surface occurs compared to a cleaned one. From the optical point of view the surfaces look similar and they have the same size (measures with 0.005 mm precision). It was not possible to analyze the inner part of the pipe with Fourier Transform Infrared Spectroscopy (FTIR), without cutting a part of the pipe and hence probably eliminating the tracks of interest or introducing new elements. On the contrary, gob cutting knife has a flat surface which allows FTIR analyses of a visible white thin layer deposited after many gobs touching. Powder and layer were analyzed with FTIR. Fig. 3.45 compares the spectra of the white thin layer on the gob cutting knife (red) and of the PET (green): the match is very good.

It is known that during poly-condensation reaction (fig. 3.46) under vacuum with catalyst, two or more BHET molecules (fig. 3.47) can react by closing on themselves and forming for example Ethylene Terephthalate Cyclic Dimers (fig. 3.48) with the release of two ethylene glycol molecules. These cyclic dimers, or generally cyclic oligomers, do not have OH groups. They hence have a higher volatility compared to their non-cyclic equivalent ones, even if they have almost the same molecular weight. OH groups increase molecules boiling temperature because they can create hydrogen bonds, so it is no more correct to use the term polymer boiling point, because, at high temperature, degradation occurs before boiling could happen. PET made in industrial reactors has a polydispersity index higher than three, as shown in fig. 3.49. According to Rieckmann and Völker PET contains about 2–3% of short-chain oligomers, which can occur as linear or cyclic molecules. Cyclic oligomers that are inside the polymer gob could vaporize and condense on pipe wall that is cold, compared to the gob temperature (about 270 °C). This could be an explanation for the adhesiveness increase after many gob passages.

Preliminary gob handling tests with a swirl flow on a real preform compression molding machine showed that it is worthy to continue the developments. Once validated, improved CFD simulations (see paragraph 3.6) of the phenomenon could help understand how to increase swirl pipe efficiency. Moreover, once the desired performances are reached, simulations could reduce costs and testing time of new pipes design. Different bottles have different preforms which have different gob dimensions in their turn, so it is necessary to have a dedicated swirl pipe for each kind or family of preforms.

The first improved simulation was without gob. The aim was to better simulate the swirl flow and it was reached through a transient simulation performed with the software AcuSolve™ that helped to better examine swirl flow instabilities. The software can also be used to find the  $\alpha$  limit value below which the gob floats and above which the gob accelerates.

The second improved simulation was with gob. The aim was to check if it was possible to simulate the phenomenon and validate it by comparing the simulation resulting video with the high-speed camera video. Three approaches were possible (see par. 3.6.2): Fluid–structure interaction (FSI), six degrees of freedom and multiphase approach. The second approach was chosen because it seemed the best compromise between accuracy and time/difficulty. The simulation was done with the commercial software FLOW-3D, which already have collisions, friction and non-interpenetration models. Gob is modelled as a rigid body with six degrees of freedom in a CFD air domain. Collisions are assumed as completely elastic and air as an incompressible fluid. The handling tool is simulated

still, neglecting transferring carousel angular speed. The first modelled step was gob floating with  $\alpha$  equal to  $15^\circ$ . The results were encouraging. After few hundredths of seconds, when simulation starting transient could be considered as finished, the gob almost reached the height it had in the test on the machine, with similar small axial oscillations. Comparing the video of the simulation with a real gob rotation in a video made with a high-speed camera at 2000 frame per second (fps), it was found that gob trajectory and motion law are almost the same, so gob floating can be considered as validated. The other steps of the swirl pipe handling cycle are still to be simulated.

As previously said, PAM002A has several limitations. For example, due to the wide angle between the nozzle and the cavity mold, it is not possible to test the gob accelerating swirl pipe ( $\alpha = 60^\circ$ ) with the gob transferring to cavity or it is necessary to keep the gob floating for about two seconds before transferring it to the cavity without a real advantage in doing it.

The idea was to design a testing machine (PAMLAB), see paragraph 3.7, that allows to test every kind of trajectory and motion law to help answer the questions raised above. To do this, two couples of synchronous linear motors were used to move two couples of axes, since a high precision is required between handling tool axis and cavity mold axis. The PET extruder is an industrial unit. Its extrusion screw has a diameter of 100 mm and its flow rate goes from 60 to 600 kg/h. As in PAM002A tests, PET dehumidification, PET extrusion process, die swelling conditions and dehumidification in the working area are the same as those on a preform compression molding industrial machine, making the test results more reliable. Moreover, the testing machine is designed to perform cutting tests with several kinds of blades and a wider range of cutting speeds with respect to the tests already done. The limit of the testing machine is that there is no feedback on preform or bottle quality. PAMLAB must be considered as a tool to make an initial selection between various solutions. It allows a huge reduction in tests time and costs: what on an industrial machine would require months of work on PAMLAB could be done in few days. PAMLAB was designed to perform endurance tests and hence it could work continuously for all the hours required. The scrap containers, which must be changed every working hour, can be moved while the machine is working. Proper sensors and protective devices allow the technicians to work in safe conditions.

To sum up, the first tests on a new PET gob handling technique gave promising results. They have to be completed and the new testing machine is almost ready for this purpose. Once handling tool best configurations are found, its technological validation tests must be done by producing preforms and bottles on an industrial machine. After many cycles, the handling tool must be cleaned since its adhesiveness increases probably due to cyclic oligomers condensation on pipe walls. To reduce the operators' costs, it will be strategic to find and test cheap and safe ways to clean the handling device periodically and automatically. This must be done in accordance with HACCP (Hazard analysis and critical control points). Some possible technical solutions are not described here due to SACMI intellectual property policy.

Chapter 4 is about the study of a new phenomenon seen during swirl pipe endurance tests described in chapter 3. As previously mentioned, in chapter 3 it was assumed that the cause of increased adhesiveness is probably the deposition of short-chain PET cyclic oligomers on the metal wall. As wall metal temperature increases, PET oligomers adhesiveness should decrease since the driving force of oligomers condensation on colder metal wall declines. Nevertheless, this did not happen. On the contrary, with an increase in the metal surface temperature, adhesiveness rose rapidly until the gob stuck at the first contact with a cleaned metal surface. A new test was designed to investigate this new and unknown phenomenon. Indeed, existing literature, cited in chapter 2, seems not to deal with adhesiveness for such a short contact time. The test consists in analyzing PET gob adhesiveness during a single short contact time (about  $10^{-3}$  s) with a cleaned surface of an aluminum alloy (EN

AW-6082-T6) and of stainless steel (AISI316) with similar roughness. 180 valid tests were done on stainless steel AISI 316 of which 87 resulted in gobs sticking to the metal plate and 93 in gob bouncing on it. Moreover, 161 tests were done on aluminum alloy EN AW-6082-T6 of which 76 resulted in gobs sticking to the metal plate and 85 in gob bouncing on it, for a total of 341 valid tests on the two plates.

In particular the aims of the test were:

1. To verify that as metal temperature increases, the adhesion between molten PET and the metal plate considerably rises resulting in the gob sticking to the metal;
2. To find the "adhesion threshold temperature" or the range of temperatures starting from which the gob sticks to the metal;
3. To verify that the adhesion threshold temperature or range of temperature is a function of the material by comparing stainless steel AISI316 and aluminum alloy EN AW-6082-T6 and to give an explanation for it;
4. To verify if below the adhesion threshold temperature, the adhesion decreases as temperature declines, or if it is an on-off mechanism.

The machine used for the test is MONOPAM: a prototype of preform compression molding machine with only one mold, already present in SACMI. The peculiarity of this compression machine is that it has, after the extruder and before the nozzle, an oleo-dynamic syringe to accumulate the PET coming from the extruder and to push it quickly so that the same die swelling as that of an industrial machine occurs after the nozzle. After the rotating blade, the remaining parts of the machine (handling tool, mold and post cooling systems) were disassembled or deactivated to adapt the machine for the adhesiveness tests to make the gob hit a metal plate. Metal plate is equipped with an electric thermo-resistance to heat it up, a miniaturized temperature sensing resistor and a PID thermoregulation controller. Plate heating system was accurately characterized to be sure of the measured values and their margins of error. Two metal plates were produced, one with stainless steel AISI316 and one with aluminum alloy EN-AW-6082-T6. A manufacturing procedure was studied to obtain the same level of surface roughness and morphology on the two plates. The results were checked with an innovative and technologically advanced opto-mechanical measuring system with a resolution of 0.6 nm.

Contact angle tests with bidistilled water and diiodomethane were performed on two samples with the same surface roughness and morphology of testing plates. Plates surface free energy were hence calculated according to the Owens-Wendt-Rabel-Kaelble (OWRK) method, resulting in  $45.1 \pm 1.5$  mN/m for EN AW-6082-T6 plate and  $46.1 \pm 2$  mN/m for AISI 316. Therefore, it is possible to affirm that the rough surfaces almost have an equal chemical attitude to create polar or disperse bonds.

The plate was accurately cleaned before starting each test. The aim was to eliminate tracks of previous contact. The cleaning methodology was the same adopted for endurance swirl pipe tests (see paragraph 3.4.4): a commercial multi-purpose cleaner spray composed of a mixture of heterocyclic nitrogen compounds with glycol ether and alcohols and a clean soft cloth (not to ruin the plate surface). For each single test, in addition to date, hour, plate temperature and gob contact behavior, the following parameters are registered: air dew point, air relative humidity, gob weight when the gob stuck. Melt PET temperature and PET humidity were measured every five gobs. Moreover, for each test, a video at 2000 frame per seconds (fps) was recorded with a high-speed video recording camera. The video includes gob cutting and bouncing till the gob exits from the video area or a few frames after the gob sticks.

Molten PET gobs hit the metal plate with almost the same trajectory and motion law, showing different behaviors depending on the plate temperature and on the plate material. In particular, below a certain temperature, which is clearly different between AISI316 and EN-AW-6082-T6, gobs never adhered. To verify if below this temperature, named "adhesion threshold temperature", the adhesion decreases as temperature declines following some mathematical law, or if adhesion is an on-off mechanism activated at a threshold temperature, it would be useful to measure the difference in gob kinetic energy a few instants before and after the gob contact with the plate. A model has been developed in paragraph 4.4. The work of adhesion, as defined in chapter 2 (paragraph 2.3), is the work that must be done to separate two adjacent phases - 1 and 2 of a liquid-solid phase boundary - from one another. Assuming to separate the phase of the gob contact with the metal plate in two steps, the first one is the bond creation while the second one is the bond destruction. During the first step some energy should be released and it will result in thermal energy, while during the second step energy should be absorbed, or, in other words, a work must be done (work of adhesion). PET is a viscoelastic material, which means that it has both viscous and elastic characteristics when undergoing deformation. In particular, its elastic behavior is predominant when a load is applied in a short time. The work of adhesion to separate the PET phase from the metal phase can be considered as given by the elastic energy which the gob accumulated when touching the metal. If this work of adhesion increases, the gob has a lower kinetic energy when leaving the metal. If the work of adhesion oversteps the available elastic/kinetic energy, the bond between gob and plate is not broken. If with subscript 1 all the variables and parameters before gob touches the metal are defined, and with subscript 2 the ones after the gob detaches from the plate, the work of adhesion ( $W_{ad}$ ) can be defined as follows:

$$W_{ad} = \Delta K_{21} = m_g * (v_{G1}^2 - v_{G2}^2) + I_g * (\omega_1^2 - \omega_2^2) \quad (4.2)$$

$m_g$  = gob mass;

$I_g$  = gob moment of inertia (calculated with respect to the axis that passes through the gob center of mass and that is perpendicular to the gob axis);

$v_{G1}$  = velocity of gob center of mass before contact gob-plate;

$v_{G2}$  = velocity of gob center of mass after contact gob-plate;

$\omega_1$  = angular velocity with respect to gob center of mass before contact gob-plate;

$\omega_2$  = angular velocity with respect to gob center of mass after contact gob-plate;

$K$  = gob kinetic energy.

The videos of the experiments show that the gobs change their rotation axis after contact, so it is difficult to evaluate  $\omega_2$ . The evaluation could be done repeating the tests with a high-speed video camera with two heads, which means two lenses placed on two orthogonal points of views. Anyway, for a first evaluation, the analysis was limited to only the first component (the translational one) of the kinetic energy in the equation (4.2). The videos were elaborated with Tracker<sup>®</sup>, which has an automatic trajectory detector but it did not work properly due to PET gob transparency and reflections. For each video, the operator manually selected a point step by step. There is hence a little margin of error. The extreme values of the range of temperatures where there are no gobs sticking to plate were firstly analyzed, in order to emphasize the phenomenon. Analyses on gob speed, hence variation in the kinetic energy before and after cutting, show no differences within the examined range of temperatures where gob never adhered.

On the other hand, above another certain temperature, which appears different between AISI316 and EN-AW-6082-T6, gobs always adhere. In between there is a temperature range where gob behavior could result in adhesion and it seems not possible to relate it to some of the monitored parameters.

Previous observations led to think that a mainly on-off mechanism with an activation threshold for PET adhesiveness on the aforementioned metal surfaces is acting.

Gobs contact time with metal is about 0.003 s and, in such a short time, the interaction taking place in conventional plastic to metal adhesion (contact time of the order of seconds) cannot occur. Moreover, as seen previously from surface free energy analyses, the chemical attitude of the surfaces to create polar or disperse bonds are almost equal.

Temperatures at which gobs start adhering to metal plates are about 80 °C for AISI316 and about 92 °C for EN-AW-6082-T6 (see paragraph 4.6). It is interesting to note that these temperatures are closed to PET glass transition temperature ( $T_g$ ) which is about 80 °C. It is known that above  $T_g$  polymer chains acquire good mobility. As seen in chapter 2, mechanical interlocking is one of the main adhesion mechanisms between polymer and metal. Its adhesion strength could increase with temperature because the latter enhances chains mobility, according to Ramani and Moriarty researches. Moreover, mechanical interlocking is a function of contact surface roughness, but the ones of the two plates are almost equal.

EN AW-6082-T6, as shown in table 4.2, has a thermal conductivity which is an order of magnitude higher than AISI316 one and three orders of magnitude higher than PET one (see paragraph 4.7). The superficial layer of PET gob in contact with metal plate is strongly cooled down, even below  $T_g$ , since the heat inside the gob takes too much time to transfer onto the gob surface and to keep it warm. PET surface equilibrium temperature is lower when it is in contact with EN AW-6082-T6 because it can dissipate heat ten times faster than AISI316.

A lower temperature on PET surface layer at the same plate temperature could be the reason of the different behavior between EN AW-6082-T6 and AISI316. For example, at a plate temperature of 92 °C, on AISI 316 PET chain mobility is enough to generate mechanical interlocking, while on EN AW-6082-T6 it is not.

The reason why at a temperature equal or higher than 115 °C all forty-nine gobs stuck on EN AW-6082-T6 plate, while, on AISI316 one, a gob bounced at about 116 °C and another one at about 126 °C out of sixty-three ones is not clear yet. The reason could be just statistical, or chemical, or maybe related to the different coefficients of thermal expansion of the two plates. Future developments of this thesis could be investigations of the phenomenon.

To sum up, this thesis describes the research done on a new way for the handling of molten PET cylinders for preform compression molding, namely the pneumatic transport through a swirl flow generated by a particular pipe design. The optimal solution was developed both with Computational Fluid Dynamic simulations and extensive field tests on a prototypal compression molding machine. The very promising results led SACMI to patent the swirl flow pipe design. A new testing machine was designed and assembled to further develop the tests, which, if validated, will lead to the ultimate validation on a new compression molding machine prototype. Simultaneously, improved CFD simulations were started with the aim to increase swirl pipe efficiency. Moreover, once the desired performances are reached, simulations could reduce costs and testing time of new pipe design. By comparing the video of the simulation with a real field test video, a part of the process simulation was validated.

The pneumatic transport of the PET gob could hence eliminate the last technological barrier in the realization of an industrial compression molding machine. SACMI will be the first company in the world to have a full compression preform molding machine, which will have all the technological and economic advantages described in detail in paragraph 1.5. As stated in paragraph 1.6, compression molding could massively enlarge the actual use of PET containers limited by injection molding technological parameters. PET could substitute glass and other plastics in Food field, Dairy, Pharms, Alcohols. Moreover, with compression it will be easier to substitute PET with recyclable plastics or biodegradable one. SACMI has already achieved important results with poly(lactic acid)

(PLA). This could lead to a significant increase in the beverage field profits of the company, both from direct selling of preform compression molding machine, and from the expected rise in selling of the other machines of the beverage line. Customers are indeed looking for the advantages of having a turnkey plant (see paragraph 1.2). Furthermore, new employment opportunities are expected to face SACMI increased capacity in machine and molds designing, selling, manufacturing and post selling assistance.

Finally, the effect of metal temperature on PET gob adhesiveness for short time contact, typical of the preform compression molding technology, was studied and an innovative kind of experiment was designed. A tests campaign was hence performed and it allowed to describe a new phenomenon for which a theoretical explanation was proposed. These results gave a valuable contribute on this topic to the scientific community.